

Université Lille 1 –Sciences et Technologies

for obtaining the PhD degree of the

Doctoral School SMRE:
Sciences de la Matière, du Rayonnement et de l'Environnement
Université de Lille1-Sciences et Technologies

Sara SCOLARO

Effects of humidity and fatty acid surfactants on the uptake of NO₂ to NaCl.
Combined study of kinetics and surface analysis.

Supervisors : Claude BREMARD - Professor at the University of Lille 1
Denis PETITPREZ - Professor at the University of Lille 1

Referees : Jean-François DOUSSIN - Professor at the University of Paris 12
Bernard HUMBERT - Professor at the University "Pointcarré" of
Nancy

Members of Jury: Nelly LACOME - Professor at the University "Pierre et Marie
Curie" of Paris
Jean-François PAUWELS – Professor at the University of Lille1

5th November 2009

This PhD thesis was effectuated at the University of Lille 1 (France) in the laboratories:

LASIR - Laboratoire de Spectrochimie Infrarouge et Raman
UMR 8516
Bâtiment C5 - 59655 Villeneuve d'Ascq Cedex

PC₂A – Physicochimie des Processus de Combustion et de l'Atmosphère
CNRS/UMR 8522
Bâtiment C11 - 59655 Villeneuve d'Ascq Cedex

Within the research projects:

“Tools and Techniques for a Changing Atmosphere” of the “Marie-Curie 6th Framework Project” (European Commission) who provided the PhD fellowship (MEST-CT-2005-020659);

and the

IRENI (Institut de Recherche en Environnement Industriel) in the “Quality of Air” research axis.

Effects of humidity and fatty acid surfactants on the uptake of NO₂ to NaCl. Combined study of kinetics and surface analysis.

Abstract

The present work deals with laboratory studies on atmospheric chemistry. In order to increase the understanding of atmospheric processes and the reliability of atmospheric models more information about chemical reactions occurring in the atmosphere are needed. Until recently, heterogeneous gas-particles reactions have not been that much taken into account, compared to the much more studied homogeneous gas-phase reactions. However, it is now established that heterogeneous reactions on the surface of aerosols play an important role in atmospheric chemistry.

In this work we study the heterogeneous reaction of a pollutants of mainly anthropogenic origin, NO₂, on NaCl(100), taken as a surrogate of the marine aerosol. The presence of a native organic coating on field-collected marine aerosol particles (Mochida J., *Geo. Res. [Atm]* 2002, 107, p. AAC1/1) pushed us to investigate the effect of some insoluble fatty acids on this removal reaction of nitrogen oxide in the marine boundary layer.

The originality of this work consists in coupling reactivity studies with high spatial resolution surface analysis techniques.

The aspect of surface status and its reorganisation after reaction has been followed via Raman micro-spectrometry and AFM techniques. Significant modifications in the morphology of the formed nitrate on the surface have been found as a function of the reaction humidity conditions. Raman spectra and images confirm different orientations of NaNO₃ crystals in the presence of surface water (Scolaro S. et al, *J. Raman Spec.* 2009 vol 40, 2, p. 157).

The organic coating on the salt surface (obtained via dip-coating) has been characterized with the same techniques: the inhomogeneous distribution and the presence of nanometric structures can then be proved.

The reactivity of the coated/uncoated salt is investigated in a static chamber allocated inside a FTIR spectrometer, so that the kinetics of the gaseous phase composition can be followed in different humidity conditions (0-80% RH). From the IR spectra we can obtain independently an evaluation of both the uptake coefficient γ (by following NO₂ consumption) and of the reaction probability coefficient ϕ (by following ClNO formation). The presence of a palmitic or oleic acid coating on the salt slightly hinders the reactivity, especially in some humidity conditions.

Moreover the use of a simple reactivity model can lead to a good fit to the experimental points, helping in the interpretation of the global mechanisms involved in the system.

By coupling all the information deriving from the surface analysis and the reactivity measurement we can conclude that the NO₂/NaCl reaction releases into the atmosphere a precursor of active chlorine atoms (ClNO) also in conditions of high humidity and that the presence of even an inhomogeneous insoluble fatty acid coating slightly slows down this process.

Keywords

Atmospheric chemistry, heterogeneous chemistry, uptake coefficient, reactivity coefficient, Raman micro-spectrometry, marine aerosol, nitrogen dioxide, ClNO.

Effet de l'humidité et de molécules tensio-actives sur la capture du dioxyde d'azote (NO₂) par le chlorure de sodium (NaCl). Etude cinétique et analyse de surface.

Résumé

Des études cinétiques et des analyses de surface ont été effectuées sur la réaction multiphasique entre le gaz NO₂ et des cristaux de NaCl en présence de molécules tensio-actives sous air humide. Ces études de laboratoire contribuent à la validation de processus de chimie atmosphérique suggérés par des campagnes de mesures sur des aérosols d'origine marine. Depuis des millénaires les vents provoquent des vagues à la surface des mers et des océans qui propulsent de nombreuses gouttelettes d'eau de mer dans la troposphère. Ces gouttelettes se déshydratent partiellement et forment l'aérosol marin. L'aérosol est constitué de particules de taille micrométrique comportant essentiellement du NaCl et de nombreux composés mineurs dont des acides gras (stéarique, oléique). Les concentrations en particule peuvent dépasser 20 µg/m³ dans l'air des zones côtières. Des quantités énormes d'oxydes d'azote NO_x (x =1, 2) sont émises actuellement par les transports et le chauffage. Les concentrations en NO_x peuvent dépasser 100 µg/m³ dans les zones fortement anthropisées. La cinétique de la réaction multiphasique montre que la capture de NO₂ par NaCl est favorisée par une forte humidité de l'air. Par contre un revêtement d'acides gras réduit peu la production de NaNO₃ et l'émission de NOCl. Les études de surfaces par microimagerie Raman polarisée et microscopie à force atomique (AFM) mettent en évidence les processus de précipitation et de migration de surface dans la production de nanocristaux de NaNO₃ et du faible rôle protecteur des molécules tensio-actives. Le passage de masses d'air d'origine marine dans des zones fortement urbanisées a des impacts négatifs sur la qualité des eaux continentales par des pluies chargées en nitrates et sur la qualité de l'air par des dégagements de gaz chlorés.

Mots clef:

Chimie atmosphérique, chimie hétérogène, coefficient de capture, coefficient de réactivité, micro-spectrométrie Raman, aérosol marin, dioxyde d'azote, ClNO.

Effet de l'humidité et de molécules tensio-actives sur la capture du dioxyde d'azote (NO₂) par le chlorure de sodium (NaCl). Etude cinétique et analyse de surface.

Forme abrégée de la thèse

Cette thèse traite par différentes techniques expérimentales de la réaction multiphasique dans un montage de laboratoire entre le dioxyde d'azote (NO₂) et des cristaux de NaCl sous atmosphère humide et en présence de molécules tensio-actives déposées sur la surface des cristaux. Les résultats expérimentaux contribuent à la validation de processus de chimie atmosphérique hétérogène en rapport avec la pollution des masses d'air d'origine marine traversant des zones fortement anthropisées.

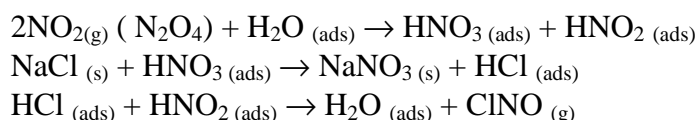
Depuis des millénaires, les vents provoquent des vagues à la surface des mers et des océans et les vagues déferlantes créent des embruns marins qui propulsent dans la troposphère de nombreuses microgouttelettes d'eau de mer. Pendant leur parcours aérien les gouttelettes se déshydratent partiellement en particules de taille micrométrique qui forment l'aérosol marin. La particule individuelle d'aérosol est un mélange interne des composants de l'eau de mer et se compose essentiellement des microcristaux de NaCl avec des composés minéraux et organiques mineurs incluant des acides gras avec des chaînes alkyl saturés et insaturés en C16, C18 et C20, acides palmitique, stéarique et oléique essentiellement. Les concentrations en particules marines peuvent dépasser 20 µg/m³ dans les zones côtières.

Des quantités énormes d'oxydes d'azote NO_x (x =1, 2) sont émises actuellement dans le monde par les transports et le chauffage. Les concentrations en NO_x peuvent dépasser 140 µg/m³ soit 1,8 10¹² molécules par cm³, dans des zones fortement anthropisées. Le séjour dans la troposphère des NO_x induit une séquence d'oxydation par des processus diurne et nocturne dont la phase terminale est HNO₃ en passant par des intermédiaires réactionnels comme NO₃, N₂O₅, HNO₂ (NO_y). Toutefois, NO₂ possède une abondance et une rémanence telles, dans les zones fortement urbanisées, qu'il est détecté comme une espèce d'oxyde d'azote majoritaire par des mesures satellitaires. Le passage de masses d'air d'origine marine dans des zones fortement urbanisées entraîne des anomalies dans la composition chimique des particules d'aérosol marin collectées qui présentent des déficits importants en chlorure (30-80%) par rapport à la stœchiométrie de NaCl. Ce déficit est le signe d'importantes transformations chimiques de l'aérosol marin lors de son parcours dans la troposphère. L'importance de la chimie des aérosols de sel marin avec les oxydes d'azote dans la couche limite de l'atmosphère a inspirée de nombreux travaux de laboratoires depuis plus de 40 ans. NO₂ a la réputation d'être une espèce peu réactive vis à vis de NaCl par rapport à la réactivité de NO₃, N₂O₅, et HNO₃ et beaucoup de phénomènes de chimie hétérogène entre NO₂ et les cristaux de NaCl sont encore inconnus notamment le rôle des composés organiques minoritaires de l'aérosol marin comme les acides gras qui ont des propriétés tensio-actives reconnues.

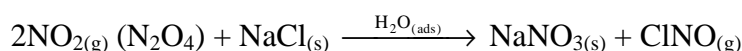
Nous avons effectué des études de laboratoire afin de contribuer à une meilleure compréhension des processus chimiques multiphasiques entre NO₂, oxyde d'azote majoritaire de l'air pollué et des cristaux de NaCl composé minéral majeur de l'aérosol marin dans des conditions réactionnelles simplifiées mais réalistes de la basse troposphère. Ainsi, nous avons reconstitué dans une cellule de réaction une atmosphère de NO₂ diluée dans N₂ ou He dans le domaine de concentration 10¹⁵-10¹⁶ molécules par cm³ avec une humidité relative (RH) dans le domaine 0-80%. Les concentrations dans la phase gaz sont contrôlées par des mesures *in situ* d'absorption FTIR. Le sel marin est représenté dans la cellule par des monocristaux de NaCl taillés selon la face (100) ou des microcristaux de NaCl sous forme de pastilles. Nous avons également maîtrisé le dépôt de sel d'acides gras sur la surface des cristaux de NaCl en utilisant des solutions alcooliques de palmitate de sodium (C16:0) de stéarate de sodium (C18 :0) et d'oléate de sodium (C18 :1) par la technique de dip-coating. Les études utilisant ce type de cellule de réaction ont été réalisées par deux approches expérimentales complémentaires. L'une est centrée sur l'analyse des phases à la surface du solide et l'autre traite essentiellement de la phase gaz en cours de réaction.

L'analyse des phases créées à la surface de NaCl a utilisé les performances de la microimagerie Raman en lumière polarisée et de la microscopie à force atomique (AFM) en mode « tapping ». Les résultats combinés des deux techniques résolues spatialement à l'échelle micrométrique (imagerie Raman) et nanométrique (AFM) ont mis en évidence l'hétérogénéité au niveau nanométrique des dépôts de sel d'acide gras dans des atmosphères de différente humidité. Ils ont également permis d'élucider les mécanismes de formation et de migration de nanocristaux de NaNO_3 . L'exposition de la face (100) d'un cristal de NaCl à une atmosphère sèche de NO_2 ($\sim 10^{15}$ moléc/cm³) pendant 30 minutes ne montre pas de modification notable de la surface (100) de NaCl pendant plusieurs jours. Par contre, si la réaction a lieu en présence d'une humidité même faible des nano cristaux de forme tétraédrique apparaissent à la surface (100) de NaCl. L'organisation des nanocristaux en microagrégats est d'autant plus facilitée que l'humidité relative (RH) est élevée. La microspectrométrie Raman met en évidence la nature chimique des cristaux par la formation de NaNO_3 cristallisé. Quand le RH dépasse 50%, la forme tétraédrique des nanocristaux évolue vers une morphologie rhomboédrique et une taille supermicronique. L'imagerie Raman en lumière polarisée a mis en évidence le changement d'orientation cristalline. Bien avant, la déliquescence (RH~70%) une phase aqueuse contenant une solution de NaNO_3 est observée par microspectrométrie Raman. La formation d'îlots de NaNO_3 est interprétée par la migration de NO_3^- dans les couches d'eau adsorbée qui renouvelle la surface de NaCl et la rend accessible de nouveau à la réaction avec NO_2 . Les principaux résultats exposés succinctement ci-dessus ont fait l'objet d'une publication en 2009 intitulée « Confocal Raman imaging and atomic force microscopy of surface reaction of NO_2 and $\text{NaCl}(100)$ under humidity » *J. Raman Spectrosc.* **2009**, Vol.40, pages 157-163. L'imagerie Raman et l'AFM montre que la technique de dip-coating sur NaCl conduit à des dépôts de sel de sodium d'acide oléique, stéarique et palmitique très hétérogènes. Des agrégats de tailles nanométriques analogues aux micelles sont mis en évidence par AFM, alors des dépôts de sel d'acides gras sous forme de filament de taille supérieure au micron sont identifiés par microspectrométrie Raman. Les taux de recouvrement de la surface de NaCl par les dépôts d'acides gras par la technique de dip-coating s'avèrent relativement faibles. L'analyse de la surface après réaction avec NO_2 dans des conditions analogues à celles décrites ci-dessus montre que les dépôts d'acides gras gênent peu la réaction de NO_2 sur NaCl dans son rendement et dans son mécanisme. Le nombre de nanocristaux de NaNO_3 augmente avec le RH jusque environ 50% et diminue ensuite jusqu'à la déliquescence de NaCl. Quelques perturbations morphologiques des dépôts d'acides gras sont constatées après réaction avec NO_2 . On constate les mêmes tendances quand on utilise du NaCl polycristallin en pastille en lieu et place du monocristal de NaCl. Des résultats préliminaires sur ce sujet ont fait l'objet d'un manuscrit accepté pour publication intitulée « Réactivité de l'aérosol marin à la pollution atmosphérique par NO_2 . Une étude de laboratoire ». Les différences de comportement dans l'adsorption d'eau et dans les dépôts d'acides gras à la surface de NaCl polycristallin en pastille peuvent être rationalisées par le nombre de défauts de joints de grain à la surface et à l'intérieur des pastilles. La porosité apportée par les joints de grains augmente sensiblement la réactivité de NO_2 vis-à-vis de NaCl. Les résultats des études sur des modèles de laboratoire de la réaction du composé majoritaire du sel de mer, NaCl, avec l'oxyde d'azote, NO_2 , le plus abondant dans un air pollué et ce dans des conditions atmosphériques simplifiées présentent des convergences évidentes avec des prélèvements de particules d'aérosol marin dans des zones urbanisées. Un déficit important (30-80%) en chlorure par rapport à la stoechiométrie de NaCl est compensé par un apport important en anion NO_3^- . Les microimageries de diffusion Raman, d'émission X et ToF-SIMS ont mis particulièrement en évidence des mélanges internes de NaNO_3 , de NaCl et de matière organique incluant des acides gras au niveau de la particule individuelle d'aérosol marin ayant séjourné dans un air pollué par NO_2 . Le même type de cellule de réaction avec des fenêtres en germanium a été utilisé dans l'approche par l'étude cinétique de la réaction multiphasique entre NaCl et NO_2 dans des conditions expérimentales analogues à celles décrites dans la première partie du travail. NO_2

est dilué dans l'azote en flux laminaire avec une phase NaCl solide statique, l'humidité relative est dans le domaine 0-80% et le dépôt d'acides gras sur des pastilles de NaCl polycristallin est réalisé par dip-coating. Il doit être noté que plusieurs cellules ont été construites avec des revêtements différents des parois internes pour minimiser l'adsorption parasite de NO₂ sur les parois. Malheureusement, la sensibilité du système de détection par FTIR dans l'infrarouge moyen n'est pas suffisamment performante pour utiliser des concentrations en NO₂ initiale inférieure à 10¹⁶ moléc/cm³. Le coefficient de capture (γ) de NO₂ par NaCl polycristallin conditionné en pastille augmente de façon significative avec l'humidité relative pour atteindre un maximum de $\gamma=3,2 \cdot 10^{-6}$ pour RH=45%. γ diminue sensiblement jusqu'à la déliquescence de NaCl qui survient vers RH=70%. Cette tendance est également observée avec des revêtements de palmitate et d'oléate de sodium sur les pastilles de NaCl. Les coefficients de capture maximum déterminés à RH=45% sont $\gamma=2,2 \cdot 10^{-6}$ et $\gamma=1,8 \cdot 10^{-6}$ pour les dépôts par dip-coating de palmitate et d'oléate, respectivement. Mis à part NO₂, N₂O₄, H₂O et NOCl, aucun autre composé n'est détecté raisonnablement en phase gaz par FTIR dans nos conditions expérimentales. Il est vraisemblable toutefois que des intermédiaires réactionnels comme (HNO₂, HNO₃, HCl) soient créés en faibles quantités tant en phase gaz qu'en phase condensée sur les parois. Après évacuation des gaz de la cellule seul NaNO₃ est présent sur les pastilles de NaCl. La mise en présence de NaCl polycristallin avec du NO₂ (N₂O₄) sous humidité provoque la diminution de la concentration en NO₂ (N₂O₄) et la production concomitante de NOCl. Les simulations des cinétiques sont en accord avec les résultats expérimentaux sur toute la gamme de temps étudiée en utilisant un mécanisme réactionnel où l'eau se comporte comme un « catalyseur » :



En donnant en définitive le bilan réactionnel suivant:



Les résultats obtenus dans ce travail montrent des coefficients de capture relativement faibles de NaCl pour NO₂ malgré un certain effet « catalytique » de l'humidité de l'atmosphère de réaction. Cet effet « catalytique » est quelque peu tempéré par un revêtement d'acides gras sur la surface des cristaux. Néanmoins, la réactivité de NO₂ sur NaCl est effective et conduit à des rendements importants en NaNO₃ après des temps de contact élevés en atmosphère humide. Les rendements en NaNO₃ obtenus par NO₂ sur NaCl sont du même ordre de grandeur que ceux obtenus en utilisant HNO₃ gazeux mais après des temps de contact beaucoup plus courts. Les réactions entre HNO₃ gaz et NaCl ont été beaucoup étudiées en fonction de nombreux paramètres en relation avec la réalité atmosphérique. Les coefficients de capture (γ) mesurés pour HNO₃ sont au moins plus élevés d'un facteur 10⁴ que ceux de NO₂ dans des conditions expérimentales analogues. γ augmente fortement avec l'humidité relative pour atteindre un maximum vers RH=50%, puis γ décroît progressivement jusqu'à la déliquescence de NaCl. Les valeurs de γ sont très dépendantes de la taille des cristallites de NaCl avec un maximum vers 1 μm et une décroissance continue en fonction de la taille des cristallites. Des augmentations moins marquées de γ avec des additifs minéraux du sel de mer MgCl₂ qu'avec le sel de mer lui-même sont constatées. Un travail récent sur l'effet de molécules à propriétés tensioactives sur la capture de HNO₃ par des particules d'aérosol d'NaCl indique que la valeur de γ diminue fortement avec un recouvrement des particules par l'acide stéarique. Il est à signaler que l'épaisseur du revêtement et la longueur de la chaîne alkyl sont des paramètres importants du rôle protecteur du tensioactif. L'épaisseur du revêtement est très tributaire de la méthode de dépôt qui peut amener à surdimensionner le revêtement d'acide gras par rapport

aux conditions atmosphériques réelles. Les similitudes entre les résultats publiés sur la capture de HNO_3 par NaCl et ceux obtenus sur la réaction de NO_2 avec NaCl dans ce travail indique que les mécanismes de réaction de surface impliquant l'eau et l'acide gras sont analogues. Il est prévisible que toute nouvelle tentative dans le système NO_2 - NaCl visant à approcher les conditions atmosphériques réelles, microparticule, additifs minéral et organique, concentration en NO_2 réaliste, produiront des effets sur la capture de NO_2 analogues à ceux obtenus dans la capture de HNO_3 , mais dans des délais beaucoup plus longs. Mis à part, la disparition des NO_y de l'atmosphère par des retombées de NaNO_3 , l'implication en chimie atmosphérique la plus évidente est la production de NOCl qui par un processus diurne produit Cl et NO et par un processus nocturne produit HCl et HNO_2 par hydrolyse.

Acknowledgements:

My grateful thanks are addressed to my supervisors, C. Brémard and D. Petitprez, and to the PC₂A and LASIR directors, Mr. J.F. Pauwels and Mr G. Buntinx who welcomed me in their research unities.

I want to thank Mr B. Humbert and Mr J. F. Doussin for having accepted to revise and judge this PhD work. I want to thank as well Mr. J.F. Pauwels and Mme N. Lacomme for having accepted to be members of the jury.

I want to thank all the people I worked with, particularly S. Sobanska, J. Barbillat for the AFM measurements, J. Laureyns and M. Moreau for the formation on the micro-Raman instrumentation and their continuous assistance, as well as F. Louis for introducing me into the atmospheric chemistry discipline. A grateful acknowledgement goes to M. M. Dia who significantly contributed to the experimental realisation of part of this work during his Master 1 internship.

My particular gratitude goes to C. Aghnatiou, for the transfer of knowledge on heterogeneous chemistry and for her precious friendship. I want to thank R. Ciuraru as well for having shared laboratory life and coffee breaks as well as science (and not) discussions. S. Gosselin, B. Lecrenier, V. Vilain and J.J. Leede and P. Bartier have always been particularly helpful and their presence has been essential in every moment of laboratory life.

I want to thank J.P. Verwaerde and R. Scolaro for the realisation of a static reactor prototype, but especially for having shared their time and their competences for helping me in the development of the engineering part of the project.

I want to thank all the members of the Heterogeneous Chemistry and of the Environmental Spectroscopy groups for having shared daily life and scientific discussion for these three years.

A particular acknowledgement goes to C. Kinowski, K. Woznika-Raulin and O. Cristini for the access to the clean room facilities and the formation on the use of the dip-coater.

I want to thank M. Marczak and the IEMN for having kindly recorded some of the AFM images present in this work.

Finally I want to thank A. Parker for his endless patience in correcting my English mistakes in this PhD work as well as in many posters and conferences presentations.

I want to thank all the other Marie Curie fellows with whom I shared this experience: Neda, Alessandro, Adriana, Alex, Claudio, Alina and Chaithanya, as well as my husband, Oliver, who supported me in all happy and difficult moments of this PhD.

I want to thank all the friends I met during these three years, because they really made the difference between a work/study and a life experience: there should be an endless list since each of them gave me so precious moments, but just to remember some of them I want to thank Alberto, Jenie, Erwan Laëtitia, Kasia, les-3-Martines Manon-Marion-Juliette, Myriam.

I want to remember and thank all the Italian friends in Italy and in France, and in particular my family, for their affection, love and continuous encouragement.

I want to thank the « Marie-Curie 6th Framework Project » (European Commission) for the fellowship (MEST-CT-2005-020659 contract), and in particular C. Fittschen, responsible of the “Tools and Techniques for a Changing Atmosphere” (TOTECAT) Project in Lille. I want to thank as well the Institute of Research in Industrial Environment (IRENI), in which this work is also ascribed.

A Calogera Morreale

Professoressa di Matematica e Scienze delle scuole medie “V. Alfieri” - Marano Vic.^{no} (I)
per aver fatto nascere questa mia passione per la chimica atmosferica.

To Calogera Morreale

*Mathematics and Science Professor at the “V. Alfieri” School – Marano Vic.^{no} (I)
for seeding in me the passion for atmospheric chemistry.*

Table of contents

Table of contents

Abstract and keywords	5
Résumé et mots clef	6
Forme abrégée de la these	7
Acknowledgements	11
Table of contents	15
1. Introduction	21
2. Laboratory model of marine aerosol reacting with NO₂	27
2.1 A model for the sea-salt: NaCl(100) surface	29
2.2 A model for the organic coating of marine aerosol particles: palmitic, oleic and stearic acid	31
2.2.1 Fatty acids	31
2.2.2 Fatty acids as sea-salt aerosol surface active species	34
2.2.3 Effect of fatty acids on surface chemical reactions	36
2.2.4 Laboratory model of fatty acids coating on NaCl surface	37
2.3 NO ₂ at different RH%: gas-phase reactions and equilibria	38
2.4 Heterogeneous reactions of NO ₂ on NaCl	40
2.4.1 Kinetic parameters for describing heterogeneous reactivity	42
Uptake coefficient γ	42
Reaction probability coefficient ϕ	44
3. Materials and methods	47
3.1 Materials	49
3.1.1 Solids	49
3.1.2 Gases	49
3.1.3 Organics	50
3.2 Surface preparation and coating	50
3.2.1 Pellets preparation	50
3.2.2 Surface coating	51
3.3 Vibrational spectroscopy	52
3.3.1 Infrared spectroscopy	54
3.3.2 Raman spectroscopy	55
Raman theory with linearly polarized light	57
3.4 Surface analysis - imaging techniques	58
3.4.1 Micro-Raman imaging	58
3.4.2 Tapping-mode Atomic Force Microscopy (TM-AFM)	61
3.5 Heterogeneous reactivity	64
3.5.1 Experimental methods	64
Flow tube reactor	65
Knudsen cell	66
Powder-gas reactor	66
Atmospheric simulation chamber	67
3.5.2 Experimental set-up for uptake measurements in static conditions - reactor optimisation	69
Experimental protocol	72
3.6 Quantification of formed nitrate	72

4.	The uncoated surface: the effect of relative humidity on the NaCl/NO₂ system	75
4.1	NaCl(100) in a dry and humid atmospheres	77
4.2	NaCl(100) exposed to NO ₂ at different humidities	79
4.2.1	Raman spectra and hygroscopic properties of the solid reagent and products	79
4.2.2	Experimental conditions	83
4.2.3	RH=0%	84
4.2.4	RH=15%	86
4.2.5	RH=45%	87
4.2.6	RH=68%	91
4.2.7	RH=80%	100
4.3	NaCl pellets exposed to NO ₂ at different humidities	103
4.3.1	RH=0%	103
4.3.2	RH=50%	104
4.3.3	RH=80%	105
4.4	Conclusion	106
5.	Fatty acid coated surfaces	107
5.1	Raman reference spectra	109
5.1.1	Experimental conditions	109
5.1.2	Raman spectra of the pure compounds	110
5.1.3	Molecular aggregation state of fatty acids: micelle, gel and solid structures. Raman diagnostic.	112
5.2	Fatty acids deposited on mica(001) surface from aqueous solution	113
5.3	Fatty acids deposited on NaCl from ethanol solution	116
5.3.1	Fatty acids on NaCl(100) monocrystals	116
5.3.2	Fatty acids on NaCl pellets	118
5.4	Fatty acids-coated NaCl pellets exposed to NO ₂ at different humidity conditions	122
5.4.1	Oleate coated NaCl exposed to NO ₂ at RH=0%	122
5.4.2	Oleate coated NaCl exposed to NO ₂ at RH=55%	123
5.4.3	Palmitate coated NaCl exposed to NO ₂ at RH>75%	124
5.5	Concluding remarks and atmospheric implications	125
6.	Reactivity study: gas phase characterisation and uptake coefficient measurements	127
6.1	Gaseous phase analysis	129
6.1.1	NO ₂ in a dry atmosphere	129
6.1.2	NO ₂ in a moist atmosphere	130
6.1.3	NO ₂ in a moist atmosphere in presence of NaCl	132
6.1.4	NO ₂ in a moist atmosphere in presence of insoluble fatty acids coated NaCl	133
6.2	Experimental conditions optimisation	134
6.2.1	NO ₂ inside a static reactor: measurements of reaction rates and constants	134
6.2.2	Optimisation strategy	136
6.2.3	Increasing NO ₂ concentration	137
	Empty reactor	137
	Reactor with NaCl	138
	Other advantages	139
6.3	Uptake coefficient following NO ₂ depletion	139
6.3.1	Low [NO ₂] experiments	141
6.3.2	High [NO ₂] experiments	143

6.4	Uptake coefficient following N_2O_4 depletion	145
6.4.1	Comparing NO_2 and N_2O_4 uptake coefficients	147
6.5	NaCl reactivity following ClNO formation	148
6.6	Comparing uptake and reactivity coefficients	152
7.	Fitting the experimental kinetic profiles with a simple reactivity model	155
7.1	Kinetic model when $RH = 0\%$	158
7.1.1	Hypothesis	158
7.1.2	Explicit Euler method and input data	158
7.1.3	Outputs and results	159
7.1.4	Fatty acids coated surfaces	161
7.2	Kinetic model when $RH \neq 0\%$	161
7.2.1	Hypothesis	162
7.2.2	Outputs	163
7.2.3	Results	163
	RH=40%	163
	RH=70%	167
7.2.4	Kinetic model for F.A. coated NaCl when $RH \neq 0\%$	169
7.3	Evaluating the effect of humidity and fatty acids coating on the heterogeneous reactivity	169
7.4	Quantification of the total reactivity of the NaCl/ NO_2 system	172
7.5	Discussion and atmospheric implications	173
8.	Conclusions and Future Work	177
8.1	Main results	179
8.2	Future works	181
9.	Bibliographic References	183
Appendix A		197
	Quantification of NO_2 in the gas phase	199
	Quantification of ClNO in the gas phase	199

Chapter 1 – Introduction

1. Introduction

The atmosphere contains many different kinds of suspended particles that differ in chemical composition as well as in particle size distribution, depending on the strata of the atmosphere considered, latitude, season, and the prevailing meteorological conditions. Atmospheric particulate matter occurs as aerosol, that is, an airborne suspension of particles whose dimensions range from a few nanometers to tens of micrometers and whose atmospheric lifetime is primarily a function of its size, owing to the strong relationship between settling speed and mass. Often they consist of an internal mixture of salt, crystal and other inorganic and organic materials of both biogenic and anthropogenic origin. Wash-out processes in which the aerosol particles are removed by rain and dry settling (depending on particle mass) are the major sources of loss of atmospheric particulates. Depending on the size of the atmospheric aerosol particle and other meteorological parameters, the lifetime of an aerosol particle is between 1h and 6 weeks. Their presence in the atmosphere has two main effects, one being a factor in the chemical transformation of gases in presence of aerosol particles and the other being a factor in the global radiative balance affecting the global climate. It must be pointed out that the presence of atmospheric particles is the single largest contribution to the uncertainty in relation to predictions of climate change [Forster P. *et al.*, 2007].

Sea-salt is the second most abundant (3.6 Tg) condensed matter suspended in the atmosphere after dust (16.8 Tg), and is the dominant aerosol species by mass over oceans. The size of marine aerosol particle (aerodynamic diameter) lies in the range of few micrometers.

Marine aerosols are produced through seawater microdroplets, which are released to the atmosphere from spray on the sea surface. The mechanism of marine aerosol formation involves breaking of the waves, bubble formation, and extrusion of microdroplets from the surface of the ocean that will evaporate to form the marine aerosol, whose chemical composition therefore reflects the composition of salts in sea-water. Sea-water is an aqueous solution (~0.5 M) of 11 major ions (present at 1 mg/kg or greater) including Na^+ , Ca^{2+} , Mg^{2+} , Cl^- , plus a host of other inorganic and organic species at trace concentrations. Approximately 86 % of the salinity of sea water is provided by NaCl (~30g /l). The pH of sea water varies between 8.3 and 7.6, and it is buffered by a dissolved $\text{CO}_2/\text{HCO}_3^-$ system [Brewer P. G. *et al.*, 2004]. The spray of sea water is estimated to release $\sim 10^{13}$ kg of NaCl [Gong S. L. *et al.*, 2002] and considerable amounts of organic species including fatty acids to the troposphere every year. These sea salt aerosol particles are usually present as internal mixtures with an organic coating.

Organic carbon may be produced from the surfactant layer on the sea surface whose main constituents are insoluble fatty acids. Fatty acid concentrations are positively correlated to marine biological activity and have a seasonal character. The most abundant saturated fatty acids in sea water are palmitic acid C_{16} , myristic acid C_{14} , lauric acid C_{12} and stearic acid C_{18} while the most abundant unsaturated fatty acids are oleic acid $\text{C}_{18:1}$ and palmitoleic acid $\text{C}_{16:1}$, with significant contributions from other analogous acids [Osterroht C., 1993]. When sea water droplets are transported to drier areas, they are expected to form a mixed phase, containing solids and the remaining liquid. Many studies have been done on the water evaporation of sea water droplets. Less soluble CaCO_3 precipitates first, then $\text{CaSO}_4 \cdot 2\text{H}_2\text{O}$ bar shaped crystals separate out, then cubic NaCl crystals followed by finally KMgCl_3 crystallites. Ultimately, MgSO_4 hydrates form a gel coating [Xiao H.-S. *et al.*, 2008]. The topmost layers of this gel coating are formed from organic species such as non-volatile surfactants e.g. FA which can include palmitic (C_{16}), stearic (C_{18}), and oleic acids ($\text{C}_{18:1}$) [Mochida M. *et al.*, 2002], [Tervahattu H. *et al.*, 2002]; this organic coating of the sea water

droplet was found to alter the efflorescence phenomenon during the drying of sea water droplets [Randles C. A. *et al.*, 2004].

Globally somewhat more than 1.4×10^{10} kg of nitrogen oxides expressed as NO_2 are emitted by human activities and natural sources each year and the anthropogenic emissions are gradually increasing. There are significant natural sources such as biomass burning (0.18×10^{10} kg), lightning (0.2×10^{10} kg) and continental biogenic sources (0.22×10^{10} kg). We shall follow the convention use that defines NO_x as the sum of ($\text{NO} + \text{NO}_2$) and NO_y as the sum of all reactive nitrogen-containing species including NO , NO_2 , HNO_3 , HNO_2 , NO_3 and N_2O_5 . In Europe the main sources of NO_x are transport (55%), residential heating, industrial activities and incinerators (22%), combustion power plants (22%), and fires and others (1%). Practically all anthropogenic NO_x enters the atmosphere as a result of the combustion of fossil fuels from both stationary and mobile sources. Atmospheric chemistry during both day and night produces several reactive NO_y species [Finlayson-Pitts B. J. *et al.*, 2000]. However, the abundant presence and persistence of NO_2 is confirmed by satellite and field measurements in troposphere. As an example, the map of NO_2 distribution over the European region is shown in Figure 1.1. It is reconstructed from satellite measurements averaged over 18 months, and it can be seen that the sources of this pollution can be clearly identified with densely populated and industrialized zones, with the addition of intense marine traffic in the English Channel: these pollutant processes are much more significant than natural ones because regionally high NO_2 concentrations can cause severe air deterioration, especially in Northern European coastal regions.

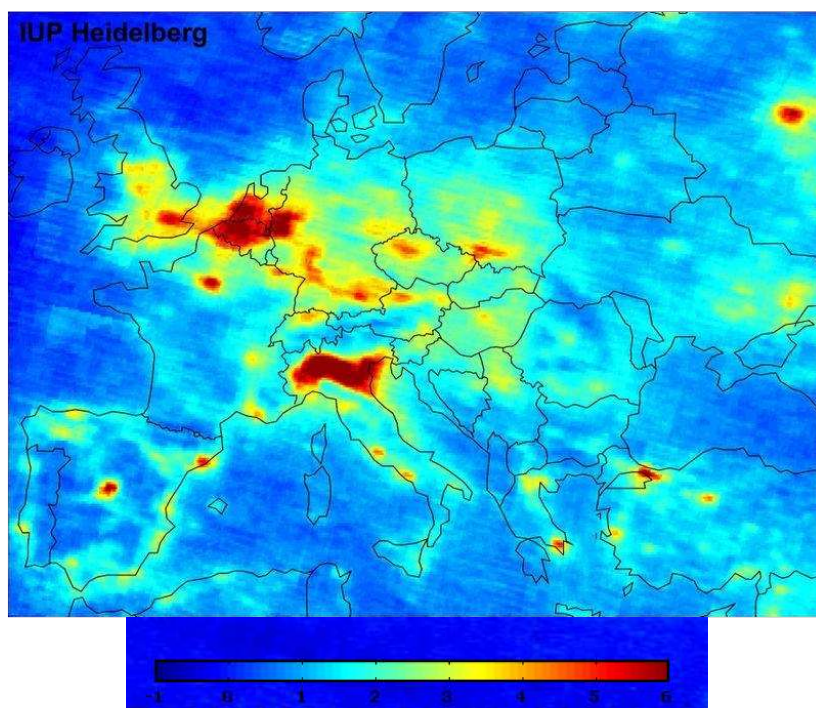


Fig. 1.1 Satellite view of the tropospheric NO_2 vertical column density (average values on 18 months from 01/2003) over the European region, ESA. The scale bar in in 10×10^{15} molec cm^{-2} . Taken from [Heilderberg I.].

Oxides of nitrogen play a central role in essentially all facets of atmospheric chemistry. Most of the primary emissions of nitrogen oxides are in the form of NO . The overall oxidation sequence in ambient air is conversion of NO to NO_2 , with is ultimately converted to HNO_3 by several daytime and nighttime atmospheric reactions. In addition, many other reactive intermediates can be detected such as nitrous acid HNO_2 , NO_3 radical, and N_2O_5 . NO_2 is key to the formation of tropospheric ozone and contributes to acid deposition. Reactive gases in the atmosphere undergo heterogeneous reactions on the surface of sea salt aerosols, thus affecting the atmospheric trace gas composition.

Many studies have shown a significant chloride deficit in aged sea salt aerosol (30-80%) when compared to bulk seawater [Zangmeister C. D. et al., 2001]. This deficit has been attributed to tropospheric reactions with inorganic nitrogen and sulphur oxide species. Single particle analysis of sea salt aerosol particles collected with aerodynamic selective sizing by cascade impaction in marine areas have improved the understanding of the reactivity, transport and removal of sea salt particles. Particularly, Raman imaging and atomic force microscopy (AFM) combined with Energy dispersive electron probe X-ray microanalysis (ED-EPMA) coupled with Scanning Electron Microscopy (SEM) and Time-of-flight secondary ion mass spectrometry (ToF-SIMS) have proven to be especially powerful techniques to demonstrate that a typical single sea salt particle originating from a marine air-mass contains an internal mixture of deliquescent NaCl crystal and NaNO₃, with an organic coating. The considerable fraction of NaNO₃ as internal mixture with aged sea salt particles comes from the efficient scavenging of reactive nitrogen species under high humidity despite the organic coating of the aerosol particle [Rimetz-Planchon J., 2007]. The reaction of particulate NaCl with reactive NO_y is an important link between a natural process, the sea salt aerosol presence and an anthropogenic process, the atmospheric pollution of NO_y derived from high temperature combustion processes. Ultimately, these reactions release volatile chlorine species into the atmosphere and NaNO₃, which then undergoes deposition processes. The release of volatile chlorine has hazardous consequences on atmospheric processes and the nitrate deposition has an environmental impact on soils and continental water.

The importance of the sea salt aerosol chemistry with nitrogen oxides in the marine boundary layer has inspired many laboratory studies for nearly 40 years. Laboratory investigations tend to provide the ultimate reality check for atmospheric chemical processes that result from indications obtained during field measurement campaigns. Today, laboratory studies are seen to take on the role of mediators between field measurement campaigns and modelling efforts to predict the effect on cloud condensation nuclei, solar light scattering and climate change. Recent works and reviews reveal quantitative information and reaction mechanisms on the reactivity of nitrogen oxides in the presence of sea salt [Rossi M. J., 2003]. These studies include the kinetics of heterogeneous reactions, the formation of reaction products, and the molar identity of all products. The heterogeneous chemical kinetic aspect is important in order to enable extrapolation of the reaction mechanism from experimental conditions of the laboratory to atmospherically relevant conditions that often involve significantly smaller concentrations of gases and sea salt density than may be encountered in laboratory experimental conditions.

Another crucial aspect of laboratory studies is the fact that often one uses surrogate substrates in the place of real atmospheric particulates. Most laboratory studies have used NaCl as a model for sea salt since it is the most abundant component (87%). It was reported that NaCl reacts with nitrogen oxides including NO₂, NO₃, HNO₃ and N₂O₅, to yield NaNO₃ and to release species rich in chlorine as described in [Rossi M. J., 2003], [Grassian V. H., 2002], [Finlayson-Pitts B. J. et al., 2000], [Finlayson-Pitts B. J., 2003]. The dramatic effect increased ambient humidity has on enhancing nitrate production was pointed out while the effect of organic coating to hinder this reactivity has recently started to be studied [Donaldson D. J. et al., 2006]. In particular, it was reported from uptake coefficient measurements that NO₂ is essentially unreactive on sea salt and deliquescent NaCl at ambient temperature compared to NO₃, N₂O₅ and HNO₃, and therefore the NO₂/NaCl reaction is thought to be unimportant in the marine boundary layer at atmospheric NO₂ concentrations [Rossi M. J., 2003]. Nevertheless, field measurement campaigns in coastal cities with industrial areas provide evidence of a high chloride deficit in sea salt aerosol when compared to bulk sea salt and relatively high NO₂ concentrations in the marine boundary layer [Kobayashi T. et al., 1979].

Supplementary laboratory studies are required to achieve a better understanding of the fundamental heterogeneous processes between NO₂ and NaCl crystals under simple but realistic atmospheric conditions. Therefore, the relative humidity of the reactive atmosphere

and the presence of a fatty acid coating on the NaCl crystal surface have been reproduced in the laboratory. The studies were performed with two complementary approaches.

- 1) The heterogeneous transformation of coated NaCl surface to NaNO₃ by NO₂ is demonstrated and supported by Raman imaging. Until today Raman spectroscopy has not been widely used in this field [Zangmeister C. D. *et al.*, 2001]. The advent of powerful confocal microspectrometers provides a potential solution for obtaining molecular information from samples of microscopic volume and spatial distribution under *in-situ* conditions. Further, tapping-mode atomic force microscopy (AFM) is used for morphological characterisation of the surface under *in-situ* conditions with high spatial resolution. The goal of this approach is to elucidate the mechanism of water-induced spatial reorganization of the fatty acid coating and the NaNO₃ film on NaCl single crystal surfaces and NaCl polycrystalline powder.
- 2) The concentrations of gaseous species are monitored using Fourier transformed infrared spectroscopy in a reaction cell during the course of the heterogeneous reaction between NO₂ and polycrystalline NaCl pellets in different relative humidities as a function of the fatty acid coating of the pellets. Special care will be exercised to quantitatively interpret the heterogeneous kinetics during the course of the reaction with the use of suitable simulations. The main aim of this approach is to assess the influence of an insoluble organic coating on the reactivity of NaCl towards the abundant polluting NO₂ species by measuring both gas concentrations and NaNO₃ yield formation.

The work of this thesis was performed in the context of the “Tools and Techniques for a Changing Atmosphere” project (TOTECAT) of the Marie-Curie 6th Framework Project (European Commission) and is organized as follows:

As detailed in this introduction chapter, the present work is placed in the context of atmospheric pollution of coastal regions and concerns laboratory experiments on heterogeneous chemistry. Heterogeneous reactions constitute a major part of the hidden chemistry of the atmosphere, and one of the aims of this work is to study the kinetics of certain reactions involving NO₂ and NaCl. The determination of the rate laws and the reaction mechanisms enables the extrapolation to tropospheric conditions.

In chapter 2 the laboratory model of marine aerosol reacting with NO₂ used throughout the present work is explained and justified.

In chapter 3, the chosen materials, methods and instruments which have been used in this work are described in detail.

Chapter 4 goes through the mechanism of water-induced spatial reorganization of NaNO₃ film on NaCl single crystal and polycrystalline surfaces.

Chapter 5 reports the results of water-induced spatial reorganization of fatty acid coating and NaNO₃ film on NaCl polycrystalline surfaces.

Chapter 6 is devoted to reactivity studies: gas phase characterisation and uptake coefficient measurements.

Chapter 7 deals with the numerical fitting of the experimental kinetics during the course of the reactions with a simple and accurate reactivity model.

Finally, the main insights of the work and the atmospheric implications are summarized in chapter 8.

Chapter 2 - Laboratory model of marine aerosol reacting with NO₂

2. Laboratory model of marine aerosol reacting with NO₂

2.1 A model for the sea-salt: NaCl(100) surface

The major mineral component of marine aerosol is NaCl, but its behaviour can be driven and strongly influenced by minor species present as impurities (such as SO₄²⁻, Mg²⁺, Br⁻, etc) because, as reported in [Rossi M. J., 2003] “a crucial aspect surrounding the laboratory study of heterogeneous reactions on salt substrates, beside mechanistic understanding, is the fact that one uses surrogate substrates or proxies to real atmospheric particulates that have the same bulk composition as the atmospheric particles as far as is known from field experiments. This aspect brings about the largest degree of uncertainty as far as reactivity with gas-phase species is concerned, because adsorbed minority or even trace components may alter the reactivity of the condensed phase substantially. Examples that may be cited are several oxidation reactions of halides by ozone interacting with either synthetic or natural sea salt substrates that have a substantially different reactivity than the majority component, NaCl. Most laboratory studies have used NaCl as a model for sea-salt since it is the most abundant component.”.

When a sea-salt aerosol drop dries, the different mineral components recrystallise so that pure crystals of different composition (NaCl, MgCl₂·6H₂O, MgSO₄·H₂O, CaSO₄·2H₂O and KMgCl₃·6H₂O) can be found in close contact, but not as a solid solution [Xiao H.-S. et al., 2008]. From this prospective, studying the pure components is important to better understand the chemical behaviour of the non-liquid aerosol particles.

The strategy for describing a complex system is indeed to separate the different constituents, and once their individual peculiarities are understood, to study the interaction between them.

NaCl (fig 2.1a, b, c) in its crystallized form is present as halite, a face centered cubic mineral structure (space group Fm3m in the Pearson notation) exposing the (100) face, which is also thermodynamically the more stable. If a drop of NaCl solution dries, the resulting crystals are mainly cubic (or an agglomeration of cubic crystals) and expose the (100) face to the air.

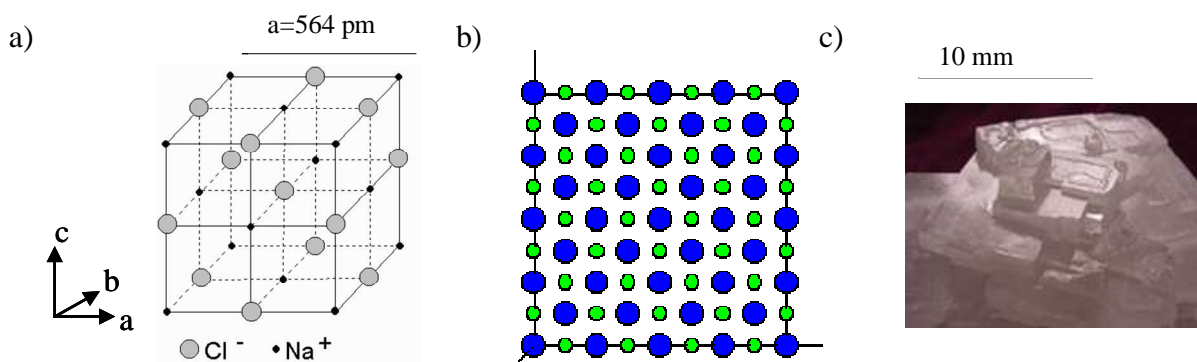


Fig. 2.1 a) Scheme of NaCl crystal structure. Each atom has six nearest neighbours, with octahedral geometry. b) NaCl(100) (and the equivalent 001 and 010) face structure, c) halite picture [Wikipedia]

The NaCl(100) surface exposes Na⁺ and Cl⁻ ions with a density of 6.3×10^{14} ions/cm², with a superficial NaCl unit occupying 1.59×10^{-19} m². The distance between the first and second layers of the NaCl is 1.4% less than that of the bulk and chloride ions in the first layer are raised by 70pm, while the sodium ions are shifted towards the bulk by the same amount. The second and third layer show no deformation and layer distances close to bulk values [Vogt J. et al., 2001].

NaCl is a highly hygroscopic salt and in the presence of water vapour the water uptake behaviour is classically described by the hysteresis diagram of deliquescence and efflorescence, as shown in fig.2.2. This diagram shows that the solid phase can turn abruptly into the liquid phase in the presence of sufficient water vapour and that this process is reversible. However, as the humidity is reduced, the solid phase suddenly reappears at a much lower relative humidity. The precise value of the DRH and ERH depend on the particle size (see for example [Gao Y. *et al.*, 2007] and [Li X.-H. *et al.*, 2006]) as it is a surface process and by changing the particle dimension the surface to volume ratio also changes.

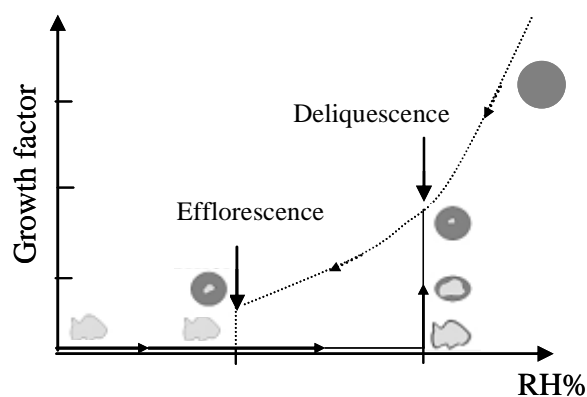


Fig. 2.2 The deliquescence and efflorescence points of bulk NaCl. Adapted from [Reid J. P. *et al.*, 2003].

To study NaCl synthetic single crystals of NaCl exposing the (100) face have been used because, as mentioned above, this surface is statistically important in dry sea-salt aerosol and when dry particles are used as a proxy for sea-salt they always refer to the NaCl(100) surface reactivity.

NaCl(100) properties are quite well described in the literature [Dai Q. *et al.*, 1997], [Allouche A., 1998], [Cabrera-Sanfeliix P. *et al.*, 2007], where we can find experimental and theoretical calculations about the behaviour of this surface in the presence of e.g. water vapour.

In [Dai Q. *et al.*, 1997], the authors have studied the structures formed on the (100) cleavage surface of NaCl when exposed to water vapour with an atomic force microscope. Above ~35% RH, a uniform layer of water is formed and the surface steps are observed to evolve slowly. At ~73% RH, the step structure becomes unstable and disappears abruptly because of dissolution (deliquescence) of the salt surface. Reversing the process by drying leads to the reappearance of new, more uniform monatomic steps. At humidity levels less than 30% water adsorbs primarily on step edges. This study indicates that the salt surfaces can actually be covered by water even though the humidity is far below the deliquescence point.

[Allouche A., 1998] questions whether water can dissociate on defective sites of the NaCl(100) surface. Using computational methods, the author determines that water cannot dissociate on steps or V_s centres (positive ion vacancies on the surface), but barrier activation on F_s centres (negative ion vacancies) fulfils the conditions of dissociation also experimentally observed by IR spectroscopy in [Dai D. *et al.*, 1995]. Here water dissociates to hydroxyl anions which are bound at the surface and the products of the reaction are trapped in the vacancies (see figure 2.3).

In [Cabrera-Sanfeliix P. *et al.*, 2007] it is reported that the raising of Cl^- from NaCl(100) at RH lower than 40%, equivalent to the water monolayer regime, is a low energy process. They propose that the facile destabilisation of Cl^- is one of the mechanisms behind catalytic activity of NaCl at low RH in reactions involving atmospheric gases.

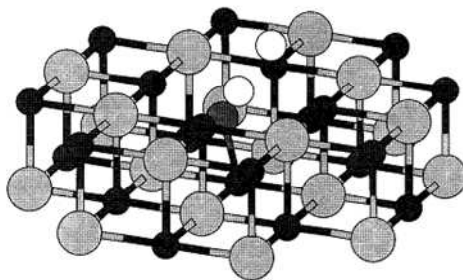


Fig. 2.3 Final product of water molecule dissociation on a F_s centre of NaCl(100) [Allouche A., 1998]. Na and Cl atoms are represented in black and light grey respectively, while in white and dark grey are H and O atoms.

2.2 A model for the organic coating of marine aerosol particles: palmitic, oleic and stearic acid

A wide range of different organic species with different functional groups (mainly oxygenated ones) can be found in or on marine aerosol particles [Russell L. M. et al., 2002]. The chemical composition of these organic mixtures is not completely resolved yet and can have strong variations depending on the aerosol particle history. In the analytically-resolved fraction, complex mixtures of ketones (R(C=O)R'), alkanes (R(CH₂)R') and carboxyl compounds (R(C=O)OH) are heterogeneously distributed on dry particles whose external organic coating shows enhanced concentrations of R(C=O)OH. This is direct evidence for surface active compounds that may serve to coat aqueous particles in humid conditions. Consequently, a number of model systems, also known as proxies, have been developed for laboratory experiments. These model systems represent one or more aspects of atmospheric particles, and they vary in their complexity and in how well they represent the real environmental matrix. The most "idealized" proxies are organic mono-layers.

2.2.1 Fatty acids

Fatty acids (n-alkanoic acids) are carboxylic acids with an unbranched aliphatic tail (hydrocarbon chain) which is either saturated or unsaturated. The schematic structure of these amphiphilic molecules is shown in fig.2.4.

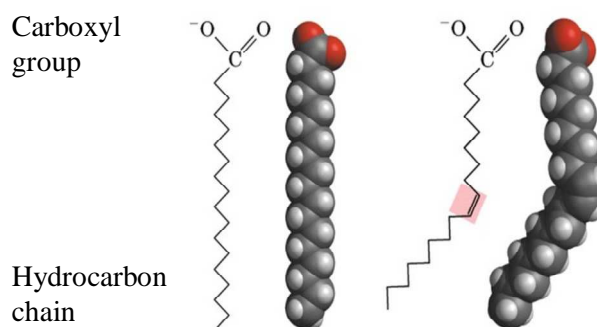


Fig. 2.4 Schematic representation of stearic and oleic acid anions.

They are usually classified as a function of the number of carbon atoms (C_n) in their tail because it reflects a certain number of physical properties, in particular their solubility in water. If C_n<12 they have short chains and are water soluble, if C_n>12 they are average or long fatty acids and they are relatively water insoluble.

Like all amphiphilic molecules in polar solvents, fatty acids behave as surfactants by repartitioning at the water/air surface with the hydrophobic tails pointing out of the solution surface. They can form expanded and compressed films at the air-water interface (fig. 2.5); if $C_n > 12$ they can only form compressed films.

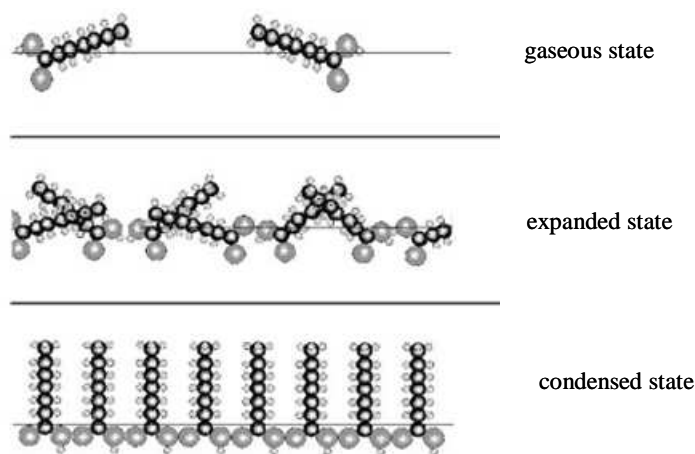


Fig. 2.5 State of phase of a monomolecular surface film. Image taken from [Seidl W., 2000].

Fatty acid monolayers on the water surface are classified as a function of their temperature, ionisation and surface pressure (π).

During a surface compression process, schematically represented in fig. 2.6 (taken from [Kajiyama T. and Aizawa, M., 1996]), the organic monolayer (a) is partially converted into bidimensional crystalline domains (b). These domains, initially grown with random crystallographic orientation, are rearranged to orient in the crystallographically equivalent direction owing to the pressure-induced fusion of sintering behaviour at the boundaries among crystalline domains (c).

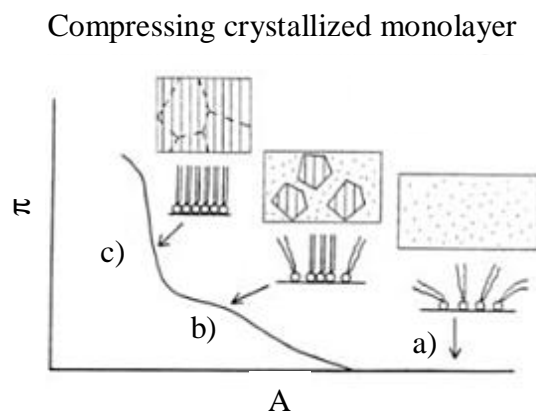


Fig. 2.6 Schematic representation of the aggregation structure of an ionic amphiphilic monolayer spread over a water surface as a function of increasing surface pressure (π). A is the average available area for each molecule on the surface. In **a**) an amorphous monolayer, in **b**) oriented crystalline domains, in **c**) fused oriented-crystalline domains forming a large homogeneous crystallised monolayer. Taken from [Kajiyama T. and Aizawa, M., 1996].

By increasing the concentration of fatty acids and reaching the critical micelle concentration (CMC), also monomers in solution have the tendency to auto-assemble, forming micelles, spherical-like aggregations in which the hydrophilic heads are pointing towards the solvent and the hydrophobic tails are oriented toward the inner part of the micelle. Micelles are dynamic structures involving fast and constant interchange of molecules between the

aggregates and the solution phase. Their dimensions and the number of constituent monomers depend on the number of carbon atoms present in the hydrophobic chain and in the size of the polar head.

In fig. 2.5 there is a schematic summary of the physical state of medium chain ($C > 10$) and long-chain fatty acids in excess water as a function of pH and temperature [Cistola D. P. et al., 1988]:

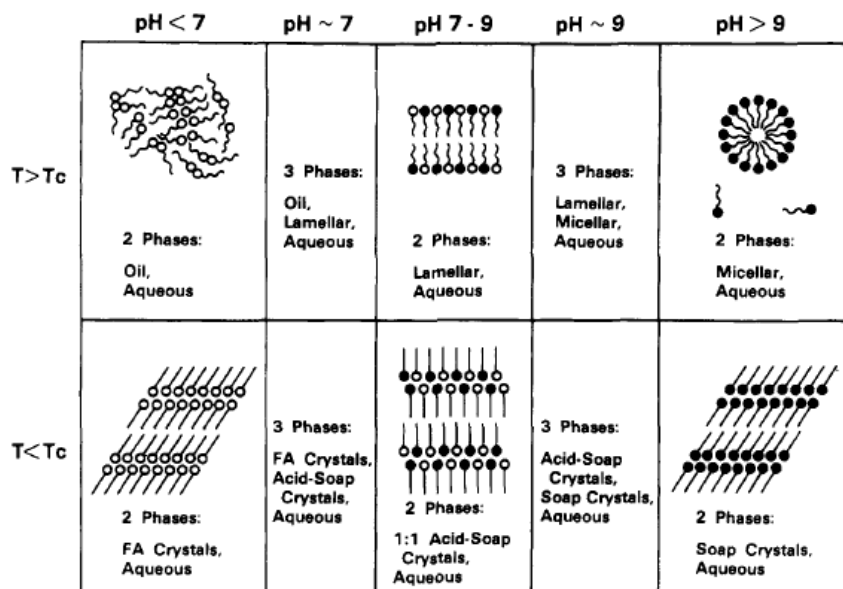


Fig. 2.5 Schematic summary of the physical state formed by medium chain ($C > 10$) and long-chain fatty acids in excess water fatty acids as a function of pH and temperature (T). T_c represents the hydrocarbon chain melting temperature in excess water, and T_c differs for fatty acids, 1:1 acid-soaps, and soaps. The aqueous phase is a saturated solution of fatty acid, acid-soap, or soap, and the concentration of these molecules varies with ionization state and hydrocarbon chain length. The closed circles represent ionized (anionic) carboxylate groups and the open circles protonated carboxyl groups. The straight lines represent ordered hydrocarbon chains and the curved lines disordered (liquid) hydrocarbon chains. Taken from [Cistola D. P. et al., 1988].

A further increase in their concentration leads to the formation of crystal-liquids, where the molecules are highly oriented in one direction, while still behaving like a liquid in all others (see fig. 2.6 taken from [Tabazadeh A., 2005]).

Fatty acids at room temperature undergo a chemical change known as auto-oxidation. The fatty acid breaks down into hydrocarbons, ketones, aldehydes, and smaller amounts of epoxides and alcohols. For this reason solutions of fatty acids cannot be kept for long time (up to 2 days) without the production of decomposition products [Najera J. J., 2007].

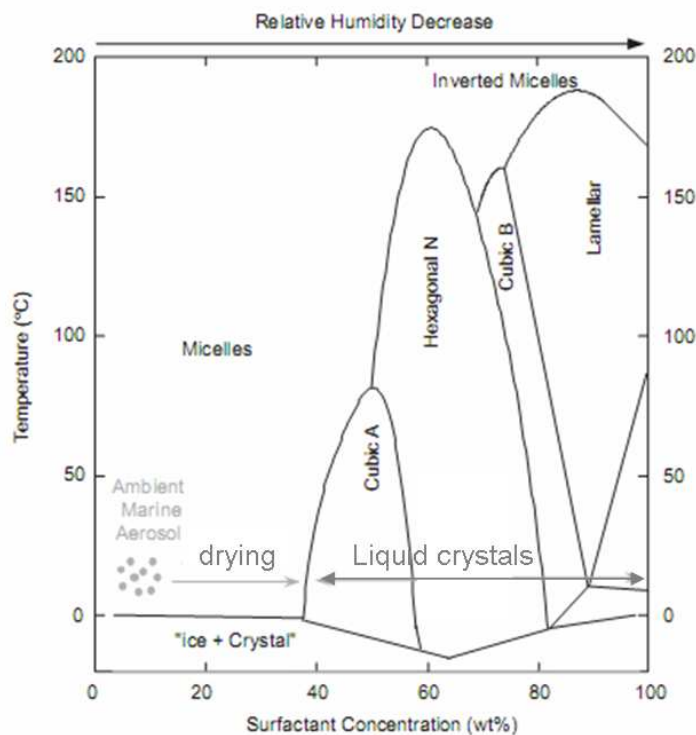


Fig. 2.6 A typical, but simplified, phase diagram of an anionic surfactant (taken from [Tabazadeh A., 2005]). The minimum below 0°C is the eutectic of ice and the surfactant molecule in a solid crystalline phase. Liquid crystals (cubic A, Hexagonal N, cubic B and lamellar), which are viscous-like liquids, have at list a dimension which is highly ordered. In other dimensions, liquid crystals behave in a manner similar to unstructured fluids. At low RH the liquid crystalline phases can still adsorb a substantial amount of water.

2.2.2 Fatty acids as sea-salt aerosol surface active species

Fatty acids have been reported to be major constituents of the organic fraction on marine aerosols in many investigations ([Barger W. R. et al., 1976], [Gagosian R. B. et al., 1981], [Sicre M. A. et al., 1990], [Stephanou E. G., 1992]), but they are also present on other inorganic aerosol particles, such as continental sulphates and nitrates [Tervahattu H. et al., 2005]. They can be considered as potentially important aerosol surfactants because they are major components of many natural atmospheric emissions (e.g. biomass burning, marine) as well as anthropogenic emissions (e.g. combustion in catalytic automobiles, meat cooking [Seidl W., 2000]); they are therefore a ubiquitous presence.

Aerosols originating from different sources have different and characteristic fatty acid chain length compositions, and even if they have not been considered good tracers of aerosol emissions [Gogou A. et al., 1996] a clear difference between continental and marine sources can easily be appreciated.

From the work of [Tervahattu H. et al., 2002], fatty acids (hereafter denoted FA) on sea-salt particles originated from dead plankton and other organisms and are composed of relatively short carbon chains. As cells die, the hydrophobic constituents of the membranes (mainly made up of fatty acids) rise toward the ocean's surface. They were able to study the surface of these particles by time-of-flight secondary ion mass spectrometry (TOF-SIMS), a technique which has unique combination of surface sensitivity and detailed molecular information. Spectra of the outmost surface showed a high intensity signal for palmitic acid (C₁₆) and lower peaks for other FA. According to TOF-SIMS images, palmitic acid was distributed on micrometric-size particles, similar to the marine ones. The stripping of the surface layer of palmitic acid by the sputtering process revealed that the inner core of the sea-salt particles

contain no FA, and therefore the FA are important ingredients of only the outmost surface layer of this kind of particle.

In other field campaigns, sampled marine aerosols showed a content of FA ranging from C₁₄ to C₁₈ with the maximum at C₁₆ [Tervahattu H. et al., 2005], in agreement with the previous studies.

The same biological origin and chain length distribution (see figure 2.7) has been confirmed in another important work [Mochida M. et al., 2002], in which the authors highlighted a positive correlation between concentrations of C₁₄-C₁₉ and sea-salt concentrations, suggesting that these FA are released from the ocean surface to the atmosphere together with the sea-salt particles. The [FA]/[sea salt] ratio had a seasonal character, with a maximum in spring-summer.

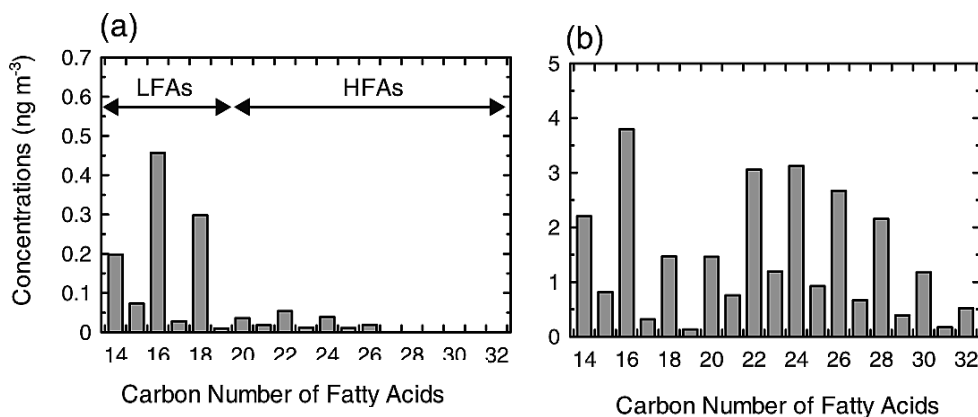


Fig. 2.7 Examples of fatty acid concentrations measured by [Mochida M. et al., 2002]. Typical chain length distributions of fatty acids collected (a) in the remote marine air mass and (b) in the air mass strongly influenced by terrestrial sources.

The enhanced FA flux into the atmosphere during this season was found to be coherent with satellite measurements of chlorophyll- α in the same region (northern North Pacific) which show high biological productivity from spring to summer.

On the basis of the [FA]/[sea-salt] ratio, relative humidity and particle size distribution, they estimated a native coverage of FA on sea-salt of 0.3-14%.

Fatty acids are likely to be presents as salts on alkaline sea-salt particles [Gagosian R. B. et al., 1982], [Sicre M. A. et al., 1990], [Seidl W., 2000]. In [Stephanou E. G., 1992] the author observed that fatty acids salts were found in higher concentrations in marine aerosol than fatty acids, while conversely fatty acids were more concentrated than fatty acid salts during wind events from inland.

Fatty acid coatings have been experimentally studied by [Xiong J. Q. et al., 1998] on ultrafine sulphuric acid aerosol. The presence of a monolayer film of stearic and lauric acid (linear molecules capable of forming highly packed films) retards the hygroscopic growth of H₂SO₄ particles, and this effect depends on the original film-coating thickness. Oleic acid, being a nonlinear molecule, has a smaller effect on the mass transport of water.

On ammonium sulphate particles (aged H₂SO₄ aerosol, neutralized by the atmospheric presence of ammonia) the impact of palmitic acid on the water uptake and loss seems to be very small [Garland R. M. et al., 2005]. Indeed 50wt % palmitic acid composition has to be reached for the mixed particles to start to take up water at RH as low as 69% and they slowly take up water up to 85% RH without fully deliquescing*.

* DRH for (NH₄)₂SO₄ is 80±3%.

Particular attention has to be given to the work of [Ming Y. et al., 2001], where a computational model for internally mixed sea salt-organic species (insoluble and soluble) is presented. An organic fraction of 30wt%, when RH value is below the deliquescent point of the inorganic salt, gives a more hygroscopic character than the sum of both species independently because of the organic-electrolyte interaction. Above the deliquescence point of the salt the insoluble compounds remain undissolved, resulting in a lower (-15%) hygroscopic growth than the strictly inorganic salt composition. In the same model the organic composition can be tuned, showing that the sea-salt particles hygroscopic behaviour is strongly sensitive to the amount of soluble or slightly soluble species.

The possible barrier effect against the transport of trace gases through the particle surface is criticized and described as unlikely to be efficient in [Seidl W., 2000], since the surface film has to be in the condensed state to be an effective barrier. On atmospheric particles, mixed films are present, and even in a compressed film, only a small area fraction of some 10-20% can be expected to be in the condensed state, so the coating is globally ineffective.

A recent computational study [Chakraborty P. et al., 2008] suggests that water droplets which are coated with lauric acid (C₁₂) should conversely attract water because of the surface tension lowering property of FA. This suggests that the coating can play a significant role in increasing the cloud condensation nuclei property.

To my knowledge there is currently no work that gives a clear picture of the effect of film-forming organics on the hygroscopic properties (DRH, ERH, growth factor) of sea-salt, and the majority of theories are still speculative and not adequately supported by laboratory experiments.

2.2.3 Effect of fatty acids on surface chemical reactions

As outlined in some reviews, i.e. [Donaldson D. J. et al., 2006], the effect of an insoluble coating on the kinetics or chemical reaction mechanisms of particles is not yet well characterised. This knowledge is of primary importance, and there is much work underway trying to better understand these processes, including this work.

Film-forming species are permeable to small molecules such as CO₂, H₂O, NH₃, SO₂ and NO₂, but they can provide a hydrophobic surface on which the solubility these molecules can differ, therefore giving a different overall uptake coefficient for these gases [Daumer B. et al., 1992], [Glass S. V. et al., 2006], [Gilman J. B. et al., 2006], [Park S.-C. et al., 2007], [McNeill V. F. et al., 2006], [Thornton J. A. et al., 2005], [Folkers M. et al., 2003]. The observed effect of different surfactants varies substantially and depends on the substrate, the monolayer properties and also on the type of gas and its sink processes in the condensed phase. The results therefore suggest that many heterogeneous atmospheric processes may depend on detailed structural features of the mixed organic/inorganic particles. In many cases more than a monolayer coating is needed to perturb the system, inferring that, i.e. a palmitic acid coating would not be in a simple inverse micelle arrangement, but rather in a more complex system with possible surface defects and both hydrophobic and hydrophilic areas [Garland R. M. et al., 2005].

The role that fat-coated aerosols can play in atmospheric chemistry strongly depends on the oxidation state of the hydrophobic shell. For this reason a substantial portion of aerosol chemistry research is also interested in the reactivity of the organic species themselves. They can react with atmospheric oxidants and radicals colliding with the surface, and this can determine the atmospheric fate and lifetime of the organic matter also adsorbed to the surface of aerosols [Voss L. F. et al., 2006]. The reaction with NO₂ for example can lead to nitration (confirmed by field measurements campaigns: [Liu D.-Y. et al., 2000], [O'Brien J. M. et al., 1997], [Mylonas D. T. et al., 1991], [Luxenhofer O. et al., 1996]) and to the formation of

products that can absorb visible light, thus changing the optical properties of the aerosol. Many studies on the reactivity of unsaturated oleic acid particles with ozone can also be found in the literature, with a transfer of knowledge from the quite well known reaction of O₃ on C=C double bonds to this new field of research (i.e. [Rudich Y., 2003], [Hearn J. D. et al., 2005], [Vieceli J. et al., 2004], [Dubowski Y. et al., 2004], [Knopf D. A. et al., 2005] and [Vesna O. et al., 2005]).

The product of oxidation of both saturated and unsaturated fatty acids films is the formation of volatile and water-soluble organics [Katrib Y. et al., 2004].

2.2.4 Laboratory model of fatty acids coating on NaCl surface

Organic monolayers are ideal surfaces for laboratory experiments: they are well-ordered, have well-defined geometry, and can be well characterised before and after reaction. Although the organic surfaces of laboratory studies are very different from the surfaces of real atmospheric particles, they enabled researchers to probe the reactive processes that are confined to the gas-surface interface, to study the wetting properties of the organic surface, and to identify the products that are formed in reactions with atmospheric radicals and oxidants. Different technical approaches for generating the insoluble coatings are hereafter described. They are presented in order from macroscopic surfaces, to bulk and single particles:

Macroscopic surfaces

The more standard methods use Langmuir troughs to vary and monitor the state of the film. Besides the surface pressure and composition measurements in mixed organic films [Gilman J. B. et al., 2006], some heterogeneous reaction kinetics on films can also be studied [Wadia Y. et al., 2000], [Mmereki B. T. et al., 2004].

Bulk particles

Important technical problems still remain in creating reproducible, well characterised aqueous particles that are natively coated with an organic film, due to the lack of solubility or to the surface tension lowering effect. A possible solution has been found to coat dry aerosol particles by condensing the organic species onto them, e.g. in [Thornton J. A. et al., 2005] and [Garland E. R. et al., 2008]. By heating the vessel containing the organic powder, vapours are generated and are then transported by a gas flux to the particulate surface. The coated particles can be re-hydrated to the desired RH. Through this expedient soluble and insoluble surfactants coating can be studied, for example in an aerosol flow tube apparatus, as reported in [Stemmler K. et al., 2008], [Thornton J. A. et al., 2005], [McNeill V. F. et al., 2006] and [McNeill V. F. et al., 2007].

Aerosol Chambers can be used for monitoring the evolution of the particulate phase (particle number and size distribution) when organic species condense on the surface, see e.g. [Folkers M. et al., 2003] so that a more realistic coating can be reproduced. The reactivity of the aerosol towards various chemical gas species can be tested in the same aerosol chamber that it is produced.

Single particles

Single particle trapping [Hopkins R. J. et al., 2004] is a promising tool that can allow reliable measurements of the droplet size as well as monitoring the evolution of the chemical composition by spontaneous and stimulated Raman scattering, as in e.g. [Buajarern J. et al., 2007a], [Buajarern J. et al., 2007b] and [Butler J. R. et al., 2008].

The choice of experimental approaches depends on which aspect of the organic coating we want to focus on: the reactivity and permeability of the organic coating, or its influence on the reactivity of the inner inorganic phase.

Organic monolayers are usually characterised using various surface techniques such as contact angle measurements, infrared spectroscopy (FTIR), X-ray photoelectron spectroscopy (XPS), laser induced fluorescence and Second Harmonic Generation (SHG) and many others.

For our specific reactivity study we choose to work on the well known NaCl(100) surface, therefore it was necessary to study and deposit our palmitic, stearic or oleic acid coatings on this solid and macroscopic surface; no bulk or single particle approach can then be used. For further details on the deposition technique used see ch. 3.2.

Several surface analysis techniques can be used to characterise macroscopic organic-coated surfaces, some more common examples of which are Atomic Force Microscopy (AFM), Time-of-Flight Secondary Ion Mass Spectrometry (TOF-SIMS), and Environmental Scanning Electron Microscopy (ESEM).

In this work we used AFM to access topographic information, such as surface status and morphology. Raman micro-spectrometry allowed us to see the spatial distribution of chemical species on the surface and to distinguish between their different environments: solid, liquid or deliquescent state.

Coupling these two complementary techniques can lead to a good description of the surface morphology and of its chemical characterisation in in-situ conditions. For a description of this see ch. 3.4.

2.3 NO₂ at different RH: gas-phase reactions and equilibria

For describing the gaseous phase composition we have to take into account a certain number of equilibria. First of all we have to distinguish a dry condition from an environment where water vapour is present. The amount of water vapour is expressed in terms of relative humidity RH (%), where:

$$(2.1) \quad \text{RH}\% = \frac{p_{\text{H}_2\text{O}}}{(p_{\text{H}_2\text{O}})_{\text{sat}}} \cdot 100$$

where $p_{\text{H}_2\text{O}}$ is the partial pressure of water vapour and $(p_{\text{H}_2\text{O}})_{\text{sat}}$ the saturated partial pressure at that temperature.

In dry conditions (RH=0%) we have only the following dimerisation reaction and equilibria:



$$(2.3) \quad K_p = \frac{p_{\text{N}_2\text{O}_4}}{p_{\text{NO}_2}^2} = \frac{X_{\text{N}_2\text{O}_4}}{(X_{\text{NO}_2})^2} \frac{1}{P}$$

Where P is the total pressure (mbar) and p_i , and X_i are respectively the partial pressure (mbar) and the molar fraction of the component i ; $K_p = 6.77 \times 10^{-3} \text{ mbar}^{-1}$ at 298K [DeMore W. *et al.*, 1997].

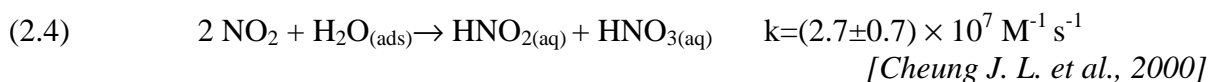
The mathematical expression of the equilibrium (2.3) means that if there is a change in $[\text{NO}_2]$, then at a constant total pressure $[\text{N}_2\text{O}_4]$ also changes, although not linearly.

This dimerisation/dissociation reaction is very fast with a dissociation rate constant $k = 4 \cdot 10 \times 10^6 \text{ s}^{-1}$ at 298K [NIST]: this means that in our specific system, it takes ~

10×10^{-7} s to reach equilibrium conditions (~1 bar, 0.36% mol), by filling our reactor with the bottle mixture (3 bars, 5% mol).

When some water vapour is present, describing the gaseous phase becomes more complex owing to the heterogeneous hydration of NO_2 and consequent decomposition reactions. Some possible reactions that can lead to the chemical composition of final gas mixture are as follows.

NO_2 can become hydrated and can dismutate following these steps:



Some studies *[Finlayson-Pitts B. J. et al., 2003]* suggest that it happens through the N_2O_4 intermediate species, viz:



This mechanism is supported by spectroscopic evidence, thermodynamic calculations and the fact that N_2O_4 is two orders of magnitude more soluble in water than NO_2 [†].



The nitrous acid can be released to the gaseous phase:



but not the nitric acid that remains in the condensed phase ($H=2.1 \times 10^5 \text{ M atm}^{-1}$ *[Schwartz S. E. et al., 1981]*)[‡]. Here it creates an acidic environment, where there is the possibility of forming the ion NO^+ , itself involved in the reaction with HNO_2 :



giving the overall reaction:



NO can also react as follows:



[†] Gas solubility can be estimated from the Henry constant, H. It describes the repartition between the gaseous and liquid phase of a component *i*, as the ratio between its solution concentration and its partial pressure: $H=[i]/p_i$

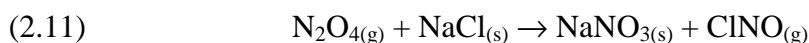
$H_{\text{N}_2\text{O}_4} = 1.4 \text{ M bar}^{-1}$ NIST NIST Webbook.

$H_{\text{NO}_2} = (1.4 \pm 0.2) \times 10^{-2} \text{ M bar}^{-1}$ Schwartz S. E. and White W. H. (1981). Solubility equilibria of the nitrogen oxides and oxyacids in dilute aqueous solution. NY, Gordon and Breach Science Publishers.

[‡] When a gaseous species can undergo some dissociation equilibrium once dissolved in the aqueous phase, the Henry's constant H is replaced by H^* , the pseudo-constant called the effective Henry's law constant:

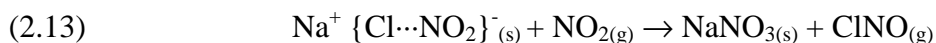
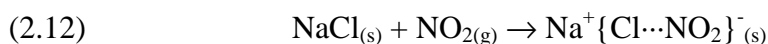
$H^* = H \left(1 + \frac{K_a}{[\text{H}^+]} \right)$ with K_a the acidic constant in mol/L. The real solubility of the gas in the condensed phase is

then strongly influenced by the solution pH.

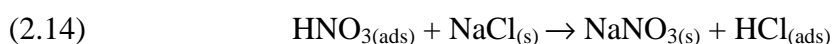


This reaction is approximately second order in NO_2 [Vogt R. et al., 1994], [Peters S. J. et al., 1996], [Li H. et al., 2006].

In one of the proposed mechanisms this reaction appears to be at least a stepwise process involving the formation of a radical anion intermediate in the solid, $\{\text{Cl}\cdots\text{NO}_2\}^-$ which has been identified by EPR[§] at room temperature [Wan J. K. S. et al., 1996]. The reaction mechanism would then be described as:



When some water vapour is present we can also have the hydrolysis of NO_2 or N_2O_4 on the surface (as seen in ch. 2.3). In this case the surface for the hydrolysis can be NaCl itself, so that the following reactions can act in the global process of nitrate formation:



HCl is likely to remain in the adsorbed state because of its high Henry's law constant $H=2.04 \times 10^6 \text{ M}^2 \text{ atm}^{-1}$ [Clegg S. L. et al., 1967].

As a consequence of the presence of new species in the gaseous phase, other possible equilibria can be found [NIST].

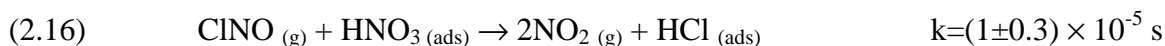
Some of them involve the destruction/formation of $\text{ClNO}_{(\text{g})}$ [Karlsson R. et al., 1996].

Reaction (2.15) is known as ClNO hydrolysis and can be a gaseous process, but catalysed by the presence of surface adsorbed water:



$$K = \frac{[\text{HONO}] \cdot [\text{HCl}]}{[\text{ClNO}] \cdot [\text{H}_2\text{O}]} = (7.9 \pm 3.6) \times 10^{-5}$$

Heterogeneous reaction (2.16) is called dry ClNO decomposition as it does not involve water and is a minor reaction when hydrolysis occurs.



It is important to note that in this reaction ClNO behaves like a source of NO_2 , as in the reverse reaction between ClNO and NaNO_3 observed by [Vogt R. et al., 1994]:

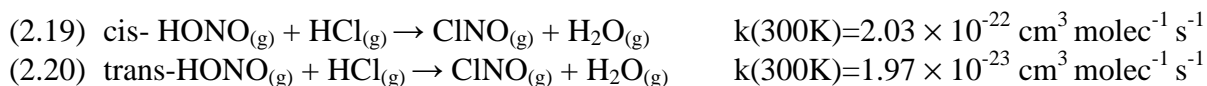


ClNO can also directly react with NO_2 , as described in the (2.18)



[§] Electron Paramagnetic Resonance

Some gas-phase reactions other than the heterogeneous reactions 2.10 and 2.11 can produce ClNO:



Some studies also report reactions between $\text{HCl}_{(g)}$ and NO_2/NO :



The heterogeneous reaction of NaCl and NO_2 has been widely studied in the literature, but still there remain many uncertainties in the mechanism and kinetics to be explained, because of the intrinsic difficulties of heterogeneous chemistry experiments and reproducible surface conditions and because the reaction itself is not simply a bimolecular one. For an overall view of the problems, see the reviews [Rossi M. J., 2003] and [Finlayson-Pitts B. J., 2003].

The reactivity has been measured for reactions 2.10 and 2.11 by various techniques: the main results are listed in table 2.1, at the end of this chapter. This table will be more extensively discussed when interpreting our results from the kinetic experiments, in ch 6. Note that some studies assume N_2O_4 rather than NO_2 as the reactive species. The kinetic parameters used in the literature for quantifying the heterogeneous reactivity are described in the next section (2.4.1).

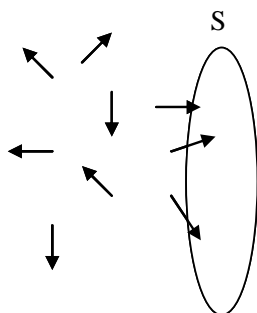
In [Peters S. J. et al., 1996] the important discrepancies in the literature are analysed and explained in term of surface differences and quantity of defect sites. The surface state is in fact a crucial parameter that controls the heterogeneous reactivity. The differences between the experimental results in tab. 2.1 are also due to the techniques used, if the kinetics are studied following the reactant or the product, if the reaction taken into account is 2.10 or 2.11. For an exhaustive overview there are two main reviews: [Rossi M. J., 2003] and [Finlayson-Pitts B. J., 2003].

2.4.1 Kinetic parameters for describing heterogeneous reactivity

The primary experimentally observable parameter in a heterogeneous system is the rate of uptake of a trace gas species and in some cases the formation rate of one or several products. In the first case an uptake coefficient (γ) can be determined, in the second case a reaction probability coefficient (ϕ) is measured.

Uptake coefficient γ :

When a gas is in contact with a condensed phase, gaseous molecules driven by thermal agitation can diffuse towards it and hit the surface S:



From the gas kinetic theory, the number of molecules of a gas A that can flow through a surface S of unitary area per unit of time is:

$$(2.23) \quad N_s = \frac{1}{4} \langle c \rangle [A]$$

with:

- N_s in molecules $\text{cm}^{-2} \text{s}^{-1}$;
- $[A]$ is the gas-phase concentration in molec cm^{-3} ;
- $\langle c \rangle$ is the average molecular velocity of A in cm s^{-1} , defined as:

$$(2.24) \quad \langle c \rangle = \sqrt{\frac{8RT}{\pi M}}$$

where

M is the molecular weight of A in g mol^{-1} ;

R is the ideal gas constant;

T is the temperature of the reactor in K.

A fraction of the molecules that hit the surface can be irreversibly taken up due to heterogeneous processes (dissolution, diffusion inside the condensed phase and/or reactivity).

The ratio of the number of collisions leading to uptake to the total number of possible collisions on the unitary surface S in 1 second is the uptake coefficient γ :

$$(2.25) \quad \gamma = \frac{\text{\# of taken up molecules per unity of surface and time}}{\text{\# of colliding molecules per unity of surface and time}} = \frac{N_{\text{up}}}{N_s}$$

γ is then a dimensionless parameter and represents the probability ($0 < \gamma < 1$) that a gas phase species is removed irreversibly from the gas phase to an active surface at that temperature, i.e. a value of $\gamma = 10 \times 10^{-4}$ means that one collision over 10000 will result in sequestration to the condensed phase.

The number of molecules taken up can be experimentally measured assuming a first order uptake for A in the gaseous phase:

$$(2.26) \quad \frac{d[A]}{dt} = -k[A]$$

The total number of taken up molecules per unit of time and surface is then:

$$(2.27) \quad N_{\text{up}} = k [A] \frac{V}{S}$$

So that the value of γ can be calculated from the rate coefficient k:

$$(2.28) \quad \gamma = 4 \frac{V}{S} \frac{k}{\langle c \rangle}$$

The specific mathematic treatment of eq. 2.28 depends on the experimental set-up chosen for determining the uptake coefficient.

The observable uptake rate of a species on a surface is a complex process and depends on several elementary processes such as gas-diffusion towards the surface of interest, the mass accommodation rate, the desorption rate from the surface back to the gas phase, the chemical

transformation at the interface, the diffusion into the bulk of the condensed phase and possible chemical reactions within the bulk phase. The uptake coefficient γ refers to a series of processes and is a description of the overall process. For extracting information about a specific aspect of the uptake process, i.e. the mass accommodation on the surface, specific corrections or experimental conditions have to be used. The uptake coefficients and reaction probabilities usually listed in tables [Rossi M. J., 2003] are presented in a variety of forms depending upon the experimental technique used:

- γ_{ss} describes an experimentally determined uptake coefficient obtained for measurements at steady state even though the physical state of the system may change fairly rapidly with time, for instance due to surface saturation. Several uptake experiments of flowing gases on solid surfaces are conducted at very low trace gas concentrations in order to avoid surface saturation.
- γ_0 corresponds to an experimentally determined initial uptake coefficient that was changing rapidly with time. This value may have been obtained either through extrapolation of time-dependent γ values or it corresponds to an uptake coefficient resulting from a pulse experiment.
- γ corresponds to uptake coefficient that was processed or corrected through major manipulations such as correction for gas-phase diffusion and condensed-phase diffusion.
- γ_{obs} , γ_{max} correspond to the observed values of the uptake coefficient under defined experimental conditions and to its maximum value, respectively.
- γ_x corresponds to the uptake coefficient of species X in cases where more than one gas species has been exposed to the surface of interest.

Some authors [Moise T. et al., 2000] also suggest the introduction of γ' , a reaction probability per reactive site, which enables the quantification of uptake as the reaction proceeds and surface reactive sites are depleted.

Reaction probability coefficient ϕ :

In previous work there are many examples (i.e. [Apostolescu N. et al., 2004] and [Ullerstam M. et al., 2003]) where product formation rate is measured instead of reagent decrease. The derived rate coefficient can then be used to calculate a reaction probability coefficient ϕ . In analogy to the uptake coefficient γ , the reaction probability (referring to the general reaction $aA+bB \rightarrow cC+dD$) is defined as the fraction of gas-solid collisions leading to reactive uptake, and it is calculated from the equivalence of the reagent consumption and product formation rates:

$$(2.29) \quad -\frac{1}{a} \frac{d[A]}{dt} = \frac{1}{c} \frac{d[C]}{dt}$$

The number of reactive collisions on the surface can then be indirectly expressed in terms of product appearance rate:

$$(2.30) \quad N_{up} = \frac{a}{c} \frac{d[C]}{dt} \frac{V}{S}$$

Leading to an equation similar to (2.28), in which the reaction probability parameter is expressed in terms of the experimentally observables:

$$(2.31) \quad \phi = \frac{a}{c} \frac{4V}{S\langle c \rangle [A]} \frac{d[C]}{dt}$$

If some conditions are respected, ϕ can then be used as an equivalent to γ . These conditions are:

- stoichiometry is correctly taken into account;
- there is no induction time for the product formation;
- there are no reactions involving A or C other than the one that is the object of the investigation.

The reaction probability coefficient is systematically used in some specific experimental methods, such as DRIFT measurements (see §3.5.1).

Its use is justified by two main advantages; the first that experimentally it allows an easy measurement of uptake coefficient in flux mode even at ambient pressure, the second concerns the data correction treatment.

reference	solid phase	surface status	NO ₂ concentration (molec cm ⁻³)	Total Pressure (bar)	reaction order in [NO ₂]	technique	observed species	γ
[Sverdrup G. M. et al., 1980]	sea salt		not reported					10 ⁻⁷ RH0% 10 ⁻⁶ RH88%
[Finlayson-Pitts B. J., 1983]	NaCl IR windows and rock salt mineral	Humidity and organics free	$1.3 \times 10^{14} \div 1.9 \times 10^{17}$	$5 \times 10^{-4} \div 1$	-	IR	CINO, NaNO ₃ , NO ₂	$> 5 \times 10^{-8}$ **
[Winkler T. et al., 1991]	NaCl tablet		$2.4 \cdot 10 \times 10^{13}$	10 ⁻³	$\sqrt{[\text{NO}_2]}$	photoelectron spectroscopy, MS	CINO, NaNO ₃ , NO, Cl ₂ ; HCl and HNO ₂ in presence of water	
[Vogt R. et al., 1994]	1-5 μ m particles	Humidity and organics free	$2\text{-}30 \times 10^{14}$	30×10^{-3}	1.6 \pm 0.2	DRIFT	NO ₃ ⁻ , NO ₂ and CINO when in static conditions	$(1.3 \pm 0.6) \times 10^{-4}$
[Peters S. J. et al., 1996]	NaCl (100)	defect-free; anhydrous	$3.7 \times 10^{15} \div 8.5 \times 10^{16}$		2	IR	CINO, NaNO ₃ , HONO. No HNO ₃ .	$(1.3 \pm 0.3) \times 10^{-6}$
[Yoshitake H., 2000]	NaCl 0.3-0.6 μ m	dry and water-vapor exposed	$1.7 \times 10^{15} \div 8 \times 10^{16}$		1.7	DRIFT	NaNO ₃ , HONO	$(4 \pm 2) \times 10^{-5}$ on dry salt $(1.5 \pm 0.2) \times 10^{-8}$ on humid salt
[Li H. et al., 2006]	NaCl particles				2	DRIFTS, IC, XPS, SEM		$(1.54 \pm 0.70) \times 10^{-5}$

Tab 2.1 Measured uptake coefficient γ for the heterogeneous reaction of NO₂ on NaCl. Uptake coefficient calculated for the reaction N₂O₄ + NaCl are reported in *italic* characters.

** Calculated by following the appearance of CINO in reaction 2.10.

Chapter 3 - Materials and Methods

3. Materials and methods

3.1 Materials

3.1.1 Solids:

The NaCl (100) surfaces used in this work have different origins, depending on the specific characteristic needed in the experiment:

- When a perfectly flat surface was needed, 10 x 10 x 1 mm crystals (Merck) were used after mechanical polishing. This surface is flat but affected by polishing defects (parallel lines coming from the abrasion process, visible with AFM, see ch. 4.1)
- When the presence of these polishing defects was not desired, 10 x 10 x 10 mm crystals (SPI-Chem TM) were cleaved with single edge razor blades along the (100) face in ambient air to obtain approximately 2mm thick sections. In this second case the surface was fresh and flat at the atomic level over a certain area, but the cleaving procedure gives rise to cleavage edges.
- For the kinetic experiments large quantities of NaCl surfaces were required and as it was impossible to use pure single crystals for each experiment, we used a sieved NaCl powder (granulometry <80 μ m) to prepare solid disks of 13mm of diameter and 1mm of thickness containing 150mg of NaCl. NaCl grain powders are $\geq 99.5\%$ of purity (SO_4^{2-} and K $\leq 0.01\%$; Ca, Cd, Co, Cu, Fe, Ni, Pb, Zn $\leq 0.005\%$).

NaCl salt is highly hygroscopic, especially if the surface has been mechanically polished, so it has to be kept in a dry and heated environment (oven at 110°C).

NaNO_3 salt (99% purity, Fluka) is used for determining the nitrate calibration curves in the IR quantification of formed nitrate on NaCl tablets exposed to NO_2 .

Mica(100) sheets of 2.54x 2.54cm (Agar Scientific) are the other model surface on which fatty acids thin layer have been studied. This is a surface which is flat down to an atomic scale.

3.1.2 Gases:

The NO_2 and N_2 gases are provided from commercial cylinders (Air Liquid) with the following nominal concentration in mol%:

NO_2/He (0.978 \pm 0.5)%

NO_2/He (0.987 \pm 0.5)%

NO_2/N_2 (4.75 \pm 0.24)%

N_2 99.996% (industrial gas).

The gas is used without any further purification. IR spectra of the gases contained in the cylinders are recorded before their use and they show the presence of trace amounts of NO, HNO_3 , and HNO_2 that are expected in every gas mixture of NO_2 containing some water [Weis D. D. et al., 1999], probably present in small amounts in the non perfectly anhydrous IR gas cell/teflon lines.

3.1.3 Organics:

The fatty acids are from SIGMA ALDRICH and used without any further purification:

- Palmitic acid sodium salt ($C_{16}H_{31}NaO_2$); 99% purity
- Stearic acid sodium salt ($C_{18}H_{35}NaO_2$); >99% purity
- Oleic acid sodium salt ($C_{18}H_{33}NaO_2$); >99% purity

Their surfactant characteristics (Critical Micelle Concentration CMC) are reported in tab. 3.1:

product name	product abbreviation in this work	MW (g/mol)	CMC in water (mol/L)
palmitic acid sodium salt	NaC ₁₆	278.41	$2.1 \cdot 10^{-3}$ at 30°C [Marsh D., 1990] $2.1 \cdot 10^{-3}$ [Akhter M. S., 1997]
stearic acid sodium salt	NaC ₁₈	306.46	$2.6 \cdot 10^{-3}$ [Mularczyk E. et al., 1996]; $1.8 \cdot 10^{-3}$ [Marsh D., 1990]; $1.8 \cdot 10^{-3}$ [Akhter M. S., 1997]
oleic acid sodium salt	NaC _{18:1}	304.44	$2.15 \cdot 10^{-3}$ [Akhter M. S., 1997]

Tab. 3.1 Used fatty acids surfactants characteristics.

The solvents used for preparing the fatty acids solution are deionised water and spectroscopic grade pure ethanol (>99%, Fluka)

3.2 Surface preparation and coating

3.2.1 Pellets preparation:

NaCl(100) surface for the heterogeneous reactivity experiments have been prepared as per the following procedure:

NaCl powder grains are ground by hand until a fine powder is obtained. This powder is sieved and the <80µm fraction is kept at 110°C for at least one day before preparing the tablets.

The pellet press working conditions are chosen after optimising the time and pressure required by checking the obtained NaCl pellet surfaces via optical microscope. NaCl micro-crystals are found to best sinter together when a weight of 7 tons is applied for 2 minutes. Fig. 3.1 shows two typical optical images at 100x magnification.

As can be seen in fig. 3.1, the single grain borders are not visible any more and the surface flatness is very good. Some microscopic linear surface defects are present because of the roughness of the press tools. Some small crystallites are nevertheless still present on the outer part of the tablet surface because the pressure is not applied perfectly homogeneously on the surface (fig.3.1b).

No more improvement is possible as 7 tons is the pressure limit of the press, and if this pressure is applied to the powder sample for a longer time, the resulting pellet is very fragile and flakes when trying to handle it.

The conclusion is that these are the most compact and homogenous surfaces from a microscopic point of view that we are able to obtain.

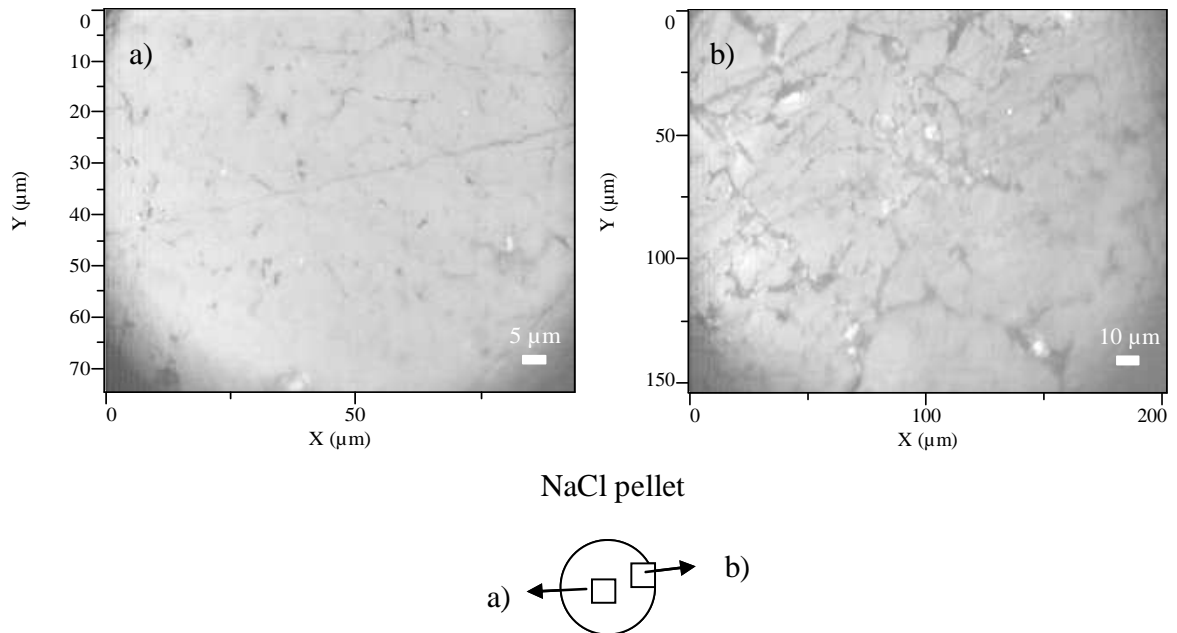


Fig.3.1 NaCl pellets optical images taken with a 100x (a) objective. In (b) a 100x image of the external border of the tablet where less pressure is applied and some fractures and small salt grains are still present on the surface.

3.2.2 Surface coating

If a known quantity of fatty acid solution is deposited on a flat surface, the characteristics of the deposit strongly depend on the solvent evaporation conditions (i.e. T, RH, P). Without having the possibility of controlling these conditions, the reproducibility of the surface deposit cannot be assured.

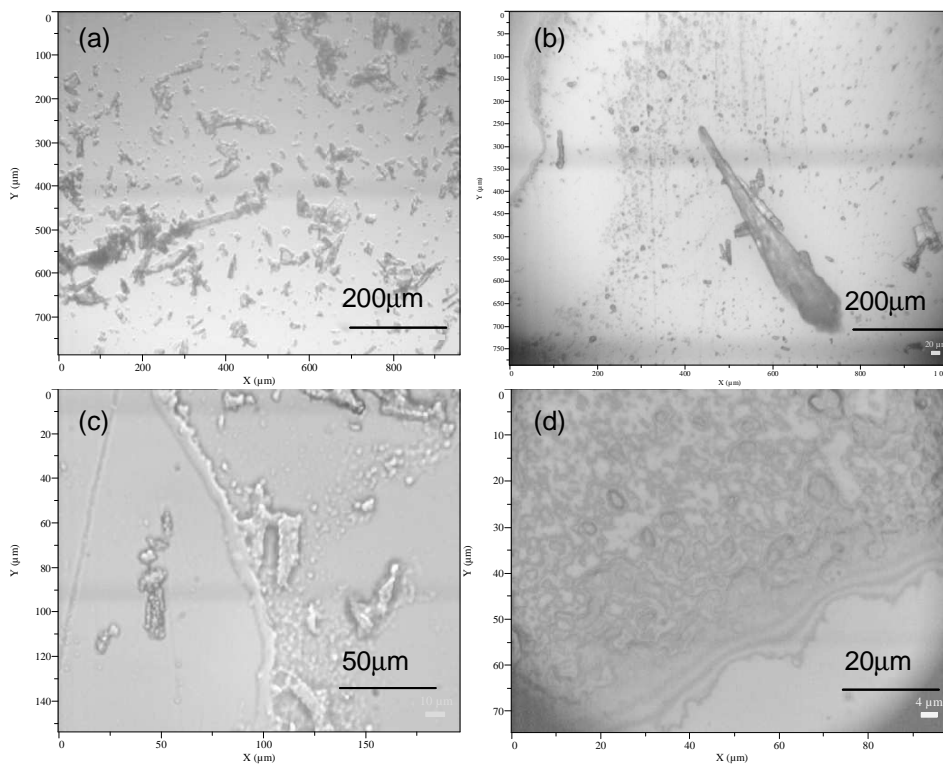


Fig. 3.2 A drop of NaC_{18} solution on mica(100) surface after drying for 1h30 under microscope light Magnification 10x (a), 50x (b) and 100x (c) - (d)

In fig.3.2 optical microscope images were presented i.e. of a drop of oleic acid sodium salt aqueous solution deposited on a mica surface, with the intention of highlighting the strong inhomogeneous character of the deposit once the solvent has evaporated.

From these images we can observe that $\text{NaC}_{18:1}$ can recrystallise with different morphologies and with different crystal sizes: from some hundreds of micrometers (fig.3.2.b) down to a few micrometers scale (fig.3.2.a and c). Not only crystalline structures can be formed, but also a sort of viscous deposit with varying thicknesses and varying packing order degrees, as can be seen in fig.3.2.c and d. These organic deposits have been studied to try to identify the Raman signature of the different F.A. agglomeration structures (see chapter 5).

In order to compare F.A. coated/uncoated $\text{NaCl}(100)$ reactivity at different humidities, a higher reproducibility of the surface characteristics is necessary. The dip-coating technique when performed in controlled environmental conditions can assure this better than any other techniques.

The NaCl surfaces are coated with a fatty acid deposit via a dip-coating procedure. The dip-coating technique is widely used in surface treatment, even at the industrial scale, especially with the sol-gel method. This procedure consists of vertically dipping the surface into a solution containing the species (or its precursors) that we want to deposit on the surface (fig.3.3). The precise control (through a motorised system) of the speed of removal of the surface is a key parameter for obtaining the desired thickness and homogeneity of the deposit.

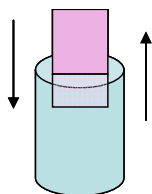


Fig.3.3 A schematic representation of a dip-coating procedure

The dip-coater apparatus used, owned by IEMN (Institut d'Electronique, Microélectronique et Nanotechnologie, University of Lille1), is located in a clean room.

Fresh F.A. ethanol solutions at the CMC are prepared by vigorously stirring the solution in a heat bath at $40\text{-}45^\circ\text{C}$ for 20 minutes so as to help the F.A. powder to dissolve. The solution is placed in an ultrasonic bath for 1-2 minutes to help disperse the floating aggregates. The solution is filtered with a $<20\mu\text{m}$ Millipore filter before use and is used within the same day.

The NaCl tablets are placed on a sample holder constructed from a glass slide onto which a special tablet housing is fixed. The sample holder is dipped into a F.A. ethanol solution at a speed of 2mm/s . After a residence time of 30s inside the solution, the glass holder is pulled out at the same speed. The tablet is left to dry in the laboratory atmosphere ($T=293\pm 2\text{K}$; $\text{RH}=50\%\pm 10\%$) for 10 minutes before being put inside a Petri box. The Petri box is then put inside a dark glass dryer (P_2O_5 drying agent) for the time between the surface preparation and the surface exposure in the reactor. The coated particles are exposed to NO_2 within the same day as the organic coating has a short lifetime due to atmospheric oxidation of the organic layer.

3.3 Vibrational spectroscopy

Infrared absorption spectrometry and Raman scattering spectrometry are based on vibrations of molecules and/or crystals. The vibrational states of a molecule or a crystal can be probed in different ways. The most direct way is through IR spectroscopy as vibrational transitions typically require an amount of energy that corresponds to the IR region of the spectrum. Raman spectrometry, which typically uses NIR, visible or UV light, can also be used to measure the vibrational frequency directly. The simultaneous excitation of vibrational and

rotational transitions gives rise to vibration-rotation spectra. A schematic representation of the IR and Raman absorption/scattering processes is shown in fig.3.4.

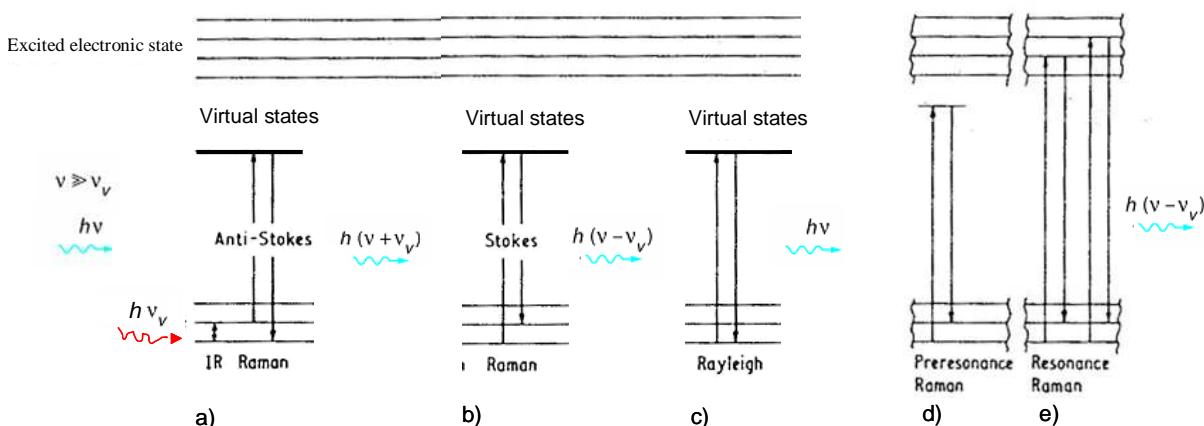


Fig. 3.4 IR absorption (in red) and Raman scattering process (in light blue)

A non linear molecule with n atoms has $3n-6$ vibrational modes, whereas a linear molecule has $3n-5$ normal vibrational modes as rotation about its molecular axis cannot be observed. The coordinate of a normal vibration is a combination of changes in the position of atoms in the molecule. It is usual to describe molecular vibrations by the change of internal coordinates: stretching, bending, rocking, etc...and the normal coordinate, Q can be constructed and described as a combination of internal coordinates. In order to carry out the quantum mechanical treatment of molecular vibrations, it is necessary to introduce a new set of coordinates called normal coordinates. One normal coordinate is associated with one normal vibrational mode.

In the harmonic approximation, the ordinary differential equation follows:

$$(3.1) \quad \mu \frac{d^2 Q}{dt^2} + kQ = 0$$

The solution to this equation is:

$$(3.2) \quad Q(t) = A \cdot \cos(2\pi\nu t); \quad \nu = \frac{1}{2\pi} \sqrt{\frac{k}{\mu}}$$

A is the maximum amplitude of the vibration coordinate Q , μ is the reduced mass and k the force constant.

Solving the Shroedinger wave equation, the energy states of each normal coordinate are given by:

$$(3.3) \quad E_v = \left(v + \frac{1}{2} \right) \frac{h}{2\pi} \sqrt{\frac{k}{\mu}}$$

Where v is a quantum number that can take values of 0, 1, 2, ...and h the Planck constant. The difference in energy when v changes by 1 is therefore equal to the energy derived using classical mechanics. For a harmonic oscillator, transitions are allowed only when the quantum number v changes by one ($\Delta v = \pm 1$). The observation of overtones $\Delta v > \pm 1$ is only possible because the vibrations are anharmonic.

Typically only small molecules exist as gases at ambient temperature. In the gas phase molecules are essentially independent with little or no effect due to the interactions between molecules. Thus, for gas-phase molecules, not only the vibrational states of molecules are quantized (v), but the way the whole molecule spins around its centre of gravity is also quantized (rotation quantum number J). One observes for gas-phase molecules a small number of vibrational transitions, each of which is split into many rotational transitions.

In a liquid, the rotational motion is normally completely quenched due to intermolecular interactions. When the molecules being observed are relatively small, or have high symmetry, it is often possible to distinguish among possible structures or isomers by counting the number of vibrational transitions. However, since the rotational transitions are absent, no information is available on bond lengths in the condensed phase from the vibrational spectra. When molecules get very large or have low symmetry, there are numerous vibrational transitions and it is impossible to assign their structure from their vibrational spectra.

Many solid materials, including minerals, are composed of molecules and ions ordered in a lattice arrangement called crystals. There are a variety of crystal structures such as cubic, hexagonal, etc...with a total of 230 spatial groups. The vibrational transitions depend on the molecule or ion at the site of the crystal and on the spatial group. In a crystal with Z molecules/ions per cell with p atoms per molecules, there are $Zp-3$ vibrations and $Z(3p-6)$ internal vibrations.

By using the different available techniques, it is possible to determine the vibrational normal modes, molecular, site and spatial group symmetry of the studied system [Decious J. C. et al., 1977], [Turrell G., 1972].

A vibrational mode is active in infrared absorption spectroscopy if the derivative of the molecular dipole moment (\vec{p}) with respect to the normal coordinate $d\vec{p}/dQ \neq 0$.

A vibrational mode is active in Raman scattering spectroscopy if the polarizability derivative with respect to the normal coordinate $d\alpha/dQ \neq 0$, with:

$$(3.4) \quad \vec{p} = \vec{p}_0 + \underline{\alpha}\vec{E}$$

\vec{p} is the induced dipolar moment, \vec{p}_0 in the intrinsic dipolar moment, $\underline{\alpha}$ is the polarizability tensor and \vec{E} the electric vector.

The classification of molecular vibrations by symmetry is useful because it is easy to derive selection rules for IR and Raman activities by using information in the character tables.

3.3.1 Infrared spectroscopy

Infrared spectroscopy is based on the interaction between matter and radiation in the IR part of the electro-magnetic spectrum. The mid-infrared, approximately $4000-400 \text{ cm}^{-1}$ ($30-1.4 \mu\text{m}$) is used to study the fundamental vibrations and associated rotational-vibrational structure.

In IR spectroscopy the transition energy is often expressed in term of wavenumber $\tilde{\nu}$ (cm^{-1}) because it is directly proportional to energy: $E(J)=1.986 \times 10^{-23} \tilde{\nu}$.

Fourier transform infrared (FTIR) spectroscopy is a measurement technique for collecting infrared spectra and its principle is shown in the scheme 3.5. Instead of recording the amount of energy absorbed when the frequency of the infra-red light is varied (monochromator), the IR light is guided through a Michelson's interferometer. The principle is the measurement of the temporal coherence of the light, using the time-domain measurements of the electromagnetic radiation. After passing through the sample, the interferogram is measured.

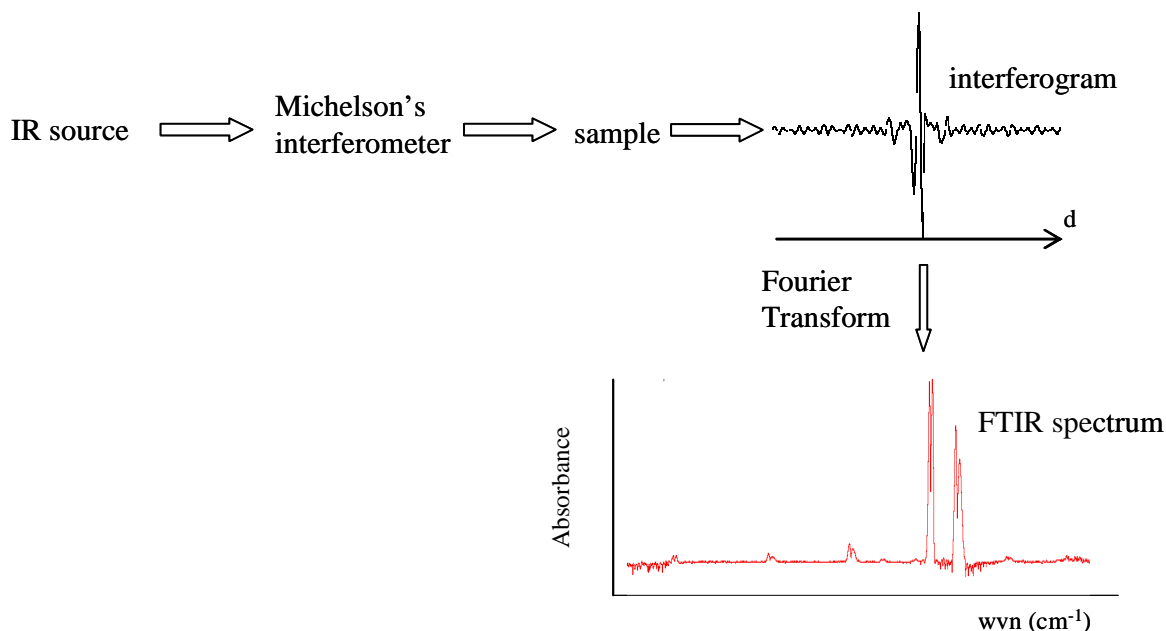


Fig. 3.5 Measurement principle of a FTIR spectrometer.

Performing a mathematical Fourier transform on this interferogram results in a spectrum identical to that from conventional (dispersive) infrared spectroscopy. Measurement of a single spectrum is faster with the FTIR technique because information at all frequencies is collected simultaneously. This allows multiple samples to be collected and averaged together resulting in an improvement in sensitivity.

Gaseous samples require little preparation beyond purification, but a sample cell with suitable windows and a long optical pathlength is normally needed as gases have relatively low densities and hence weak absorbencies (a typical IR gas cell is 10 cm long).

Solid samples can be prepared in different ways. The method used in the present work is to finely grind a quantity of the sample with a specially purified salt, i.e. NaCl. This powdered mixture is then crushed in a mechanical press to form a translucent pellet through which the IR beam of the spectrometer can pass.

The diffuse reflectance technique allows the recording of IR absorption spectra with fine powdered samples. This technique is often combined with in-situ reactors to monitor reactions between fine powders and gases.

3.3.2 Raman spectroscopy

Raman spectroscopy is based on the principle of spontaneous Raman scattering, whose schematic process is shown in figure 3.4.

The incident ray of frequency ν is very high in energy compared to the vibrational transition ν_v . After excitation from the fundamental level the molecule can lose its excess energy *via* various radiative pathways:

- emitting a photon with the same energy. This is the case of an elastic scattering, or Rayleigh diffusion (fig.3.4.c).
- if the molecule relaxes to a vibrationally excited level (fig. 3.4.b), the emitted photon will have an energy equal to $h(\nu-\nu_v)$, lower than the excitation energy. In this case the phenomenon is called Raman Stokes scattering.
- if the molecule was originally in a vibrationally excited state and after excitation to a virtual excited state falls back from the virtual state to the fundamental state (fig. 3.4.a),

the emitted photon has an energy of $h(\nu+\nu_v)$, higher than the incident light. This case is anti-Stokes Raman scattering.

In standard conditions Stokes scattering is more intense than anti-Stokes, mainly because the lower vibrational states have a larger population, as given by a Boltzmann distribution:

$$(3.5) \quad \frac{I_{\text{Stokes}}}{I_{\text{anti-Stokes}}} = \left(\frac{\nu - \nu_v}{\nu + \nu_v} \right)^4 \cdot e^{\frac{h\nu}{kT}}$$

Inelastic scattered light contains unique information characteristic of the vibrations of the probed molecule, because it is linked to the variation of polarisability α of the molecule during a transition from the i to the j level.

The polarisability of the molecule finds its origin in a change of electron distribution when an incident electro magnetic field perturbs differently nuclei and electrons of the molecule because of their different masses.

A description of polarisability in the internal coordinate (Q) reference system as a function of incident electro magnetic field gives the following expression when we only take the first term in the expansion:

$$(3.6) \quad \underline{\alpha} = \underline{\alpha}_0 + \sum_{Q=0} \frac{d\underline{\alpha}}{dQ} \cdot \vec{Q}$$

So that equation (3.5) becomes (3.7) in a simplified form^{††}:

$$(3.7) \quad \vec{p} = \vec{p}_0 + \underline{\alpha}_0 \cdot \vec{E}_0 \cos(2\pi\nu t) + \sum_{Q=0} \frac{d\underline{\alpha}}{dQ} \cdot \frac{Q\vec{E}_0}{2} [\cos(2\pi(\nu + \nu_v)t) + \cos(2\pi(\nu - \nu_v)t)]$$

In this expression we can identify the Rayleigh scattering in the term containing $\cos(2\pi\nu t)$, and the Raman anti-Stokes and Stokes scattering in the $\cos(2\pi(\nu + \nu_v)t)$ and $\cos(2\pi(\nu - \nu_v)t)$ terms respectively.

The intensity of the Raman scattering is then proportional to $\left| \frac{d\underline{\alpha}}{dQ} \right|^2$, described as the Raman activity of the vibrational modes.

A Raman spectrum (i.e. fig.3.6) contains peaks or bands identified by a Raman shift in wave number units ($\tilde{\nu}$ in cm^{-1}). A Raman shift represents the energy difference between two vibrational states. The Raman spectrum of a liquid sample represents the molecular vibrations of molecules oriented in all directions. In the solid state, molecules are “frozen” in specific orientations. In solid crystals, molecules are oriented in three-dimensions.

^{††} Including only the non-parametric processes (where there is some energy exchange involved) in the first order term of polarisation.

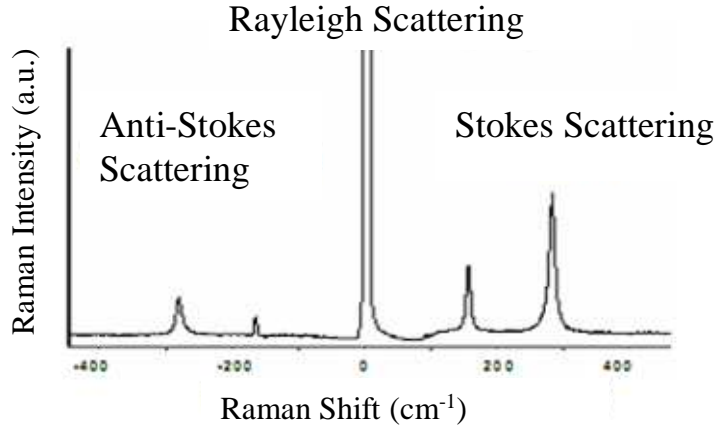


Fig. 3.6 Stokes and anti-Stokes Raman signature of calcite excited at $\lambda=632.5\text{nm}$

Raman theory with linearly polarized light

An insight into the theory of Raman scattering using highly focused excitation and scattered linearly polarized light is summarized below ([Batonneau Y. *et al.*, 2000; Sourisseau C., 2004]).

A surface irradiated with a focused laser beam in the visible range emits a flux of photons Φ_S that can be described as the sum of different components:

$$(3.8) \quad \Phi_S = \Phi_R + \Phi_E + \Phi_T + \Phi_F$$

Raman Φ_R and elastic Φ_E scattering are often present together with thermal radiation Φ_T and luminescence and fluorescence radiation Φ_F . Elastic scattering can be easily cut off with filters, whilst the other components cannot and can be present in the Raman spectrum. Organic components in particular are able to emit a bright luminescence which covers and hides Raman scattering in the majority of cases. Fluorescence effects that can mask the Raman signal are usually produced in the same spectral region of the probe wavelength (visible), but not in the case of excitation in the UV, where Raman scattering is produced far enough from the fluorescence window so as to be unaffected.

An expression for the scattering signal intensity Φ_R in a Raman microprobe instrument can be written in the following form:

$$(3.9) \quad \Phi_R = K \int_V \int_{\Omega} |\tilde{\mathbf{E}}_e \cdot \boldsymbol{\alpha}_{XYZ} \cdot \mathbf{E}_s|^2 d\Omega \cdot dV$$

With $K = 4 \pi^2 \gamma^2 \Phi (v_0 - \Delta v)^4$, where $\gamma=1/137$, Φ is the exciting flux, v_0 and Δv are the wavenumbers of the exciting and Raman-shifted radiation, respectively, \mathbf{E}_e is the electric vector ($\tilde{\mathbf{E}}_e$ is the transpose of the electric vector) of the excitation light, \mathbf{E}_s is the electric vector of the scattered light, $\boldsymbol{\alpha}_{XYZ}$ is the Raman tensor of the sample system in the space-fixed coordinates XYZ. V is the total scattering volume and Ω is the solid angle defined by the angular semi-aperture of the objective. The Raman tensor in the space-fixed coordinates XYZ relates to the Raman tensor in the crystal-fixed coordinates xyz assuming some approximations by

$$(3.10) \quad \boldsymbol{\alpha}_{XYZ} = \tilde{\mathbf{R}} \cdot \boldsymbol{\alpha}_{xyz} \cdot \mathbf{R}$$

where \mathbf{R} is the rotation matrix (and its transpose $\tilde{\mathbf{R}}$) defined with respect to Euler angles. The Raman spectra of crystallized particles is found to depend on the orientation (\mathbf{R}) while the Raman spectra of amorphous compounds and randomly oriented nanocrystals exhibit typical powdered Raman spectra. The use of an analyser located in the scattered beam in the Y direction parallel to polarization exciting light suppresses the α_{XX} , α_{YX} and α_{ZX} elements. Φ_R can finally be reduced to :

$$(3.11) \quad \Phi_R = K \times \alpha_{YY}^2$$

when the effect of large aperture objectives is neglected, which is the case for samples with low birefringence [Batonneau Y. *et al.*, 2003], [Sourisseau C., 2004]. The expression of the Raman tensor element α_{YY} in the laboratory frame in term of Raman tensor elements α_{ij} of the crystal and Eulerian angle functions is detailed in [Jen S. *et al.*, 1977]. Polarized confocal Raman can help in detecting orientation changes if they occur during an experiment by measuring changes in the relative intensities of Raman peaks.

3.4 Surface analysis – imaging techniques

The principle characteristic required from a surface analysis technique for our case study is the ability to operate under ambient conditions so as to be in as similar a situation as possible to real surfaces in the atmosphere. Therefore vacuum techniques are not suitable as even though they are very surface sensitive, they can substantially alter the surface organisation of our hygroscopic samples. Techniques using a high energy probe are not adapted to a thin fragile coating of thermally labile organic species.

Raman micro-spectroscopy has been systematically used to obtain molecular information and is adapted to *in-situ* conditions. Non-contact atomic force microscopy (AFM) has been used to estimate surface morphology, always under *in-situ* conditions, with high spatial resolution. The goal of our surface analysis is to elucidate the spatial arrangement of the surface after exposure to NO_2 with different humidities, and to eventually test the effect of organic molecules on surface reorganisation in this same process. The coupling of these two techniques can give us information about the surface status (AFM) and about the chemical species on the inner part of the surface.

3.4.1 Micro-Raman imaging

The confocal Raman microspectrometry combines the molecular capabilities of Raman spectroscopy and the spatial resolution of optical microscopy.

Raman microscopes using optical microscopes were introduced in the 1970s, and take advantage of diffraction-limited optics^{††} to provide molecular and crystalline information. The spatial resolution of a Raman microscope is reported to be of the order of the laser wavelength. A Raman microscope equipped with an automated stage records Raman maps using the point mapping method, which is, so far, the most popular method of recording Raman maps.

Successful data processing of Raman spectra within a Raman map results in Raman images that represent the spatial/volumetric distribution of different chemical components within the sample.

^{††} Minimum diameter of the light spot $D = \frac{1.22\lambda}{NA}$; NA= numerical aperture of the optics; valid for light in the visible spectral window.

The surfaces are analysed at the “University Measurement Centre for Raman Microspectroscopy” in the LASIR laboratory, mainly using a LabRAM Dilor. A LabRAM HR UV is also used for testing the more superficial layer of sample surfaces.

The samples are mounted on the microscope stage of a LabRAM confocal Raman microspectrometer (Horiba, Jobin-Yvon), in back scattering geometry. The instrument is optimised for visible wavelength excitation, green (514.5 nm) and red (632.8 nm). For a schematic representation of the instrument see figure 3.7.

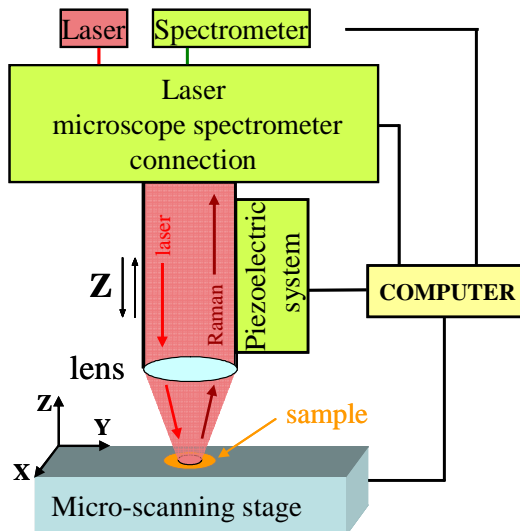


Fig. 3.7 Schematic representation of the confocal micro-Raman spectroscopy.

The constituent elements are as follows:

- A video camera provides an optical view of the samples on a video monitor.
- Excitation laser source: a Y-polarised beam at 632.8 nm is generated by a He-Ne laser with an output power of 18 mW. The laser power delivered to the sample is approximately 8 mW and can be attenuated by a set of neutral density filters with optical densities ranging from 0.3 to 4. If the 514.5 nm wavelength is used, the LabRAM instrument is coupled to an external Spectra – Physics low-power Ar⁺ laser (max 200 mW), also with its polarization directed along Y.
- An Olympus microscope, equipped with objectives of magnification 10x, 50x, 100x with a numeric aperture of 0.8 or 0.9, allowing us to obtain an estimated beam diameter on the focus plane of about 1µm² (0.856 µm for λ=632.8 and 0.697 µm for λ =514 nm)
- The spectrometer: back-scattered light is collected by the optical objectives and Rayleigh scattering is filtered by a Super Notch PlusTM filter. The confocal pinhole aperture can range from 0 to 1500 µm so that the axial resolution (i.e. the diffusing volume at the focus point) can be tuned^{§§} [Brémard C. *et al.*, 1985]. The holographic diffraction grating with 1800 g/mm allows the recording of a spectrum. In this case the spectral window recorded is 1000 cm⁻¹ wide with a spectral resolution of 4 cm⁻¹.
- The LabRAM is equipped with a front-illuminated liquid-nitrogen-cooled charge-coupled device (CC Spex) detector (2048 × 512 pixels).

Spectral calibration is performed with the silicon band at 520±0.5 cm⁻¹.

The LabRAM HR UV uses the same geometry and principle, but there are some peculiarities due to using a different wavelength. The excitation source is a solid-state Nd:Yag laser whose frequency is doubled twice so that λ_{exc}=266 nm and the output power is 230 mW. UV beams have a low penetration pathlength in the majority of materials (10 ÷ 10² nm) so that the probed sample volume can be greatly reduced and the information more surface-specific. The

^{§§} The axial resolution along z axis can be significantly reduced in the case of an absorbing sample.

working confocal hole (100 μm) gives a measured spot at the surface of the sample of 1.7 μm with a 40x, NA=0.50 objective. The highest lateral resolution achievable is <0.6 μm with a 100x, NA=0.9 objective^{***}. This is not the case for many materials which are transparent to light in the visible range. The Raman signal is amplified when exciting in the UV range, because it is proportional to ν_{exc}^4 (see equation 3.5). The photon energy itself can induce an amplification process because the frequency of the excitation light is near to the frequency of electronic transitions. As a consequence pre-resonance or resonance phenomena can appear and enhance the intensity of the Raman signal by some orders of magnitude.

A long focal length inside the spectrometer (80.0 cm) coupled with gratings of high groove density (2400 g/mm) can lead to a spectral resolution of 1.5 cm^{-1} . Rayleigh scattering is eliminated by edge filters, so that the minimum Raman shift that can be detected is 350 cm^{-1} . All of these characteristics are promising for the detection of surface species such as organics deposited on NaCl or thin layers.

Unfortunately, all the attempts to detect the fatty acid coating by UV Raman microspectrometry failed. Indeed, the use of low power laser excitation of the sample such that a suitable signal/noise ratio would be obtained, still leads to severe damage of the sensitive thin organic coating. In addition, the expected advantages of UV Raman microspectrometry to detect NaNO_3 microcrystal on a NaCl surface are hampered by photochemical conversion of NaNO_3 to NaNO_2 by UV radiation. No further investigation was carried out in this way throughout this work. It should be noted that the UV photochemical reaction of NaNO_3 does not occur in the troposphere but is effective in the stratosphere.

The confocal Raman mapping was carried out directly in the laboratory atmosphere with a measured RH of around 45% and a controlled temperature of 293 ± 2 K.

The computer controlled Raman (XYZ) mapping consists of recording many spectra in a point-by-point XY scanning mode with 0.1 μm as a minimum step thanks to a motorized translation stage controlled by the program *Labspec v4.02*. With a focus diameter on the sample of between 0.5 and 1 μm at the given working wavelengths results in the ability to have a reasonable XY resolution of 1 μm^2 .

The system is equipped with a piezo translator (Z-direction) and feedback loop to automatically obtain perfect laser focus on the surface in the case of severe surface roughness.

Accumulation and spectrum acquisition time are optimized differently depending on the analysis. The scanning Raman mapping generates a three-dimensional data set ($m \times n \times \lambda$), that is, $m \times n$ spectra, each containing $\lambda = 2040$ spectral elements. So, each ij^{th} pixel is a microzone of the sample for which a complete characteristic Raman spectrum can be recorded.

The conventional data processing of Raman imaging is the following: a narrow spectral region corresponding to a characteristic Raman band of a compound of interest is selected from the entire recorded spectral range. Then, the integration of the area under this peak over all of the $m \times n$ spectra gives an estimation of the relative concentration of the compound of interest in each ij pixel and provides a ($m \times n$) Raman image of the compound of interest (see fig. 3.8).

*** Measured and not estimated values.

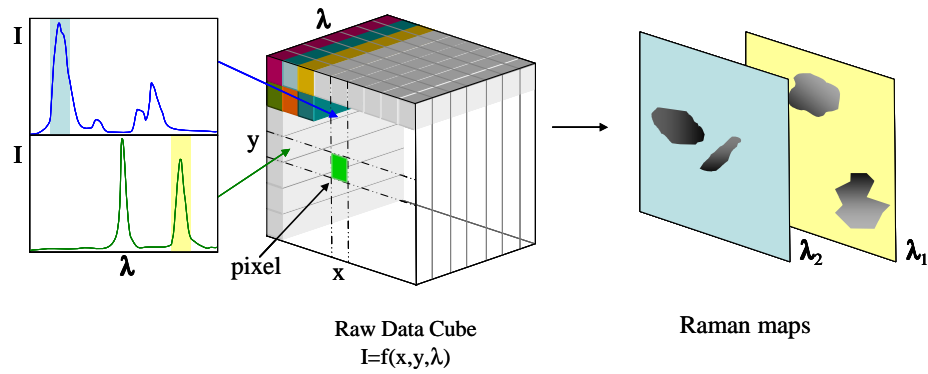


Fig. 3.8 Schematic process of Raman imaging data process.

3.4.2 Tapping-mode Atomic Force Microscopy (TM-AFM)

Atomic force microscopy is a technique allowing access to surface morphological information as it is sensitive to surface roughness which can be estimated with high spatial resolution, especially in z. This technique is based on the principle that attractive or repulsive forces exist at the atomic level between the sample and the probing tip, as shown in fig. 3.9.

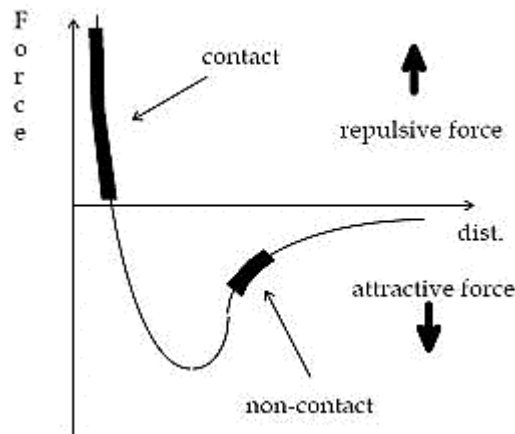


Fig. 3.9 Force vs distance tip-sample from Lennard-Jones equation. AFM can be designed to operate in either of the two regimes indicated by heavy lines.

The main goal is then to detect forces in the range $10^{-6} - 10^{-8}$ Newton. This can be achieved by placing a nanometre-size tip (surface force probe) on a cantilever, whose movements can be detected via deflection of a laser beam. The cantilever displacements over the sampling surface have to be nm-scale precise, thus use of a piezoelectric system is necessary (see fig.3.10).

The whole system requires a synergy of technically complex devices and was only invented in 1986 by Quate and Gerber building on the work of Gerd Binnig and Heinrich Rohrer who developed STM in the early '80s, work which earned them the Nobel Prize for Physics in 1986. As a surface technique AFM has several advantages. AFM provides a true three-dimensional surface profile and samples do not require any special treatment (such as metal/carbon coatings) that would irreversibly change or damage the sample. In addition, AFM can work perfectly well in ambient air or even in a liquid environment. In principle, AFM can provide higher resolution than a scanning electron microscope (SEM). It has been shown to give true atomic resolution in ultra-high vacuum (UHV) and, more recently, in liquid environments. High resolution AFM is comparable in resolution to Scanning Tunneling Microscopy and Transmission Electron Microscopy.

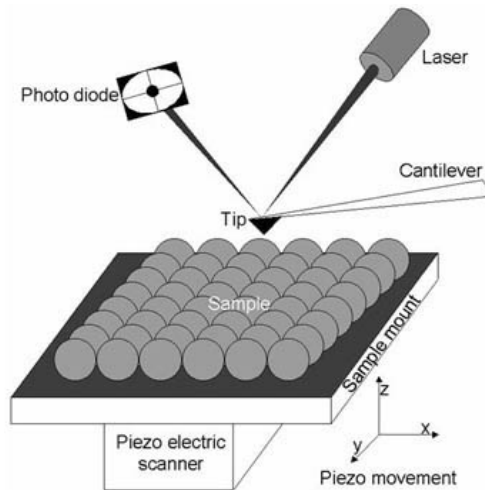


Fig. 3.10 AFM system elements

A disadvantage of AFM compared with SEM is the image size. The SEM can image an area on the order of millimetres by millimetres with a depth of field on the order of millimetres. The AFM can only image a maximum height on the order of micrometres and a maximum scanning area of around 150 by 150 micrometres.

The relatively slow rate of scanning during AFM imaging often leads to thermal drift in the image, making AFM microscopy less suited for measuring accurate distances between artifacts on the image; however these image distortions induced by thermodrft can be eliminated by several methods[Lapshin R. V., 1995].

There are different ways of probing the surface with an AFM instrument. Principally they are the static and the dynamic modes.

In static mode the cantilever deflection is used as feedback signal, and since close to the surface of the sample attractive forces can be quite strong, causing the tip to 'snap-in' to the surface, static mode AFM is almost always done in contact where the overall force is repulsive. Consequently, this technique is typically called "contact mode". In contact mode, the force between the tip and the surface is kept constant during scanning by maintaining a constant deflection.

In the dynamic mode, the cantilever is externally oscillated. The oscillation amplitude, phase and resonance frequency are modified by tip-sample interaction forces; these changes in oscillation with respect to the external reference oscillation provide information about the sample's characteristics. Schemes for dynamic mode operation include frequency modulation and the more common amplitude modulation. In amplitude modulation, changes in the oscillation amplitude or phase provide the feedback signal for imaging. In amplitude modulation, changes in the phase of oscillation can be used to discriminate between different types of materials on the surface. Amplitude modulation can be operated either in the non-contact or in the intermittent contact regime. In ambient conditions, most samples develop a liquid meniscus layer. Because of this, keeping the probe tip close enough to the sample for short-range forces to become detectable whilst preventing the tip from sticking to the surface presents a major hurdle for the non-contact dynamic mode in ambient conditions. In dynamic contact mode (also called intermittent contact or tapping mode) the cantilever is oscillated such that the separation distance between the cantilever tip and the sample surface is modulated.

In *tapping mode* the cantilever is driven to oscillate up and down at near its resonance frequency by a small piezoelectric element mounted in the AFM tip holder. The amplitude of this oscillation is greater than 10 nm, typically 100 to 200 nm. Due to the interaction of forces acting on the cantilever when the tip comes close to the surface, Van der Waals force or

dipole-dipole interactions, electrostatic forces, etc cause the amplitude of this oscillation to decrease as the tip gets closer to the sample. An electronic servo uses the piezoelectric actuator to control the height of the cantilever above the sample. The servo adjusts the height to maintain a set cantilever oscillation amplitude as the cantilever is scanned over the sample. A *Tapping AFM* image is therefore produced by imaging the force of the oscillating contacts of the tip with the sample surface. This is an improvement on conventional contact AFM, in which the cantilever just drags across the surface at constant force and can result in surface damage. Tapping mode is gentle enough even for the visualization of supported lipid layers or adsorbed single polymer molecules under liquid medium.

The topographic images presented in this work were acquired with a home-made atomic force microscope (J. Barbillat, LASIR) using electrochemically generated gold tips. Gold tips with diameters down to 30 nm are attached to the end of one prong of a quartz tuning fork (32 kHz) and move perpendicularly to the sample (tapping mode) with an amplitude of a few nm. The distance between the very end of the tip and the sample is maintained constant with a feed-back loop including a lock-in amplifier (Signal Recovery 7280) which drives the tuning fork and senses its vibration and the Z piezo element (Nanoblock Melles Griot) which moves the sample vertically. Raw data are further treated with Gwyddion 2.9 (Open Source software) to obtain useable topographic images. A schematic view of the instrument is shown in fig 3.11:

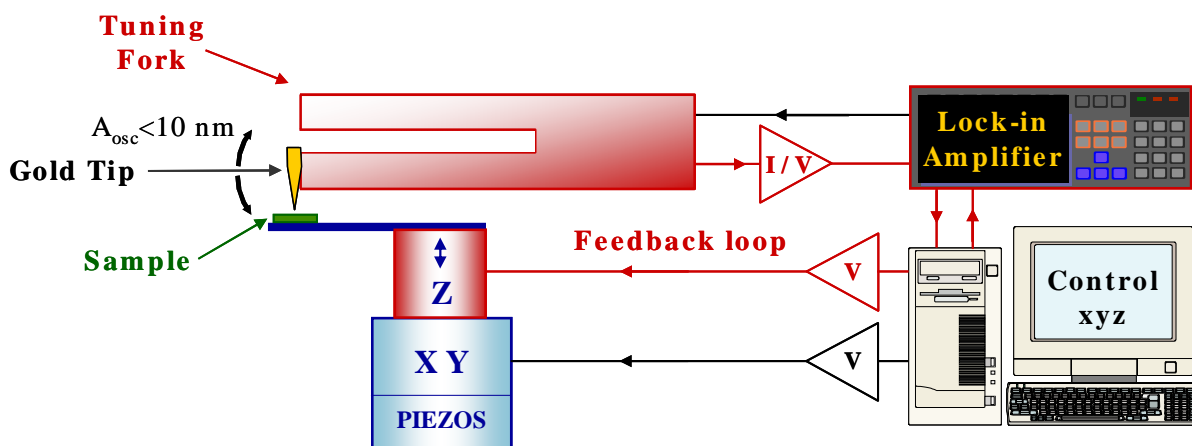


Fig. 3.11 Schematic view of the home-made AFM instrument operating in tapping-mode.

The AFM image is a deconvolution of the surface details and the point shape and interaction, such that image resolution depends on the sample roughness and the quality of the tip. Typically with the home-made instrument and tips we have a lateral resolution of 20-100 nm. The axial resolution is dictated by the piezoelectric crystals to 5-20nm and the maximum z contrast is limited by the electronics and is on the order of 4.5 μm .

Some AFM images have also been recorded during a demonstration of AIST-NT® with a SmartSPM™ 1000 microscope working in true non-contact mode.

Some others have been recorded in the IEMN installed in Villeneuve d'Ascq with the kind supervision of M. Marczak.

3.5 Heterogeneous reactivity

Heterogeneous chemistry is the study of the evolution of the gaseous and/or the condensed phases when they come into contact together.

In homogeneous chemical kinetics, there have been many experimental and theoretic studies performed in order to gain a better understanding of the reactions involved, allowing us in many cases to elucidate the reaction mechanism. However, heterogeneous reactions taking place at the gas-solid (or gas-liquid) interface have been less studied and are also more complex in contrast to the gas-phase rate processes which involve elementary reactions^{†††}. When a gas molecule collides with a solid/liquid phase, it can be taken up by the condensed phase reversibly or irreversibly. In the first case the molecule is released to the gaseous phase, in the second it is permanently incorporated. A pertinent and representative parameter for the process that can be unambiguously used by the scientific community is the uptake coefficient or the reaction probability, already described in ch.2.4.1.

In our specific case we will determine both the initial uptake γ_0 of NO_2 (and of N_2O_4) on NaCl and the reaction probability coefficient ϕ_0 (from ClNO formation).

3.5.1 Experimental methods

Some experimental methods have been developed for studying gas-solid phase interactions and for measuring the uptake coefficient. The measure principle is simple: the gaseous phase is put in contact with a solid phase of known area. The number of gaseous molecules taken up by the solid/liquid is measured during a known time interval. Generally it is the gas-phase composition which is followed as a function of time. Nevertheless, in certain cases the kinetic study follows the product formation in the condensed phase. The two main motivations for the choice of the second option are here detailed:

a) Technical advantage:

When the gas phase is put in contact with the reactive surface the reagent disappears with a consequent depletion of its gaseous phase concentration if it is not constantly renewed. The reaction then proceeds with a constantly diminishing rate, since the rate is proportional to the reagent concentration $[\text{A}]_g$. As a consequence, specific corrections must be introduced during the data treatment process. One solution is to work at flux conditions ($[\text{A}]_g = \text{const}$) and to detect the solid product formation instead of the reagent disappearance. This is in some cases the easier procedure.

b) Data correction:

When following the reagent depletion in the reactive system, the observed uptake rate has to be corrected for wall absorption that is always present, except for in some particular cases (i.e. the internally coated flow tube) or for very fast heterogeneous reactions:

If the reaction kinetics are followed by product formation this correction is unnecessary because the measured rate coefficient is already a direct measurement of the heterogeneous process.

In this section the main experimental methods for the measurement of γ are shortly described: flow tube, the Knudsen cell, the in-situ cell combined with Diffuse Reflectance Infrared Fourier Transformed (DRIFT) and the atmospheric simulation chamber.

^{†††} Elementary reactions are defined as those that cannot be broken down into one or more simpler reactions. Generally they consist of one or two reactant species and are referred to as unimolecular and bimolecular processes, respectively.

Flow tube reactor

a) Internally coated flow tube reactor:

It is a double wall Pyrex reactor of internal diameter 2.5 cm and 40 cm long (see fig.3.12). Its constituent parts are a cylindrical tube and a central movable injector used for trace gas introduction.

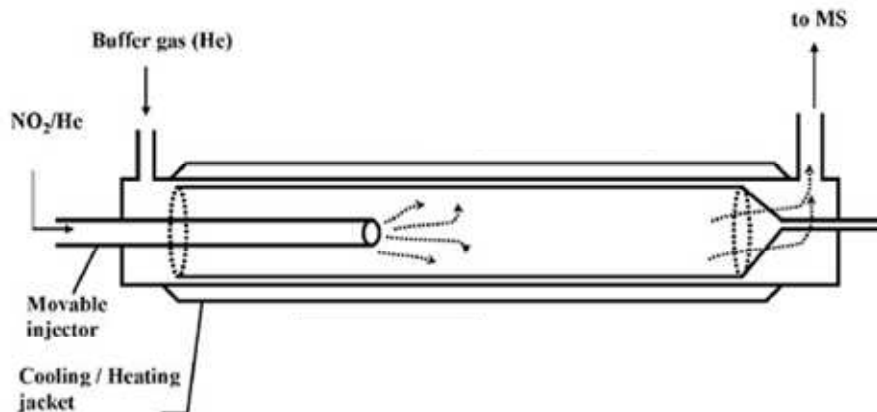


Fig. 3.12 Schematic view of an internally coated flow tube reactor ([George C. et al., 2005]).

The solid phase is deposited on the internal wall of the Pyrex tube, which is placed inside the reactor. By changing the injector position the contact time between the solid and the gaseous phase is varied; the gas phase composition is continuously followed by using a suitable analytic technique depending on the gaseous species or the experimental conditions. Large pressure (1-760Torr) and temperature ranges can be studied with such an experimental set-up. The measured uptake coefficients can vary between 10^{-4} and 10^{-1} . Temperature as low as 183K can be reached, but the solid surface cannot be renewed during the experiments so that its ageing is a possible experimental inconvenience.

b) Aerosol flow tube:

An evolution of the internally coated flow tube is the aerosol flow tube, where the condensed phase is a flux of aerosol particles, as shown in fig. 3.13. This allows the study of reactions on a condensed phase under conditions more representative of the real atmosphere.

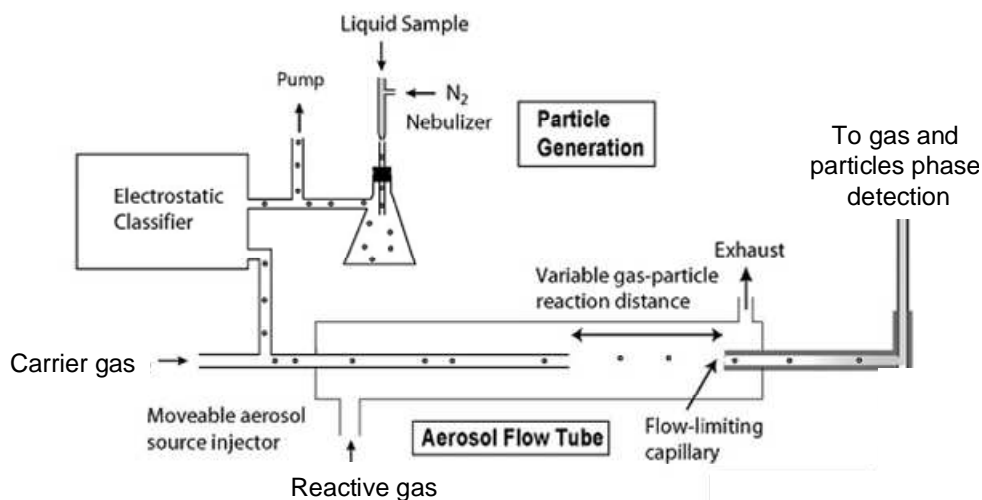


Fig.3.13 Schematic aerosol flow tube experimental set-up adapted from [Hearn J. D. et al., 2005].

Knudsen cell

This technique has been widely used for 40 years to measure gas phase and heterogeneous kinetics. It is particularly well adapted for working at pressures lower than 10mTorr. In these particular experimental conditions effects due to gas-phase collisions and diffusion-limited reactivity are strongly diminished.

Usually the reactor is a cubic stainless steel cell of about 100 cm³ which is internally coated with a Teflon film to limit wall reactivity.

Inside the cell the condensed phase is put in a sample holder with removable lid allowing the isolation of the sample from the rest of the cell. The gas phase flows inside the cell and is continuously analysed by a Low Pressure Quadrupole Mass Spectrometer. The residence time of the gas in the cell is tuned by varying the escape hole dimension (1-14 mm). See fig. 3.14 for a schematic diagram of the reactor.

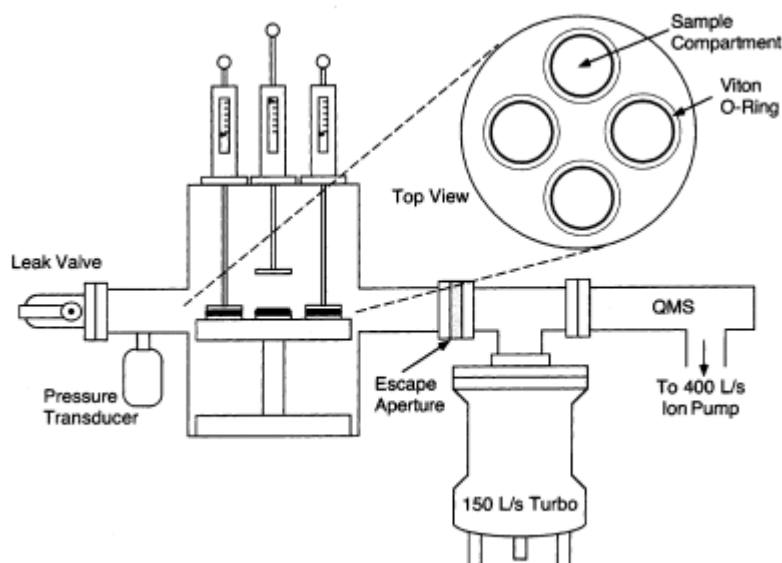


Fig.3.14 Knudsen cell of 1500cm³ equipped with 4 sample holders.[Johnson E. R. et al., 2005].

The kinetic parameters are derived by following the gas phase composition.

This technique allows the measurements of uptake coefficients in the range of 10^{-7} - 0.1 [Carloz F. et al., 1997].

The main advantage of this experimental set-up is the wide range of condensed phases that can be used – the condensed phase can be a liquid, a powder, a thin layer, a frozen surface and a monocrystal. Other important characteristics are the extended working temperature range (130-750 K) and the *in-situ* degassing of the sample.

The main disadvantages are the limited use for low vapour pressure samples, the ageing of the condensed phase that cannot be renewed during the experiment and the analysis of only the gaseous phase.

Powder-gas reactor

This method allows the *in-situ* simultaneous monitoring of the solid and gaseous phases put in contact inside the reactor (see fig.3.15). The detection technique usually employed is the Diffuse Reflectance Infrared Fourier Transformed (DRIFT), but Diffuse Reflectance UV-Vis Absorption or Raman Scattering can also be used.

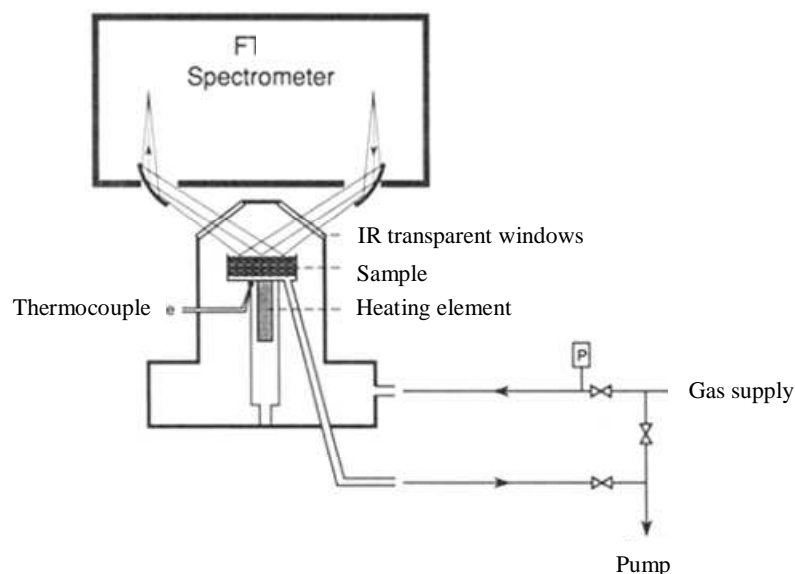


Fig. 3.15 Diffuse Reflectance -coupled gas-powder experimental set-up, adapted from [Vogt R. et al., 1994]

The powdered sample is put in the reaction chamber, which, in the case of DRIFT detection, is located inside a FTIR instrument. A parabolic mirror focuses the probe beam on the solid sample and the diffused reflected radiation is focused by another parabolic mirror onto the detector surface.

This method allows the measurements of uptake coefficients (or more precisely ϕ) in the range of 10^{-4} - 10^{-2} by monitoring the solid-phase products formation.

Its main advantage is that the diffused reflected radiation contains information on the absorption of both gaseous and solid phases.

Its main disadvantage is surface ageing, and sometimes the difficulty in estimating the extent and kinetics of the gas-phase diffusion inside the powdered macroscopic sample.

Atmospheric Simulation Chamber

The Atmospheric Simulation Chamber is of all laboratory techniques the nearest to real atmospheric conditions, because the reactivity volume is much bigger than in the previously described reactors: it can range from some litres to more than 250 m^3 . For heterogeneous reactivity studies an aerosol can be introduced or generated by photochemical reactions inside the chamber itself, where the mixture with the gaseous phase can be monitored in static conditions, usually with long optical length FTIR [Preszler Prince A. et al., 2007], [Prince A. P. et al., 2007], MS [Folkers M. et al., 2003] and UV-Vis spectroscopic [Mogili P. K. et al., 2006] techniques. Internal walls are coated with an inert material to minimise wall loss. In some cases a particle analyser is coupled to the simulation chamber, such that information on the evolution of particle size distribution and particle number can also be followed.

The chamber has many different apertures as shown in fig. 3.16, to allow pumping and the insertion of probes to continuously monitor pressure, temperature and relative humidity.

Uptake coefficients in the range of 10^{-8} - 10^{-4} (relatively slow reactions) can be measured from the evolution of the composition of the gaseous phase. One of the main problems in this technique is the difficulty in estimating the reactive surface area, S , which is reflected by large uncertainties in the value of the uptake coefficient.

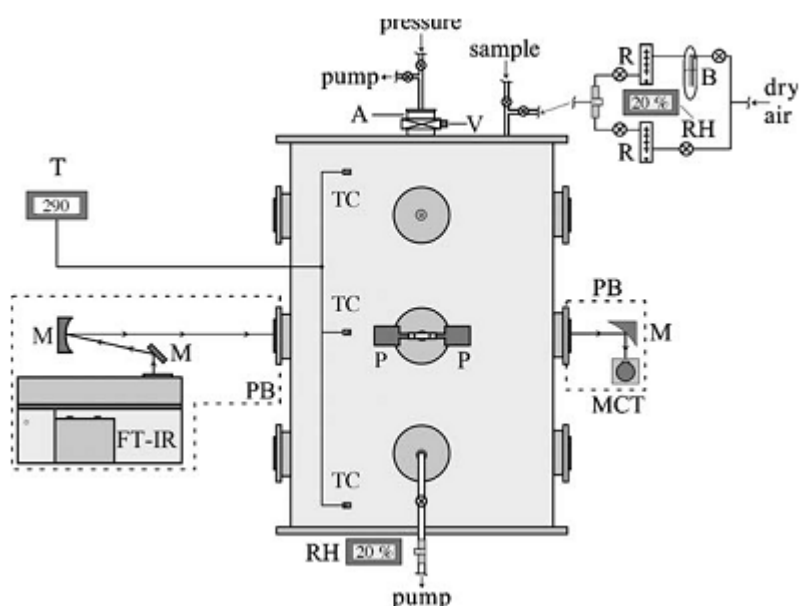


Fig. 3.16 A schematic diagram of an atmospheric chamber of 151 L [Mogili P. K. et al., 2006] showing the sample cartridge (A), antechamber valve (V), water bubbler (B), flowmeters (R), relative humidity sensors (RH), FT-IR spectrometer (FT-IR), mirror for external IR beam (M), IR detector (MCT), purge boxes for external beam path (PB), thermocouples (TC), temperature read out (T) and pressure transducers (P).

In tab. 3.2 the experimental characteristics of previously described methods are summarized: the type of solid surface studied, the accessible range of γ , the gas-solid contact time, the working pressure and some important references.

Each of the methods outlined above have specific advantages and limitations, and choosing which one is the more suited to a specific reaction system mainly depends on the initial reactivity estimation (the range of γ) and the desired operational conditions (pressure and temperature).

For our purpose we need an apparatus allowing the study of reactivity differences in the coated/uncoated NaCl+NO₂ system under pressures and humidities as similar as possible to those of the real troposphere. It is already known from the literature that the system has a low reactivity ($\gamma \approx 10^{-7}$), and the problem is therefore particularly challenging.

The techniques able to measure uptake coefficients in this range are the atmospheric simulation chamber for the large reactive surface area used (aerosol) and the Knudsen cell, even if the latter operates at low pressure.

A home-built [Aghnatiotis C., 2008] static reactor coupled to an FTIR spectrometer has been adapted to our specific needs. It is described in § 3.5.2.

Method	Surface	Accessible γ range	Contact time	Working pressure (Torr)	Some literature references
Internally coated flow tube	Solid film	10^{-4} - 10^{-1}	0-10 sec	1-760	[Thornberry T. et al., 2004], [George C. et al., 2005]
Aerosol flow tube	Aerosol particles	10^{-4} - 10^{-1}	0- 30 sec	1-760	[Abbatt J. P. D. et al., 1998], [Moise T. et al., 2000], [Guimbaud C. et al., 2002], [Thornton J. A. et al., 2005], [McNeill V. F. et al., 2006], [McNeill V. F. et al., 2007]
Knudsen Cell	Powder sample or aerosol particles	10^{-7} - 10^{-1}	10-10000 sec	$< 10^{-2}$	[Underwood G. M. et al., 1999], [Underwood G. M. et al., 2000], [Underwood G. M. et al., 2001], [Li P. et al., 2002], [Hoffman R. C., Gebel, M. E. et al., 2003b], [Hoffman R. C., Gebel, M. E. et al., 2003a], [Hoffman R. C., Kaleuati, M. A. et al., 2003], [Ullerstam M. et al., 2003], [Johnson E. R. et al., 2005]
DRIFT Cell	Solid surface or aerosol particles	10^{-4} - 10^{-2}	40 -800 min	2-760	[Vogt R. et al., 1994], [Langer S. et al., 1997], [Yoshitake H., 2000], [Ullerstam M. et al., 2003]
Atmospheric simulation Chamber	Aerosol particles	10^{-8} - 10^{-4}	100 -900 min	760	[Mogili P. K. et al., 2006], [Prince A. P. et al., 2007], [Preszler Prince A. et al., 2007]

Tab 3.2 Table summarising the principle commonly used methods for the measurement of reactive uptake in gas-solid reactions. The surface characteristics, the range of accessible γ , the gas-solid contact time and the working pressures are reported. In last column some references for the specific techniques are cited.

3.5.2 Experimental set-up for uptake measurements in static conditions – reactor optimisation

To detect small changes in the gas phase composition (low heterogeneous reactivity), if it is not possible to increase the reactive surface S , then high sensitivity techniques (like Mass Spectrometry) have to be used. This technique needs a low working pressure, thus we have to deviate from atmospheric conditions, and water vapour is not introduced to the system.

An alternative solution is to increase the reaction rate by increasing the concentration of the gaseous reactant, $[A]_g$. In this case also, the conditions are not atmospherically realistic as the trace gas concentration is too high, and thus attention has to be paid in order to avoid immediate surface saturation. This last approach has been used when designing the home-made reaction cell.

The experimental system used in this work is a static reactor located inside an FTIR sampling compartment which allows the continuous, *in situ*, monitoring of the gas-phase composition at atmospheric pressure and temperature. A schematic representation is shown in fig. 3.17.

With this particular configuration the evolution of the gas composition can be followed without any delay as it avoids the need to transfer the sample from the reaction chamber to the analysis system, e.g. as reported in the work of Sayer [Sayer R. M. et al., 2003]. The measurement cell (a) is in fact the reactor itself. In this static configuration there is a continuous depletion of the reagent in the gaseous phase, but it is also possible to monitor the formation of new gaseous products, which do not escape from the closed reaction system and can therefore accumulate inside it.

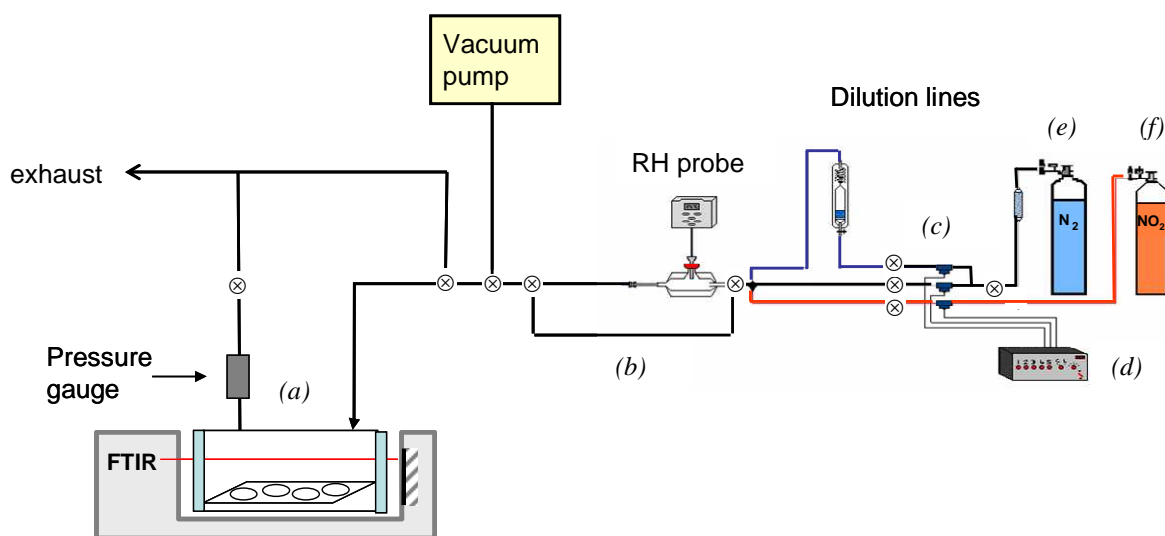


Fig. 3.17 Schematic representation of the experimental set-up for uptake coefficient measurements.

The reactive surface is NaCl tablets placed horizontally on a Teflon plane inside the IR cell.

Two types of cell have been used in this work:

- A Teflon cell of 10 cm length and an internal diameter of 3 cm ($V=67 \text{ cm}^3$ calculated with sample holder inside).
- An glass cell internally coated with inert wax of 10 cm length and a diameter of 4 cm ($V=135 \pm 1 \text{ cm}^3$ from weight and volumetric measurements)

Both are equipped with Ge windows, chosen for being the least reactive material in presence of $\text{NO}_2/\text{H}_2\text{O}$ of all the IR transparent windows. The optimisation of the reaction cell for heterogeneous uptake measurements is described in more detail in chapter 6.

There are two inlets in the upper part of the cell to allow the entrance and exit of the gas flux through two Teflon lines, both fitted with a valve to allow them to be closed.

The cell is equipped with a pressure transducer capable of reading total pressure values from the order of bars down to 10^{-4} bar.

This configuration permits the isolation of the cell for experiments in static conditions.

A Humidity and Temperature transmitter HMT334 VAISALA (precision $\text{RH}=0\text{-}90\% \pm 2\%$; $\text{RH}=90\text{-}100\% \pm 3\%$) is placed inside a glass cell through which the gas mixture can flow. This glass cell can be bypassed (b) if a corrosive gas is used, e.g. NO_2 at high concentration and high humidity, to prevent damage to the probe.

A vacuum pump is used to check the seal of the connected gas lines and cell. Together with nitrogen purge cycles (10 minutes of pump and 10 minutes of purge), this assures the cleaning of the whole apparatus.

The gaseous phase is prepared by the controlled mixing of flows from three different lines (shown in different colours in fig.3.17) carrying:

- Dry N₂ (in black),
- N₂ saturated with water vapour (in blue),
- NO₂ diluted in He or N₂ (in red).

Mass flow controllers (*c*) (Mykrolis type FC 100SCCM, 1SLPM and 2SLPM He; Tylan General type FC 1SLPM He) are used to dilute the reactive NO₂ as desired, and to vary the relative humidity of the gas mixture. Humidity variation is possible by changing the ratio of dry/saturated N₂ flows whilst keeping the total flow of the carrier nitrogen gas constant.

After calibration of the mass flow controllers, a known gas flow can be set for every line by setting a certain voltage on the controller (*d*).

Calibration with N₂ gives a linear dependence of flow Q⁰ ([mL/min] under standard conditions of pressure and temperature: P₀=760 Torr; T₀=273 K) over the set voltage [V]:

$$(3.12) \quad Q^0 = a \cdot V + b$$

The N₂ flow through a flow mass controller set to voltage V (at the working T and P) is then calculated using coefficients a and b from equation 3.12:

$$(3.13) \quad Q = (a \cdot V + b) \cdot \frac{P_0}{T_0} \cdot \frac{T}{P} \cdot c$$

If the gas used is different from the one used for the calibration, a correction coefficient c has to be applied (see tab.3.3).

calibration gas	correction factor c	
	NO ₂ /He 1%	NO ₂ /N ₂ 5%
N ₂	1.4025	0.9833
He	0.9912	0.6949

Tab. 3.3 Correction coefficients c for calculating the gas fluxes Q if the flowing gas is different from the gas used for the mass flow controller calibration.

The gases are supplied from commercial gas cylinders (*e*) and (*f*), whose specifications are described in §3.1.2.

To obtain a specific relative humidity, voltages at the flow mass controller of N₂ and H₂O/N₂ are chosen *viz*:

$$(3.14) \quad \%RH = 100 \cdot \frac{Q_{H_2O/N_2}}{Q_{TOT}}$$

Q_{TOT} is 1000 mL/min in our experiments.

NO₂ concentration in the gas mixture is initially calculated by volumetric dilution, but a more accurate estimation is given by the IR absorption spectrum which is calibrated by adding a known quantity of dry NO₂ to the used gas cell (see appendix A for more details).

The Fourier transform infrared spectrometer used for the gas-phase analysis is an Avatar 360 E.S.P. (Thermo Nicolet) with the following elements:

- EverGlo IR source
- KBr beam splitter
- DTGS detector
- He-Ne laser alignment
- Ge windows

The spectra are taken with a 4 cm^{-1} spectral resolution and 16 or 32 scans are averaged for a spectrum acquisition. These parameters allow us to follow the NO_2 IR signal evolution during the experiment and to identify new gaseous species with a good S/N and an acquisition time per spectrum of 19 or 30 seconds.

Experimental protocol:

The prepared NaCl tablets are horizontally aligned over the Teflon sample holder and located inside the IR cell. The cell is then emptied of laboratory air by 3 cycles of vacuum pumping/ N_2 purging of 10 minutes each. The cell, filled with dry nitrogen, is then isolated. A known mixture of dry and saturated nitrogen are flowed through the RH probe glass cell. The gas pressure and temperature are recorded after 10 minutes. The humidified nitrogen flux is then sent into the cell and left to flow for 2-5 minutes. The IR cell is isolated again and the RH probe bypassed through (b).

The NO_2 is then added and N_2 is reduced by the same amount so as to keep the relative humidity of the gas mixture constant. After 10 minutes of premixing the flow is sent into the IR cell and an automatic IR spectra collection procedure is started. The background spectrum is recorded immediately before the reactive gas is sent to the IR cell. The cell is isolated again after 30s and its pressure recorded. By comparing the gas flow and the cell volume, it can be shown that the gas originally present in the IR cell is totally replaced by the reactive mixture within this time. Spectra are collected over 1h of time and the kinetics of the heterogeneous process are thereby studied under static conditions.

3.6 Quantification of formed nitrate

The IR spectrum of the NaNO_3 formed on the NaCl tablets is recorded immediately after exposure to the reactive gas mixture. The recorded signal can be used for a qualitative analysis of the product formed on the surface and for an estimation of the NaNO_3 formed. Spectra are recorded for every tablet with the same instrument used for the kinetic measurements. The acquisition parameters are a 4 cm^{-1} resolution and 64 scans/spectrum. An example of a typical IR spectrum is reported in fig.3.18.

NaCl has a fcc centered cubic cell with $F_m \bar{3}_m (\text{Oh}^5)$ space group. Translation modes (F_{1u}) are IR active in the far IR region $\sim 200\text{cm}^{-1}$.

NaNO₃ crystal has an ordered structure at room temperature with two formula units per unit cell and $R \bar{3}_c (\text{D}_{3d}^6)$ space group. The NO_3^- ions are located on D_3 sites and the Na^+ ions on S_6 sites. Consequently, five Raman-active modes are expected, three of which are nitrate ion internal modes ν_1 (A_{1g}), ν_3 (E_g) and ν_4 (E_g), the other two being E_g lattice oscillations.

It is well established that a nitrate ion is characterized by four fundamental vibrational modes, reported in tab 3.4.

$\nu_1 (A'_1)$	1050 cm^{-1}	symmetric stretching	Raman
$\nu_2 (A''_2)$	831 cm^{-1}	out of plane bending	IR
$\nu_3 (E')$	1390 cm^{-1}	asymmetric stretching	IR
$\nu_4 (E')$	720 cm^{-1}	in plane bending	Raman

Tab. 3.4 Fundamental vibrational modes of the NO_3^- ion of D_{3h} symmetry.

For quantitative applications of IR spectroscopy we need to measure the intensity of a suitable peak which is proportional to concentration (from the Beer-Lambert law). It is the limitation of reproducibility (usually within $\pm 5\%$) that generally restricts IR spectra to semi-quantitative use. We tried to estimate a w/w% of NO_3^- on the tablets as far as possible within this limitation.

The IR signal chosen is the intensity of the A_{2u} band at 835 cm^{-1} because it is very sharp, not sensitive to water content (no broadening due to the presence of hydrated forms of the nitrate ion) and behaves linearly over a wide concentration range. The possibility of measuring other peak areas or intensities, (in particular the more IR intense E_u transition), has been explored, but the chosen parameter is the most suitable.

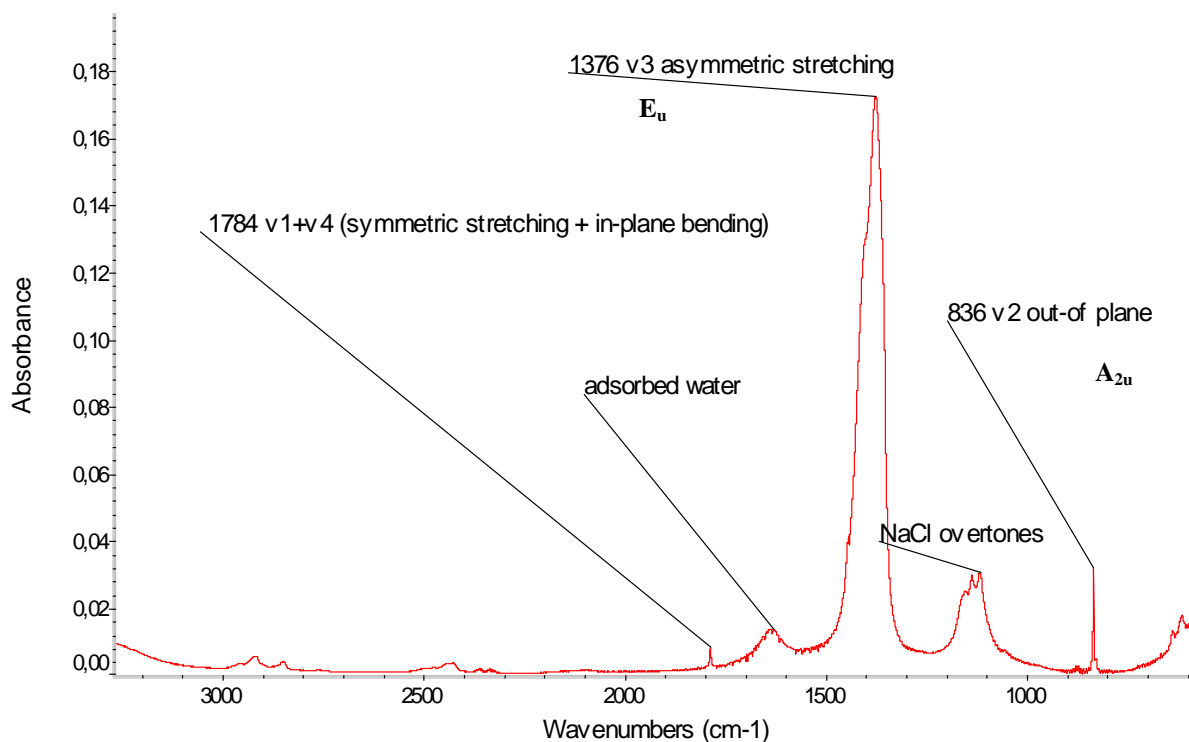


Fig. 3.18 FTIR spectrum of a $\text{NaNO}_3/\text{NO}_2$ tablet with band assignment.

A calibration curve is obtained by preparing mixed $\text{NaCl}/\text{NaNO}_3$ tablets with different quantities of nitrate (0.01-20%) and measuring their IR spectrum.

The tablets are prepared by separately grinding and sieving ($<80 \mu\text{m}$) NaCl and NaNO_3 powders. The two powdered salts are used to prepare mixtures of the powders weighing 1000mg and containing different % of NaNO_3 .

The nitrate percentage in the mixture is calculated as:

$$(3.15) \quad \% m_{(\text{NaNO}_3)} = \frac{(m_{\text{NaNO}_3} \cdot \text{purity}_{\text{NaNO}_3})}{m_{\text{NaNO}_3} + m_{\text{NaCl}}}$$

Where m is the mass of NaNO_3 or NaCl .

From each of these mixture 3 tablets of 150 mg are prepared in the same conditions as reported in ch. 3.2.1. The whole procedure is repeated to verify the reproducibility. After being stored at 383 K for at least 1h, their IR spectra are recorded. Each of the points in fig. 3.19 is the average of the IR signal intensity measured for every tablet at 835 cm^{-1} , corrected by a linear baseline in the range $927.6\text{ cm}^{-1} - 788.8\text{ cm}^{-1}$. Here we report only the range of %nitrate most pertinent for measuring the experimental values obtained in our experiments.

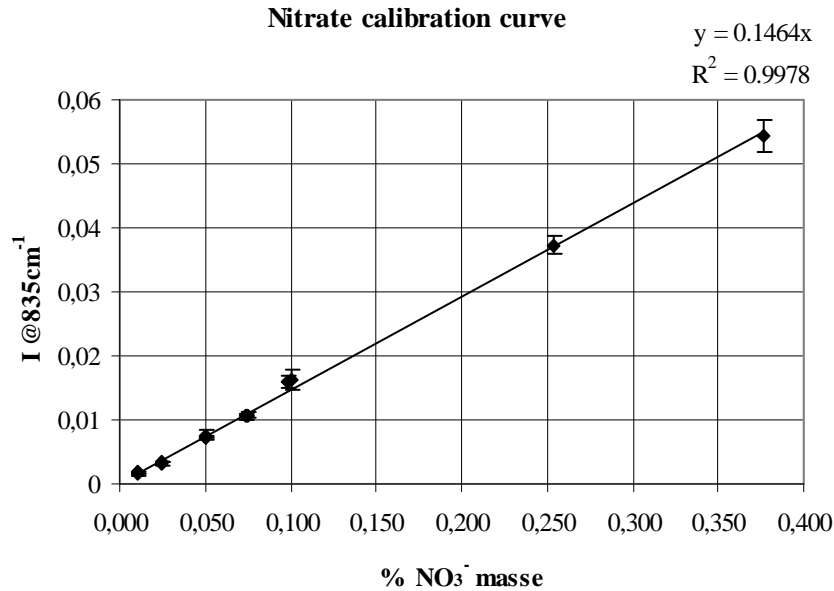


Fig. 3.19 Nitrate calibration curve in the range 0.01-0.4 % NaNO₃

The equation obtained from this calibration is then:

$$(3.16) \quad I_{835\text{cm}^{-1}} = (0.146 \pm 0.002) \cdot \% m_{(\text{NaNO}_3)}$$

which allows the estimation of the $\% m_{(\text{NaNO}_3)}$ of the formed nitrate and the error associated with it.

The measured intensity of a sample $\bar{I}_{835\text{cm}^{-1}}$ is the average of the intensities at 835 cm^{-1} of the 8 tablets exposed at the same time in that experiment, and $\varepsilon_{\bar{I}_{835\text{cm}^{-1}}}$ is the standard deviation associated with that average value.

The $\% m_{(\text{NaNO}_3)}$ estimation and error are then described by (3.17) and (3.17b):

$$(3.17) \quad \% m_{(\text{NaNO}_3)} = \bar{I}_{835\text{cm}^{-1}} / 0.146$$

$$(3.17b) \quad \varepsilon_{\% m_{(\text{NaNO}_3)}} = \% m_{(\text{NaNO}_3)} \cdot \left(\frac{\varepsilon_{\bar{I}_{835\text{cm}^{-1}}}}{\bar{I}_{835\text{cm}^{-1}}} + 0.0015 \right)$$

Chapter 4 - The uncoated surface: the effect of relative humidity on the NaCl/NO₂ system

4. The uncoated surface: the effect of relative humidity on the NaCl/NO₂ system

In chapter 2.1 the main properties of the NaCl(100) surface were presented from theoretical and experimental observations reported in previous work.

In the first part of this chapter we mainly focus on the effect of atmospheric humidity on the pure NaCl(100) surface, which is used as a model for marine aerosol. The effects are studied using AFM measurements and comparison to the current knowledge in the literature.

In the second part NaCl(100) is put in contact with the polluting species NO₂ under different conditions of humidity. After reaction the surface is observed with AFM and Raman microspectrometry and imaging. The resulting images are used in combination to understand the surface modification and the reorganisation of the formed nitrate on the surface.

Micro-Raman analyses are also performed on the exposed NaCl pellets, which are constituted of sintered micro-crystals. The small effect of grain borders is assessed and validates the use of these substrates for the kinetic studies.

4.1 NaCl(100) in a dry and humid atmospheres

NaCl(100) surfaces obtained from cut and mechanically polished monocrystals are analysed through non-contact AFM operated in tapping mode (see ch.3.4.2). The native surface status of this (100) face is then determined under laboratory atmosphere conditions (RH=45±10%, T=298±2K) before any other chemical or physical treatment occurs.

The optical microscope shows the presence of surface damage due to the mechanical polishing by detecting parallel rays scratching the surface. AFM images give some additional information about the depth and width of these artificially created surface defects. In fig.4.1 we report an example of a 3µm x 3µm surface area scan in which deep scratches are observed. An example of a vertical profile is also reported in fig. 4.2, from which we can measure the depth and width of the scratches to be approximately 10 to 15 nm and 0.5 µm respectively. These values are consistent with the polishing history of the surface. The rest of the surface is flat and within the instrumental noise (±3 nm) and no other particular features can be observed. Smaller morphological details, like the presence of monoatomic or multiatomic steps (observed i.e. in [Dai Q. et al., 1997] in the scale of 0.5 to 5 nm), cannot be detected.

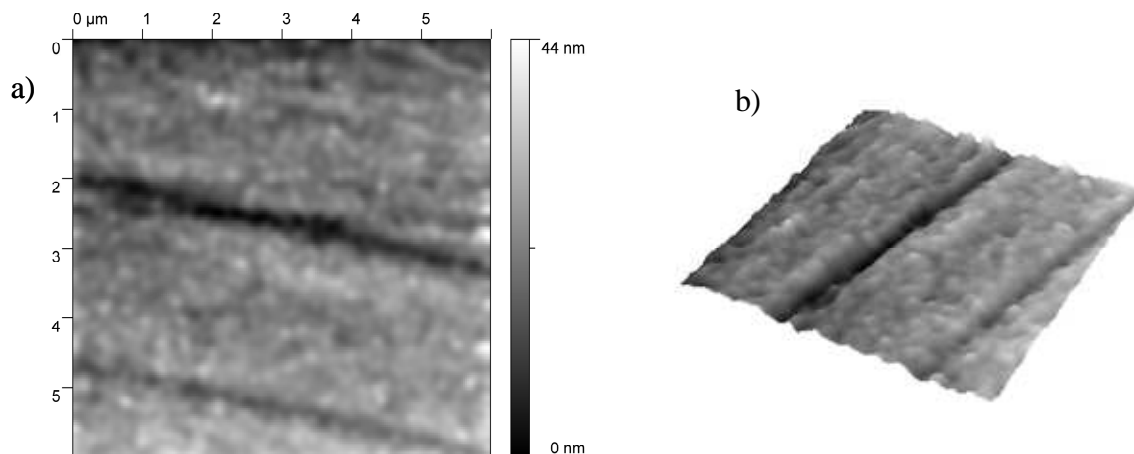


Fig. 4.1 NaCl(100) mechanically polished crystal surface 3µm x 3µm AFM image: 2D and 3D surface reconstruction.

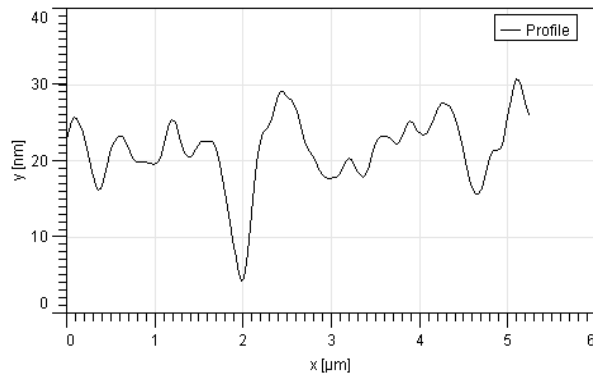


Fig. 4.2 Profile of the NaCl(100) portion of surface presented in fig. 4.1

From previous work [Verdaguer A. *et al.*, 2008] the NaCl(100) surface displays ion mobility at the step edges when $RH < 35-40\%$ because of absorbed water in these defective zones of the surface. Hydration of surface ions weakens ionic bond strength to the point where they become mobile.

With increasing humidity, there is a substantial change on the superficial ion mobility caused by the formation of at least one monolayer of adsorbed water on the hygroscopic surface [Peters S. J. *et al.*, 1997], [Foster M. C. *et al.*, 2000]. The main consequence of this is the beginning of large scale modifications of the surface step structure [Dai Q. *et al.*, 1997], [Verdaguer A. *et al.*, 2008]. The steps and terraces evolve more rapidly when more water vapour is present because of a progressively higher amount of dissolved surface ions that diffuse from zones with excess energy (i.e. accumulation of defects due to the cleavage, the polishing treatment, etc) to a lower energy surface configuration. An abrupt change finally happens when the DRH point is reached ($\sim 75\%$ RH), accompanied by a total dissolution of the surface.

We are also interested in investigating the surface in this extreme case of reconstruction after the total dissolution of the top-most layers. A NaCl monocrystal is cleaved along the (100) plane and is subsequently exposed to a highly humid atmosphere ($RH=80\%$) for 30 minutes. Once dried under a nitrogen flux it is returned to the laboratory ambient humidity ($\sim 45\%$) and the surface is scanned with the AFM.

The ion mobility reaches a maximum at the DRH so that their diffusion is facilitated. This allows the surface to relieve the stress energy accumulated at the cleavage steps. The surface changes are then similar to the ones due to an annealing process, because the high mobility of the ions drives towards the lower-energy surface which is the (100). The reconstructed surface indeed shows large terraces, as reported by a $6\mu\text{m} \times 6\mu\text{m}$ image in fig. 4.3. No other particular structures or features are observed within the noise level.

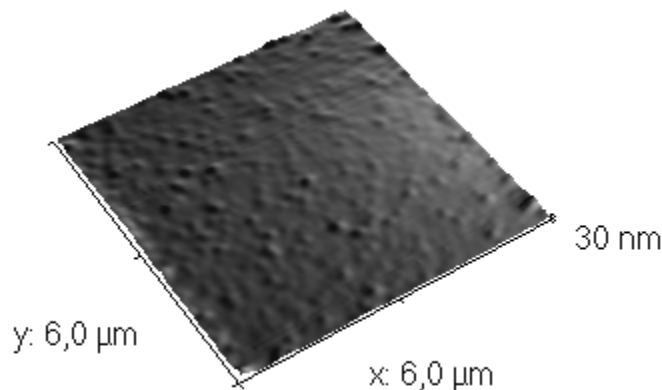


Fig. 4.3 NaCl crystal (100) surface $6\mu\text{m} \times 6\mu\text{m}$ AFM image after exposure to $RH=80\%$ followed by drying to $RH=0\%$: 3D reconstruction.

In [Dai Q. et al., 1997] the authors report that large multiatomic steps originating from the monocrystal cleavage disappeared after a similar treatment in humid conditions, leading to a flat surface where only monoatomic steps were observed (fig. 4.4).

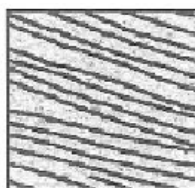


Fig. 4.4 A contact AFM image ($2\mu\text{m} \times 2\mu\text{m}$) taken on NaCl(100) after surface complete dissolution and subsequent drying at RH=20%. Only monoatomic steps of 0.4 nm are observed. Image taken from [Dai Q. et al., 1997].

Indeed “this surface is much closer to the equilibrium structure of the salt crystal, since the strain energy stored in the cleavage steps is annealed off in the dissolution process”. They also make clear that “the terrace width of the new steps depends on the rate of drying” but they did not go into further detail.

The quite rapid change of humidity, passing from 80% to 0% in some seconds, leads to a surface which is, from a macroscopic point of view, frozen in a sort of vitreous morphology. The macroscopic crystal borders (1cm x 1cm) are indeed rounded and instead of well delimited terraces the optical microscope shows a smoothed surface. These observations are coherent with the presence of the distribution of monoatomic steps on the surface which give a fine structure at a sub-microscopic level, but that appears like a continuum at our observation scale. We are only able to see where the hypothetical monoatomic steps are more dense by detecting a slope on an otherwise perfectly flat surface. As with the [Dai Q. et al., 1997] study we did not study this in further detail, except to observe that there is a substantial surface reorganisation after its total dissolution.

4.2 NaCl(100) exposed to NO₂ at different humidities [Scolaro S. et al., 2009]

When NaCl is put in contact with NO₂ it is well established that on the solid phase NaNO₃ crystals are formed. It is useful at this point to recall some elements of spectroscopy and hygroscopicity that are important to correctly interpret the experimental results, before they are presented and discussed.

4.2.1 Raman spectra and hygroscopic properties of the solid reagent and products

The Raman spectra can be interpreted by taking into account their vibrational spectroscopy characteristics:

NaCl has a fcc cell with $F_m\bar{3}_m$ (Oh^5) space group. No fundamental Raman bands are expected and the translation modes (F_{1u}) are IR active in the far IR region $\sim 200\text{cm}^{-1}$.

NaNO₃ crystal has an ordered structure at room temperature with two formula units per unit cell and $R\bar{3}_c$ (D_{3d}^6) space group. The NO₃⁻ ions are located on D₃ sites and the Na⁺ ions on S₆ sites.

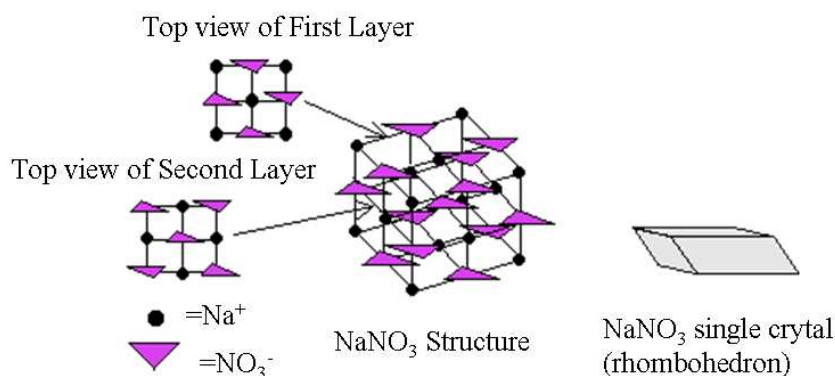


Fig. 4.5 Schematic representation of NaNO_3 crystalline structure and single crystal shape.

Nitrate ions have a triangular shape which causes the repeating units in NaNO_3 to distort from a cube-like shape (as in the case of NaCl) to a rhombohedron (see figure 4.5).

It is well established that a nitrate ion is characterised by four fundamental vibrational modes, as reported in tab 4.1:

$\nu_1 (A'_1)$	1050 cm^{-1}	symmetric stretching	Raman active
$\nu_2 (A''_2)$	831 cm^{-1}	out of plane bending	IR active
$\nu_3 (E')$	1390 cm^{-1}	asymmetric stretching	Raman and IR active
$\nu_4 (E')$	720 cm^{-1}	in plane bending	Raman and IR active

Tab 4.1 Fundamental vibration modes of the isolated NO_3^- ion of D_{3h} symmetry.

As a consequence of the allocation of the anions in the crystalline structure, five Raman-active fundamental modes are expected (summarized in tab.4.2), three of which are nitrate ions internal modes $\nu_1 (A_{1g})$, $\nu_3 (E_g)$ and $\nu_4 (E_g)$, the other two being E_g lattice oscillations, as represented in fig. 4.6.

$A_{1g} (\nu_1)$	1068 cm^{-1}	symmetric stretching	NO_3^- ion internal mode
$E_g (\nu_3)$	1385 cm^{-1}	asymmetric stretching	NO_3^- ion internal mode
$E_g (\nu_4)$	724 cm^{-1}	in plane bending	NO_3^- ion internal mode
E_g	185 cm^{-1}	libration	lattice oscillation
E_g	98 cm^{-1}	translation	lattice oscillation

Tab 4.2 Fundamental Raman vibration modes of the NO_3^- ion in the D_{3d}^6 space group symmetry.

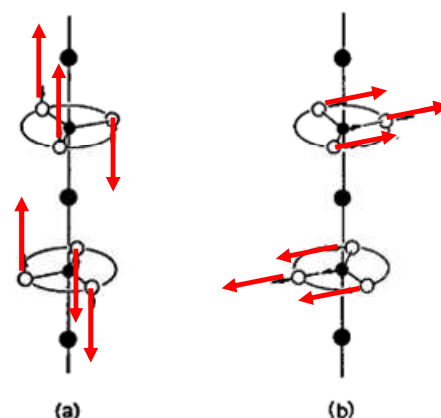


Fig. 4.6 Schematic representation of the E_g modes in nitrate crystals: libration (a) and translation (b) (taken from [Rousseau D. L. et al., 1968]).

Crystals are typically rhombohedral plates. The optical axis of the crystal extends from one corner of the rhombohedron to the body-diagonally opposite corner, and thus has three-fold symmetry about the optical axis. The Raman scattering from crystalline NaNO_3 has been observed in all polarization orientations [Rousseau D. L. et al., 1968].

For example, the 1068 cm^{-1} band intensity has relative magnitude as $\alpha_{xx}^2 = \alpha_{yy}^2 \sim 10 \alpha_{zz}^2$ of the Raman tensor of the A_{1g} vibration.

The 185 cm^{-1} band intensity has relative magnitude as $\alpha_{xz}^2 \sim 10 \alpha_{zz}^2$, $\alpha_{xx}^2 = \alpha_{yy}^2 = \alpha_{xy}^2 \sim 0$ of the Raman tensor of the E_g vibration being studied.

The small residual intensity is ascribed primarily to the birefringent nature of crystalline NaNO_3 . Thus, polarized confocal Raman spectra can help in detecting orientation changes if they occur during an experiment.

Fig. 4.7 shows a typical Raman spectrum of a powdered NaNO_3 sample, where the small crystals are oriented in all directions generating an anisotropic environment. We can observe all the previously described Raman transitions and their relative intensities with the exception of the lattice translation at 98 cm^{-1} because of the cut-off imposed to eliminate the excitation wavelength. Also free nitrate signature is detectable at 1045 cm^{-1} , indicating the presence of a small quantity of deliquescent nitrate.

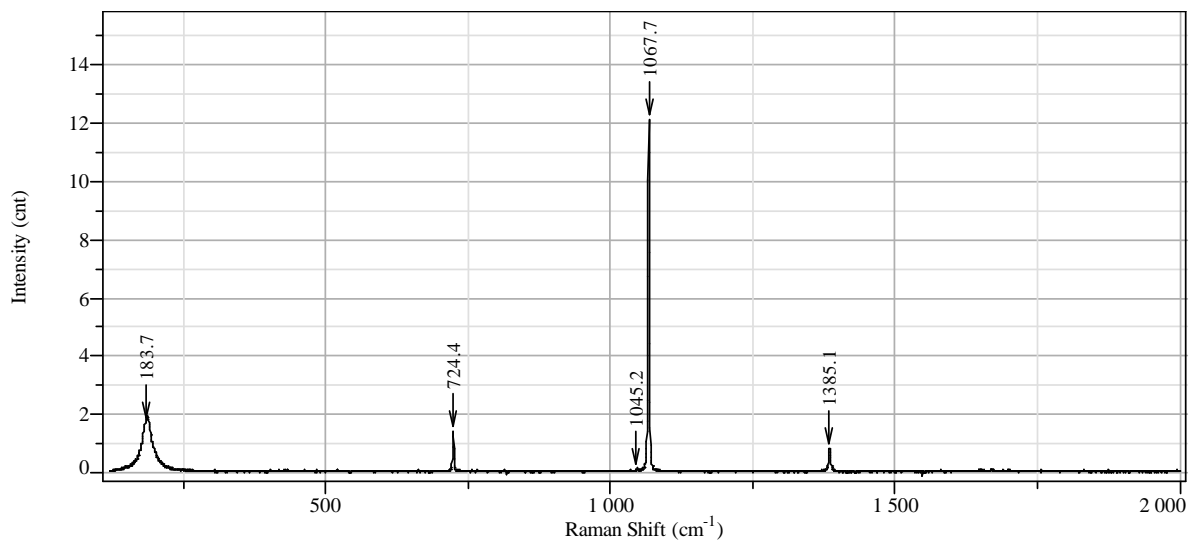


Fig. 4.7 Raman spectrum of a powdered NaNO_3 sample excited at 632.8 nm

We also need to remember the importance of RH on the hygroscopic properties of the $\text{NaNO}_3/\text{NaCl}$ system.

Though many researchers have studied phase transitions of sodium nitrate particles, there is no agreement on their hygroscopic properties [Li X.-H. et al., 2006]. We have to remember that the deliquescence process strongly depends on the particle size and, from recent evidence, also on their morphology. An example is shown in fig. 4.8, taken from [Li X.-H. et al., 2006] of two NaNO_3 crystals with different morphologies which are deposited on quartz and followed by optical microscope as long as RH increases.

While the rhombohedral crystal abruptly deliquesces at RH 86-93%, the maple leaf shape crystal starts to take up water below RH 69% and completely dissolves at RH=87%.

Deliquescence is a surface process involving water vapour condensing on the surface and starting to dissolve the salt. Until a certain ratio of H_2O molecules/salt units is reached (indicated by the thermodynamics of the solvation process), the deliquescence process is not completed and aqueous and solid phases can coexist [Tang I. N. et al., 1995].

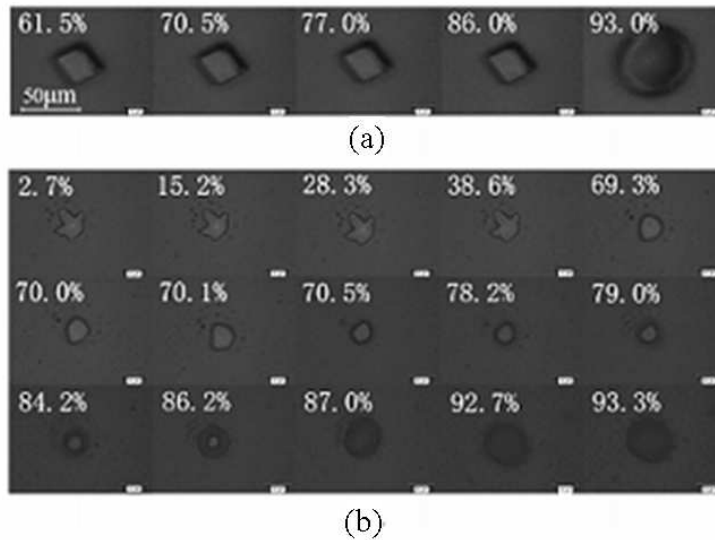


Fig. 4.8 Morphological changes of solid NaNO_3 particles with (a) rhombohedral shape and (b) maple leaf shape in the deliquescence process (taken from [Li X.-H. et al., 2006]).

When looked at in this way it is also easy to understand, for example, why smaller droplets exist in the liquid state at much lower RH than bigger droplets. Also the efflorescence process, when a supersaturated droplet is present, is governed by this solute/solvent ratio.

For this same reason also the DRH of salt mixtures can be different from the single components hygroscopic behaviour. In the specific case of $\text{NaNO}_3/\text{NaCl}$, mixed particles of 6-8 μm diameter form a drop at 68% RH (298K) instead of at the 75.5% of the single bulk components [Tang I. N. et al., 1994].

The DRH does not depend on the initial dry-salt composition, but it is only governed by the water activity at the eutectic composition (fig. 4.9). At 298K it is of approximately 33% wt NaNO_3 and 12% wt NaCl (the remaining 55% is water).

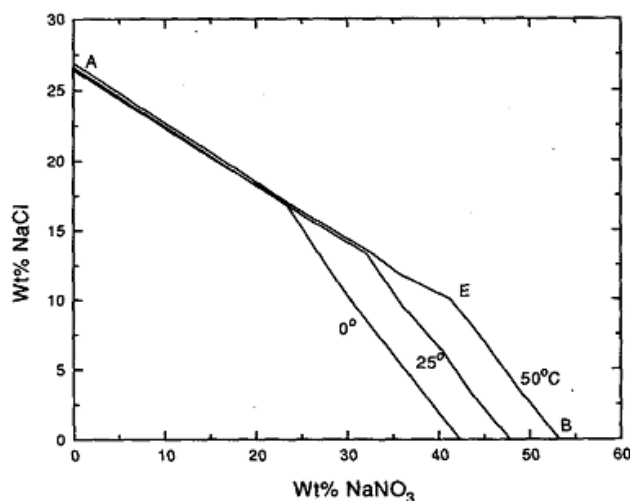


Fig. 4.9 Solubility diagram for the $\text{NaCl} - \text{NaNO}_3 - \text{H}_2\text{O}$ system, from [Tang I. N. et al., 1994].

The deliquescence state of nitrate can be checked by Raman spectroscopy, because of some important changes in the position of the ν_1 band that can tune from the 1048 cm^{-1} of free nitrate (in solution) to the 1068 cm^{-1} of the nitrate in a crystalline environment (solid state), passing through some intermediate supersaturated solution where some structures, called coupled ion pairs (CIP) absorb typically at 1052 cm^{-1} (see fig.4.10).

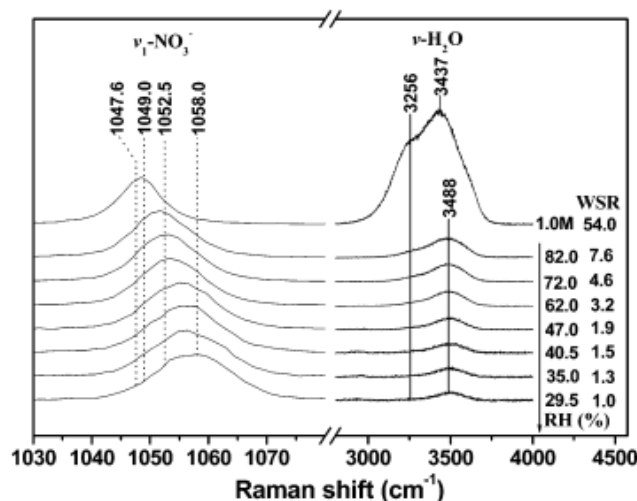


Fig. 4.10 Raman spectra of the NaNO_3 droplets at various RH in the efflorescence process. The top one is the Raman spectrum of a 1.0 M NaNO_3 solution. Taken from [Li X.-H. et al., 2006].

From this spectra we can observe that during the efflorescence process some characteristics typical of a solution (CIP ν_1 absorption band at 1052 cm^{-1}) remain until $\text{RH}=62\%$ and that some adsorbed water ($\nu\text{-OH}$ at 3488 cm^{-1}) is always detected.

When interpreting the data we have then to remember the effects of the size and composition on the hygroscopic properties of $\text{NaCl}/\text{NaNO}_3$.

4.2.2 Experimental conditions

The cut and polished monocrystal slabs of NaCl are exposed to NO_2 inside the reactor described in ch.3.5.2 after pump and purge cycles with dry N_2 . In the absence of high temperature pre-treatment some strongly surface adsorbed water will always be present on the surface, and particularly on defective sites.

The gas-phase concentration of the reactive NO_2 used is $8 \times 10^{15}\text{ molec}/\text{cm}^3$ and the RH is tuned from 0 to 80%. The salt crystals, after 30 minutes of static exposure to NO_2 , are purged with dry nitrogen for 2 minutes to quench the reaction. They are then immediately transferred into a closed glass Petri box to prevent any external contamination of the surface. The samples are kept in laboratory conditions of temperature and humidity, which are approximately $45 \pm 10\%$ and $298 \pm 2\text{K}$.

The morphology (AFM) and chemical mapping (Raman microspectrometry with an excitation wavelength of 632 nm) analyses are performed at laboratory humidity and temperature. In these conditions, as seen in section 4.1, the surface step structures are thought to slowly evolve over a period of few hours, the time of the acquisition of an AFM or μ -Raman image. When a monolayer of water covers the (100) plane of NaCl (for $\text{RH}>35\%$) Cl^- ions are displaced at a very low energetic cost from their crystal lattice position towards the plane of water molecules [Cabrera-Sanfeliix P. et al., 2007]. In this way they leave some vacancies that can be occupied by NO_3^- ions which can also migrate over the surface. Calculations suggest that the nitrate species interact at these Cl^- deficiencies in an orientation in which the ion is parallel to the surface [Zangmeister C. D. et al., 2001]. Because of the already mentioned mismatch between the dimensions of Cl^- and NO_3^- ions, nitrates have the tendency to agglomerate together and crystallise, so that small crystalline structures of NaNO_3 start to form after some surface ageing. This process is also possible in the absence of superficial water but it is very slow: nitrates systematically undergo a change in orientation from parallel to the surface to a perfect vertical orientation because of the changing crystalline field force

due to other nitrate present in their neighbourhoods. A certain degree of surface ageing has therefore to be taken into account during the data interpretation.

The obtained information about the NaNO_3 which is formed from the $\text{NaCl}(100)$ surface reaction with NO_2 are reported in the following paragraphs. The experimental observations are ordered by increasing values of the imposed RH of the reactive gas mixture.

4.2.3 RH=0%

The NaCl slab is exposed to a dry gas mixture containing the reactive species NO_2 . Even if no moisture is present in the gaseous phase, some water clusters are distributed on the surface, especially on defective sites. The surface is analysed immediately after reaction with the optical microscope. The surface aspect, seen with the optical microscope (100x magnification), is similar to the non-reacted one. Very weak solid nitrate Raman peaks are recorded only along the polishing scratches corresponding to some spots of less than $1\mu\text{m}$ diameter. In fig. 4.11 we report as an example an optical and a Raman image, which are obtained from the integration of the A_{1g} band of nitrate (1068 cm^{-1}). One pixel of the Raman image corresponds to $1\mu\text{m}^2$ and the grey scale indicates the presence of nitrate in the white/grey pixels. The scanned portion of the surface contains an area of marked surface polishing damage.

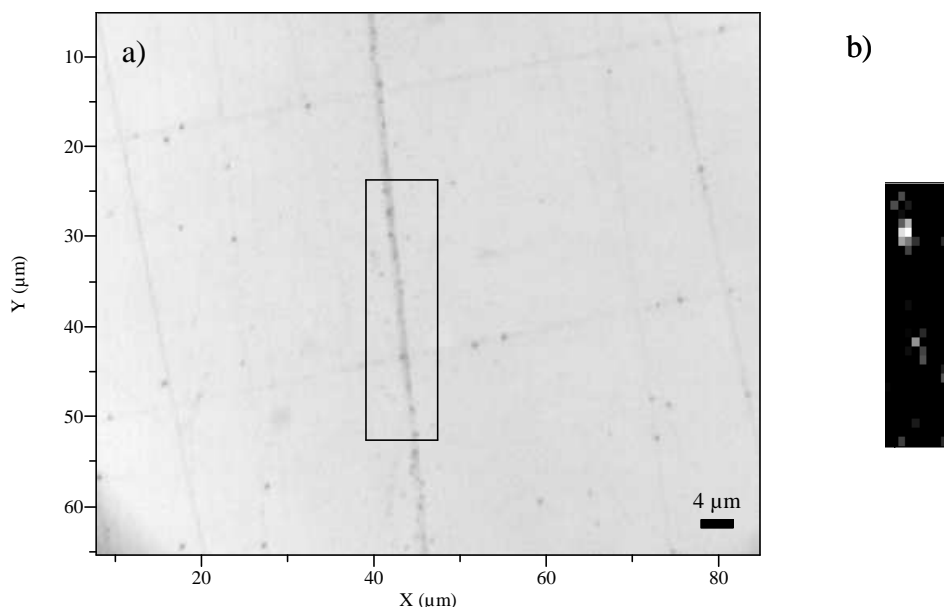


Fig. 4.11 100x optical (a) and Raman (b) images of $\text{NaCl}(100)$ immediately after reaction with NO_2 at $\text{RH}=0\%$.

Morphological images obtained by AFM show the presence on the surface of grains of 163nm mean size, especially along the superficial scratches (i.e. a $6\times 6\mu\text{m}$ image is reported in fig.4.12).

The surface adsorbed water clusters, mainly localised along the polishing defects, can facilitate on one hand the surface reorganisation which is at the origin of the quite regular rhombohedral crystals and on the other hand they can facilitate NO_2 reactivity inducing its possible hydrolysis to the more reactive HNO_3 .

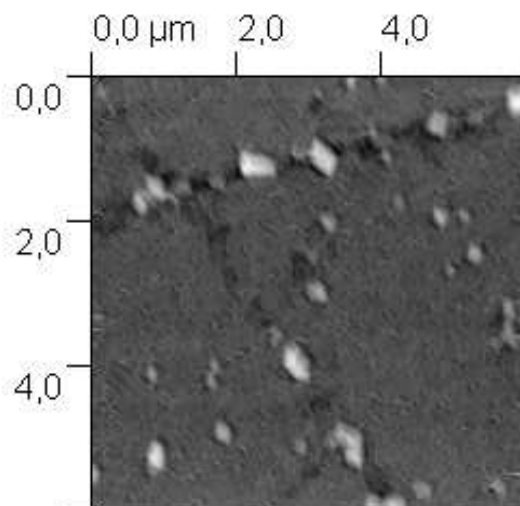


Fig. 4.12 6x6 μm AFM 2D surface reconstruction image of NaNO_3 crystals formed on NaCl after reaction with NO_2 at $\text{RH}=0\%$.

The surface status is checked continuously for 4 days with the AFM and no change is detected on it.

We left a crystal, previously exposed for 1h to NO_2 , ageing for 20 days in laboratory conditions to check surface reconstruction at longer times. At this state of ageing we can observe the progressive formation on the surface of dendrimeric structures (fig. 4.13a) mainly driven towards the position of the surface defects. We can clearly see a migration in progress on the surface and the coalescence of smaller crystals into bigger ones, as clarified in fig. 4.13b.

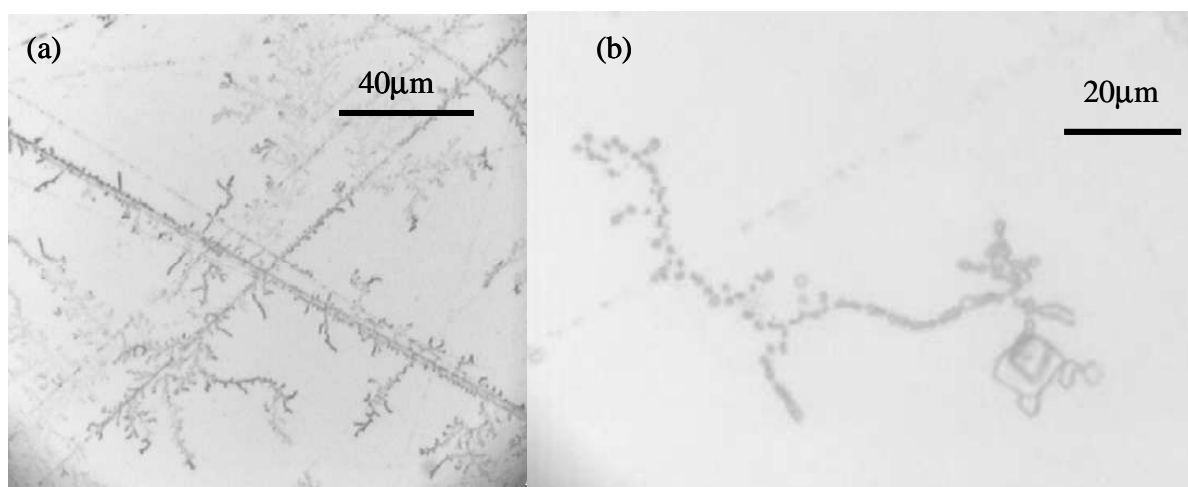


Fig. 4.13 Optical images of $\text{NaCl}(100)$ exposed for 1h to NO_2 at $\text{RH}=0\%$; ageing of 20 days in room atmosphere conditions. In (a) the formation of dendrimeric structure is evident and in (b) the coalescence of smaller crystals into a bigger crystal of rhombohedral shape is shown.

We would like to give here another example of surface ageing and nitrate reorganisation to check if there is an effect of higher surface nitrate coverage on its evolution. A NaCl monocrystal is exposed to NO_2 for 15h. Immediately after reaction we can already notice, from the Raman microspectrometry, sub-micrometric nitrate crystals along the polishing defects. By following the surface ageing we can observe a strong nitrate reorganisation leading to the formation of big NaNO_3 regular shaped rhombohedral crystals. This phenomenon is consistent with a slow crystallisation without constraint from a nitrate solution: there is enough surface adsorbed water to dissolve the initially formed sub-

micrometric nitrate crystals and to make them coalesce and reorganise into a well-ordered rhombohedral crystal, as presented in fig. 4.14.

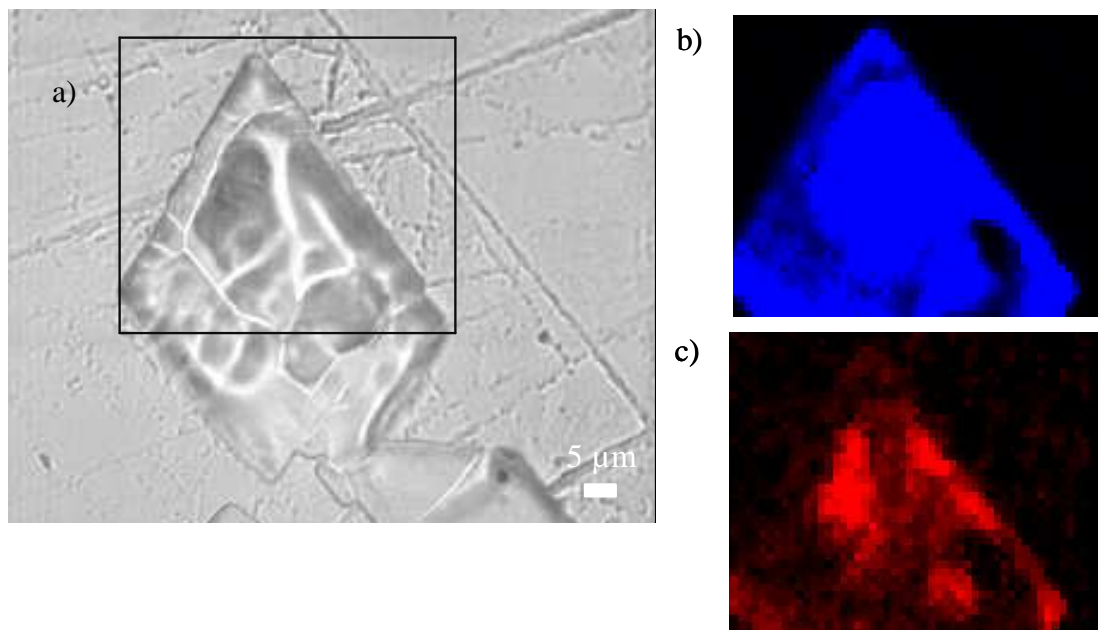


Fig. 4.14 NaCl(100) exposed to NO₂ (RH=0%) after 5 days of ageing at RH>45%. In (a) the optical image (transmission mode), in (b) the Raman image of solid nitrate, in (c) the Raman image of the liquid nitrate.

It is interesting to note that on the crystal, near to the solid nitrate Raman signal at 1068 cm⁻¹ (whose integration gives the Raman image in blue in fig. 4.14b), also some liquid nitrate is present (Raman peak at 1052 cm⁻¹, giving the reconstructed red image in fig. 4.14c).

This observation is consistent with previous work ([Zangmeister C. D. *et al.*, 2001], [Vogt R. *et al.*, 1994]) where the 1052 cm⁻¹ band is observed even after 12h of dry air flow through the powdered NaCl sample exposed to HNO₃. Concluding: even if we are far below the deliquescent point, we can detect the coexistence of solid and dissolved nitrate. The presence of NaNO₃ solution induces an ordered reorganisation of the salt surface resulting, after some ageing, in rhombohedral shaped nitrate crystals. A higher surface covering of nitrate accelerates this process.

4.2.4 RH=15%

By introducing some water vapour in the reactive gas-phase we expect an increase in the conversion of superficial Cl⁻ to NO₃⁻. In parallel we expect, from the observations of experiments at RH=0%, that a certain degree of surface reorganisation already occurs concomitantly to the heterogeneous reaction.

Immediately after reaction (1h of gas-solid contact) the surface is covered by sub-micrometric deposits mainly concentrated along the polishing defects, as depicted in the optical microscope image of fig.4.15.

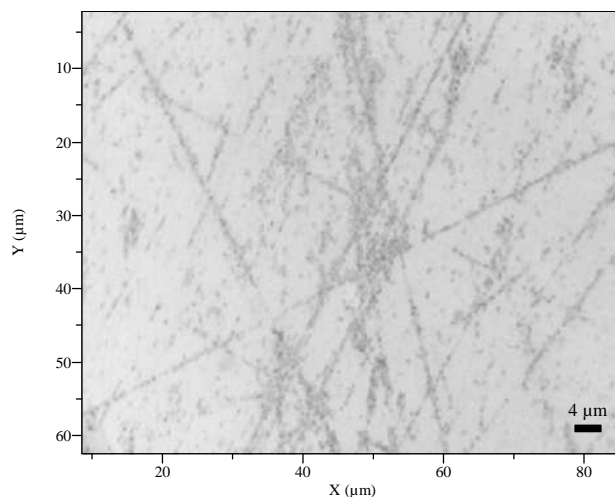


Fig. 4.15 Optical (100x) microscope image of NaCl exposed to NO_2 at $\text{RH}=15\%$.

The morphological characteristics of the NaCl substrate and of the formed NaNO_3 are obtained by AFM images. In fig.4.16 we can observe small hillocks of 160-280 nm equivalent radius (190 nm mean size), slightly bigger than the NaNO_3 nano-crystals formed at $\text{RH}=0\%$. Their heights are between 60 and 90nm.

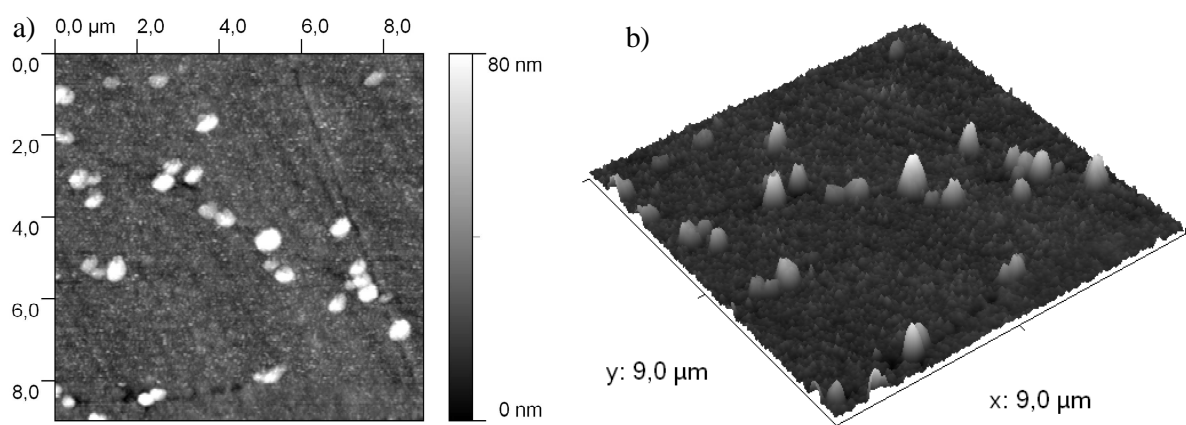


Fig. 4.16 $9 \times 9 \mu\text{m}$ AFM surface reconstruction (a) 2D and (b) 3D image of NaNO_3 crystals formed on NaCl after reaction with NO_2 at $\text{RH}=15\%$.

The conclusion is that by slightly increasing the RH of the reaction more water is absorbed along the defective sites where the formation of solid NaNO_3 crystals of nanometric scale is favoured.

4.2.5 RH=45%

At $\text{RH}=45\%$ we are just above the threshold of the formation of a uniform monolayer of water on the NaCl surface, therefore the reorganisation during the reaction itself should be stronger. From optical microscope observations (fig. 4.17) the characteristics of the reacted surface are completely different from the ones observed in the two previous cases.

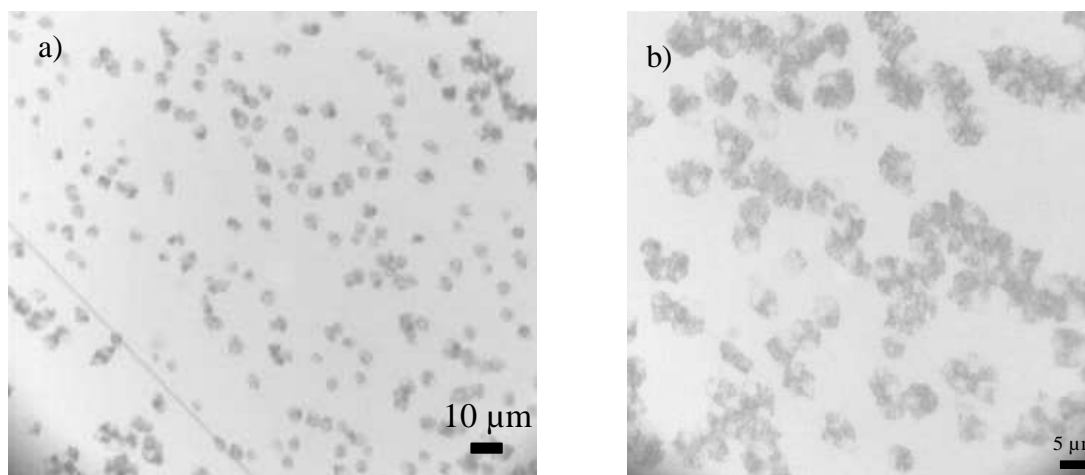


Fig. 4.17 50x (a) and 100x (b) optical images of NaCl(100) immediately after exposure to NO₂ RH=45%.

Some flower-like structures of about 5 μm in diameter are formed all over the surface. The rest of the surface has the appearance of non-reacted NaCl. This can be confirmed by acquiring some Raman images (reconstructed by integrating the A_{1g} band of NaNO₃ at 1068 cm⁻¹), as reported in fig. 4.18. In this image we can observe the solid nitrate signal over the flower-like structures, whilst no Raman signal is recorded elsewhere. We can suppose that the nitrates formed on the surface initially migrate to form these micrometric agglomerations and revealing the underlying fresh NaCl surface.

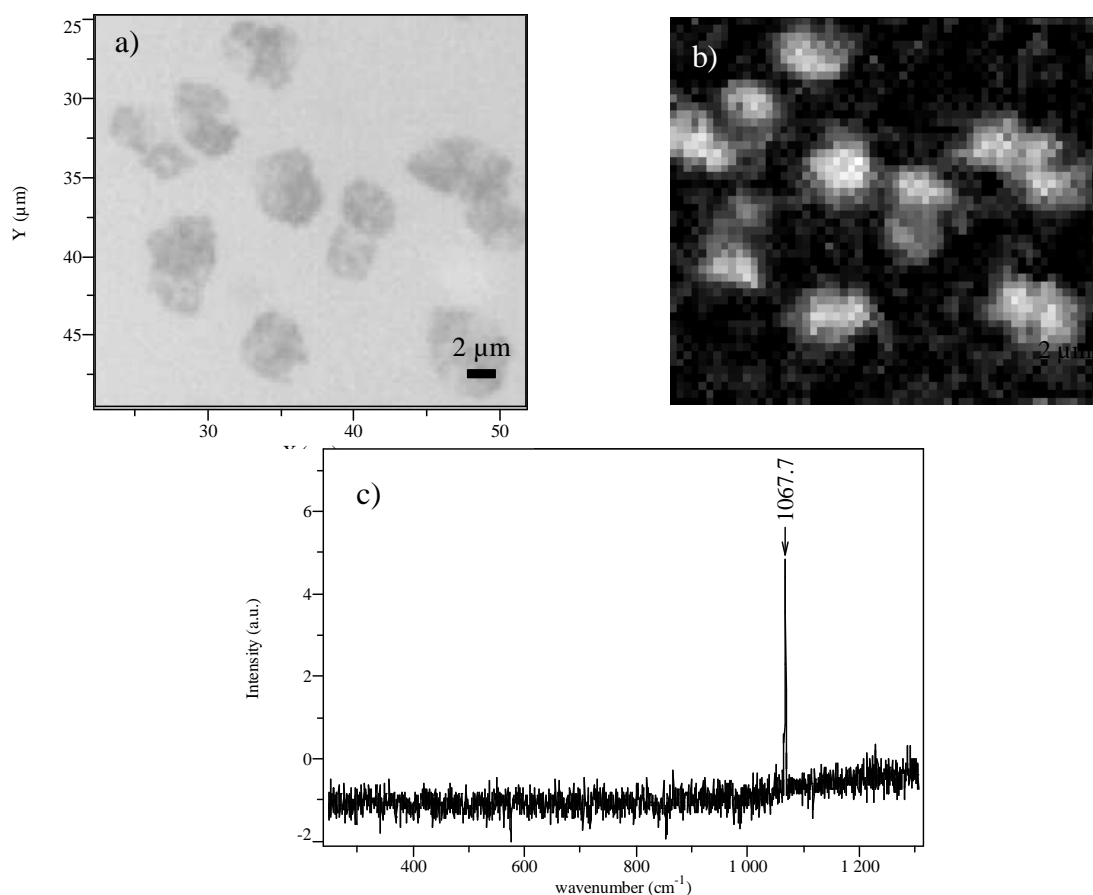


Fig. 4.18 100x optical (a) and Raman (b) images of NaCl(100) exposed to NO₂ at RH=45% and recorded immediately after reaction. The spectra Raman (c) indicates the presence solid nitrate on every white pixel of the Raman image.

As soon as we try to investigate these deposits in more detail, we have to deal with their quite rapid evolution from which, after some hours, small hillocks clearly emerge. On these zones some AFM images are recorded (fig. 4.19) and surface morphology parameters are measured.

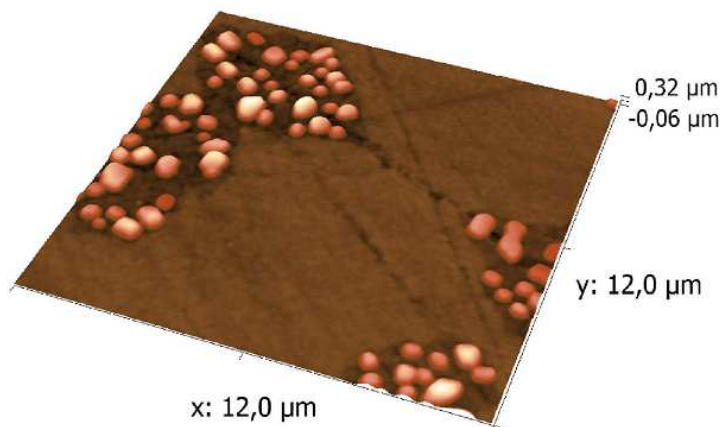


Fig. 4.19 6x6 μm AFM image reconstruction of NaCl(100) exposed to NO_2 at RH=40% after 1 week.

The hillocks mean diameter is around 540 nm and their heights are between 180 and 350 nm. Some typical profiles are reported in fig. 4.20.

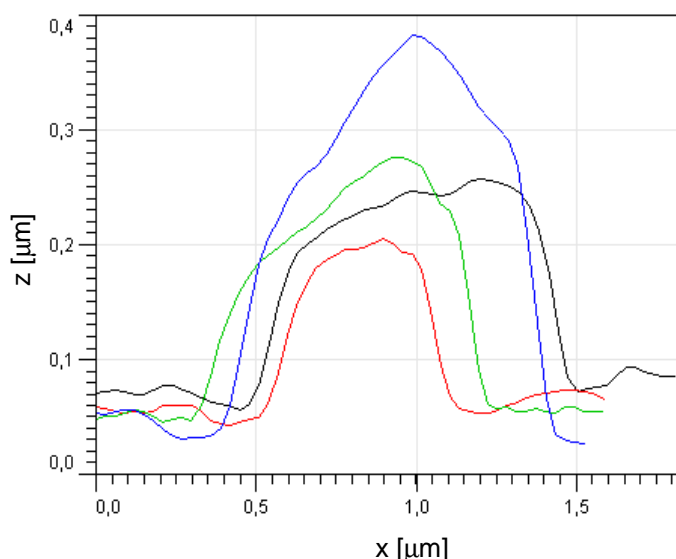


Fig. 4.20 Some hillock profiles measured from the AFM image of NaCl exposed to NO_2 at H=45%.

In previous work ([Zangmeister C. D. et al., 1998]) nitrate towers with similar morphological characteristics were observed after exposure of cleaved NaCl(100) to HNO_3 and H_2O . The authors observe that the presence of a H_2O adlayer facilitates NaNO_3 formation presumably occurring as precipitation from a saturated solution instead of a progressive growth from a gas-solid reaction. Even if the dissolution of the whole nitrate being formed is not possible in the small quantity of surface adsorbed water, we think that the H_2O layer globally facilitates the surface mobility. Since there is a mismatch between the bulk NaNO_3 and NaCl crystallographic parameters, the formed nitrate has a tendency to reorganise into clusters instead of staying spread on the surface. In this case we observe that nitrate is present in a metastable form in the flower-like clusters of 5-8 μm of diameter. They have the tendency to reorganise themselves into separate hillocks under ambient humidity conditions. In this new conformation the contact with the subsiding NaCl surface is minimised, therefore we turn to an energetically favoured situation.

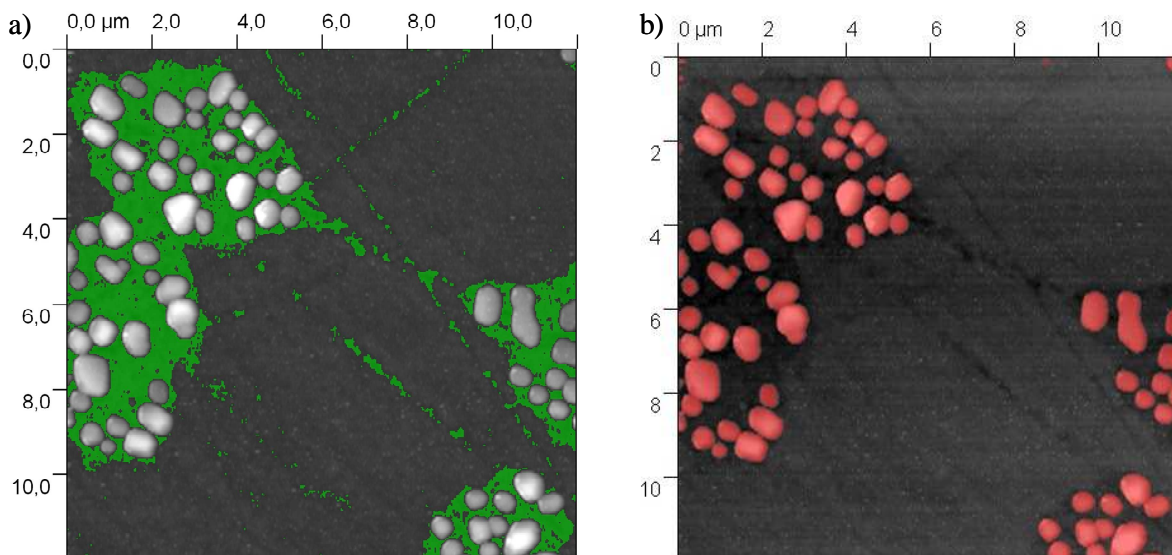


Fig. 4.21 12x12 μm AFM image reconstruction of NaCl(100) exposed to NO_2 at RH=40% after 1 week: in (a) the zones lying under the (100) surface level are coloured in green; in (b) on the right the nitrate hillocks are coloured in red.

We observe that these hillocks (fig. 4.21b) are located inside a surface depression, lying 150-300 nm lower the rest of the flat NaCl surface. These depressions, which are shown in green in fig. 4.21a, have the shape and dimensions of the flower-like structures observed immediately after reaction. This is an indication that they are the traces of the original nitrate surface occupation. The rest of the surface shows the same polishing defects and roughness as if no chemical reaction with NO_2 occurred on it.

From these observations we can suppose that at RH=45%, despite the theoretical presence of a monolayer of adsorbed water, the NaCl/ NO_2 reaction occurs preferentially in some specific spots, which are quite homogeneously dispersed on the surface. The reaction then proceeds around these spots, consuming the surrounding NaCl surface. The formed nitrate is present in a very thin and metastable solid which evolves, after some ageing under ambient humidity conditions, into more stable hillocks of 1 μm diameter. In this new configuration the NaCl/ NaNO_3 contact surface is minimised. We do not observe any long range migration on the surface during surface ageing, due to the confinement of nitrate inside these NaCl hollows.

Some additional information, in particular about the crystal orientation, can be given if we observe in more detail the relative intensities of the nitrate vibrational modes obtained with the polarised Raman spectroscopy (see ch.3.3.2 for Raman theory with polarized light). More specifically we find a difference in the 1068/185 cm^{-1} intensity ratio. An example is reported in fig. 4.22, where a single agglomeration is imaged by integrating the Raman signal of the 1068 cm^{-1} band associated to the internal NO_3^- symmetric stretching (in b) and of the 185 cm^{-1} lattice oscillation (in c). We can observe that the relative intensities between these two bands (i.e. see the spectra reported in b and c), are not the same all over the deposit.

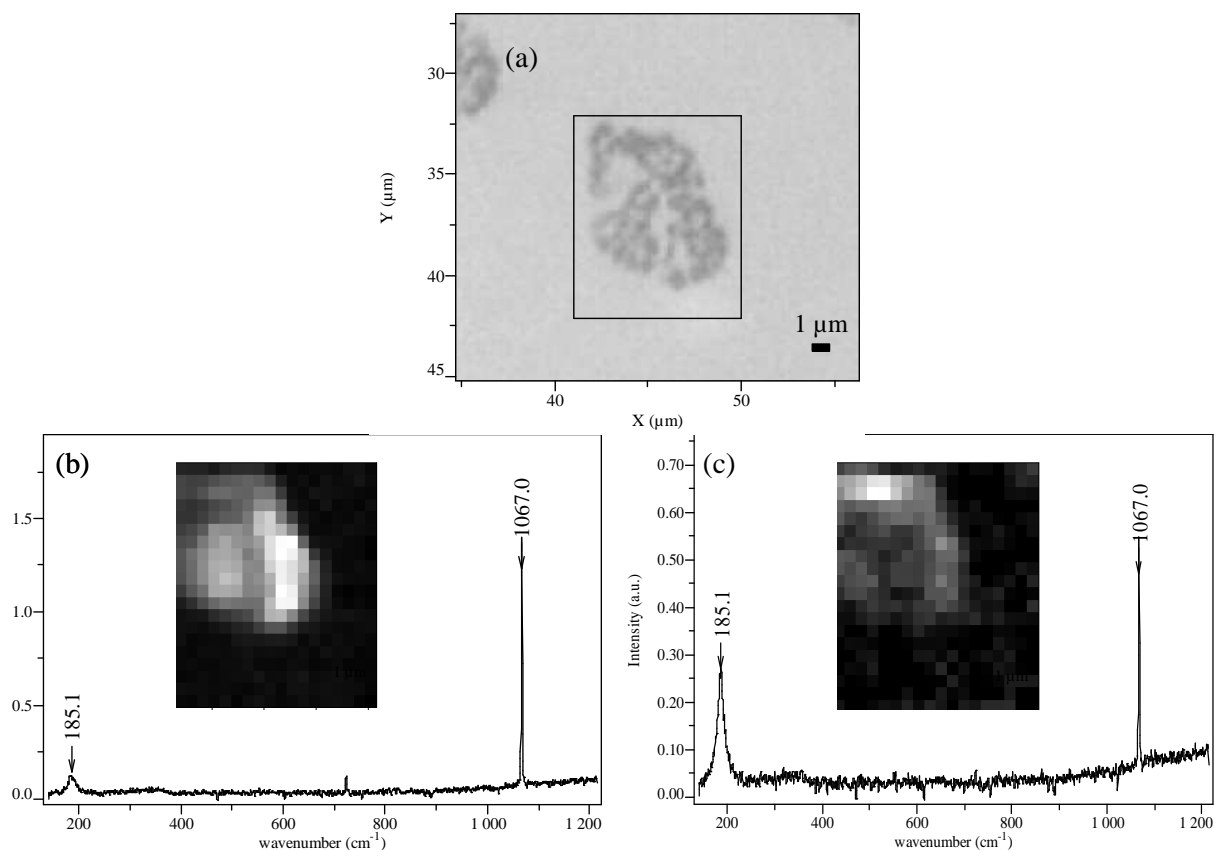


Fig. 4.22 In (a) a 100x optical image of NaCl(100) exposed to NO₂ at RH=45% one day after reaction. The Raman spectra in (b) and (c) are examples of intense absorption at 1067 and 185 cm⁻¹ respectively and are used to reconstruct the corresponding Raman images.

This observation suggests that inside the deposit itself there are differently orientated nitrate nano-crystals, even if it is not possible to go more into the details and to know their exact angle of orientation on the NaCl(100) plane. NaNO₃ solutions are known to form heteropitaxy overgrowth and randomly oriented platelets on NaCl(100) ([Anuradha P. *et al.*, 1985]).

4.2.6 RH=68%

This particular value of RH has been previously introduced as the deliquescent point of a binary mixture of NaNO₃ and NaCl [Tang I. N. *et al.*, 1994]. For this reason it is also interesting to check the NaCl surface behaviour when exposed to NO₂ near to this very specific condition.

Immediately after reaction and purging with dry N₂, the coexistence of two main kinds of nitrate deposits can be seen on the surface, which can be optically distinguished by their dimensions. The smaller ones have a diameter of about 1 μm and can be identified as the darker points (fig. 4.23 a) on the NaCl surface, while the second type have a diameter of approximately 10 μm (fig. 4.23b).

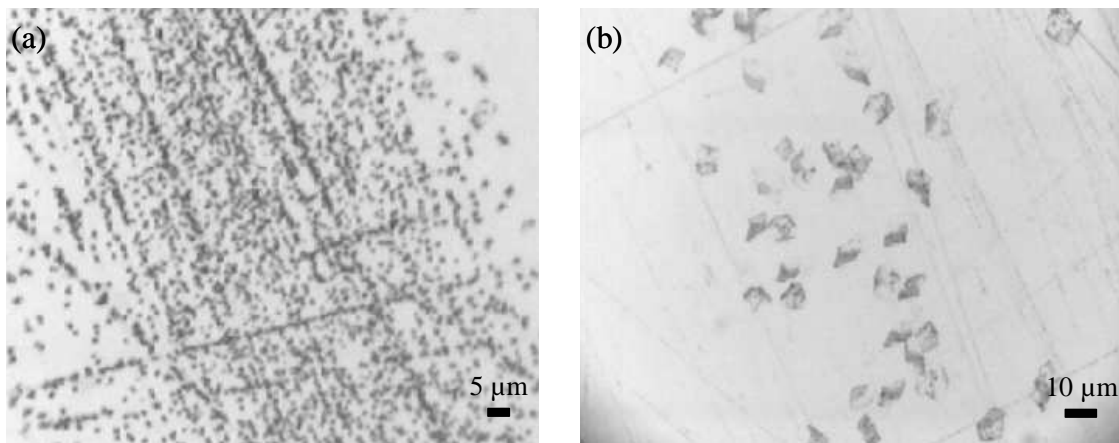


Fig. 4.23 Optical (50x) images of NaCl(100) after reaction with NO₂ at RH=68%: in (a) the small, micrometric-size deposit, in (b) the bigger polygonal crystals.

We present their characteristics here, starting with the smaller ones (fig. 4.23a). By exploring the surface chemical characteristics we can confirm by Raman spectroscopy the nature of reaction product of the formed small crystals: solid nitrate signal is collected all over the small dark points (fig.4.24). A Raman image, giving the nitrate distribution on the surface is reported in fig. 4.25: the black pixels are where no Raman signal was detected.

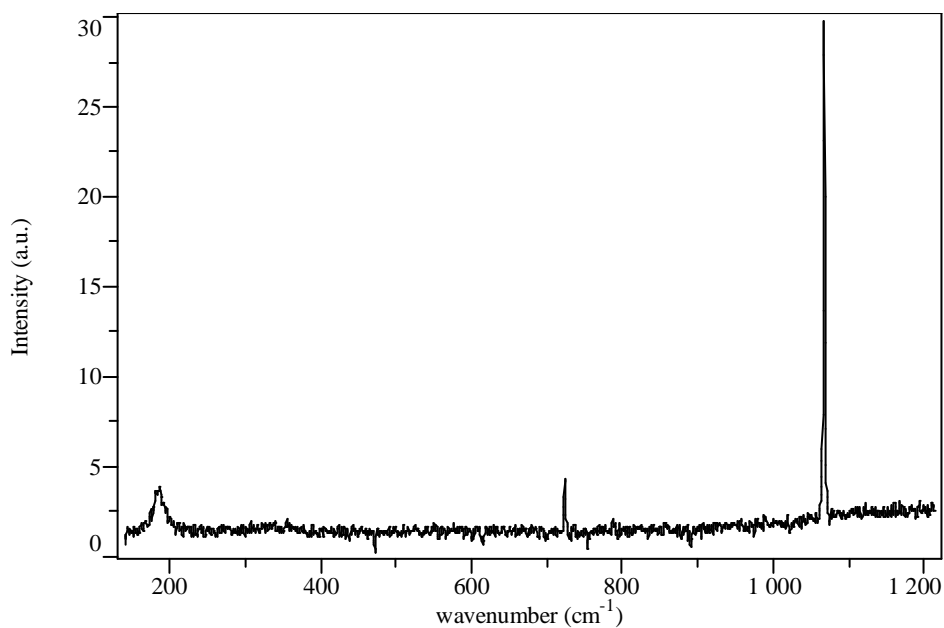


Fig. 4.24 Raman spectrum observed corresponding to the dark deposits on the NaCl surface exposed to NO₂ at RH=68%.

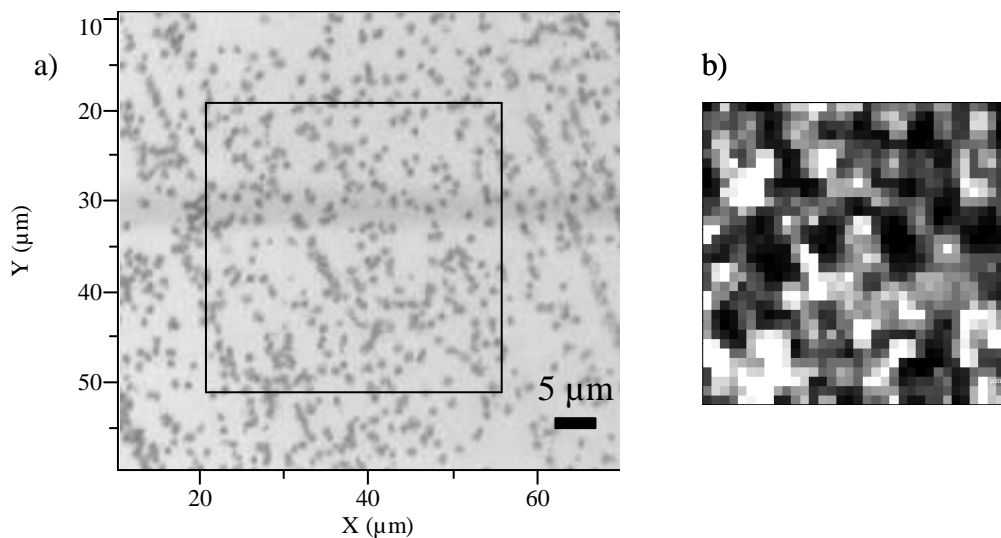


Fig. 4.25 Optical (100x) and Raman images of NaCl(100) exposed to NO₂ RH=68% one day after reaction.

Going into further detail on their morphology we can describe them as small, quite regular and homogeneous pyramids, as observed in the AFM image of fig. 4.26.

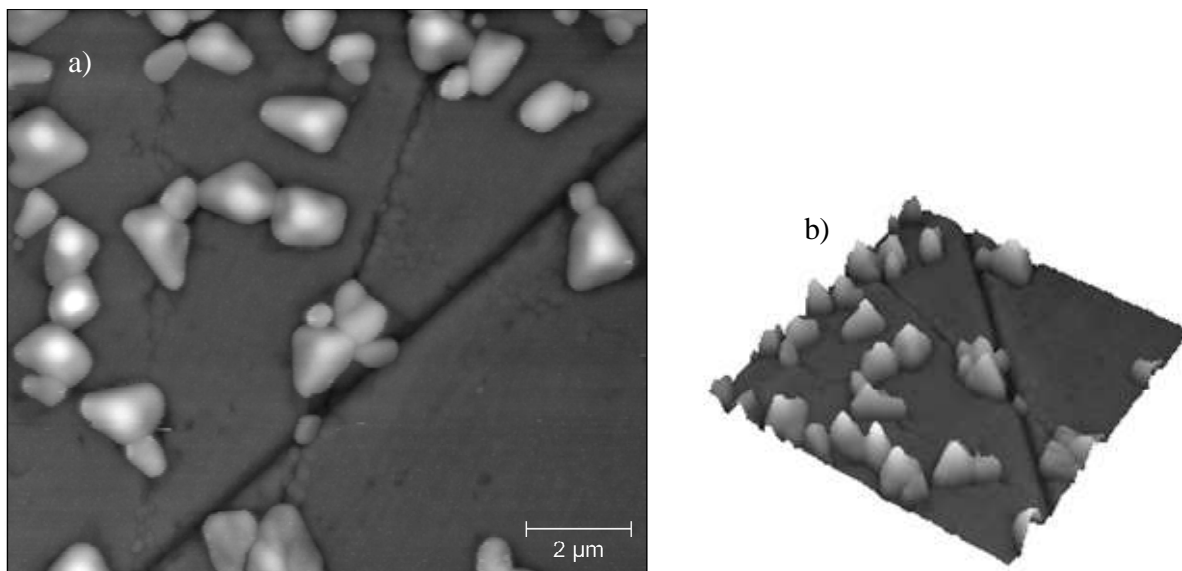


Fig. 4.26 12x12μm AFM images reconstruction of NaCl(100) exposed to NO₂ at RH=68% after 1 day.

The base size of these tetrahedrons is 1-1.5μm and the vertex is approximately 400 nm above the surface. In fig.4.27 there are three profiles of three different hillocks taken as an example: their morphological characteristics are quite similar and it is interesting to observe, once again, a depression of the NaCl surface immediately surrounding the small nitrate crystals of approximately 15-50 nm depth.

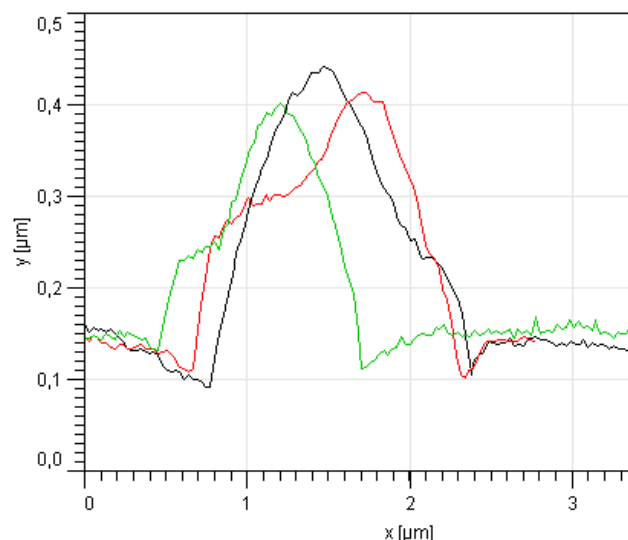


Fig. 4.27 AFM profiles of three different hillocks formed on NaCl (100) after exposure to NO₂ at RH=68%.

We confirm by interpreting the Raman spectra that the bigger crystals we observe on the surface are also formed of solid nitrate. We can reconstruct the surface distribution of nitrate and verify that the surface surrounding the nitrate deposits is made of pure NaCl (fig. 4.28).

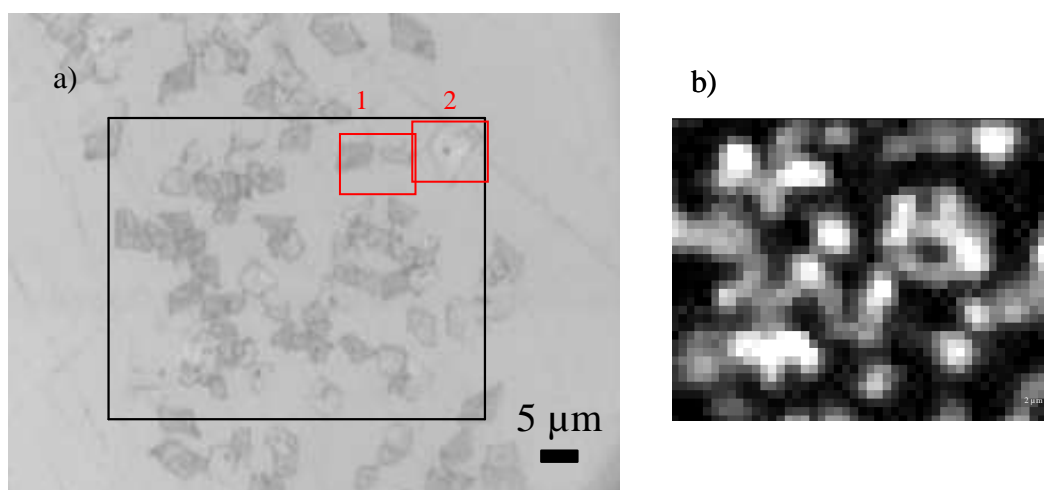


Fig. 4.28 (a) 100x optical (b) and Raman images of 5-micrometer size nitrate crystals formed on NaCl(100) exposed to NO₂ at RH=68%.

From the same Raman image we can obtain some extra information, i.e. the Raman signal has not the same intensity over all the deposits. This could derive from different thickness of the nitrate formation, but looking more carefully at the relative intensities of the A_{1g} mode associated with the nitrate stretching and at the E_g lattice libration, we see that there is also a contribution given by different crystal orientations. In fig. 4.29 we zoom on the upper-right corner of the Raman image on two different nitrate deposits (in the red squares). On the two crystals of fig. 4.29a the 185 cm⁻¹ band signal has a significant intensity, whilst being practically absent from the crystal in fig. 4.29d. This third crystal is thicker than the others as shown by the more intense 1068 cm⁻¹ band recorded on it (fig. 4.29e).

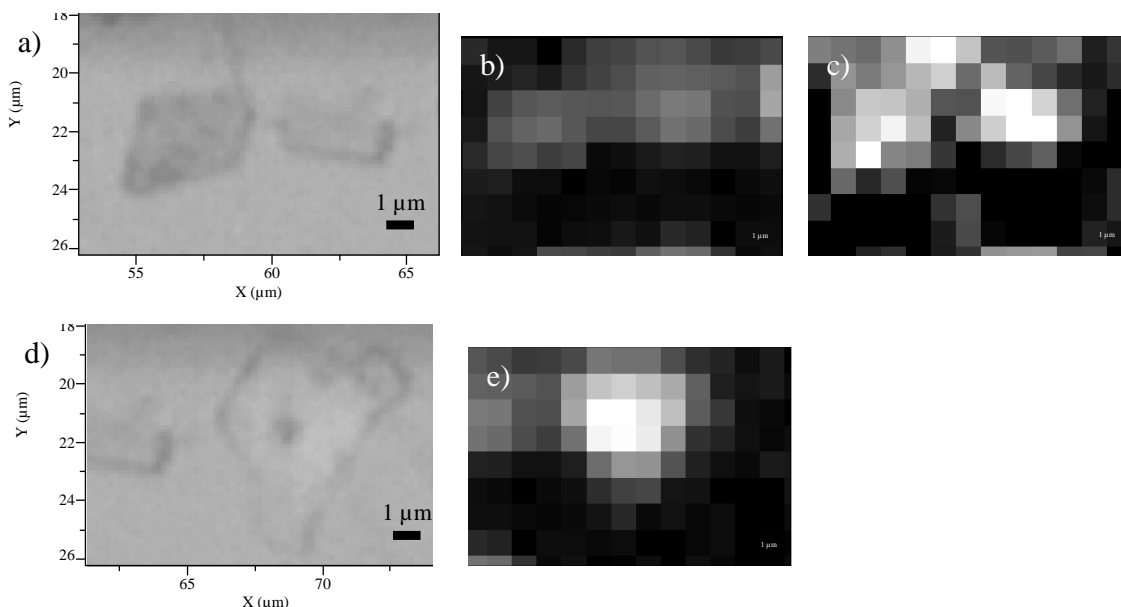


Fig. 4.29 a) and b) Zoom on zones 1 and 2 of the optical image in fig.4.28a; in b) and e) the Raman images are obtained from the integration of the symmetric nitrate stretching band at 1068 cm^{-1} , in c) from the 185 cm^{-1} lattice vibration (libration).

The specific morphologies of these two different types of crystal are investigated by AFM mapping.

Crystals like the one in fig. 4.29d are, instead of a single crystal, formed from an aggregation of smaller units, as depicted in fig. 4.30. The darker points observed in the optical images correspond to the vertex of the central micro-crystal. The sub-units of irregular shape try to assemble to form a regular-shaped rhombohedral crystal. In the same AFM image we can also observe, on the right hand side, some “amorphous” and much thinner nitrate.

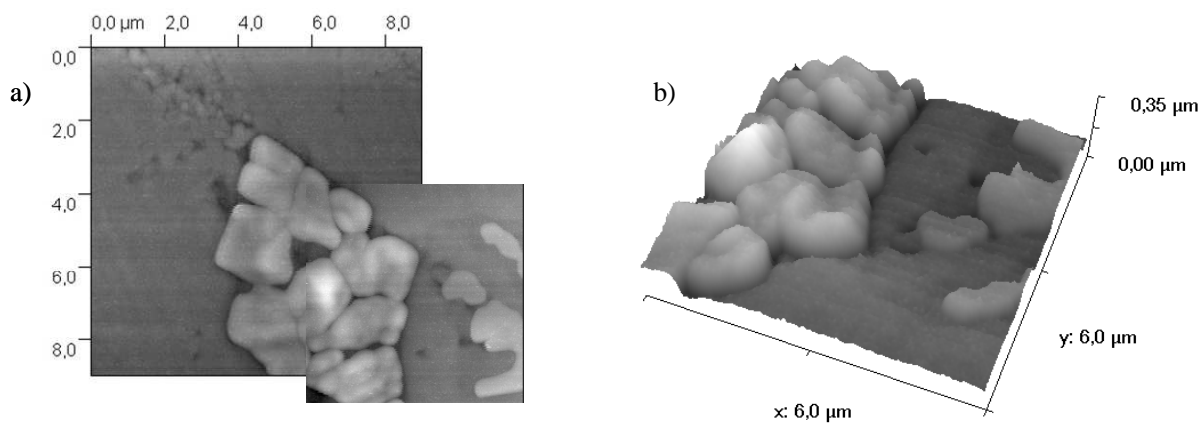


Fig. 4.30 AFM reconstructed 2D (a) and 3D (b) images of a nitrate agglomeration formed on NaCl(100) exposed to NO_2 at RH=68%.

In fig. 4.31 we report the morphological features of a crystal similar to the ones of fig. 4.29a. We can immediately notice, also from the vertical profiles reported in fig.4.32, that the thickness of the deposit is only 40-100 nm, therefore 4 to 5 times less than the previously described hillocks and micro-crystals.

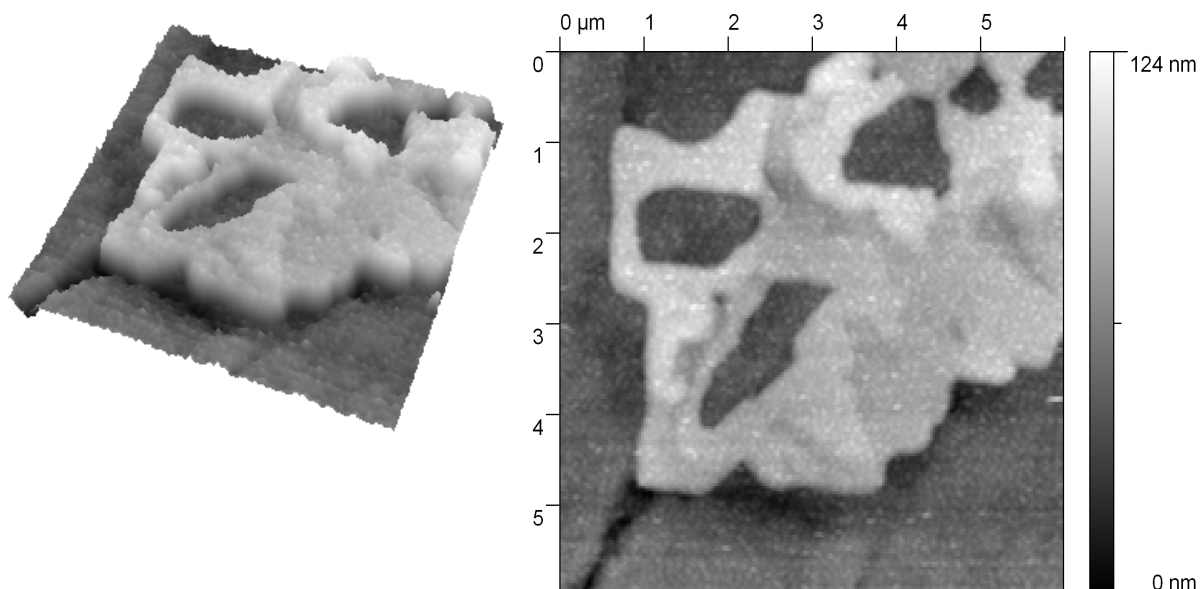


Fig. 4.31 $6 \times 6 \mu\text{m}$ AFM reconstructed 2D and 3D images of 5-micrometer size nitrate crystals formed on NaCl(100) exposed to NO_2 RH=68%.

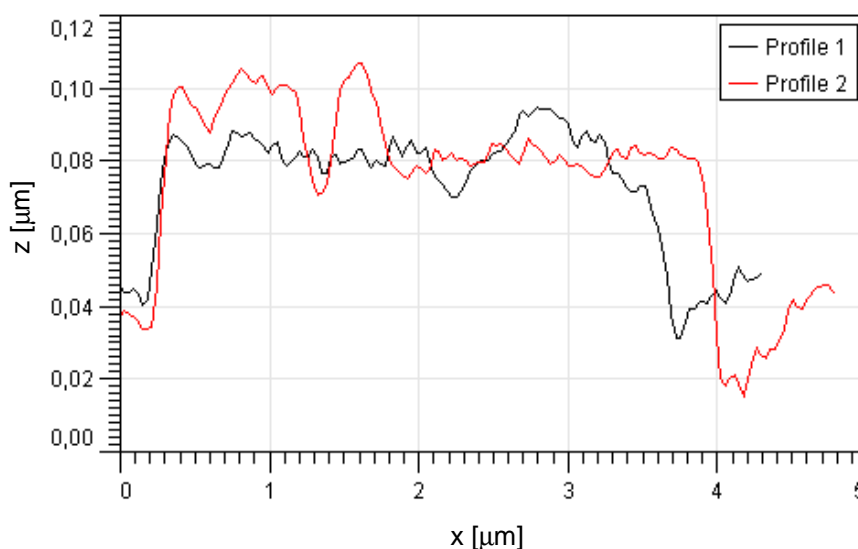


Fig. 4.32 Two vertical profiles of the NaCl crystal presented in image 4.31.

The non well-defined and irregular shape is coherent with a rapid precipitation, of efflorescence, instead of a slow crystallisation without constraints. Taking into account the hygroscopic properties of the NaCl/ NaNO_3 mixtures and the low deposit thickness we can reasonably suppose the presence of a thin solution layer on the surface before the crystal is purged with dry nitrogen at the end of the reaction. The irregular shapes and profiles, to which we can add the discontinuity of the crystal (there are some “holes” from where we can observe the underlying NaCl flat surface) leads us to think that the rapid change in the humidity content of the surrounding atmosphere did not leave time for a more ordered reorganisation into the classical (rhombohedral) crystal.

In some other zones the nitrate pyramidal crystals are interconnected to very thin amorphous plates. An AFM image is then recorded in one of these “mixed” zones and reported in fig. 4.33. Nitrate plates of 40nm thickness are adjacent to micro-crystals of 250 nm height. In some parts they are interconnected and the whole nitrate agglomeration is once again located inside a NaCl depression lying 20-30nm below the rest of the surface (in green in fig. 4.33b). This observation leads us to think that an initial liquid nitrate layer, occupying the NaCl

hollow, dried and leads to the nitrate structures observed. This hypothesis is also supported by the fact that the hollow volume corresponds to the volume of the solid nitrate ($\sim 2.5 \mu\text{m}^3$) contained in it.

Indeed thinner deposits can exist in the liquid state at lower RH. During the rapid surface drying to quench the reactivity, different structures can be stabilized at different humidities with the result that different solid nitrate crystals are present on NaCl(100) as already reported by [Anuradha P. et al., 1985]. The pyramidal structures could be an intermediate between the amorphous and metastable thin layers and the more organised rhombohedral crystals that are observed after some days of surface ageing. To support this, we can observe in fig. 4.33c, that there is always the presence of some inclines at the thinner platelets borders. They could be the precursors of the pyramidal micro crystals of the central part of the image.

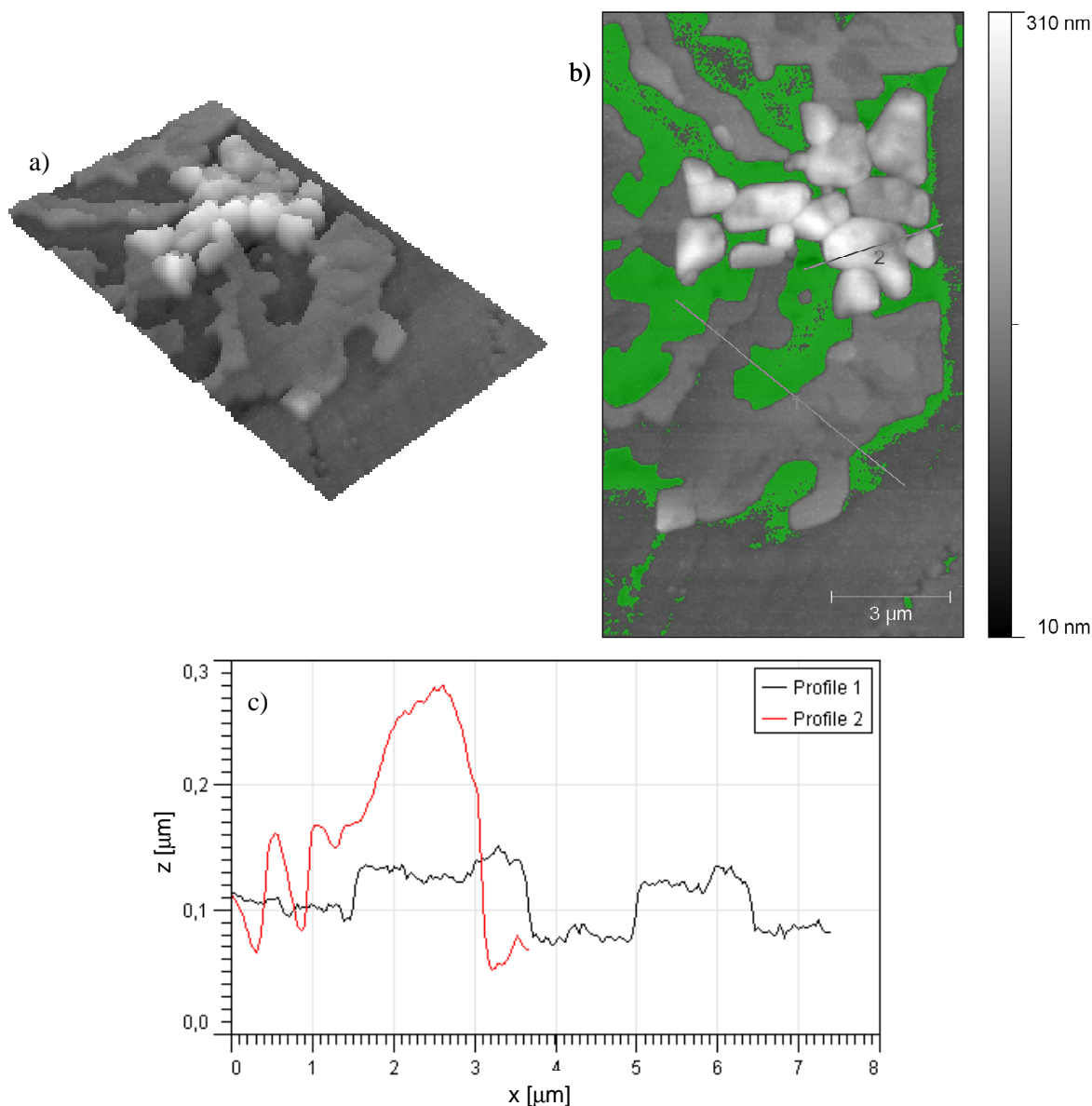


Fig. 4.33 $9 \times 15.6 \mu\text{m}$ AFM 3D (a) and 2D (b) image reconstruction where in green is the surface ranging from 0 to 100nm of height (referred to the lowest value registered in the image). In correspondence to the lines labelled with 1 and 2 the morphological profiles are reported in the bottom graph (c).

Also from optical images of these crystal agglomeration zones (fig. 4.34a) we can recognise zones of different thicknesses and, from the darker points, that some tetrahedrons are encompassed by the structure. The Raman images are obtained from the collection of a spectrum every $0.5 \mu\text{m}$. In fig. 4.34b the image derives from the integration of the 1068 cm^{-1}

band, and in 4.34c by integrating the band at 185 cm^{-1} . We clearly see that inside the same crystal there are different relative intensities of the two bands, meaning different orientations of the sub-crystals. This observation combined with the morphological information leads to another conclusion: while the smaller $1\mu\text{m}$ crystals of pyramidal shape show a small E_g/A_{1g} intensity ratio (spectrum in fig. 4.34a), the flatter ones conversely have the tendency to have a $185/1068\text{ cm}^{-1}$ ratio equal to one (spectrum in fig.4.34b). Their different morphologies are also accompanied by different orientations of the crystal axis relative to the $\text{NaCl}(100)$ surface: during the surface reorganisation the nitrate crystals twist from the an amorphous and thin structure to a more stable, pyramidal one.

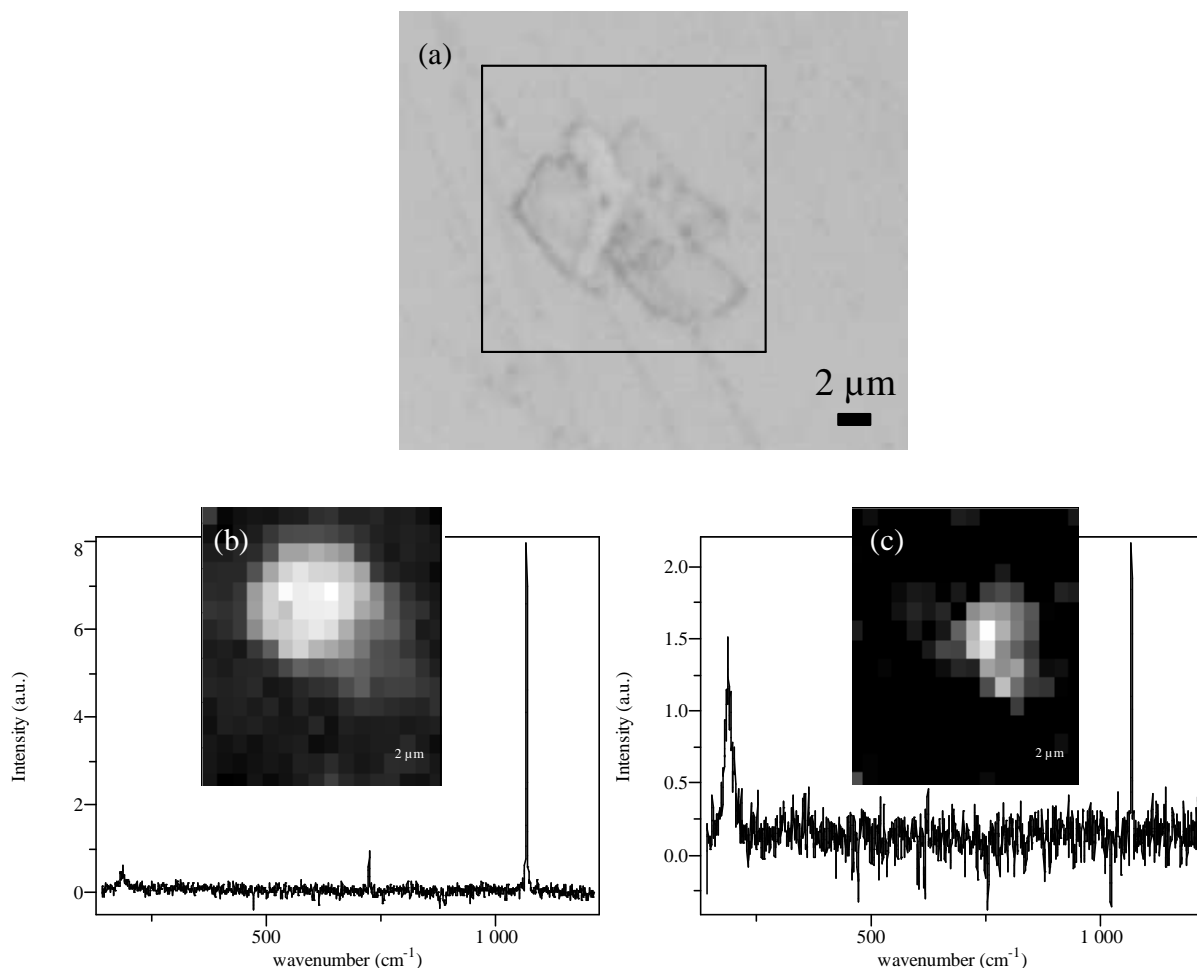


Fig. 4.34 (a) 100x optical images of a 10-micrometer size nitrate formation on $\text{NaCl}(100)$ exposed to NO_2 $\text{RH}=68\%$. Raman images are reconstructed by integrating the band at 1068 cm^{-1} (b) and 185 cm^{-1} (c) respectively. Under the Raman images two example of Raman spectra with a low (b) and high (c) $185/1068\text{ cm}^{-1}$ signal.

If we now perform the same experiment on a freshly cleaved $\text{NaCl}(100)$, we are sure that there is no effect due to some artificial surface defects from polishing.

What we observe is indeed the formation of well ordered rhombohedral NaNO_3 crystals along the cleavage steps, where water is assumed to adsorb more easily (fig. 4.35).

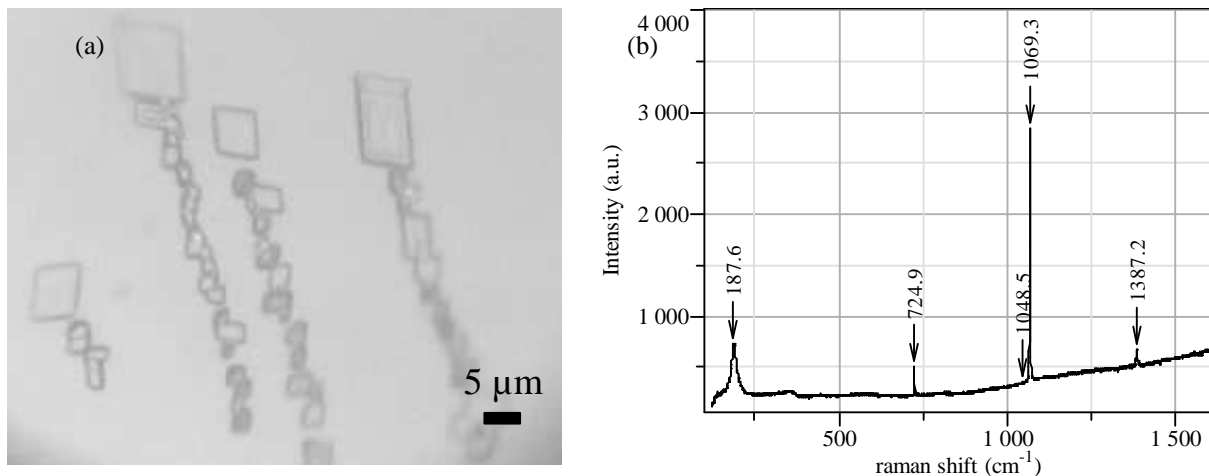


Fig. 4.35 Rhombohedral NaNO_3 deposits on freshly cleaved $\text{NaCl}(100)$ after exposure to NO_2 at $\text{RH}=68\%$: (a) optical image (100x magnification) and (b) Raman spectrum.

At the same time we observe the “amorphous” nitrate deposits on the NaCl terraces (fig. 4.36a) surrounded by very small, sub-micrometric nitrate spots that can be seen only slightly through the optical microscope images. The Raman spectra collected confirm the presence of solid NaNO_3 corresponding to all three different formations (fig. 4.35b, 4.36b and c). On the contrary no micrometric nitrate with a pyramidal shape are observed at this stage.

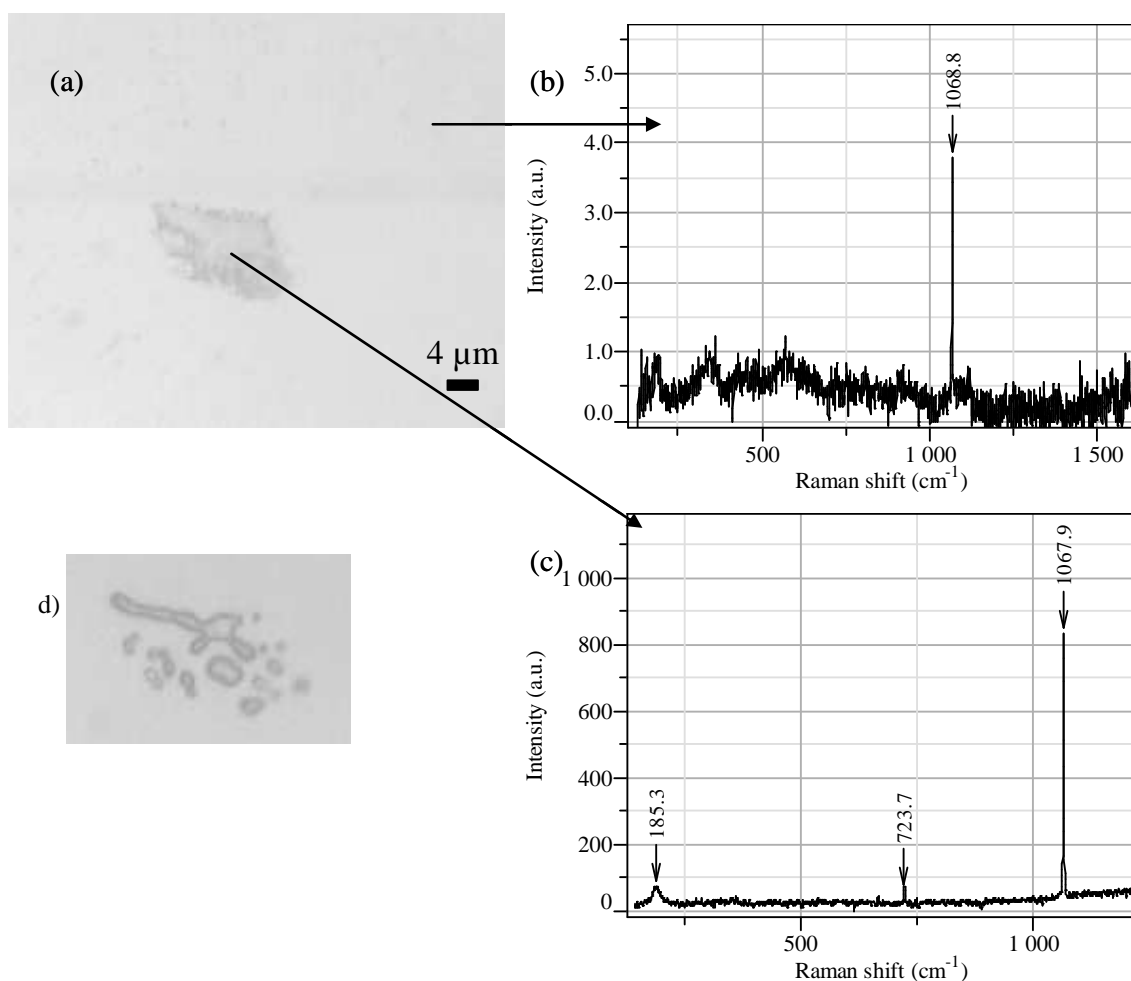


Fig. 4.36 (a) Optical image (100x) and Raman spectra collected in correspondence of (b) the submicrometric deposits present all over the terrace surface and (c) on the $10\mu\text{m}$ central agglomeration. In (d) the optical image of the same deposit after 3 days of ageing at the laboratory humidity.

From experimental observation we can conclude that at RH=68% the ion mobility on the surface is high enough to reorganise the forming or formed nitrate into bigger structures. On flat and relatively defect-less terraces, the nitrate microscopic aggregations are not completely well ordered and near to sub-micrometric nitrate deposits there are also relatively thin deposits which, despite being non-liquid, have the shape of a viscous liquid drop (fig.4.36a). If a very thin layer of nitrate (10-50nm) were present on NaCl(100) it is reasonable to think that it could be partially solvated at the humidity set during the experiment. For this reason we are led to make the hypothesis that the thin deposits can derive from a fast precipitation induced by the dry purging we applied at the end of exposure to NO₂. This metastable phase does not have a regular shape and has the tendency to evolve, as in the case observed at RH=45%, and to form smaller hillocks (fig.4.36d). Where the surface is more mobile, i.e. along the polishing defects, the forming nitrate can more easily migrate on the surface resulting in well ordered micrometric tetrahedral crystals (fig.4.25 and 4.26). This reorganisation process also concerns both the thin amorphous and tetrahedral crystals at longer ageing times: these structures evolve towards more regular-shaped rhombohedral crystals of super-micrometric dimensions.

4.2.7 RH=80%

At this value of RH the NaCl should become deliquescent, meaning that at least the topmost layer should be a very concentrated solution containing Cl⁻ and Na⁺ ions. The effect of this different phase of the substrate on the reactivity towards NO₂ is investigated.

Immediately after reaction the optical microscope images of the NaCl surface surprisingly appear to be free from any reaction products. An AFM image reveals indeed that only few and very thin (100nm) micrometric crystals are present. Some examples are reported in fig 4.37, 4.38 and 4.40. Each of them has some peculiarities: in fig.4.37 the NaCl surface shows some roughness and particularly some deep ditches of 5 to 30nm, where presumably a nitrate deposit lies. From the asymmetric response of the tip in the forward and backward scans, we could suggest a liquid-like nature of this deposit which has a 25nm thickness in the centre while the borders are 40-45nm above the surface layer. It is possible that the dry N₂ purging procedure (10L/2 min) was not long enough to give complete efflorescence of the nitrate solution formed after the reaction at such a high humidity. In any case the deposit is more similar to the amorphous ones already observed at RH=68%.

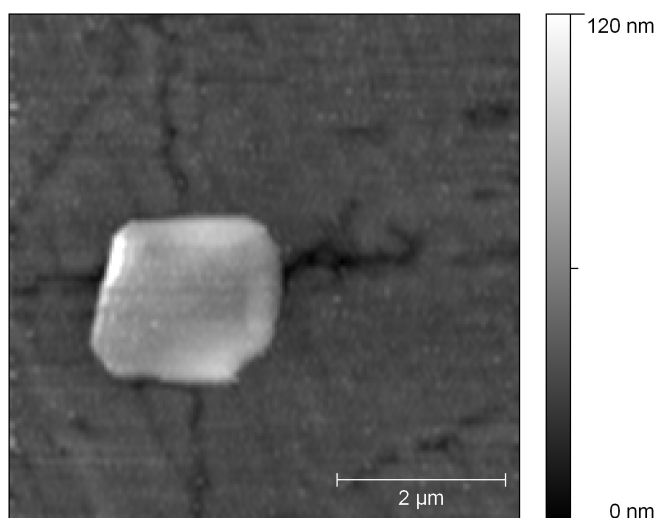


Fig. 4.37 6x6μm AFM 2D image reconstruction of a deposit formed on NaCl(100) after reaction with NO₂ at RH=80%. From the tip response it could be constituted of a supersaturated solution.

In the bottom part of fig. 4.38 a micrometric formation has similar characteristics to the one just described in fig.4.37, but 4 times thicker with its top roughly 120 nm over the NaCl surface level.

The central part of the image shows a zone of NaCl erosion: the hollow is quite deep (170nm) and large (~1 μ m), so that it is not compatible with a polishing scratch which, moreover is visible running diagonally on the right. In addition to that, inside the cavity lots of smaller grains (about 40nm of height) are visible (fig. 4.38c).

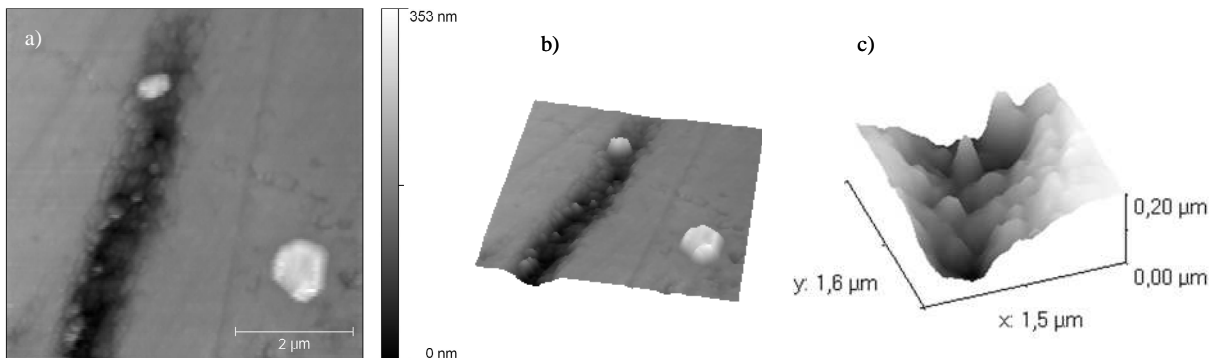


Fig. 4.38 6x6 μ m AFM (a) 2D and (b) 3D image reconstruction of NaCl(100) after reaction with NO₂ at RH=80%. In (c) a zoom inside the hollow.

Finally we can find all the structures we have just described in fig. 4.39: from the eroded NaCl surface crystals of different dimensions are emerging and the hollow shape clearly indicates that it can not be attributed to some surface defect.

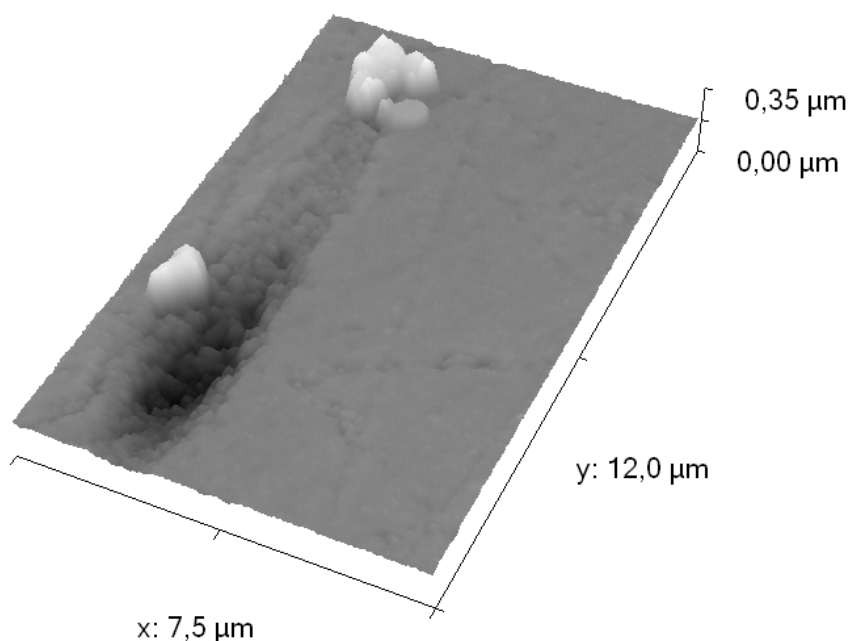


Fig. 4.39 7.5x12 μ m AFM 3D image reconstruction of NaCl(100) after reaction with NO₂ at RH=80%.

Raman images are collected of a zone showing, under the optical microscope, similar characteristics in order to check the chemical composition of the hillocks inside the hollow. From the Raman images reported in fig. 4.40, we can exclude that they are merely the consequence of NaCl reconstruction, because a peak at 1068 cm⁻¹ is also measured inside the NaCl depression. The relative intensities of the 1068 and 185 cm⁻¹ differ from a nitrate crystal to the other. In particular the two crystals on the left part of the hollow have a higher

185/1068 cm^{-1} intensity ratio and an example of spectrum collected over them is reported in fig. 4.41b.

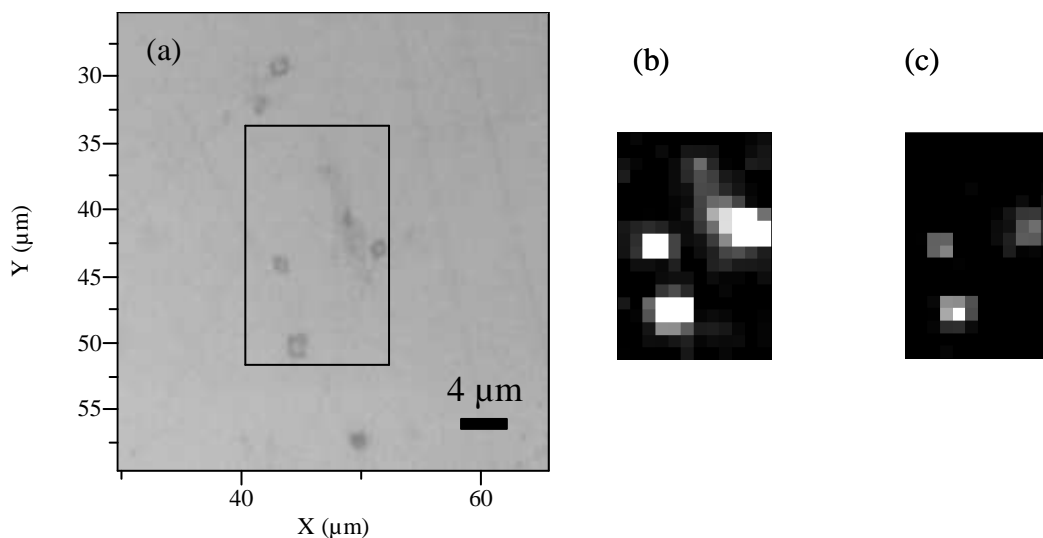


Fig. 4.40 (a) 100x optical image of NaCl(100) exposed to NO_2 RH=80%. In (b) a Raman image is reconstructed by integrating the absorption peak at 1068 cm^{-1} , while in (c) the image is obtained by integrating the peak at 185 cm^{-1} .

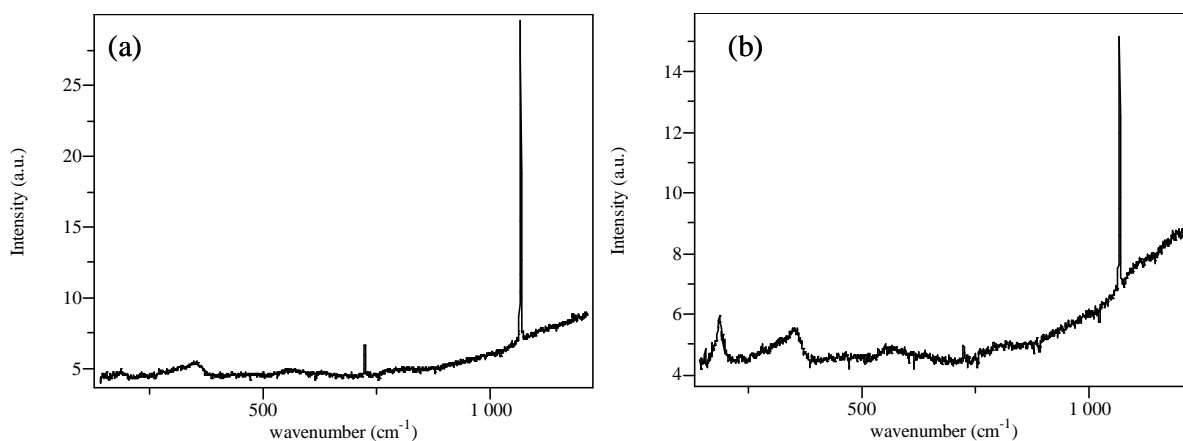


Fig. 4.41 Raman spectra collected (a) near the NaCl hollow and (b) over the rhombohedral crystal.

Surface ageing leads to the emergence of small nitrate crystals from the hollows all over the surface. The collected AFM images (as i.e. fig. 4.42) suggest the presence of a NaCl/ NaNO_3 solution during the reaction. The mixture of these two solids then slowly evolves separating out into two phases so that nitrate appears at the surface. The emerging new phase (28 nm of thickness around the furrow borders) crystallises into hillocks of approximately 180nm mean diameter and 30 to 100 nm thickness.

The same phenomenon is observed on other zones without furrows (fig. 4.43). Again, the newly-formed nitrate deposits are of 25-35 nm thickness and 220 nm mean diameter. The appearance of a surface that has not reacted too much (i.e. compared to 40 and 68% RH) derives from the fact that the nitrate is actually also trapped under the surface and so not immediately visible. It is difficult to say if some liquid nitrate is also present on the surface because of the too low Raman sensitivity. However, we can confirm from the spectra interpretation that these nanometric particles are formed of solid nitrate.

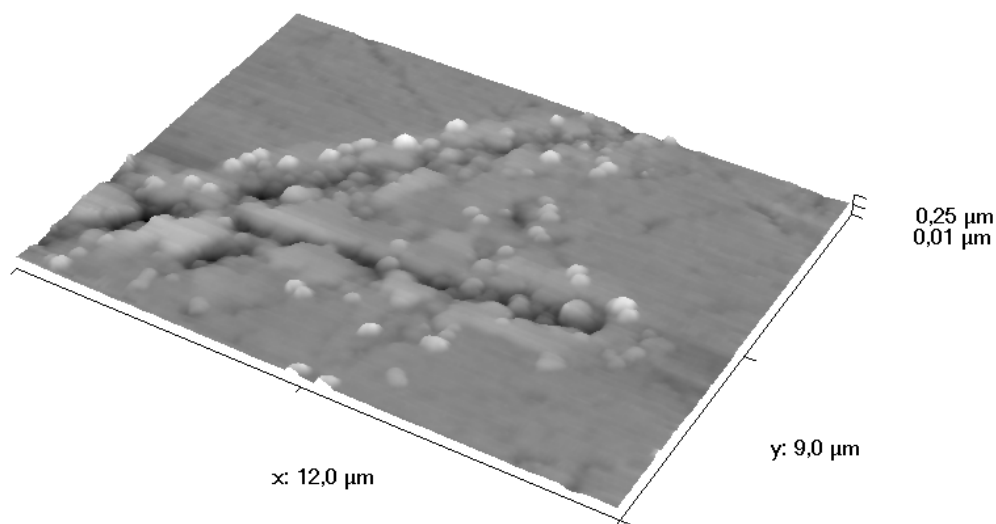


Fig. 4.42 AFM 3D topography on 3 days-aged NaCl(100) reacted with NO₂ at RH=80%.

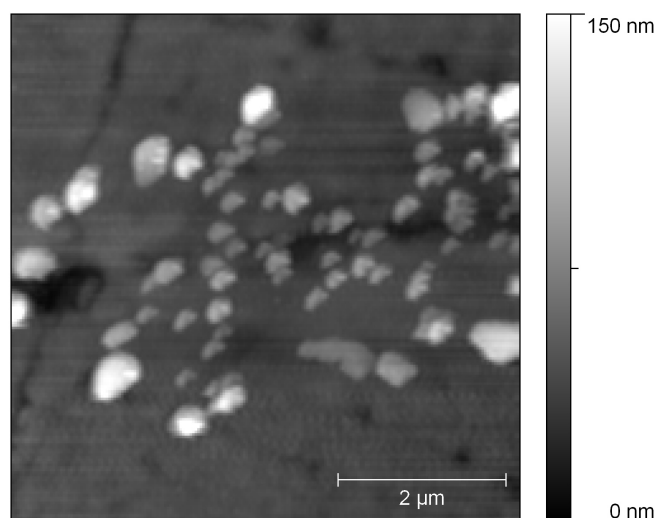


Fig. 4.43 AFM 2D topography on 3 days-aged NaCl(100) reacted with NO₂ at RH=80%.

4.3 NaCl pellets exposed to NO₂ at different humidities

The NaCl disks used for the kinetics studies are also analyzed by Raman microspectrometry. The main aim is not to study again the process of nitrate formation and reorganization under different RH which has already been discussed in the previous section of this chapter, but to verify the presence on the pellets of the expected solid product, NaNO₃ and the location of NaNO₃ crystals with respect to NaCl grain connections. We will report here only some meaningful examples.

4.3.1 RH=0%

If we consider the pellets exposed to NO₂ in dry conditions we can obtain a strongly homogeneous distribution of solid nitrate all over the salt surface (fig. 4.44a), where the nitrate Raman peak can be easily collected. This observation indicates an equal reactivity all over the NaCl disk zones.

Moreover it is interesting that we can detect nitrate signal also under the surface corresponding to some imperfect grain connections, as shown in fig. 4.44: the nitrate Raman peaks collected 3 μm under the surface corresponding to the white points of fig.4.44b are two times more intense that the peak recorded on the surface. This denotes a partial NO_2 diffusion through the three holes visible in the bottom part of the image and the consequent reaction with NaCl inside the pellet itself.

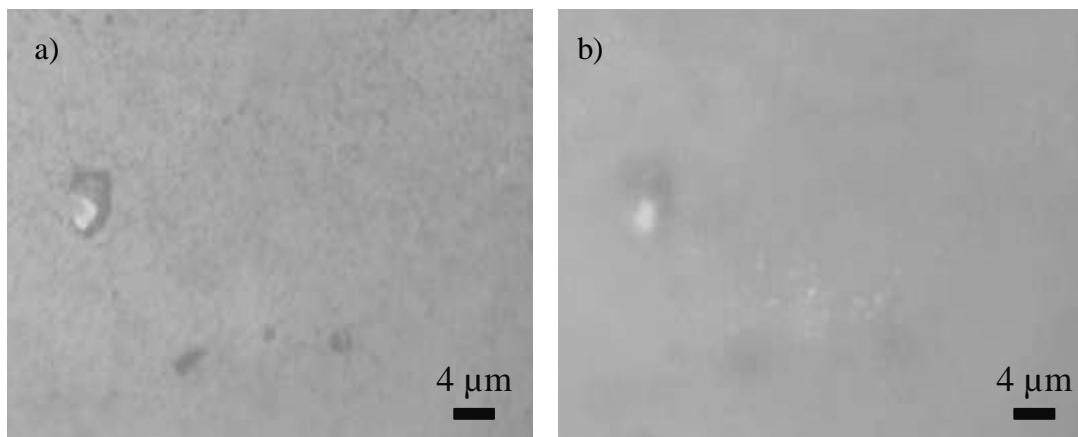


Fig. 4.44 Optical images (100x) collected (a) over a NaCl pellet exposed to NO_2 at $\text{RH}=0\%$ and (b) 3 μm under the surface.

4.3.2 $\text{RH}=50\%$

The Raman images collected on the NaCl pellets exposed at $\text{RH}=50\%$ show, in parallel to what was already observed on the monocrystal surfaces, the presence of NaNO_3 agglomeration of 5-10 μm size (fig. 4.45). Some deliquescent nitrate signal at 1048 cm^{-1} is also recorded on them. This is a sign of surface reorganization as already discussed in §4.2.5 and it is interesting to observe the same phenomenon also on a polycrystalline surface. Also the different sub-crystal orientations inside the same agglomeration are confirmed, and an example is reported in the difference between the Raman image obtained by integrating the 1068 cm^{-1} band (fig 4.45b) or the one at 185 cm^{-1} (fig. 4.45c).

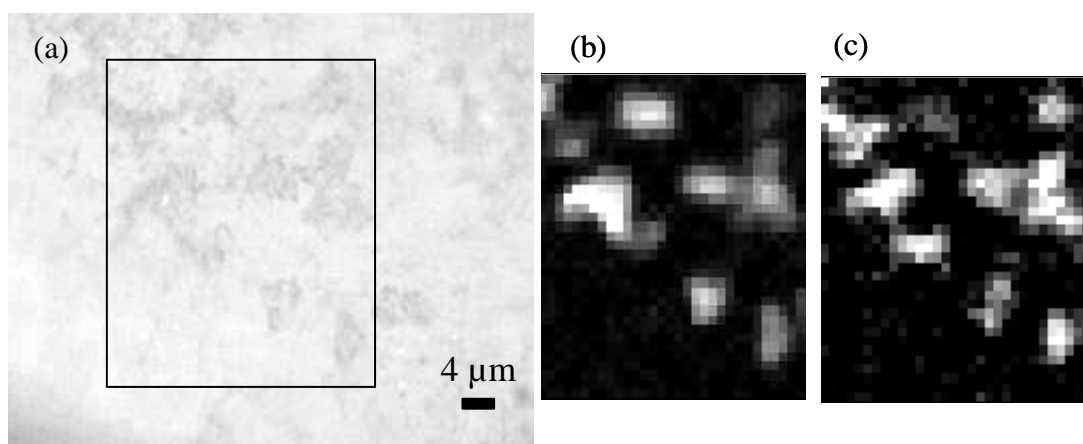


Fig. 4.45 NaCl pellet exposed to NO_2 at $\text{RH}=50\%$: optical image in (a). In (b) the Raman image reconstructed by integrating the 1068 cm^{-1} band; in (c) by integrating the 185 cm^{-1} band.

4.3.3 RH=80%

We previously hypothesized that, when the deliquescent NaCl is put in contact with NO₂, the formed nitrate could be segregated inside the surface during the reactivity quenching treatment. We also observe this on the reacted pellets: no Raman peak is collected on the surface and only by focusing the excitation laser beam below it can we record the solid nitrate presence. This can be optically observed i.e. in fig. 4.46, where there are the two images are obtained by focusing on (a) and below (b) the surface. Only if the excitation laser beam is focused some micrometers under the surface, can some nitrate signal at 1068 cm⁻¹ be collected corresponding to the white spot in the middle of the image (optical image in b, Raman images in c).

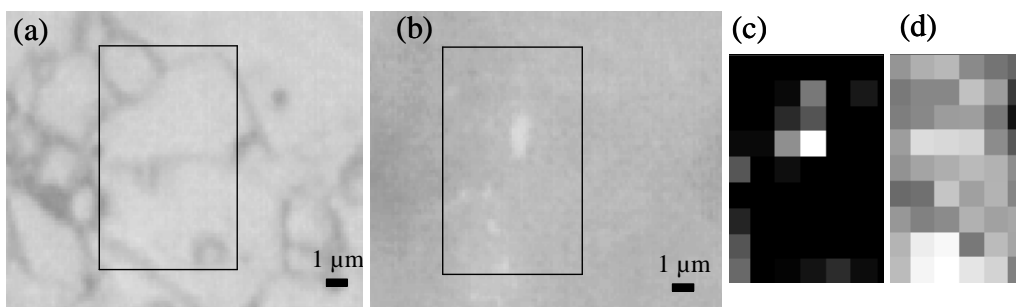


Fig. 4.46 Optical images (100x) by focusing on the surface (a) and some micrometer below (b). Raman images collected under the surface and reconstructed by integrating in (c) the 1068 cm⁻¹ solid nitrate band and in (d) the 234 cm⁻¹ N₂O₄ or N₂O₄·HNO₃ band.

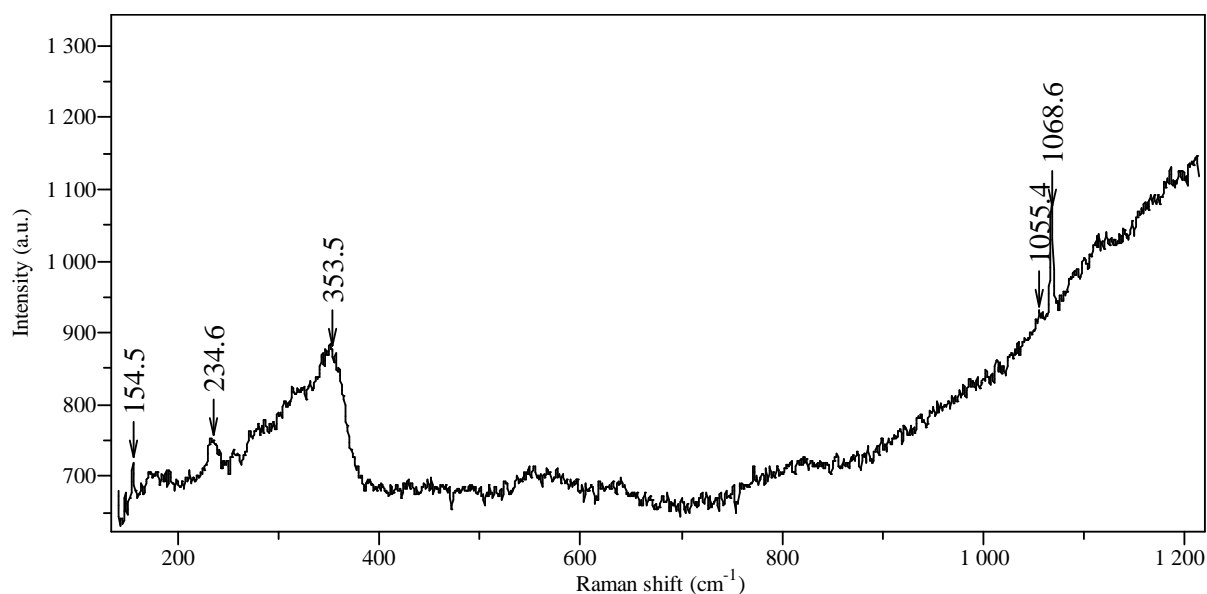


Fig. 4.47 Raman spectrum collected under the NaCl pellet surface after reaction with NO₂ at RH=80%.

By analyzing a Raman spectrum collected under the surface and reported in fig. 4.47, we can see a small contribution at 1055 cm⁻¹ from coupled ion pair nitrate which denotes the presence of deliquescent nitrate trapped under the surface.

Some supplementary bands at ~234 cm⁻¹ and 154 cm⁻¹ can be attributed to N₂O₄ and NO₂ or to their complexes with NO₃⁻ (or HNO₃) occluded under the surface of the crystalline NaCl [Kamboures M. A. et al., 2008].

4.4 Conclusion

The observations of NaCl (100) surfaces can be transposed to the case of pressed NaCl powder pellets. Immediately after reaction the nitrate surface agglomerations are indeed similar in the two cases: a uniform distribution of sub-micrometric NaNO₃ crystals at RH=0%, larger agglomerations made of smaller crystals with different orientations at RH=50% and nitrate trapped under the surface at RH=80%.

We can also observe that some NO₂, after having diffused through the very few grain borders present on NaCl pellets, react forming solid nitrate below the surface level.

Adsorbed water plays a crucial role on the reorganization of the surface and on NaNO₃ recrystallisation. When more than a monolayer of water is present (RH>35%) the uptake process is accompanied by surface ion mobility which assembles the forming nitrates and freshly generates NaCl sites which are then available to react. Formed nano or micro-crystals of NaNO₃ have different morphologies and orientations on NaCl(100), as reported in [Anuradha P. *et al.*, 1985], due to the mismatch between the crystallographic parameters of the two salts,. These different morphologies indicate a fast precipitation from a thin liquid layer of nitrate when the reaction occurs at RH~68%. The thinner and more “amorphous” solid nitrate is unstable and evolves, under ambient humidity conditions, to tetrahedral structures which tend to aggregate and evolve further towards microscopic and macroscopic crystals of rhombohedral shape.

When the NaCl deliquescence point is reached (RH>75%) we have some spectral indications of the presence of NO₂ and N₂O₄ complexes with NO₃⁻ or HNO₃ trapped below the surface. This snapshot of the composition of a “frozen” solution could give useful suggestions about a possible reaction mechanism. NO₂ and N₂O₄ are not the species which directly react with NaCl_(aq): there is an intermediate step, probably an hydrolysis, that can form HNO₃, which can then exchange H⁺ with Na⁺ to form NaNO₃.

Chapter 5 – Fatty Acid Coated Surfaces

5. Fatty acid coated surfaces

In order to better understand the nature of coated mineral surfaces it is necessary to determine the characteristics of the fatty acid coating. This information is crucial point to the understanding of the heterogeneous chemical and physical processes occurring at the surface. In particular we are interested in how the surfactants influence the reaction of NO₂ on NaCl crystals.

In the first part of the chapter, bulk fatty acids and their aqueous solutions deposited on model surfaces are investigated with the micro-Raman technique. The inter and intra-molecular order of the fatty acid chains can then be determined in different conditions and on different substrates. Palmitic, oleic and stearic acid are deposited and studied on perfectly flat mica(001) surfaces. The use of this mineral support is justified by the initial need to explore the behaviour of F.A. when dispersed on a perfectly flat mineral surface. Once we have understood the dynamics driving the surface dispersion and the molecular aggregation state of the fatty acids on these simplified systems a modified technique for obtaining reproducible coatings is defined.

In the second part the dip-coating technique is used to obtain reproducible fatty acid deposits on NaCl(100) monocrystals. The formed F.A. deposits are characterized with micro-Raman and AFM techniques, allowing us to couple the molecular information to a morphological evaluation of the formed coating.

Finally, the fatty acid-coated NaCl pellets are investigated after reaction with NO₂ at different humidities with the same surface techniques. The influence of FA on the NaCl/NO₂ interaction is assessed.

5.1 Raman reference spectra

5.1.1 Experimental conditions

The reference spectra of powdered palmitic, stearic and oleic sodium salts and their acid form (with the exception of oleic acid HC_{18:1}^{†††}) are collected using different excitation wavelengths. In tab. 5.1 the effect of the different wavelength on the quality of the collected spectra is summarized.

exciting laser wavelength	observation on the Raman spectra	conclusion
785 nm	poor S/N in the 3000cm ⁻¹ region	no
632 nm	good S/N	yes
514 nm	optimum S/N	yes, the best condition
266 nm	formation of amorphous carbon	no

Tab. 5.1 Effect of excitation wavelength on the quality of F.A. Raman spectra

The relative intensities or the shapes of the different Raman peaks are not influenced by the choice of the excitation laser beam, with the exception of the highly energetic UV excitation (266nm) where we observe the formation of amorphous carbon even at low powers (see ch. 3.4.1).

Good S/N are obtained after excitation at 632 and 514 nm, but the best performance is obtained with the excitation at 514 nm.

^{†††} Too much sensitive towards air oxidation and rapidly decomposing to NaC_{18:1} for being used in this study.

5.1.2 Raman spectra of the pure compounds

The characteristic peaks of the pure powdered compounds are assigned to the different internal vibrational modes of the molecules as suggested in previous work ([Kobayashi M. *et al.*, 1986], [Wong P. T. T. *et al.*, 1983]).

Fig. 5.1 shows a typical Raman spectrum of a bulk powdered FA, NaC_{18:1} in this example, where the C-H stretching at 3000cm⁻¹ is easily identified (zoom in fig. 5.2a). The C-C stretching (880-1100 cm⁻¹), twisting (~1300 cm⁻¹) and scissoring (~1430 cm⁻¹) modes are also readily observed, but with much lower Raman signal intensities (zoom in fig. 5.2b). For the unsaturated NaC_{18:1} we can also observe additional features due to the ethylenic group and particularly the $\nu_s(\text{C}=\text{C})$ at 1654 cm⁻¹ and the $\nu_s(\text{C}=\text{H})$ at 3006 cm⁻¹.

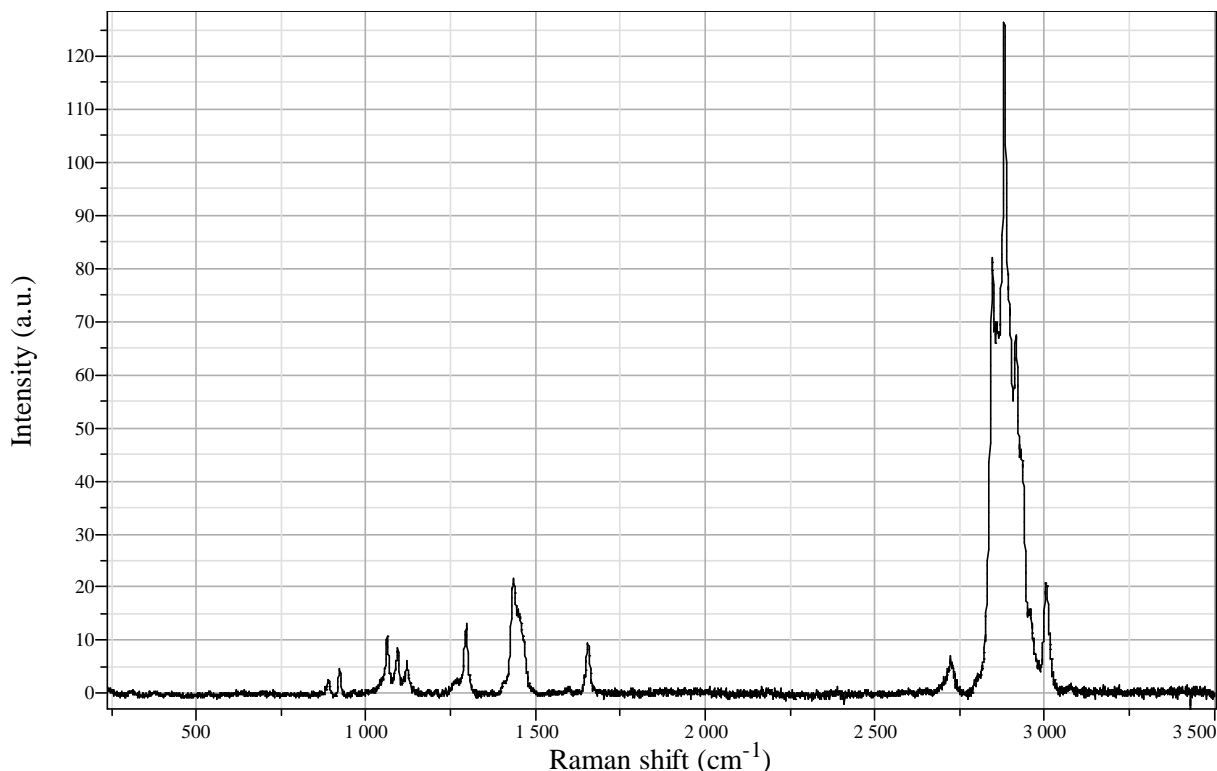


Fig. 5.1 The Raman spectrum of pure bulk NaC_{18:1} powder; $\lambda_{\text{exc}}=514$ nm.

Raman shift (cm ⁻¹)	Attribution
888	ν C-C
923	ν C-C
1063	ν_{as} C-C (trans)
1093	ν_s C-C (trans COO ⁻ side)
1121	ν_s C-C (trans CH ₃ side)
1295	t CH ₂
1433	δ CH ₂
1451	δ CH ₃
1655	ν_s C=C cis

Tab. 5.2 Attribution of the Raman peaks of the C-C region of bulk NaC_{18:1}.

Raman shift (cm ⁻¹)	Attribution
2846	ν_s CH ₂
2858	packing
2882	ν_{as} CH ₂
2898	2 δ (CH ₂) FR
2917	ν (α CH ₂)
2959	ν_{as} CH ₃
3006	ν (H-C=C)

Tab. 5.3 Attribution of the Raman peaks of the C-H region of bulk NaC_{18:1}.

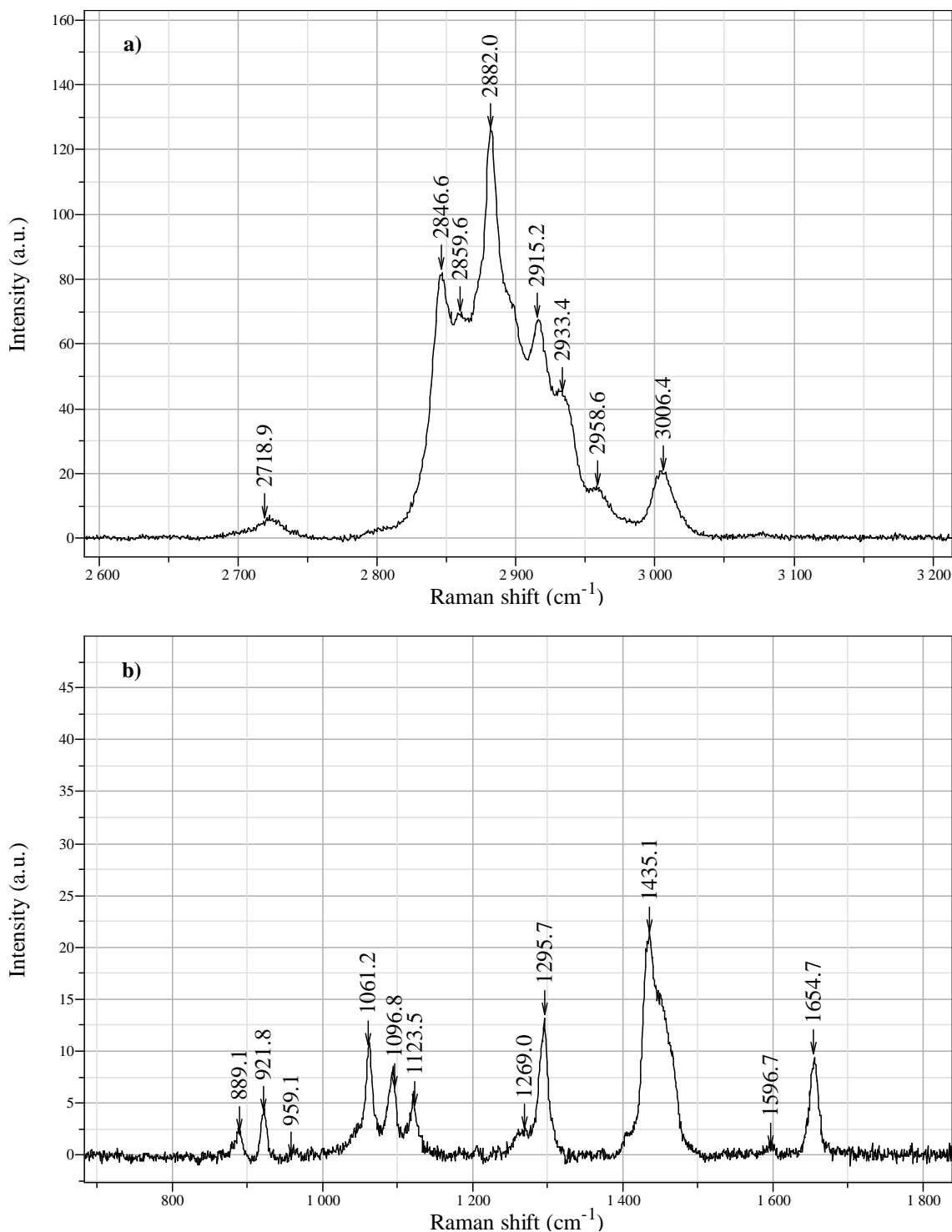


Fig. 5.2 Raman spectra of pure bulk NaC_{18:1} powder ($\lambda_{exc}=514$ nm): the C-H zone in **a**, and the C-C zone in **b**.

The spectra of the saturated fatty acids (palmitic and stearic) are similar to that described above, with the exception of the signatures typical of C=C and those characteristic of the asymmetry of the molecules induced by the presence of the double bond in the aliphatic chain.

5.1.3 Molecular aggregation state of fatty acids: micelle, gel and solid structures. Raman diagnostic.

As already seen in ch.2.2.1, between the main characteristics of amphiphiles molecules like fatty acids, there is the self-aggregation property, which can be expressed as differently ordered structures (i.e. micelles and membrane-like structures).

The position and width of some of the previously described Raman bands are sensitive to the conformation of the molecule. Tab. 5.4 shows the bands that principally indicate a high degree of chain packing order (taken from [Jores K., 2004]).

In particular:

- the symmetric and antisymmetric stretching of the methylene groups (at 2842 and 2880 cm^{-1}) are indicators for highly ordered chains;
- when the band at 2852 cm^{-1} occurs it indicates failing order.

Band position [cm^{-1}]	Assignment	“Diagnostic value”
between 800 to 900	CH_3 rocking	Sharp band indicates 3 consecutive trans
1060	C-C asymmetric stretching	Sharp band indicates 3 consecutive trans
1130	C-C symmetric stretching	Sharp band indicates 3 consecutive trans
1295	CH_2 twisting	
1420/1440/1465	CH_2 scissoring	Indicator of packing behavior
2842/2852	CH_2 symmetric stretching	Low band position and high intensity indicate trans
2880	CH_2 antisymmetric stretching	Sharp band indicates 3 consecutive trans

Tab. 5.4 Raman band position and assignment in a mixture of medium weight F.A. and triglycerides as in [Jores K., 2004].

In previous work [Wong P. T. T. et al., 1983] the authors measured the Raman spectra of bulk $\text{NaC}_{18:1}$ as a solid, aqueous coagel and micellar solution, so that the intermolecular order is also taken into account and is reflected in the Raman spectra (fig. 5.3).

The presence of a micellar organisation of the amphiphiles molecules is also indication in the spectra in the 800-1600 cm^{-1} region. The $\nu_s(\text{C}=\text{C})$ and $\nu_t(\text{C}-\text{C})$ intensity ratio (I at 1655 cm^{-1} / I at 1295 cm^{-1}) is 0.6 in the solid phase and >2 in the micellar phase.

All these indications can help us in identifying the different intra and inter-molecular organisation from the fatty acids Raman spectra.

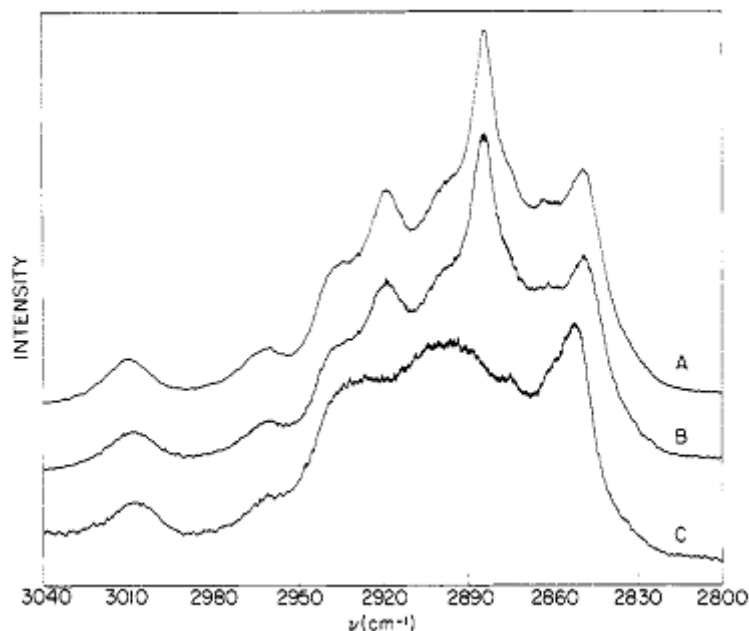


Fig. 5.3 Bulk Raman spectra in the $\nu_s(\text{C-H})$ region of $\text{NaC}_{18:1}$ as a solid (A), aqueous coagel (B), and micellar solution (C), as reported in [Wong P. T. T. et al., 1983].

5.2 Fatty Acids deposited on mica(001) surface from aqueous solution

Mica(001) surfaces are often used in the literature (such as in [Bailey A. I. et al., 1970], [Kajiyama T. et al., 1994], [Kajiyama T., Oishi, Y. et al., 1996], etc) because it is an almost perfect surface down to the atomic scale. This characteristic makes it an ideal support for surface analysis techniques such as AFM: any effect due to roughness or surface defects that could influence the rearrangement of the fatty acids can be avoided. In addition, the use of this mineral surface is also justified by atmospheric interest. Indeed mica is a phyllosilicate, which is present in the composition of mineral dust aerosols particles (i.e. [Usher C. R. et al., 2003]).

To explore the possible configurations of FAs on the surface, single drops (100 μL) of aqueous solution at the critical micellar concentration of palmitic, oleic and stearic acid (and their sodium salts) are deposited on mica(001) surfaces and left to dry under laboratory humidity and temperature conditions. For every FA used, optical images and Raman spectra and images are collected on different zones of the surface and at different degrees of water evaporation from the surface itself.

The acidic forms of FA have the tendency to precipitate on mica(001) as micro-crystal dispersed on the surface.

When the sodium salts of FA are used we observe with the optical microscope that the drying process leads to the precipitation or reorganisation of structures of different shape and size, as already briefly reported in ch. 3.2.2.

Some crystalline agglomerations precipitate and have shapes and Raman spectra similar to the pure bulk FA. Others assume more exotic configurations, forming much thinner films spread over the surface. An example of a dendritic growth is given in fig. 5.4, where we can see structures similar to the ones reported in [Iimura K.-i. et al., 2001] and deriving from spread monolayers of cis-unsaturated fatty acids on the water surface.



Fig. 5.4 100x optical image of $\text{NaC}_{18:1}$ thin deposits formed after drying of a CMC aqueous solution deposited on mica(001).

We focus here on the Raman signature of some of this second type of thin deposits. The collected Raman spectra characteristics show heterogeneous reorganisation of the molecules, with different features appearing in both the 3000 cm^{-1} and 1100 cm^{-1} zones. A close up the 3000 cm^{-1} region of a typical spectrum is reported in fig. 5.5. The spectrum is recorded at the centre of a circular deposit, whose optical image is reported as an insert in fig. 5.5. No particular differences are observed if the Raman spectrum is collected near to the borders of the deposit.

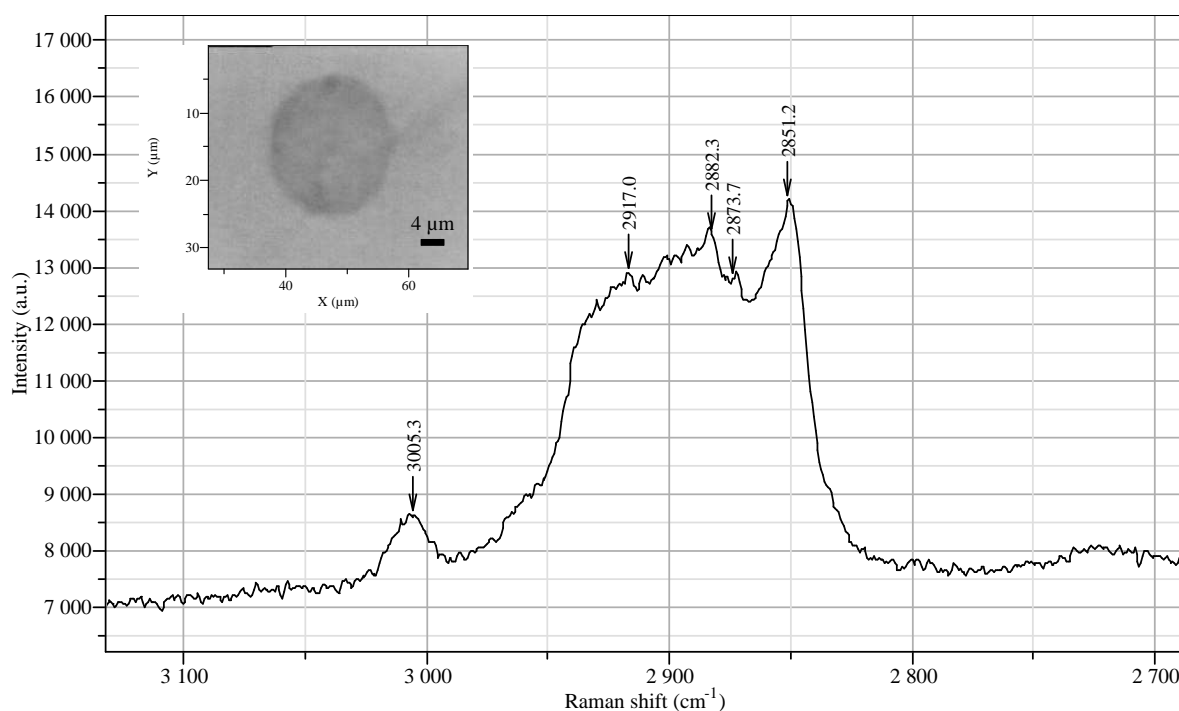


Fig. 5.5 Close up of the $\nu_s(\text{C-H})$ region of the micro-Raman spectrum of a $\text{NaC}_{18:1}$ deposit on mica (100) from a CMC aqueous solution. In the insert the optical image of the deposit on which the spectrum is collected.

We can compare this spectrum with the bulk compound spectrum reported in fig. 5.2a and we observe that the relative intensities of the different bands are not the same. In particular in the drying drop deposit of fig. 5.5 the band at 2882 cm^{-1} is not very pronounced compared to the one recorded on the powdered sample. Furthermore, the CH_2 symmetric stretching is mainly expressed at 2852 cm^{-1} , instead of 2846 cm^{-1} . Both these spectral characteristics indicate a failed internal order of the hydrophobic chains, as previously discussed.

We can also compare this spectrum with the spectra reported in [Wong P. T. T. et al., 1983]: we can observe a strong similarity to the micellar solution spectral features in the 2800-3000 cm^{-1} zone of fig. 5.3C.

The presence of micellar reorganisation is further confirmed, by observing a ration of 2 between the intensities of the 1655 cm^{-1} and 1295 cm^{-1} bands.

By following the progressive drying of this deposit under laboratory temperature and humidity conditions, after 24h we observe a stronger concentration of fatty acids in the central part as can be seen in the optical and Raman images in fig. 5.6a and b respectively. Regarding the molecular order/disorder, in fig. 5.6c we report the Raman image reconstructed on the intensity of the 1655/ 1295 cm^{-1} band intensity ratio. The regions in white show where the ratio is > 2 . The heterogeneous nature of the deposit is then expressed also in a different spatial distribution of the intermolecular organisation. In the central part the $\text{NaC}_{18:1}$ deposit is thicker and the hydrophobic chains are packed in an orderly way. Near to the border of the deposit there is a thin layer of micellar solution instead, persisting even 24h after the solution has been deposited on the surface.

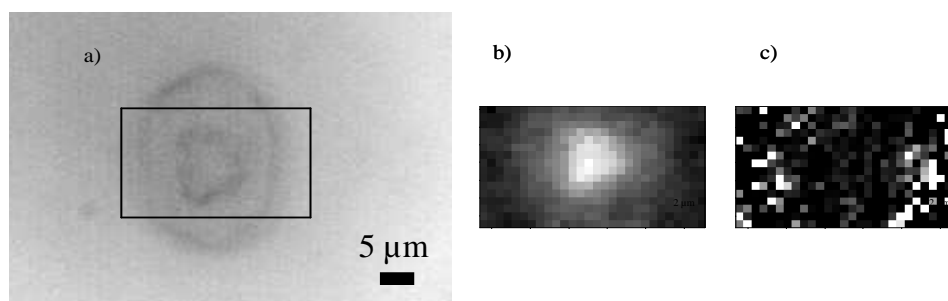


Fig. 5.6 Optical (a) and Raman images recorded on a $\text{NaC}_{18:1}$ agglomeration 24 h after deposition on mica(001). In (b) the image is reconstructed by integrating the 1655 cm^{-1} $\nu_s(\text{C}=\text{C})$ band, in (c) the image reports the pixels where the 1655/1295 cm^{-1} intensity ratio (index of micelle presence) is > 2 .

Similar observation can be made when the drop of NaC_{16} aqueous solution (at CMC) is deposited on mica and left to dry in the laboratory atmosphere.

In fig. 5.7 the evolution over 24h of the Raman spectra of a palmitate thin deposit on a mica(001) surface is reported. The spectra are recorded after 6, 8 and 24 hours from the drop being deposited on the surface. For comparison, the spectrum of the pure powdered NaC_{16} is shown in green.

Once again we notice a progressive evolution of the internal order of the chains packing, starting from a micellar rearrangement going towards a coagel. We can confirm that within the first 8h the evaporation of the solvent is not complete and that the organisation of the F.A. into micelles is preserved. At longer times the solution does not become a crystalline solid, but instead a coagel structure. The typical micellar features are lost (also in the C-C stretching region), but the highly ordered chain packing is not present with its characteristic intense band at 2882 cm^{-1} .

Unfortunately we observed that the surface dispersion of this thin micellar films formed by a drop drying is sensibly influenced by many factors that we cannot control, which leads to an intrinsic difficulty in obtaining a reproducible and homogeneous distribution of FA on the mineral surface. Moreover, we can never avoid having the concomitant precipitation of FA crystals caused by progressive concentration of the solution.

In addition, this procedure is not transferable to the $\text{NaCl}(100)$ surface: depositing even a small volume of FA aqueous solution on the (100) surface of a NaCl monocystal induces a drastic surface reconstruction after its rapid solvation. The salt surface is extremely wettable therefore the solutions immediately spreads over the macroscopic crystal, covering the entire

ionic surface and reaching the underlying glass support. Here, for the salting-out effect, the FA present in the micellar form immediately precipitate in a crystalline form out of the borders of the NaCl monocrystal. Raman microspectrometry and ATR analysis confirm the absence of any organic coating on the NaCl crystal, and identify the organic molecules in the outer layer of micro-crystals.

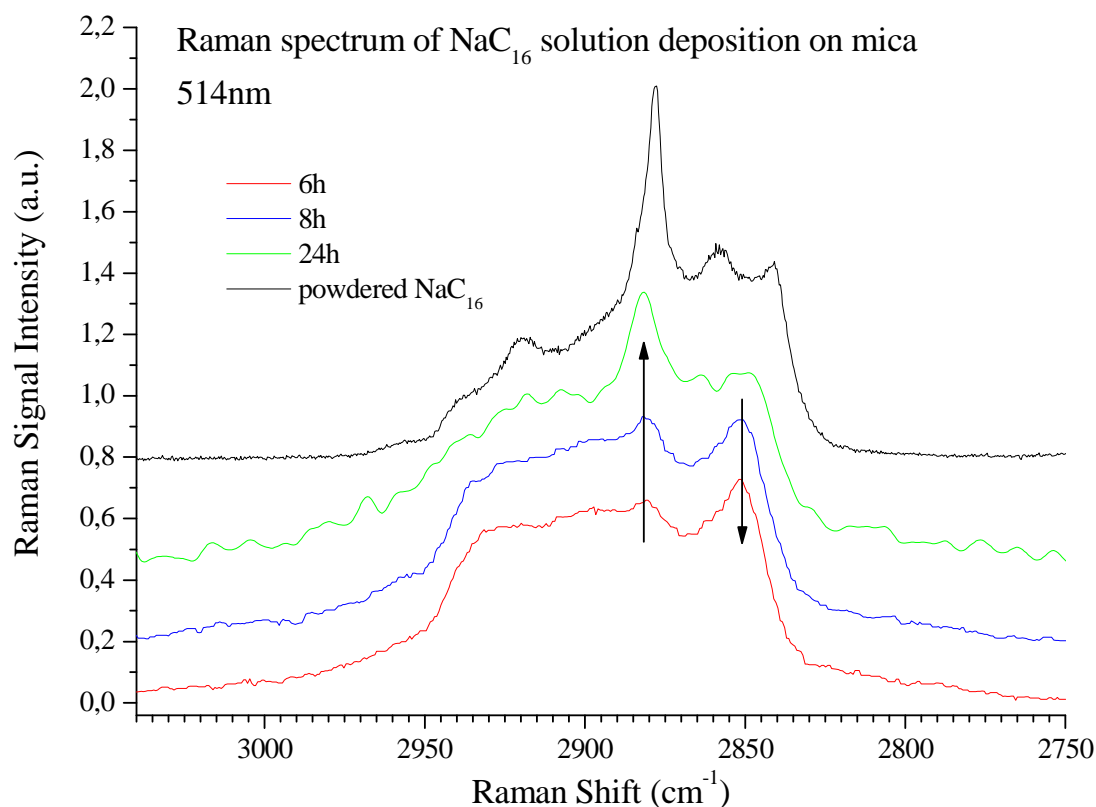


Fig. 5.7 Time evolution of the $\nu_s(\text{C-H})$ region of the micro-Raman spectrum collected over a NaC_{16} deposit on mica(001) from aqueous CMC solution. The spectra collected after 6 h (in red), 8 h (blue), 24 h (green) are reported. In black the powder reference spectrum is plotted for comparison.

5.3 Fatty acids deposited on NaCl from ethanol solution

The transfer onto a macroscopic surface of a micellar solution of fatty acids can be obtained through the use of the dip-coating technique (see ch. 3.2.2). This method can solve the problem of the precipitation of large crystals onto the surface, because the quantity of solution transferred is very low. Moreover this transfer is accurately reproducible as the speed of extraction is very accurately controlled via a motorized system. The solvent evaporation conditions themselves are relatively constant inside the instrument cage and complete the intrinsic reproducibility of this surface treatment technique.

The main limitation of the available dip-coater was the impossibility of modifying the immersion duration, set at 30 seconds. For such long time the use an aqueous solvent is excluded and substituted by absolute ethanol, as a solvent of FA and a non solvent of NaCl.

5.3.1 Fatty acids on NaCl(100) monocrystals

NaCl(100) 10x10x1 mm monocrystals were covered with F.A. with the method briefly described above and without undergoing significant surface reconstruction. Fig. 5.8 shows an

optical image of the coated surface, where the polishing defaults on the surface are still visible.

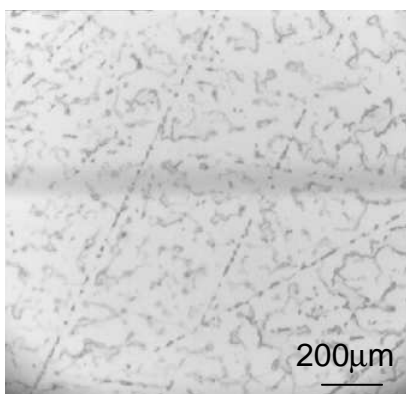


Fig. 5.8 Optical image of the NaCl(100) covered in NaC_{18:1} via dip-coating

From Raman microspectrometry analysis we obtain images showing a heterogeneous distribution of the fatty acid on the surface. In fig. 5.9 for example, the optical image (a) shows the presence of structures of different thickness which do not fully cover the surface. These structures are formed from NaC_{18:1}, as verified by the Raman microspectrometry. The intensities of the spectra reported in fig. 5.9b and c confirm an inhomogeneous dispersion of the fatty acid on the surface. The zones where the CH stretching mode is quite intense (in the red Raman image of fig. 5.9b) correspond to the darker spots of the optical image; thinner layers of oleate, in green in fig. 5.9c, surround them and perfectly reproduce the shape of the optically observed deposit. The low S/N ratio of the Raman spectra on these very thin deposits do not allow us to give a detailed description of the molecular arrangement.

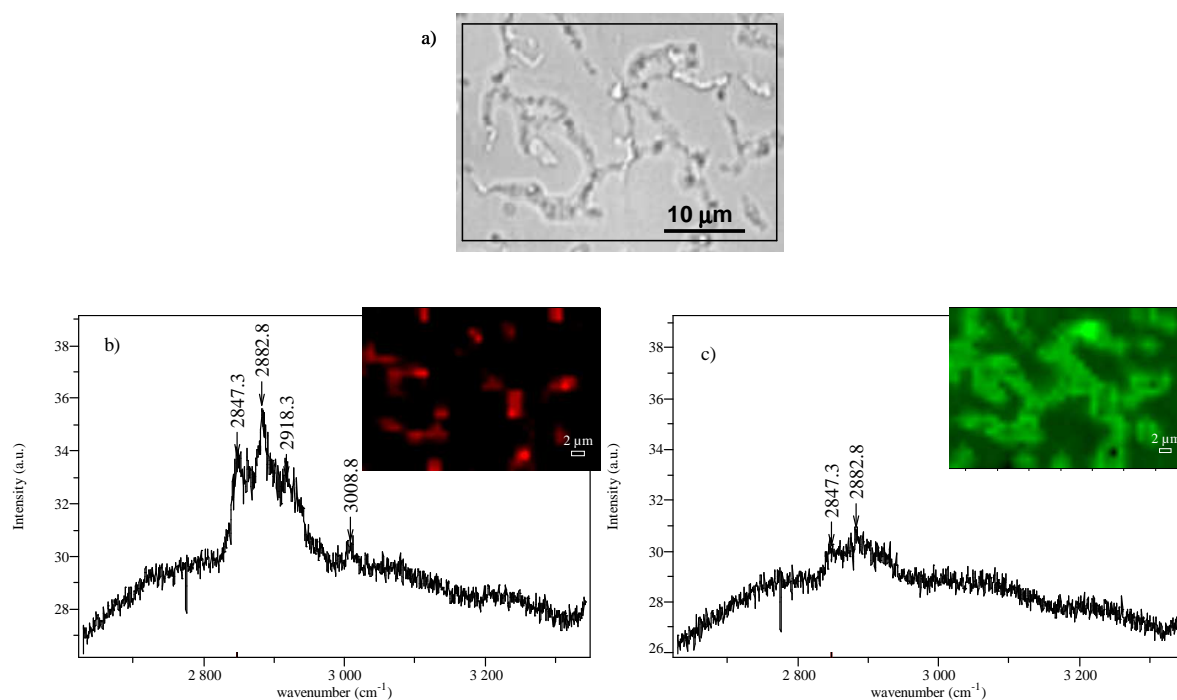


Fig. 5.9 Optical (a) and Raman images of NaCl(100) after dip-coating with CMC solution of NaC_{18:1} in ethanol. The Raman images, collected after excitation at 632 nm, represent the different amounts of fatty acid deposited on the surface. The red zones (b) correspond to the more intense organic signal, the green ones (c) the less intense $\nu(\text{CH})$ intensities.

On NaCl(100) monocrystals treated via dip-coating the fatty acid is not homogeneously distributed over the surface but the coating is easily reproducible and the precipitation of large organic crystals is absent.

5.3.2 Fatty acids on NaCl pellets

We apply the same dip-coating technique to the NaCl pellets that are used for the kinetic experiments. We explore by AFM the surface characteristics and the organic deposit morphology^{§§§}. In fig. 5.10 there is a comparison between the AFM images recorded on non-coated and coated NaCl pellets. The roughness^{****} R of the sintered pellet before any treatment is of the order of 100-300 nm. After dip-coating it increases to 650 nm, and (fig. 5.10c) in some zones particularly affected by surface reconstruction, to more than 6000 nm (fig. 5.10b).

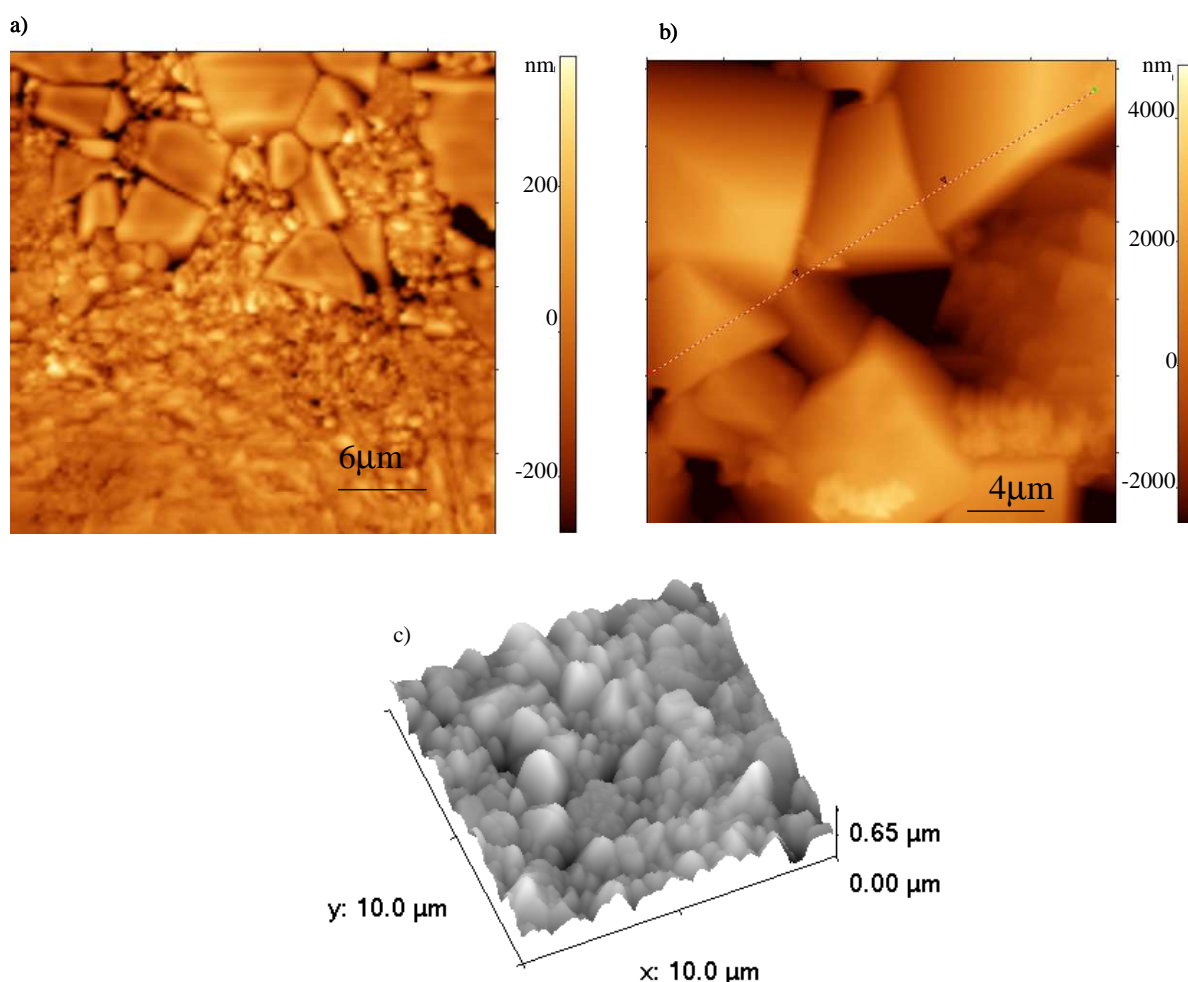


Fig. 5.10 AFM images of NaCl pellets before (a) and after (b-c) dip-coating in an ethanol solution of F.A. NaCl recrystallisation can originate regular-shape micrometric crystals like in (b) and smaller and with less defined geometry hillocks in zones of lower roughness, like in (c)^{††††}.

^{§§§} The AFM images collected during a demonstration of AIST-NT® with a SmartSPM™ 1000 microscope working in true non-contact mode can be seen in orange.

^{****} Roughness R is defined as the vertical deviation of the real surface from its ideal form. In this work it is quantified by the maximum peak to valley distance measured on the surface.

^{††††} Images recorded in the IEMN facilities with the kind supervision of PhD M. Marczak.

The pellets seem to be much more sensitive towards surface reconstruction than monocrystals. For this reason we decided that in the reactivity measurements to compare F.A.-coated pellets to NaCl pellets which are dipped into ethanol. In this way we can take into account this surface reconstruction effect induced by residual water in the non-perfectly anhydrous ethanol.

The transfer of fatty acids over the pellets is confirmed by Raman microspectrometry. We can detect the C-H stretching signal in the 3000 cm^{-1} zone everywhere on the surface.

The fatty acids precipitated on the surface have very different dimensions and morphological characteristics: micrometric agglomerations are found near to nanometric structures. We report here some examples of NaCl pellets coated with $\text{NaC}_{18:1}$.

In fig. 5.11a there is the topography of a micrometric-size oleate agglomeration. It is almost 350 nm thick and presents an irregular shape, similar to the non-cubic structures present in the right part of fig. 5.10b.

We present in fig. 5.11b a secondary electron image collected on dry oleate aerosol particles taken from [Najera J. J., 2007]. In his work the author generates the purely organic aerosol from an oleate aqueous solution at concentrations higher than the CMC value.

The particles formed in this way are depicted as spherical aggregates of micelles which developed a porous structure during the solvent evaporation.

Owing to the strong similarities with the morphology of the deposit that we observe on the NaCl surface after drying of the CMC oleate solution, we can imagine that our micrometric-size deposits are also formed of aggregation of micelles.

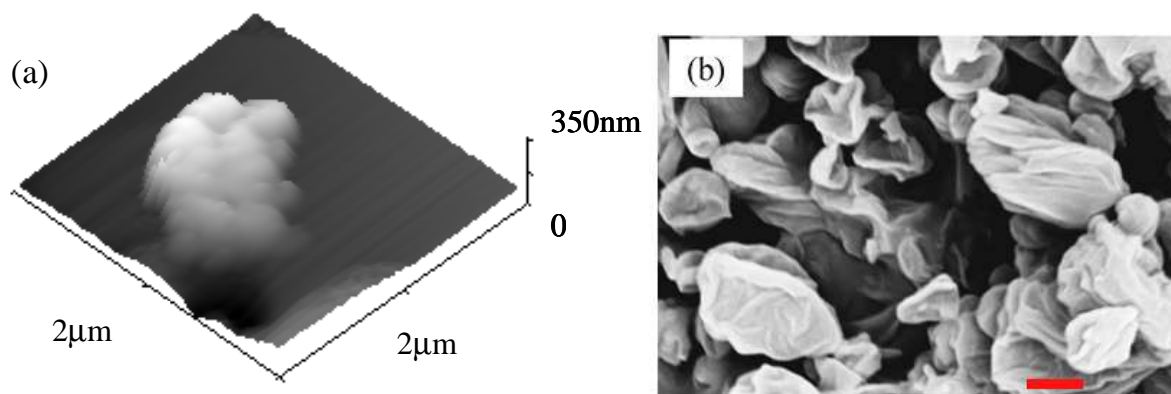


Fig. 5.11 (a) An AFM 3D image of a $\text{NaC}_{18:1}$ agglomeration on NaCl pellet. (b) Scanning electronic microscopy image of collected dry oleate aerosol taken from [Najera J. J., 2007]. The red bar denotes $1\text{ }\mu\text{m}$.

This deposit and similar ones correspond to the spots giving the more intense organic signal in the Raman images. All other zones of the surface present structures that are much thinner and which can explain also the very weak intensities in the Raman spectra.

On relatively flat crystals like the ones shown in fig. 5.12, we can find FA with completely different morphologies.

Filamentous structures lay on this kind of surface and intertwine with each other, as can be seen in the AFM image of fig. 5.13. The organic stripes are about 10-15 nm thick, and can reach no more than 30 nm where they mutually overlap. These characteristics can lead back to the fusing oriented crystalline domains described in ch.2.2.1. Hydrophobic chains are aligned and tightly packed forming a compact film.

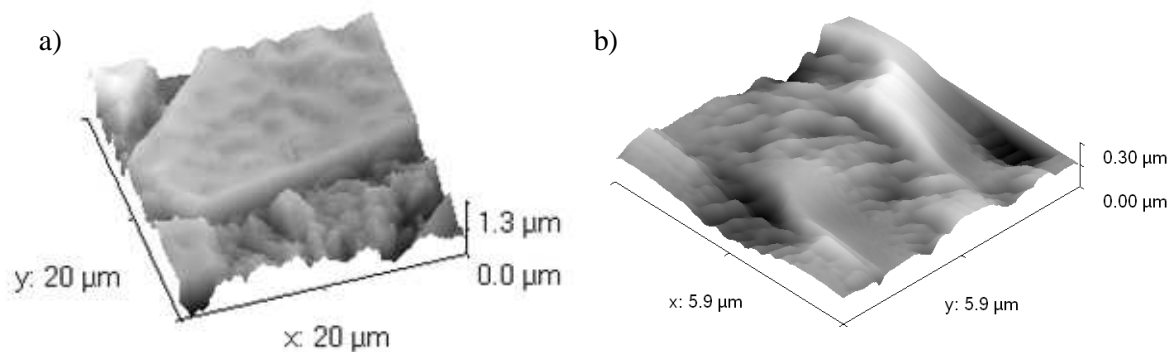


Fig. 5.12 a) AFM image of a flat NaCl crystal whose surface shows a wave-like reconstruction. In b) a zoom on the topmost NaCl surface^{††††}.

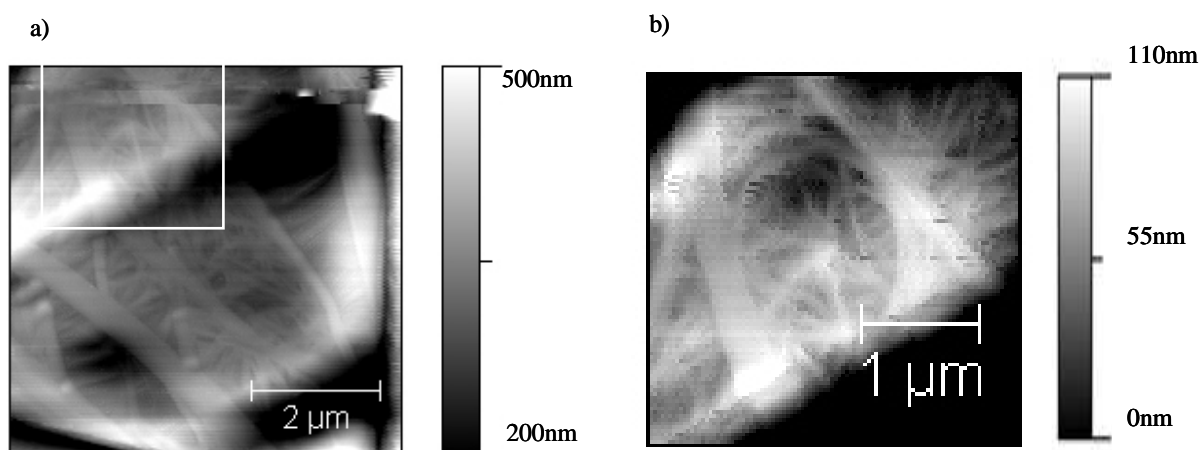


Fig. 5.13 a) AFM 2D image of NaC_{18:1} filamentous deposits over a NaCl pellet. In b) a more detailed image is recorded on the upper-left part of the first image.

In other zones even smaller structures are registered. AFM images provide evidence of the presence of nano-deposits with homogeneous characteristics: they are circular deposit of less than 3 nm thickness and 60 nm of diameter. They are reproduced in fig. 5.14a, and a typical profile is shown in fig 5.14c.

Always from [Najera J. J., 2007] we know that the characteristic length of the hydrophobic section of oleate molecules is 2.3 nm, which is exactly the thickness of the observed nanometric deposit. We can then suppose that they are the print of originally spherical micelles that misshaped into flat deposits once the solvent evaporated. The morphological information suggests that the oleate molecules are compact and are in vertical position on the surface, tilting from the vertical near the borders (as indicated by the halo surrounding the spots in the phase image 5.14b).

^{††††} Both images are recorded in the IEMN facilities with the kind supervision of PhD. M. Marczak.

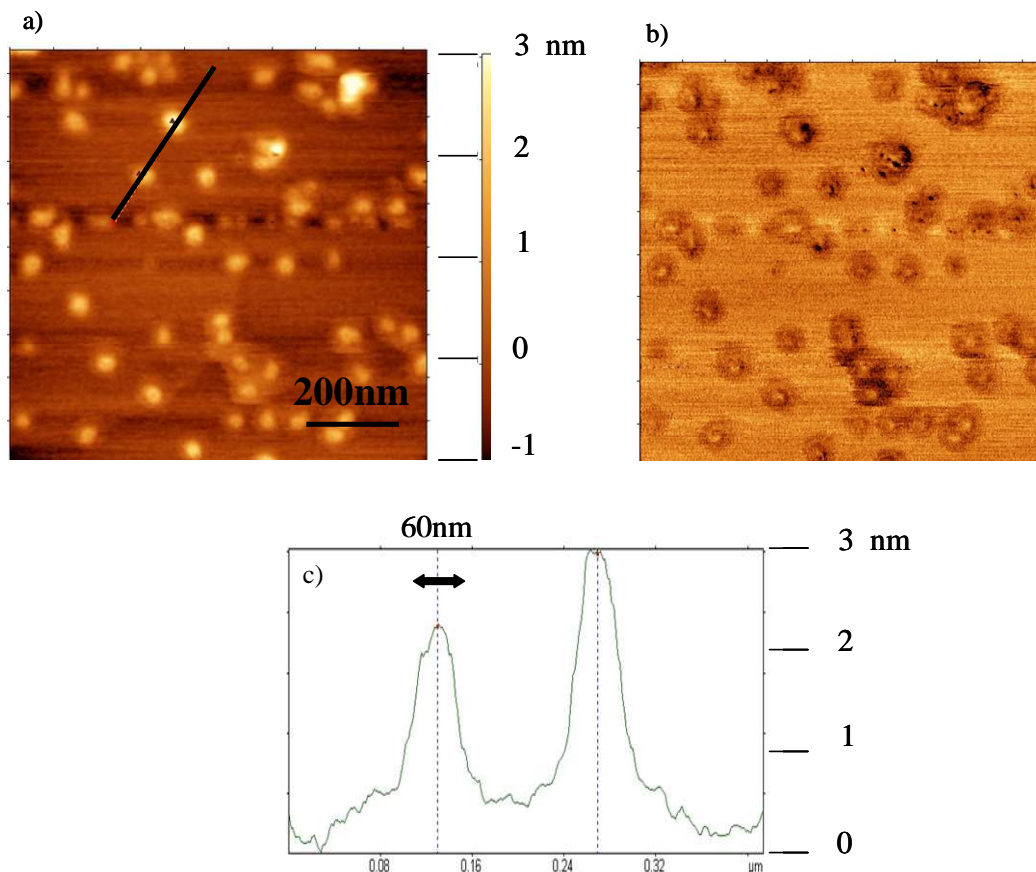


Fig. 5.14 (a) AFM image and (b) phase image of a 800x800 nm zone of NaC_{18:1}-coated NaCl(100). The presence of some contrast in the phase image indicates the presence of a different material compared to the surrounding NaCl. The vertical profile along the black line in (a) is given in (c).

Concluding, the use of the dip-coating technique for depositing fatty acids on a macroscopic NaCl surface is effective. The coatings formed are not ideal monolayers and do not show a homogeneous distribution of organic matter over the surface but instead show the presence of an incomplete coating constituted of structures with different characteristics. They are the result of the concentration of the fatty acid solution increasing during the solvent evaporation. The different agglomerations of amphiphiles which can be generated reflect the tendency of these insoluble molecules to self-aggregate instead of forming a uniformly dispersed mono or multi-layers.

We observe the fatty acid rearrange themselves on the surface into:

- nanometric islands less than 3 nm thick, probably deriving from micelle-like structures present in the bulk solution;
- compact filamentous structures approximately 15 nm thick, probably with origin in the fusing crystalline multilayers present at the air-solvent interface;
- aggregations of hundreds of nm thick, probably deriving from the aggregation of micelles.

The presence of all these different forms is justified as the solvent drying process can be quite different in different zones of the pellet and by the different structures that can intrinsically exist in a CMC solution and at the solution-air interface.

This phenomenon can reasonably reproduce the natural process of the marine aerosol droplets drying, in which the surfactant-water mixture can form a liquid crystalline phase at low humidity.

All the phase diagram of the fatty acid in a given temperature range can then be explored, with the appearance of different crystalline form as previously reported in ch.2.2.1.

5.4 Fatty acids-coated NaCl pellets exposed to NO₂ at different humidity conditions

Fatty acid coated NaCl pellets were exposed to NO₂ for 30 minutes at different degree of moisture (0-80%). NO₂ concentrations used are both $(8.4 \pm 0.3) \times 10^{15}$ molec cm⁻³ and $(8.7 \pm 0.3) \times 10^{16}$ molec cm⁻³.

All analysed tablets reveal, under optical microscope and Raman microspectrometer, some common characteristics, regardless the RH and the coating fatty acid.

An organic signal is recorded everywhere on the surface, confirming the presence of the coating after reaction.

Nitrate spatial distribution depends on the initial NaCl surface status and can be summarised as in tab. 5.5, and detailed in the following paragraphs.

NaCl surface characteristics	Fatty acid coating characteristics	Detected NaNO ₃ after reaction	Ref. image(s)
Strongly reconstructed: R > 2-3 μm [fig. 5.10b]	Micrometric crystal (micelle aggregate precipitation)	Yes, also in correspondence of the organic crystals	Fig. 5.15 Fig. 5.16
Small crystals R < 0.5 μm [fig. 5.10c]	?	Yes, very intense Raman signal	Fig. 5.17
Almost flat, wave-like reconstruction [fig. 5.12]	Oriented crystalline domains	No	Fig. 5.17

Tab. 5.5 Relationship between NaCl surface morphology, fatty acid coating characteristics and nitrate which is detected after NO₂ exposure.

5.4.1 Oleate coated NaCl exposed to NO₂ at RH=0%

In zones showing high NaCl reconstruction after dip-coating, nitrates are mainly distributed in the same zones as fatty acids. This can be observed e.g. in fig. 5.15, where optical and Raman images are collected on an oleate-coated pellet exposed to NO₂ at RH=0%. The solid nitrate distribution (in green, image b) can be compared to the distribution of the organic signal (red image, in c). The presence of micrometric crystalline aggregations of fatty acid does not prevent the salt reaction.

This situation is systematically observed over every micrometric fatty acid crystal.

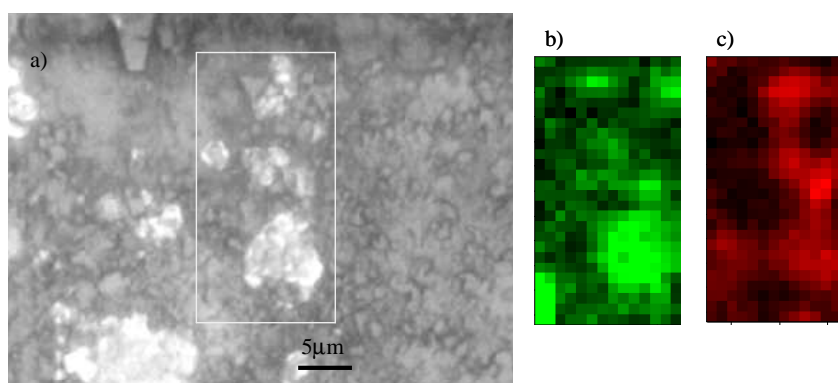


Fig. 5.15 NaC_{18:1}/NaCl pellet exposed to NO₂ at RH=0%: a) optical image and the corresponding Raman images reconstructed on b) solid nitrate (1068 cm⁻¹) and c) FA (CH stretching in the 3000 cm⁻¹ zone).

5.4.2 Oleate coated NaCl exposed to NO₂ at RH=55%

Similarly to the previous case, in fig. 5.16 we show the optical and Raman images of the same kind of tablet (oleate/NaCl) exposed to higher RH (55%). Solid NaNO₃ signal is collected from every pixel of the image, but with different intensities. The most intense signal, revealing the highest surface concentration of product, is represented in image b with the blue colour. In magenta there is the distribution of less intense solid NaNO₃ signal. In green the strong organic signal, coupled with weak nitrate too.

The strongest nitrate intensities correspond to some grain borders, where probably more defects are present on the NaCl surface, therefore enhancing the surface reactivity towards NO₂. On the rest of the surface the nitrate signal distribution is quite homogeneous.

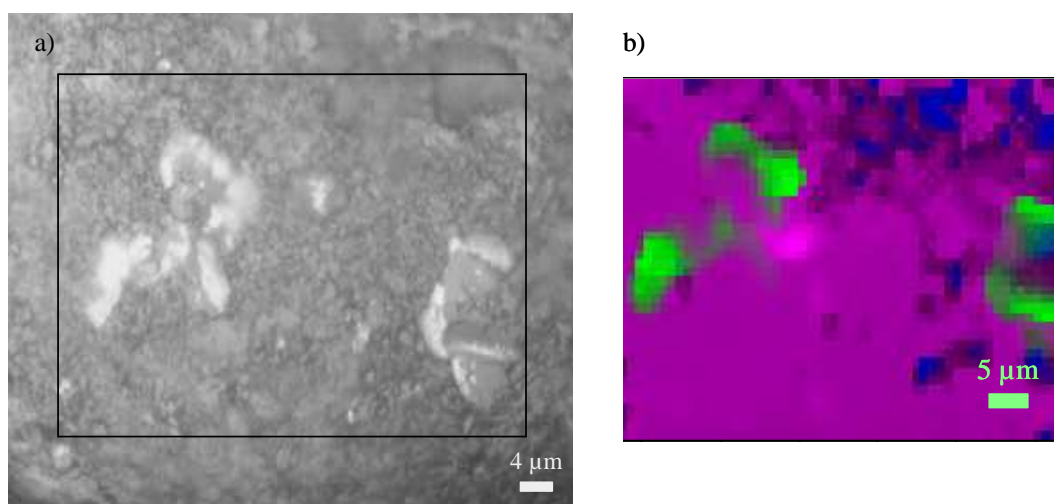


Fig. 5.16 NaC_{18:1}/NaCl pellet exposed to NO₂ at RH=55%: **a)** optical image (100x) and the corresponding **b)** Raman image. Nitrate signal is recorded in every pixel. Green colour indicates the presence of organic signal, the magenta the low intensity nitrate, in blue strong solid nitrate Raman signal.

We cannot detect any nitrate signal on zones where relatively flat crystals are present. In fig. 5.17 the black pixels of image b indicate the absence of product in correspondence of these zones. We remind that we detected quite compact filamentous deposits of fatty acids on morphologically similar zones (fig. 5.12). These fatty acid configuration seem then to be effective in preventing NaCl reactivity towards NO₂ even at RH=55%.

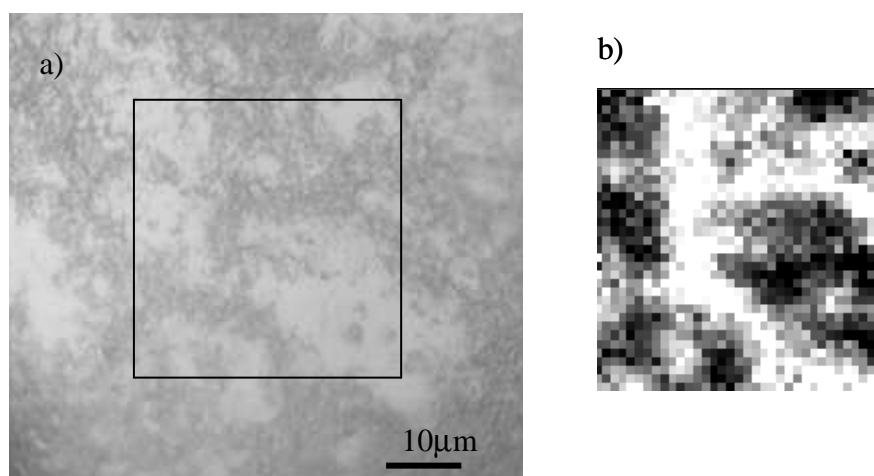


Fig. 5.17 NaC_{18:1}/NaCl pellet exposed to NO₂ at RH=55%: **a)** optical (100x) image and **b)** Raman image reconstructed by integrating the solid nitrate peak at 1068 cm⁻¹ (white pixels).

5.4.3 Palmitate coated NaCl exposed to NO₂ at RH>75%

We report here an example of insoluble fatty acid-coated surface which reacted at high RH. At this value of moisture the topmost layer of the surface should be solvated. What we observe after NO₂ exposure is a further surface reorganisation.

Relatively flat crystals maintained their morphology, whilst the zones with small NaCl crystals reorganised to give more regular terrace zones (fig. 5.18).

Organic CH stretching signal can be recorded all over the surface; in blue (fig. 5.18b) we report an example of spectrum recorded on the large terrace, indicated by a blue arrow.

Nitrate signal (in blue, fig. 5.18b) is only recorded where we see the brighter crystals, indicated by the red arrow.

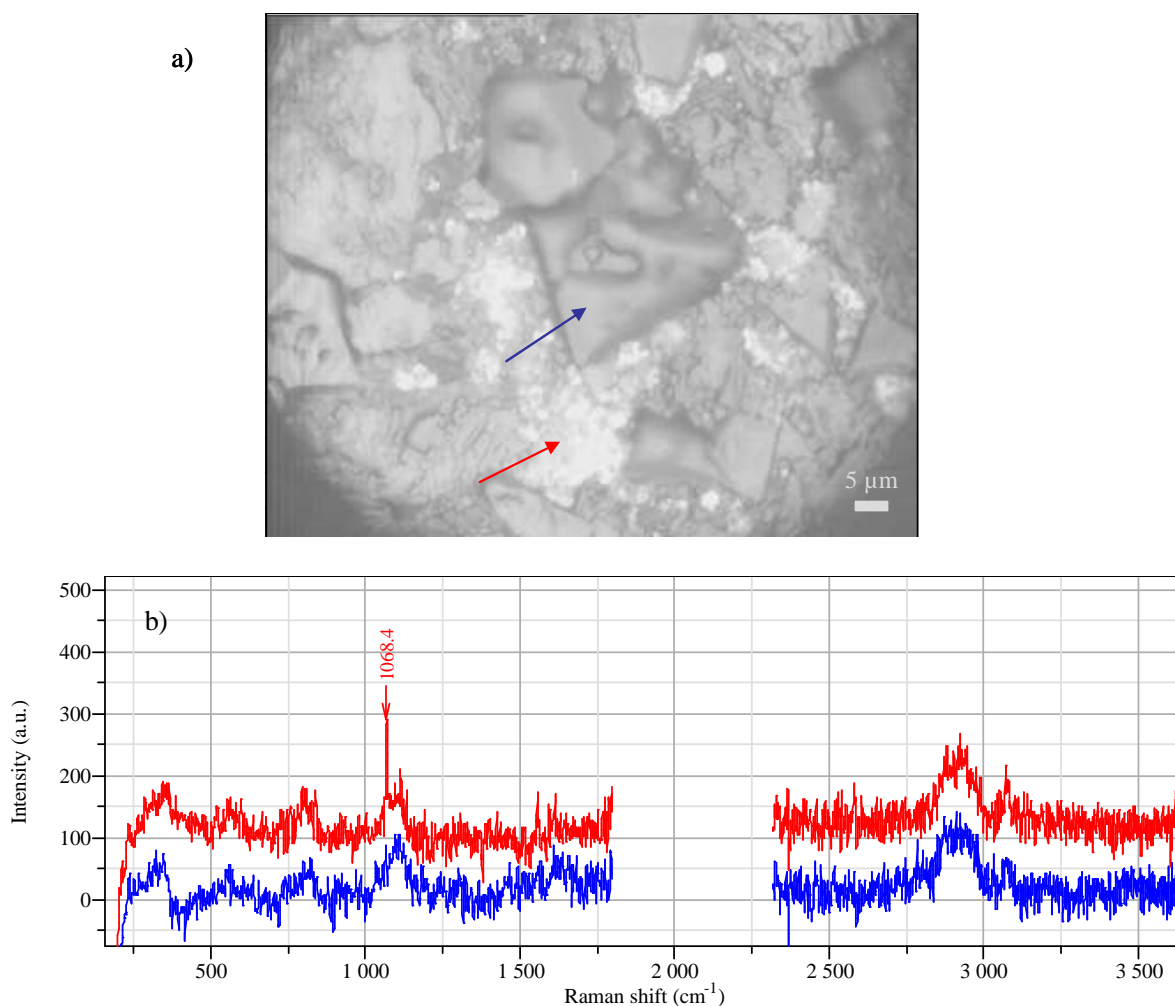


Fig. 5.18 a) Optical image of NaC₁₆/NaCl pellet exposed to NO₂ at RH=80%. In b) the Raman spectra collected on the surface. In **red** the spectrum collected in correspondence of the bright crystals where nitrate and fatty acid bands are detectable. In **blue** a spectrum collected over the central flat NaCl crystal, where only the organic signal is detected.

We already observed NaNO₃ trapped under the surface in the case of uncoated NaCl exposed at high humidity (ch. 4.3.3). We find the same phenomenon on coated pellets. In fig. 5.19 there are the optical images of NaC₁₆/NaCl pellet exposed to NO₂ at RH=75%: in a) the image is focused on the surface, where some imperfect grain joints are visible as darker spots. In b) the focus is set at 8 μm under the surface level and it shows the presence of some material with optical properties different from the surrounding NaCl matrix.

Raman spectra are collected on (d) and beneath (c) the surface and both reveal the presence of solid NaNO₃, probably formed after the diffusion of NO₂ into the surface cracks.

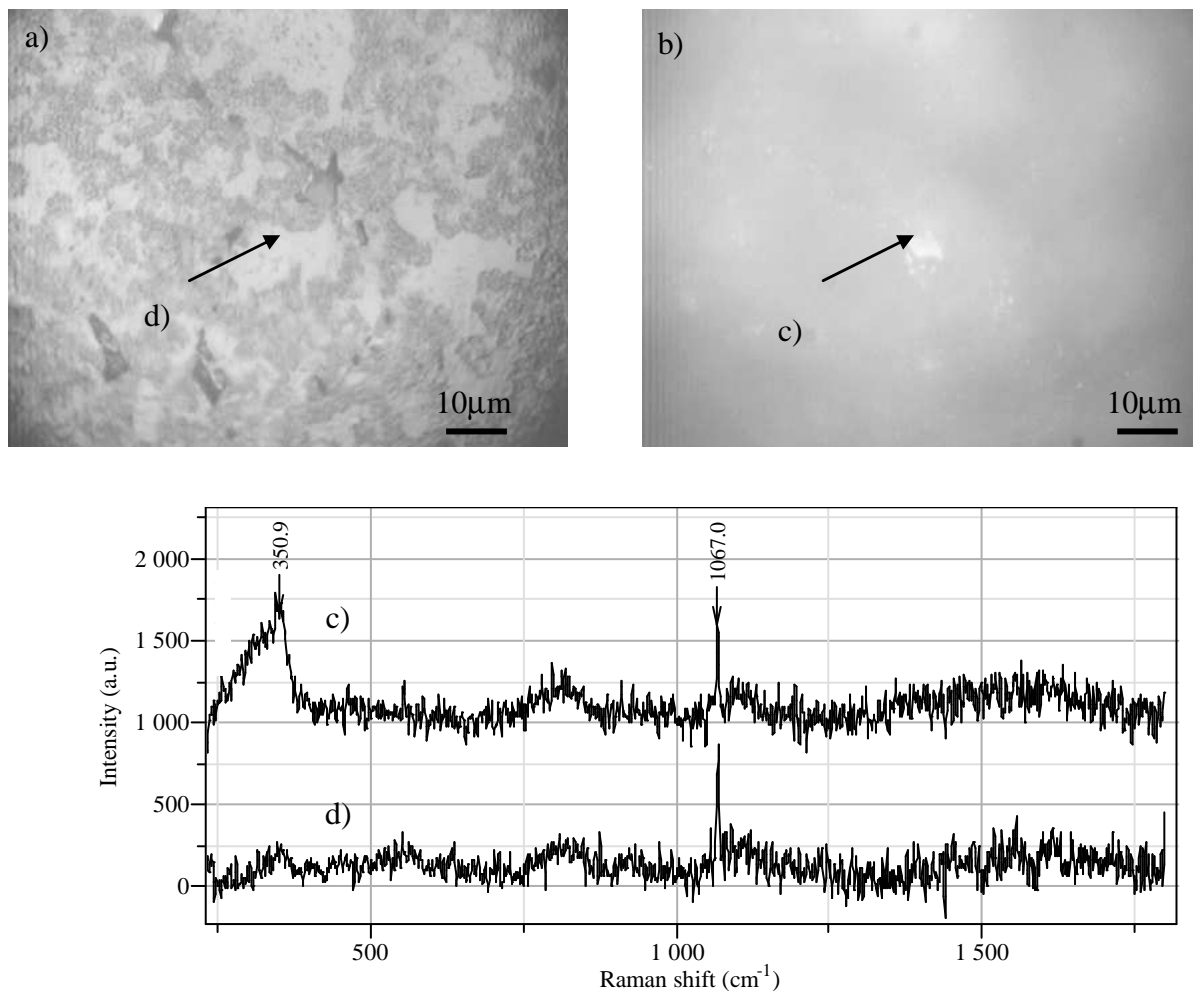


Fig. 5.19 NaCl₁₆/NaCl pellet exposed to NO₂ at RH=75%. **a)** optical (100x) image of the surface, **b)** optical image 8 μm under the surface. Raman spectra of solid nitrate are recorded on the surface (**d**) and under it (**c**).

5.5 Concluding remarks and atmospheric implications

The surface coating of (100) single crystals and of polycrystalline pellets of NaCl with sodium salts of palmitic, stearic and oleic fatty acids was carried out by dip-coating technique in an alcoholic solvent. The sodium salt of fatty acids was chosen with respect to the pH of sea water (pH~8). Unfortunately, the ethanol solvent was required because it avoids the dramatic reconstruction of the NaCl surface that occurred when an aqueous solution was used. AFM and Raman imaging provides evidence of a heterogeneous FA layer on the NaCl (100) substrate. Nanometric-size deposits, probably originating from solution FA micelles, precipitated on the NaCl surface. In addition, compact filamentous deposit probably constituted of tightly packed molecules in oriented crystalline domains also lay on the surface. These findings are reproducible but do not efficiently protect the NaCl surface from NO₂ uptake. The bare areas of unprotected NaCl are available to NaNO₃ formation after exposure to NO₂ under moisture.

The difference in surface reconstruction and fatty acid coating behaviour on polycrystalline vs. single-crystal faces of NaCl may be rationalized by the presence of specific surface defects on the former: grain junctions can readily dissolve in presence of water traces in the ethanol solvent so that surface roughness increases significantly. The heterogeneous coating could weakly hinder the deliquescence and the chemical attack by NO₂ or N₂O₄. The grain borders present in pellets probably promotes the heterogeneous chemical process on pellets. The effect of humidity on the reactivity of NO₂ is analogous to the effect reported in chapter 4

for uncoated substrates: the surface reorganizes in the presence of at least a monolayer of water and fresh NaCl sites are available to react.

A comparison with sea salt aerosol particles collected in marine and NO₂ polluted air masses from many areas of the world provides some suitable convergence. Many studies have shown a significant chloride deficit in aged sea salt aerosol (30-80%) and large amounts of NaNO₃ when compared to bulk seawater. This has been attributed to reactions in the marine boundary layer with inorganic nitrogen species. Single particle analysis of sea salt aerosol particles collected with aerodynamic selective sizing by cascade impaction in marine area has improved the understanding of the reactivity and transport of sea salt particles.

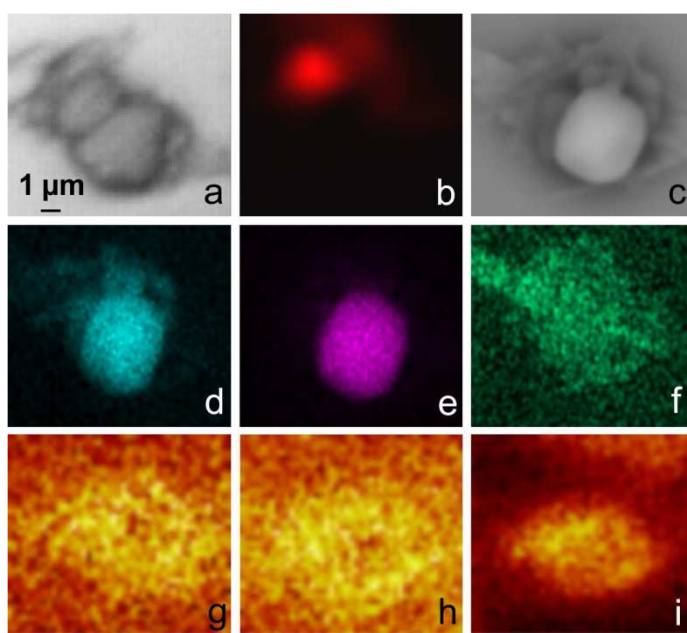


Fig 5.20 Single sea-salt particle of the 2.5-10 μm size fraction collected at Dunkerque, France. **a)** optical image RH~60%; **b)** NaNO₃ Raman image RH~60%; **c)** secondary electron image RH~10%; **d)** Na X-ray image; **e)** Cl X-ray image; **f)** S X-ray image; **g)** C₂H₅⁺ (m/z 29) secondary ion image generated by Ga⁺ primary ion bombardment in ToF-SIMS RH~0% ; **h)** C₃H₅⁺ (m/z 41); **i)** Mg⁺ (m/z 24).

The images in figure 5.20 taken from a recent PhD thesis devoted to field studies of sea salt aerosol particles indicate the complex internal mixing state of single sea salt particle [Rimetz-Planchon J., 2007]. Particularly, Raman imaging, atomic force microscopy (AFM) combined with Energy Dispersive Electron Probe X-ray MicroAnalysis (ED-EPMA) coupled with Scanning Electron Microscopy (SEM) and Time-of-flight secondary ion mass spectrometry (ToF-SIMS) have proven to be especially powerful techniques to demonstrate that a typical single sea salt particle originated from marine air mass with a high NO_x concentration (~ 60 μg m⁻³) contains an internal mixture of deliquescent NaCl crystal, NaNO₃ and an organic coating. The considerable fraction of NaNO₃ as an internal mixture with aged sea salt particles comes from efficient scavenging of reactive nitrogen species under high humidity despite organic coating of the aerosol particle. While the laboratory experimental models are quite far from the complex reality of the atmosphere some analogies can be done with true sea salt: NaNO₃ has grown from the NaCl crystal under high relative humidity despite the presence of an organic coating; this inefficient barrier is due to a non homogeneous organic coating on the surface. It should be noted that the organic coating on field-collected particles includes fatty acids as well as many other organic species; some of them can condense on particles in a second step (particles passing over polluted areas enrich their carbon content) and could also alter the ability of FA of forming tightly packed liquid crystal or micelle structures.

Chapter 6 - Reactivity study: gas phase characterisation and uptake coefficient measurements

6. Reactivity study: gas phase characterisation and uptake coefficient measurements

6.1 Gaseous phase analysis

The gas phase composition and its temporal evolution inside suitable reaction cells were monitored using FT-IR spectrometry in the mid-IR region. The spectra acquisition was performed with a 4 cm^{-1} spectral resolution in the $400\text{-}4000\text{ cm}^{-1}$ range, with a number of scans depending on the particular experimental conditions (see ch. 6.2).

6.1.1 NO_2 in a dry atmosphere

In tab.6.1 we report, in order of decreasing wavenumber, the IR peak/bands positions and attribution of the main reacting species, NO_2 (N_2O_4):

wavenumber (cm^{-1})	mode description	molecule	reference	intensity
3258		Ge surface		
3201				
2918 2891	$\nu_3+\nu_1$	NO_2	W	m
2362 2337	ν_3	CO_2	W	
1754 1744	ν_3	N_2O_4	W G	
1744	symmetric stretch	N_2O_4 surface ads	G	
1740		N_2O_4 surface ads	B	
1628 1600	ν_3	NO_2	P2	vs
1318	ν_1	NO_2	P2	l
1270	ν_{11}	N_2O_4	W	
1265	asymmetric stretching	N_2O_4 surface ads	G	
1261	ν_{11}	N_2O_4	W	
1256				l
900-660	ν_2	NO_2	W	l
760	ν_{12}	N_2O_4	W	l
750	ν_2	NO_2	P2	l
<600		Ge surface		

Tab. 6.1 Main gas-phase and solid-phase adsorbed (on the Ge windows) signatures of the species present in a dry NO_2 IR spectrum. In the first column the band central position or, in bold character, the positions of the more intense absorption lines at 4 cm^{-1} of spectral resolution are reported. In the second column the IR mode is identified, in the third one the absorbing molecular species is assigned to that specific transition and in the fourth there are the references used for the band assignment. In the last column, when possible, the relative intensities of the IR mode referred to the more intense one are reported, with vs=very strong (100-80%), s=strong (~50%), m=medium (~15%), l=low (<5%).

All the IR bands reported in the tables of this chapter are assigned to the different molecular vibration on the basis of [Perrin A., 1998] (P), [Perrin A. et al., 1998] (P2), [Weis D. D. et al., 1999] (W), [Goodman A. L. et al., 1999] (G), [Barney W. S. et al., 2000] (B), [Feierabend K. et al., 2004] (F), Hitran database (H) and [Hallou A. et al., 1998] (HL) works.

In fig.6.1 we report a NO₂ (1% in He) reference spectrum as it is obtained in our experimental conditions. We notice that the vibration bands typical of the dimer species N₂O₄, are also detectable (at 1745 and 1259 cm⁻¹).

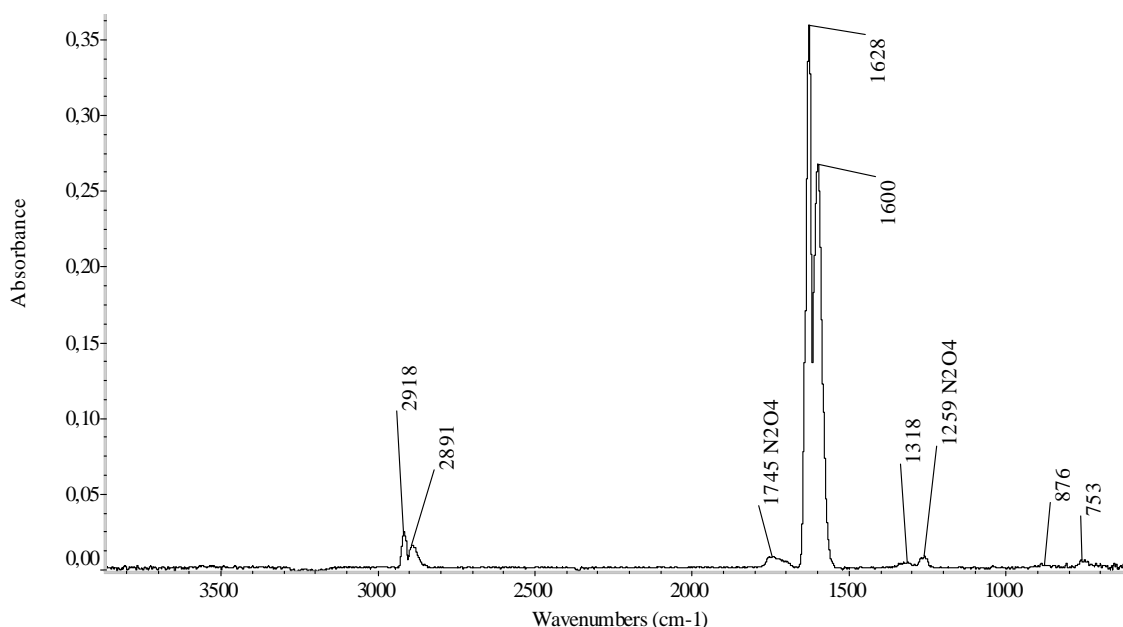


Fig. 6.1 FTIR spectrum (4 cm⁻¹ of spectral resolution and 16 scans/spectrum) of NO₂ 1% in He. The dimer species N₂O₄ is also present (~7% of NO₂ concentration) and its bands are reported at 1745 cm⁻¹ and 1259 cm⁻¹.

6.1.2 NO₂ in a moist atmosphere

The presence of water vapor in the gas phase is expected to generate many by-products. The minor species in a moist atmosphere or deposited on the wall/windows of the cell are consequence of chemical equilibria which have been previously described in ch.2.3.

These NO₂ hydrolysis products, mainly HNO₂ and HNO₃, are formed at concentrations high enough for being detected in our FTIR cell. The intensities of their IR absorptions are very low, sometimes very near to the noise level. As a consequence only qualitative observations can be given. We report in tab. 6.3 the IR bands assignment of these new species.

Not all of these species can be detected simultaneously in all the experimental conditions, as it is reported in tab. 6.2. As humidity increases, these acidic species decompose (heterogeneous reaction 2.6) leading to the formation of NO. This secondary reaction becomes faster at higher RH and NO accumulates inside the reactor, while a parallel decrease of HNO₂ and HNO₃ signals is observed.

RH%	Supplementary detected species	Other observations
0	-	-
20	HNO ₃ , HNO ₂	-
40	NO, HNO ₃ , HNO ₂	NO appears after 30 min
55	NO, HNO ₃ , HNO ₂	NO appears after 20 min
70	NO, HNO ₃ , HNO ₂	NO is present also after 5 min

Tab. 6.2 Supplementary identified species in the gas phase by FTIR spectroscopy when [NO₂]₀ = 8 × 10¹⁶ molec cm⁻³ at different RH%.

wavenumber (cm ⁻¹)	mode description	molecule	reference	intensity
3591	ν_1 (OH stretch)	trans-HONO	G	
3551	ν_1 (OH stretch)	HNO ₃	F	vs
3400	ν_1, ν_3	H ₂ O	W	
2920-3055	$\nu_2+\nu_4, \nu_2+\nu_3$	HNO ₃	F	m
2460-2710	$\nu_2+\nu_5, 2\nu_3, 2\nu_4$	HNO ₃	F	m
2337 2211	ν_3	N ₂ O	W B	
2224	ν_1	N ₂ O	H	s
2150-2240	$\nu_3+\nu_5, \nu_2+\nu_9$	HNO ₃	F	m
1903 1875 1850		NO	W	
1876		NO	G	
1710	ν_2 (NO ₂ asymmetric stretch)	HNO ₃	F, P	s
1708	ν_2 (NO ₂ asymmetric stretch)	HNO ₃	G	
1703	N=O stretching	trans-HONO	G	
1680		HNO ₃ surf. ads.	B	
1677		HNO ₃ surf. ads.	G	
1650	ν_3	H ₂ O	W	
1399	OH bending	HNO ₃ ads	G	
1339 1331	ν_3 OH bending	HNO ₃	W G	s
1326	ν_3 (NO ₂ symmetric stretch)	HNO ₃	F, P	s
1321 1314	ν_4	HNO ₃	W	
1315	ν_3 (NO ₂ symmetric stretch)	HNO ₃ surf. ads.	G	
1303	ν_4 (H-ON bend)	HNO ₃	F	m
1285	ν_1	N ₂ O	H	m
1263	ν_4 (H-ON bend)	HNO ₂	B, G	
1206	$\nu_8+\nu_9$	HNO ₃		
896	$2\nu_9$	HNO ₃	P	m
879	ν_5 (NO ₂ bend in-plane)	HNO ₃	F, P, G	s
879 869	ν_5	HNO ₃	W	
868 853 842	ν_4	cis-HNO ₂	W	
806 791 777	ν_4	trans-HNO ₂	W	l
763	ν_8 (NO ₂ bend out-of plane)	HNO ₃	F, P, G	l
647	ν_6 (O-NO ₂ stretching)	HNO ₃	F, P, G	l

Tab. 6.3 Gas-phase and adsorbed phase (on the Ge windows) IR signature of the minor species present in a moist NO₂ atmosphere.

6.1.3 NO₂ in a moist atmosphere in presence of NaCl

Whenever the solid NaCl is put in contact with the nitrogen dioxide in a closed reactor, NO₂ and ClNO are respectively depleted and formed in the gas phase, according to the heterogeneous reactions described in ch. 2.4. The temporal evolutions of their concentrations are RH dependent, and a more detailed analysis of their kinetics can be found in chapter 7.

We report in fig. 6.2 a ClNO reference spectrum as it has been obtained in our experimental conditions.

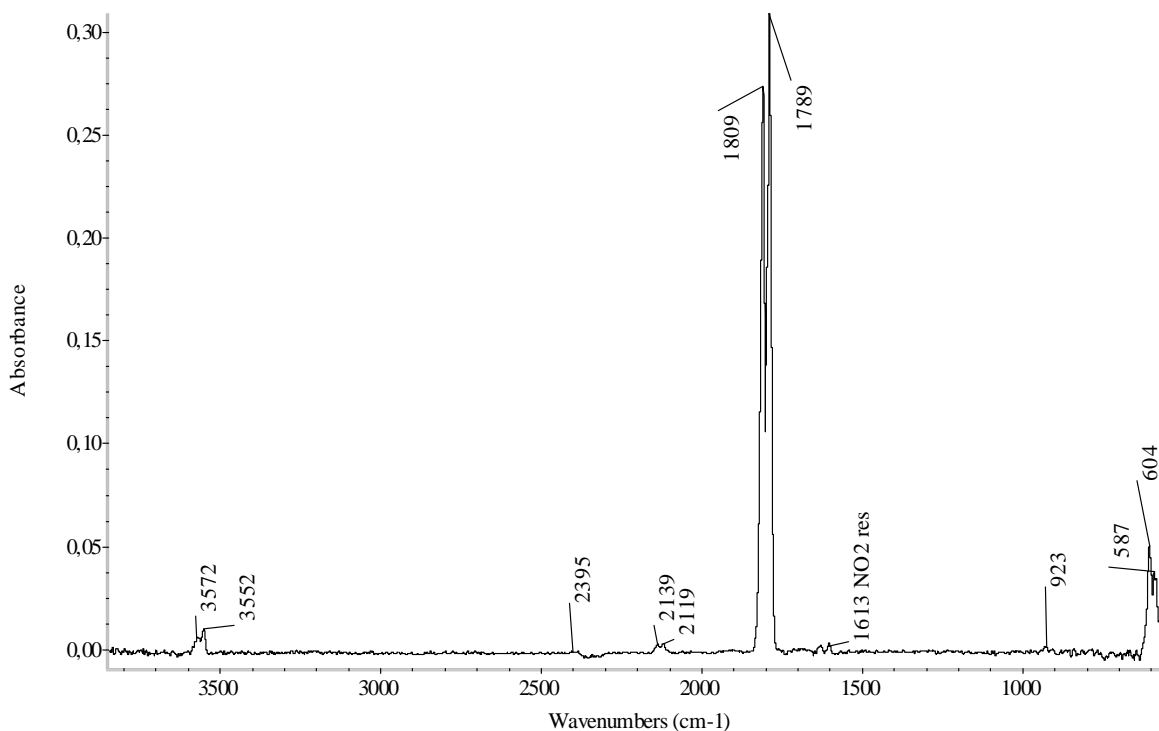


Fig. 6.2 FTIR spectra at 4 cm⁻¹ of spectral resolution and 16 scans/spectrum of ClNO.

The IR transition frequencies of the main products of the NaCl/NO₂ reaction are reported in tab. 6.4.

wavenumber (cm ⁻¹)	mode description	molecule	reference	intensity
3564	2ν ₁	ClNO	HL	l
2830-2700	ν ₁	HCl	W	s
2395	ν ₁ +ν ₂	ClNO	HL	
2139	ν ₃ +ν ₁	ClNO	W, HL	
2132				
2119				
1809	ν ₁	ClNO	W, HL	vs
1789				
923	ν ₂ +ν ₃	ClNO	HL	
595	ν ₂	ClNO	HL	m

Tab. 6.4 Main gas-phase and IR signatures of the expected products of the heterogeneous reaction between NO₂ and NaCl.

Gaseous HCl, even if expected between the products as in eq. 2.14, is actually not observed in the FTIR spectra collected. Almost all previous works report the impossibility of detecting HCl, the gaseous product of the “wet” NO₂/NaCl reaction. Only in [Winkler T. et al., 1991] the authors experimentally found that HCl (and HNO₂) can be formed as the results of a partial hydrolysis of ClNO on the NaCl surface. The authors detected the gaseous species with a mass spectrometer right in front of the NaCl tablet samples.

Consequently it is not astonishing that we could not detect gaseous HCl by IR: even in the case it is one of the reaction products or by-products, known its high Henry’s constant, it will have a preferential repartition to the aqueous phase which can be adsorbed on the salt or reactor walls. We have verified this by introducing gaseous NO₂ inside the empty reactor in which NaCl was previously exposed to the reactive gas. The reactor was pumped and purged with dry N₂ for several times, but deliberately not internally rinsed with water. We observed the formation of gaseous ClNO once NO₂ was introduced in the reactor. Therefore we concluded that HCl was still adsorbed on the reactor walls and that it reacted with NO₂ as described in reactions 2.19 and 2.20 to give back ClNO.

Other species which were already observed in moist conditions in absence of NaCl (HNO₃, HNO₂, NO), are still detected when the reactive surface is introduced into the reactor (see tab. 6.5).

As observed when NaCl is not present, HNO₃ signal has a general tendency to diminish throughout the reaction, probably because of its “sticking” character.

HNO₂ behavior is somehow now more complex because this species can derive from both NO₂ and ClNO hydrolysis. As nitric acid, HNO₂ has the tendency to diminish, but only at higher RH. Its IR absorption intensity is too close to the noise level to allow us any more detailed description.

NO formation seems to be retarded in presence of NaCl and can be detected over the noise level only when RH>50%.

Solid phase	RH%	Supplementary detected species	Other observations
NaCl	0	-	
	20	HNO ₃ ,HNO ₂	Very low quantities of acids
	40	HNO ₃ ,HNO ₂	
	55	NO, HNO ₃ ,HNO ₂	NO appears after 30 min
	70	NO, HNO ₃ ,HNO ₂	NO is present even after 5 min

Tab. 6.5 Supplementary identified species in the gas phase by FTIR technique when [NO₂]₀ = 8 × 10¹⁶ molec cm⁻³ is put in contact with NaCl at different RH%.

6.1.4 NO₂ in a moist atmosphere in presence of insoluble fatty acids coated NaCl

When an insoluble fatty acid coating is present, we observe the formation of the same gaseous species already described in §6.1.3. We do not detect particular differences between the coated/uncoated NaCl surfaces reaction gaseous products.

The same NO₂ or ClNO hydrolysis products are detected when RH increases. They are listed, in function of the experimental conditions, in tab. 6.6.

As in the previously described cases, HNO₂ and HNO₃ appears as soon as some water vapor is present in the reactor.

The by-product NO appears again with some retardation. This delay is shortened at higher RH values. The Ge-window adsorbed acid species are also detected.

Solid phase	RH%	Detected species	Other observations
NaC ₁₆ /NaCl	0	-	
	20	HNO ₃ , HNO ₂	
	40	HNO ₃	NO appears after 1h
	55	gaseous and surface adsorbed HNO ₃ , HNO ₂	NO appears after 20 min
	70	NO, HNO ₃ , HNO ₂	NO is present even after 5 min
NaC _{18:1} /NaCl	0	-	
	20	HNO ₃ , HNO ₂	Very low quantities of acids
	40	HNO ₃ , HNO ₂	
	55	NO, HNO ₃ , HNO ₂	NO appears after 1h
	70	NO, gaseous and surface adsorbed HNO ₃ , HNO ₂	NO is present even after 5 min

Tab. 6.6 Supplementary identified species in the gas phase by FTIR spectroscopy when $[\text{NO}_2]_0 = 8 \times 10^{16}$ molec cm^{-3} is put in contact at different RH% with sodium palmitate (NaC₁₆) or oleate (NaC_{18:1})-coated NaCl.

6.2 Experimental conditions optimisation

In our experimental apparatus 8×10^{15} molec cm^{-3} is the lowest reasonable NO₂ concentration that can be used when NO₂ kinetics is followed. At lower concentrations we reach the detection limit of the FTIR spectrometer, which is of 4×10^{14} molec cm^{-3} when 32 scans are accumulated for one spectrum. In any case these conditions are still very far from the real atmospheric average values of the NO₂ polluting species, which are about 1×10^4 more diluted. Nevertheless these values are in the concentration range which is experimentally used by many works concerning NaCl/NO₂ reactivity, like in [Finlayson-Pitts B. J., 1983], [Peters S. J. et al., 1996] and [Yoshitake H., 2000] (see table 2.1).

In this work two types of experimental conditions have been chosen for exposing NaCl to nitrogen dioxide, differing for the reactive gas concentration and the IR cell material:

- Low [NO₂] exposure:
These experiments are carried out for reproducing the same conditions of previous works in which the same reactor was used [Aghnatiou C., 2008]. We expose 6.94 cm² of NaCl to NO₂ at $(8.4 \pm 0.3) \times 10^{15}$ molec cm^{-3} inside the Teflon cell at different RH (0-85%). The gas phase evolution is followed over 30 minutes by recording a spectrum every 30 s (32 scans/spectrum).
- High [NO₂] exposure:
We expose 13.89 cm² of NaCl to NO₂ at $(8.7 \pm 0.3) \times 10^{16}$ molec cm^{-3} inside the halo-carbon wax glass cell in a range of relative humidities from 0% to 75%. The gas phase evolution is followed over 1 h by recording a spectrum every 30 s (16 scans/spectrum).

6.2.1 NO₂ inside a static reactor: measurements of reaction rates and constants.

The first set of measurements at low [NO₂] gives some preliminary results which are afterwards used for optimising the experimental conditions.

Mainly two different processes are involved in the observed NO₂ depletion, as already mentioned in ch. 3.5.1: the real heterogeneous reaction(s) and the losses on the reactor walls.

We report in fig. 6.1 an example of gaseous phase NO₂ depletion in the empty reactor and in presence of NaCl (no water vapour is present in the gaseous phase).

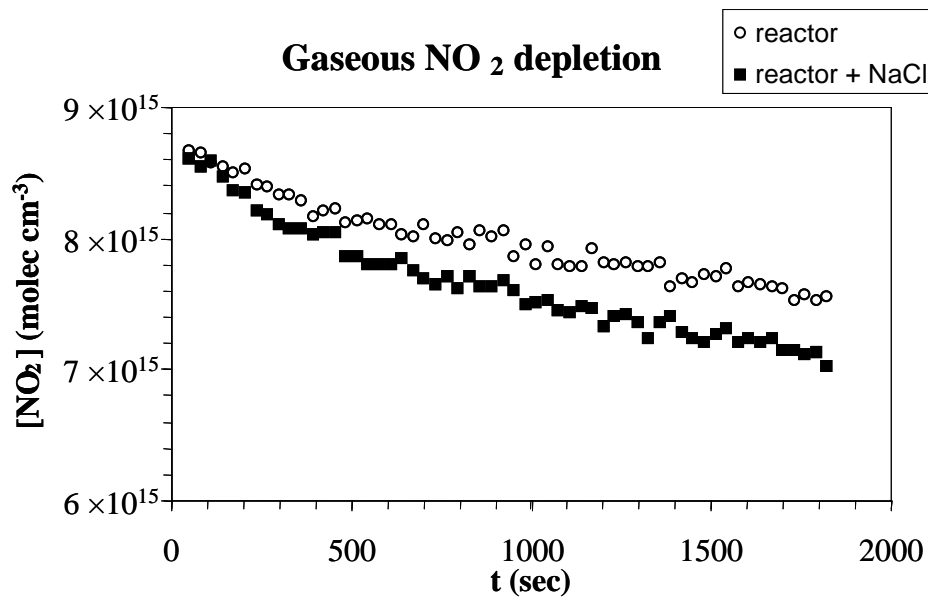
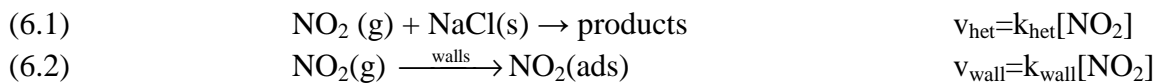
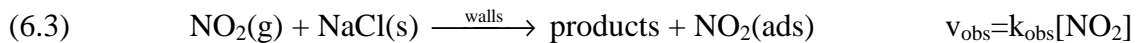


Fig. 6.1 Gaseous NO₂ depletion inside the static reactor (empty circles) and in presence of NaCl (filled squares). [NO₂]₀ = 8.6 × 10¹⁵ molec cm⁻³.

For describing the kinetics of these two processes we introduce the rate constants k_{het} and k_{wall} so that their reaction rates can be reported, in the case of a first order process, as described in eq. 6.1 and 6.2:



When the heterogeneous reaction 6.1 occurs inside the reactor, the experimentally observed NO₂ depletion rate, v_{obs} , is then the result of these two different processes:



If we assume that the heterogeneous reaction and the wall losses are two independent phenomena, we can express the observed NO₂ depletion rate as the sum of the heterogeneous reaction and wall loss rates (eq. 6.4):

$$(6.4) \quad -\frac{d[\text{NO}_2]}{dt} = v_{\text{obs}} = k_{\text{obs}}[\text{NO}_2] = (k_{\text{het}} + k_{\text{wall}})[\text{NO}_2]$$

For determining the real heterogeneous reaction, then these two components have to be separated; k_{obs} can indeed be considered as the result of the linear combination of k_{het} and k_{wall} . In this way the heterogeneous reaction constant can be calculated as in eq. 6.5:

$$(6.5) \quad k_{\text{het}} = k_{\text{obs}} - k_{\text{wall}}$$

Where k_{obs} derives from the observed depletion rate of NO₂ put in contact with NaCl inside the static reactor, and k_{wall} is measured from the observed NO₂ depletion rate in the empty reactor.

From the integration of eq. 6.4, we obtain the equation of a straight line (eq. 6.6) which can therefore be used for the experimental determination of the rate constants values:

$$(6.6) \quad \ln \frac{[\text{NO}_2]}{[\text{NO}_2]_0} = -k_{\text{obs}} t$$

Where $[\text{NO}_2]_0$ is the initial NO_2 concentration ($t=0$).

The $\frac{[\text{NO}_2]}{[\text{NO}_2]_0}$ ratio is determined by integrating the area of the most intense vibrational band of

NO_2 , ν_3 , centered at 1615 cm^{-1} , in the interval $[1576-1649] \text{ cm}^{-1}$ with a correction for a linear baseline $[1163-1944] \text{ cm}^{-1}$. In some cases the spectra need a correction by subtracting/adding the water vapor spectrum that causes some interference with the NO_2 bands.

The integrated area A gives a better sensitivity and a higher S/N ratio than the simple absorption intensity at a certain wavenumber.

When $\ln \frac{A}{A_0}$ quantity is plotted in function of the reaction time t , the graph will be a straight

line if the initial hypothesis of first order kinetics are actually verified.

In fig. 6.2 we plot this quantity for the same experimental data previously taken as an example (in fig. 6.1). We can indeed observe that the behaviour is linear at the beginning, while it has the tendency to deviate for longer reaction times, due to saturation processes both on the reactor and on the salt surfaces.

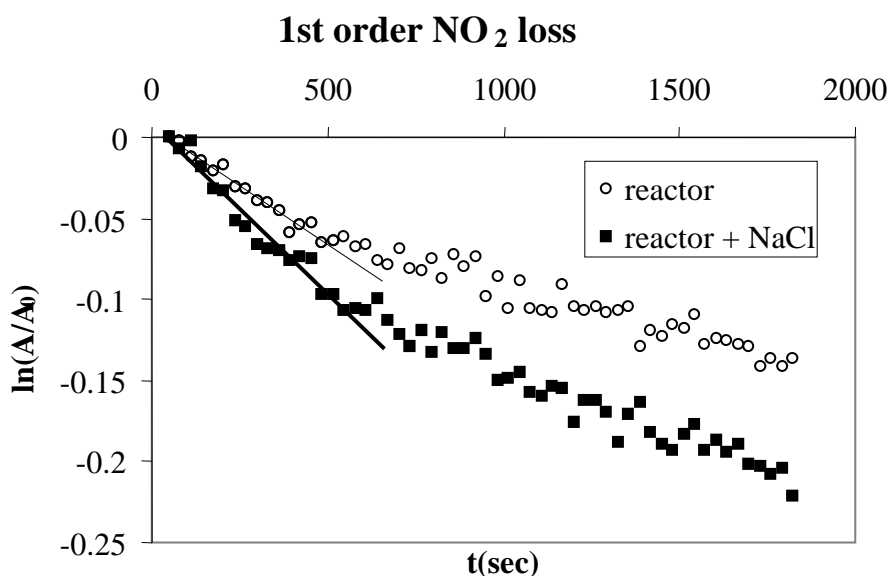


Fig. 6.2 Initial linear behaviour for the NO_2 depletion inside the static reactor in presence (filled squares) or in absence (empty circles) of NaCl reactive surface. The straight line corresponds to a first order kinetic loss of NO_2 . $[\text{NO}_2]_0 = 8.6 \times 10^{15} \text{ molec cm}^{-3}$.

6.2.2 Optimisation strategy

We already knew from previous works that NO_2 reactivity on NaCl is quite weak; the general consequence is a more difficult discrimination between the heterogeneous reaction and the NO_2 wall loss. Indeed, if k_{wall} is the main process occurring, because of a very slow heterogeneous reaction, further data exploitations become difficult or even impossible.

To be able to observe the heterogeneous process in our experimental set-up we have to maximise the $k_{\text{het}} = k_{\text{obs}} - k_{\text{wall}}$ difference. We carried out the following actions:

- 1) Increase of NO₂ gas concentration:
It leads to a lower wall absorption rate, probably because of a faster wall surface saturation. It is better discussed further ch. 6.2.3.
- 2) Increase of the reactive surface:
by doubling the number of the exposed NaCl tablets; it allows to increase the observed k_{het} contribution to NO₂ depletion.
- 3) Reduction of k_{wall} by choosing a different reaction cell material:
a glass cell is internally coated by an inert halocarbon wax and is used instead of the Teflon cell. The internal walls in both cases are hydro-repellent and chemically inert, but Teflon seems to be a porous material for NO₂ since it is not an efficient barrier against small gas molecules passage. On the contrary glass, being relatively non porous to gases, minimises this wall loss. We proved this with different tests (not reported here) on a third, home-made, cell, in which the thickness of the Teflon walls could be modulated.

6.2.3 Increasing NO₂ concentration:

We report here some examples on how increasing [NO₂]₀, we can improve the measurement of the rate constants.

Empty reactor

An example of decreasing NO₂ wall depletion by increasing its initial concentration is reported in fig.6.3. The slopes on the graph represent the observed experimental rate coefficients for the NO₂ taken up by only the Teflon reactor walls and windows. Initial NO₂ concentration is varied from 1 × 10¹⁶ molec cm⁻³ to 1 × 10¹⁷ molec cm⁻³.

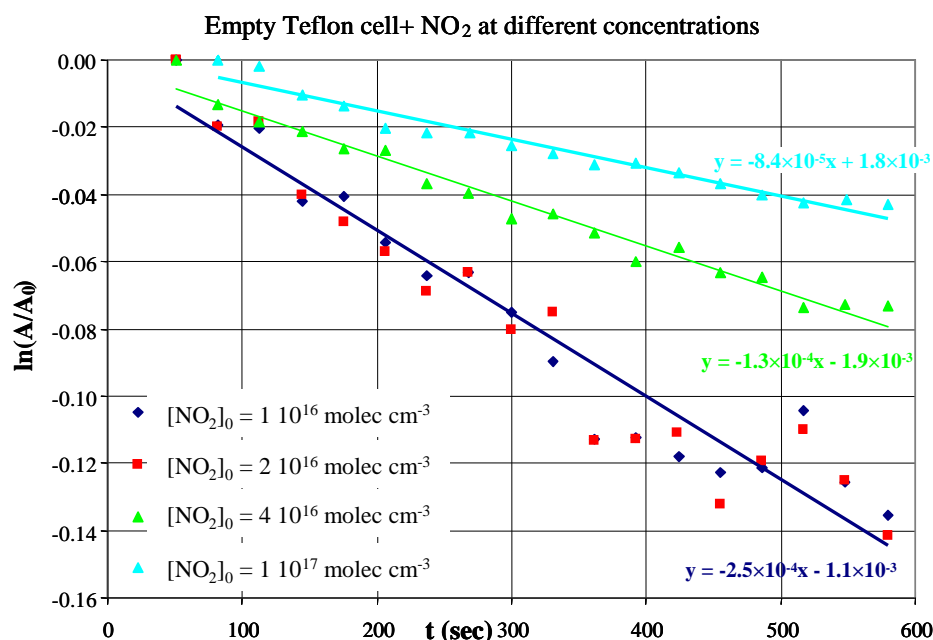


Fig. 6.3 A Teflon cell and different [NO₂]₀ at RH=0%: the slopes indicate the wall loss rates. Initial NO₂ concentration ranges from 1 × 10¹⁶ to 1 × 10¹⁷ molec cm⁻³.

We can observe that, increasing by a factor of 10 the initial concentration of NO_2 , the wall loss rate diminishes of approximately 65%. At higher NO_2 concentrations the non-reactive surface saturation process on the walls of the reactor is, indeed, accelerated.

Reactor with NaCl

At the same time, by increasing $[\text{NO}_2]_0$, a higher heterogeneous reaction rate is measured, as reported in fig. 6.4. The heterogeneous component at a given $[\text{NO}_2]_0$ is the difference in slope between the two experimental curves k_{obs} and k_{wall} . In this figure we can have a direct and visual comparison of the behaviour of the initial NO_2 kinetics in the glass cell when it is filled with $\sim 1 \times 10^{16}$ (a) and at $\sim 1 \times 10^{17}$ molec cm^{-3} (b) of reactive gas in dry conditions. The first observation is the neat evidence of the heterogeneous process when the higher NO_2 concentration is used because of a NaCl/ NO_2 reactivity magnification.

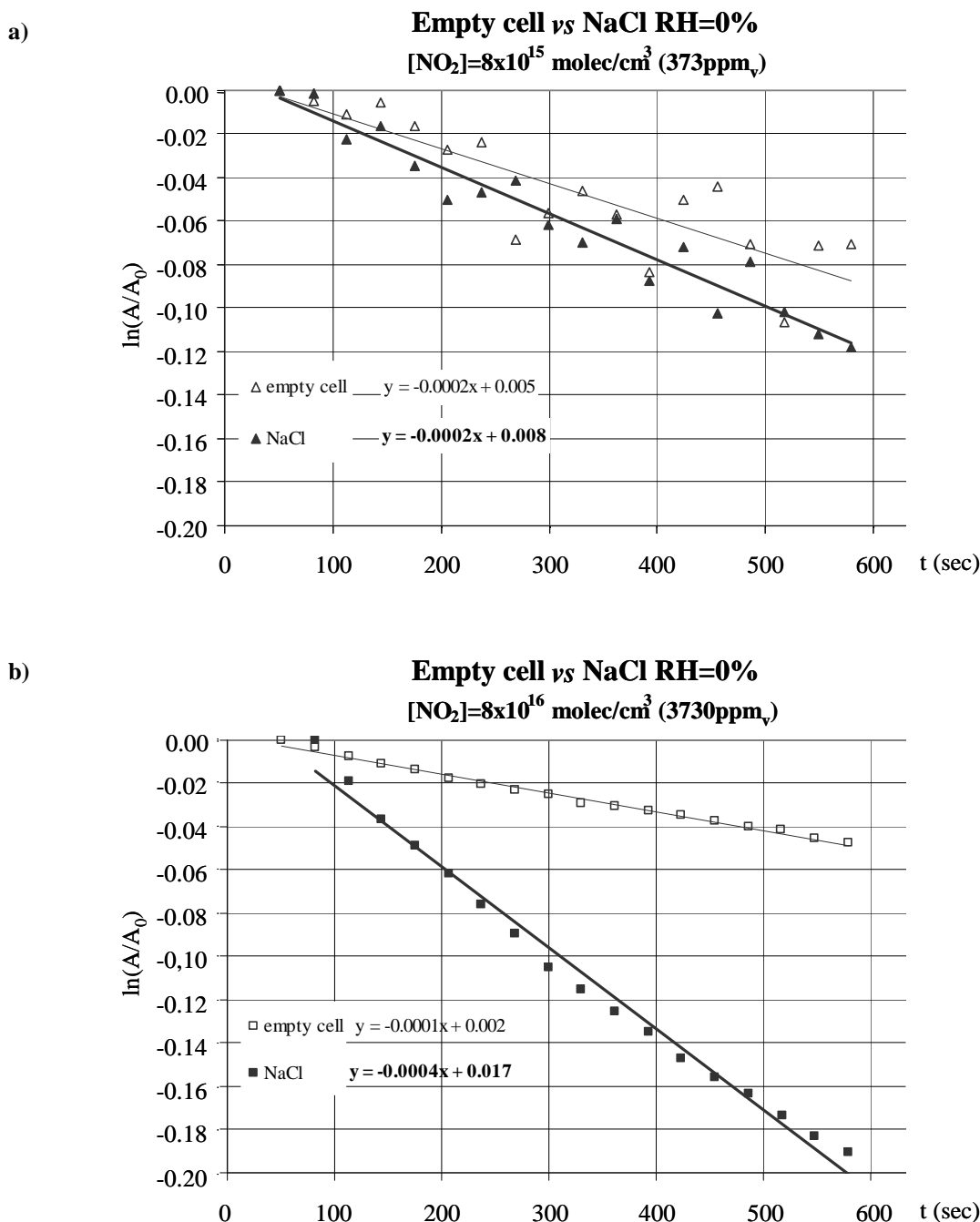


Fig. 6.4 NO_2 kinetics in the glass cell (RH=0%) represented as $\ln(A/A_0)$ vs time. In **a)** experimental data for $[\text{NO}_2]_0=8.4 \times 10^{15}$ molec cm^{-3} , in **b)** data for $[\text{NO}_2]_0=8.7 \times 10^{16}$ molec cm^{-3} . The empty cell values are presented in empty squares; when 8 tablets of NaCl are put inside the reactor the data are presented in filled squares.

Other advantages

There are some other advantages in choosing high $[\text{NO}_2]$ exposure conditions:

- a) an improvement in the kinetic temporal resolution,
 - b) a better quality data for the kinetic measurements
 - c) a direct N_2O_4 kinetics measurement.
-
- a) As a matter of fact each interferograms accumulation takes ~ 30 s when 32 scans are recorded, with the result that individual spectra represent the mean value taken over 30 s of changing extent of the reaction rather than an instantaneous snapshot of the system. By increasing $[\text{NO}_2]_0$ the number of scans per spectrum for achieving a satisfactory resolution is lower: each accumulation takes only ~ 19 s so that a better temporal resolution of the kinetic is achieved.
 - b) Another important advantage of increasing $[\text{NO}_2]$ is a better quality in term of S/N of the collected gas-phase IR spectra, an aspect inducing higher precision in determining the NO_2 peak area (A and A_0). The obtained values, used for reconstructing the kinetic profiles, result in less dispersed points in the $\ln(A/A_0)$ vs time graphical representation, as it can be seen by comparing fig. 6.4a and 6.4b. The main effect is to lower the parameter k error. With a higher S/N ratio the temporal profiles of NO_2 , ClNO and even N_2O_4 can be analysed more in details and used as entering data in a reactivity model, described in ch.7.
 - c) Working at such high NO_2 partial pressures between 4 and 5% of the total NO_2 is in the form of the dimer species; the presence of N_2O_4 starts to become so important that a direct measurement of its IR signature is possible. This is, indeed, the first time that N_2O_4 kinetics are directly experimentally measured for determining the uptake coefficient of N_2O_4 on the NaCl solid phase.

All these overviewed aspects guided us to the choice of the optimized parameters, summarised under the “high $[\text{NO}_2]$ ” exposure conditions at the beginning of this paragraph.

6.3 Uptake coefficient following NO_2 depletion

The aim of these uptake coefficient measurements as a function of the relative humidity is to see if the insoluble fatty acid coating on NaCl has an effect on its reactivity towards NO_2 . With this purpose we follow via FTIR spectroscopy the gaseous phase depletion of NO_2 in static conditions. As previously discussed (§6.2.1), the measured NO_2 profile gives access to the estimation of k_{obs} parameter which can be corrected by the wall losses (k_{wall}) for obtaining the real heterogeneous reaction component k_{het} . k_{wall} is measured in the same reactor, in the same experimental condition, but in absence of NaCl .

The so obtained k_{het} can be introduced in the uptake coefficient expression (2.28) already described in ch. 2.4.1:

$$(2.28) \quad \gamma = 4V \frac{k_{\text{het}}}{\langle c \rangle S}$$

We associate to this measured uptake coefficient an error (eq. 6.7) deriving from the standard deviations of the linear fitting parameters (ϵ_k) and considering the errors on V , S and $T^{\text{§§§§}}$ as negligible compared to it:

§§§§ T is used for calculating $\langle c \rangle$, the average velocity of the reactive molecules in the gaseous phase.

$$(6.7) \quad \varepsilon_{\gamma} = \gamma \cdot \left(\frac{\varepsilon_{k_{\text{obs}}}}{k_{\text{obs}}} + \frac{\varepsilon_{k_{\text{wall}}}}{k_{\text{wall}}} \right)$$

When more than one experience is repeated in the same conditions, the averaged value of γ is kept and the associated error is the dispersion of the γ values:

$$(6.8) \quad \varepsilon_{\gamma} = (\gamma_{\text{max}} - \gamma_{\text{min}}) / 2$$

In reference work the reaction rate is often suggested to be of order 2 in $[\text{NO}_2]$ in absence of water vapour (see tab.2.1). If it was the case, the expression 6.1, 6.2, 2.28, and all the previously described mathematic data treatment could not be used any more because they are set for a first order reaction rate. For this reason the literature values are usually referred to N_2O_4 .

Nevertheless the aim of this study was not to measure the reaction order in presence of a fatty acids coating and in different RH conditions. We suppose first order kinetics for γ_0 , and when we plot $\ln \frac{[\text{NO}_2]}{[\text{NO}_2]_0}$ vs time we always observe a linear behaviour of the data for at least the first 230 seconds of the experiment (equivalent to the 8 experimental points used in the fitting procedure). In this way our initial hypothesis is verified.

We report here an example of experimental determination of γ_0 in the case of NO_2/NaCl at $\text{RH}=0\%$. The evolution of NO_2 IR signal (the integrated area A) in presence of NaCl that we can observe in the optimized condition is shown in fig. 6.5:

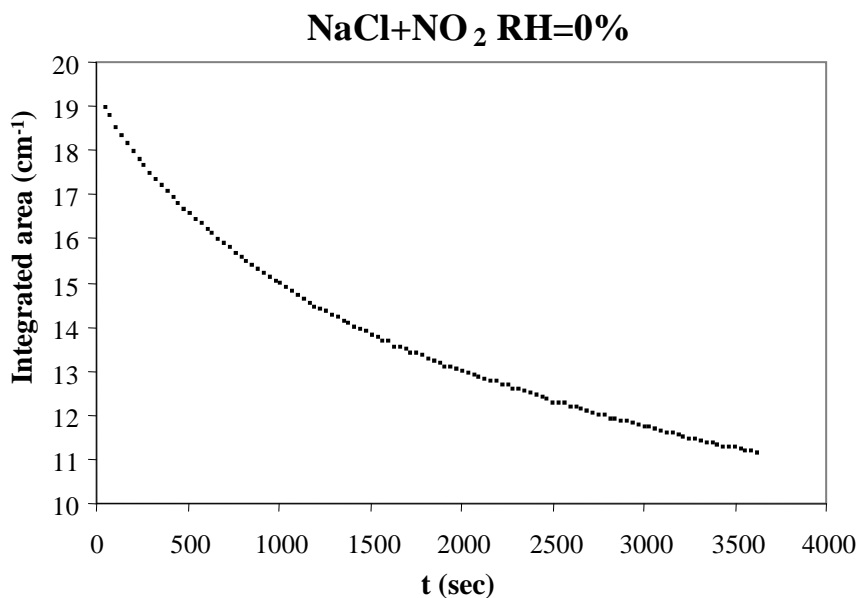


Fig. 6.5 A typical profile of $[\text{NO}_2]$ evolution measured as the integrated area of its most intense IR peak when the gaseous phase is put in contact with NaCl at $\text{RH}=0\%$. $[\text{NO}_2]_0 = 8 \cdot 10^{16} \text{ molec cm}^{-3}$.

In the same conditions we record NO_2 evolution when no reactive surface is present.

We plot for both experiments the graph $\ln \frac{[A]}{[A]_0}$ vs time (fig. 6.6) from which we can measure, through the slope of the straight line, k_{obs} and k_{wall} .

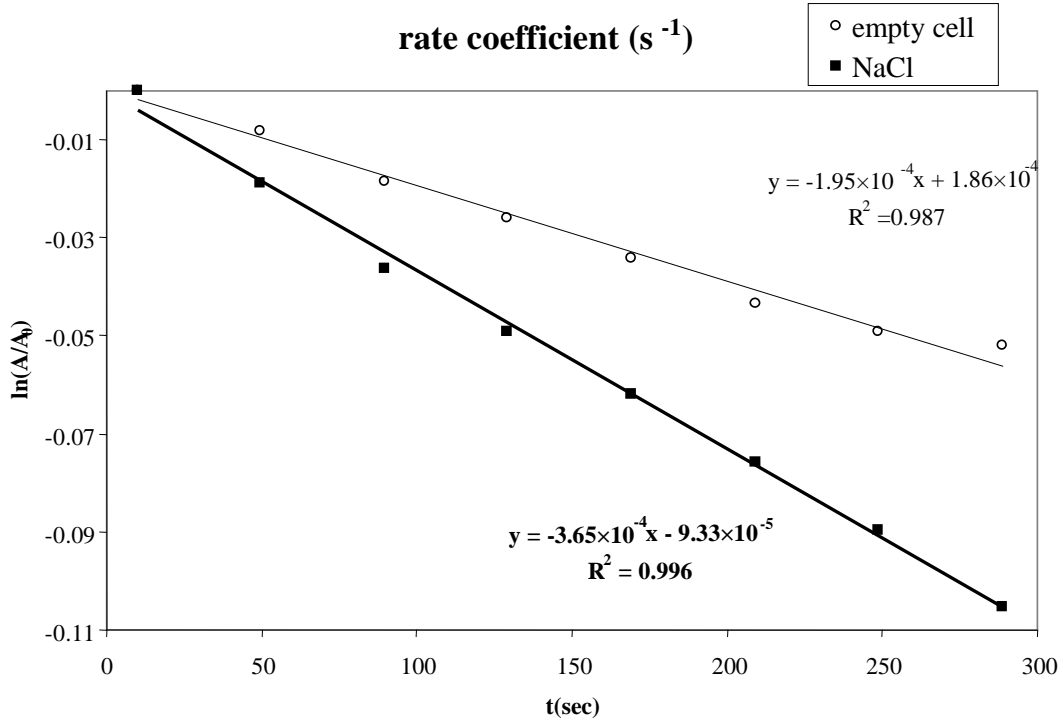


Fig. 6.6 Rate coefficients with/without NaCl RH=0%. $[\text{NO}_2]_0 = 8 \cdot 10^{16} \text{ molec cm}^{-3}$.

In this case $k_{\text{obs}} = 3.65 \times 10^{-4} \text{ s}^{-1}$ and $k_{\text{wall}} = 1.95 \times 10^{-4} \text{ s}^{-1}$.

The average molecule velocity in the gaseous phase, $\langle c \rangle$, is temperature dependent (eq. 2.22), and T can slightly vary from one experiment to the other. For assuring no influence of this fluctuation on k_{het} , we subtract the rate constants already normalized for the calculated $\langle c \rangle$ at the specific experimental temperature:

In this outlined case:

$$\frac{k_{\text{het}}}{\langle c \rangle} = \frac{k_{\text{obs}}}{\langle c \rangle} - \frac{k_{\text{wall}}}{\langle c \rangle} = \frac{3.65 \times 10^{-4}}{36880} - \frac{1.95 \times 10^{-4}}{36936} = 4.62 \times 10^{-9} \text{ cm}^{-1}$$

The initial uptake coefficient value can then be calculated introducing the reactor volume V, and the reactive salt surface S:

$$\gamma = 4V \frac{k_{\text{het}}}{\langle c \rangle S} = 4 \cdot 210 \cdot \frac{4.62 \times 10^{-9}}{13.89} = 2.79 \times 10^{-7}$$

$$\varepsilon_{\gamma} = \gamma \cdot \left(\frac{\varepsilon_{k_{\text{obs}}}}{k_{\text{obs}}} + \frac{\varepsilon_{k_{\text{wall}}}}{k_{\text{wall}}} \right) = 2.79 \times 10^{-7} \cdot \left(\frac{7 \times 10^{-6}}{3.65 \times 10^{-4}} + \frac{5 \times 10^{-6}}{1.95 \times 10^{-4}} \right) = 0.13 \times 10^{-7}$$

$$\gamma_0 = (2.79 \pm 0.13) \times 10^{-7}$$

6.3.1 Low $[\text{NO}_2]$ experiments:

In fig. 6.7 we report the measured NO_2 uptake coefficients for the low $[\text{NO}_2]$ exposure of 4 tablets of the pure NaCl salt or coated with NaC_{16} or $\text{NaC}_{18:1}$ as a function of the relative humidity. The averaged results of the repeated measurements are resumed, with their

associated experimental error, in tab. 6.7. In all cases the wall loss correction is far beyond the maximum recommended value of 40% consequently precautions have to be taken in results interpretation.

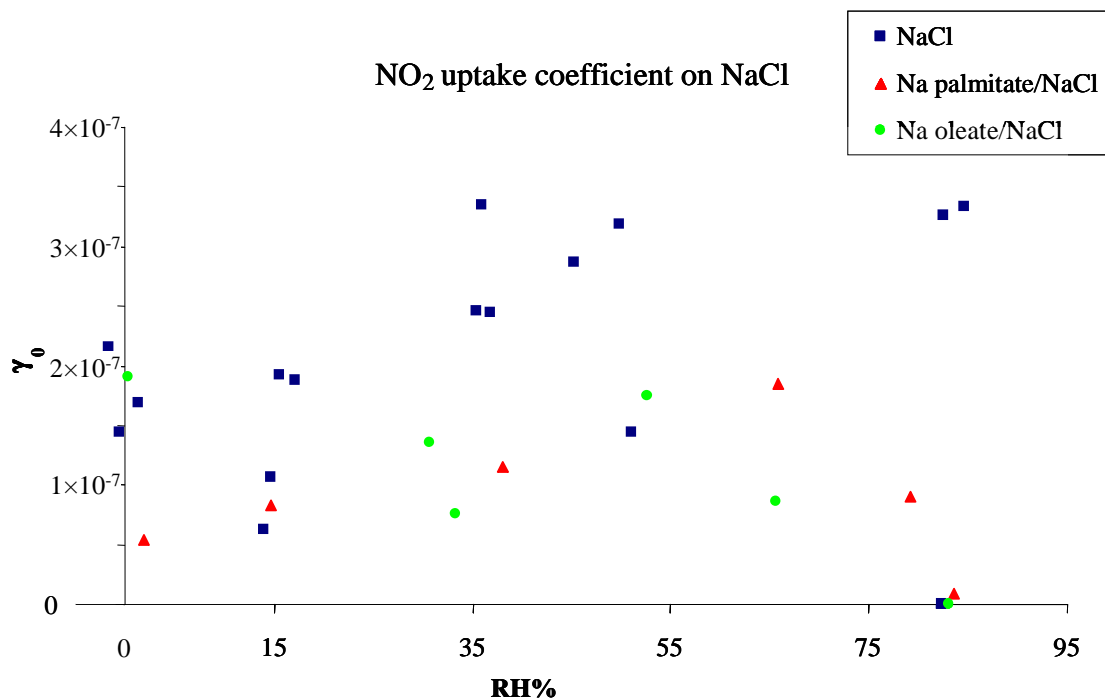


Fig. 6.7 Measured NO_2 initial uptake coefficient (γ_0) as a function of RH%; $[\text{NO}_2]_0 = (8.4 \pm 0.3) \times 10^{15} \text{ molec cm}^{-3}$.

solid phase	RH%	γ_0	wall loss correction (%)
NaCl	0	$(1.7 \pm 0.7) \times 10^{-7}$	48
	15	$(1.4 \pm 1.0) \times 10^{-7}$	70
	35	$(2.8 \pm 0.9) \times 10^{-7}$	66
	50	$(2.4 \pm 1.2) \times 10^{-7}$	74
	85	$(1.8 \pm 2) \times 10^{-7}$	85
$\text{NaC}_{16}/\text{NaCl}$	0	$(7 \pm 7) \times 10^{-8}$	68
	15	$(8 \pm 7) \times 10^{-8}$	80
	35	$(1.4 \pm 0.9) \times 10^{-7}$	80
	65	$(1.9 \pm 1.7) \times 10^{-7}$	81
	80	$(0.8 \pm 1.2) \times 10^{-7}$	93
	85	-	>100
$\text{NaC}_{18:1}/\text{NaCl}$	0	$(1.9 \pm 0.7) \times 10^{-7}$	45
	30	$(1.3 \pm 0.8) \times 10^{-7}$	79
	50	$(2.0 \pm 0.9) \times 10^{-7}$	77
	65	$(0.9 \pm 1.0) \times 10^{-7}$	90
	85	-	>100

Tab. 6.7 Averaged measured NO_2 initial uptake coefficient (γ_0) as a function of RH%; $[\text{NO}_2]_0 = (8.4 \pm 0.3) \times 10^{15} \text{ molec cm}^{-3}$.

Even if strongly affected by wall losses, the data still can give some information on the general trend of the reactivity as a function of humidity:

- NaCl reactivity increases with increasing RH, reaching the maxima values between 35-60 RH%. This is still true when the surface is coated by sodium palmitate and oleate;
- When F.A. covers the reactive surface they lower the reactivity of approximately 50% with the difference between the absolute values of γ increasing with increasing RH. The reactivity lowers again for RH>75%.
- Comparing the obtained values with the previous measurements done on the same reactor [Aghnatiou C., 2008], where the wall loss correction was not taken into account we obtain uptake coefficient values smaller by one order of magnitude.

6.3.2 High [NO₂] experiments:

In fig.6.8 we report, as a function of RH%, the measured NO₂ uptake coefficients for the high [NO₂] exposure of 8 NaCl tablets. The reported error bars in x and y are the instrumental incertitude on the measured RH and the associated measure error ϵ_γ respectively. The plotted curves have simply an eye-guide function. The NaCl tablets can be dipped in EtOH (in blue in the graph) or in a ethanol solution of NaC₁₆ (in red) or NaC_{18:1} (in green). The averaged results of the repeated measurements are resumed, with their associated experimental error, in tab. 6.8.

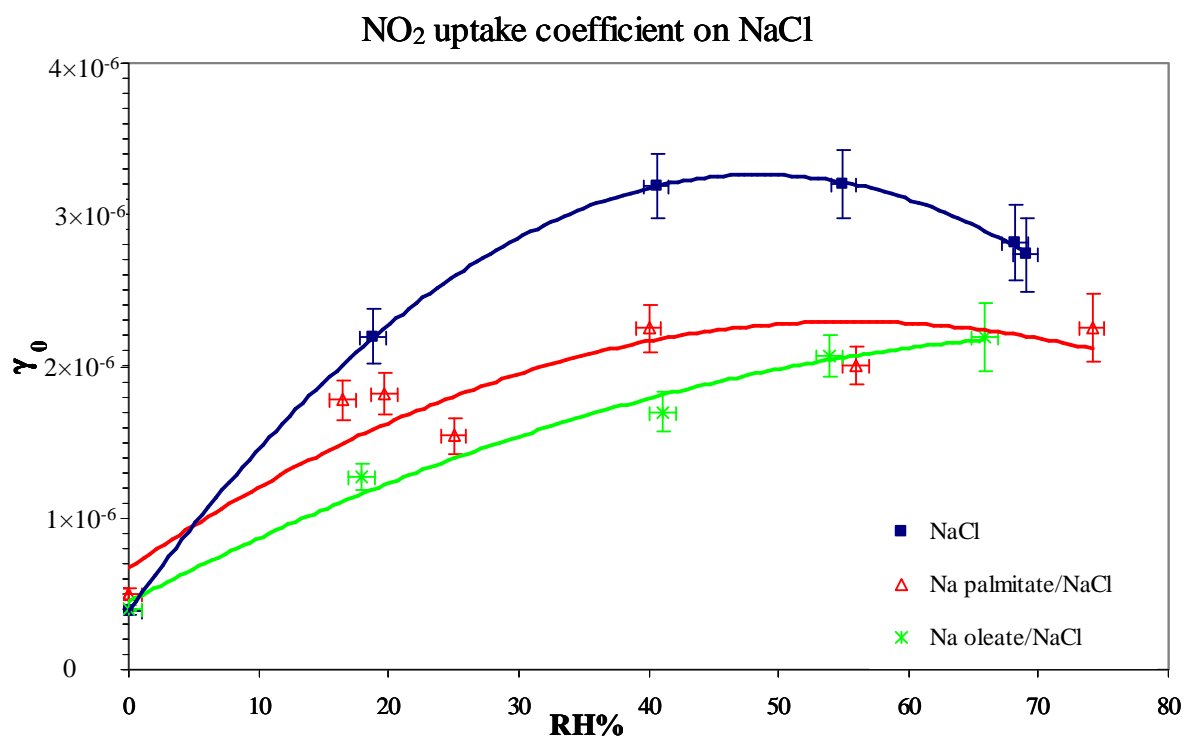


Fig. 6.8 Measured NO₂ initial uptake coefficient (γ_0) as a function of RH% at $[\text{NO}_2]_0 = (8.7 \pm 0.3) \times 10^{16} \text{ molec cm}^{-3}$. The plotted curves have a function of eye-guide.

solid phase	RH%	γ_0	wall loss correction (%)
NaCl	0	$(3.8 \pm 0.2) \times 10^{-7}$	31
	20	$(2.2 \pm 0.2) \times 10^{-6}$	17
	40	$(3.2 \pm 0.2) \times 10^{-6}$	24
	55	$(3.2 \pm 0.2) \times 10^{-6}$	26
	70	$(2.78 \pm 0.04) \times 10^{-6}$	28
NaC ₁₆ /NaCl	0	$(5.0 \pm 0.4) \times 10^{-7}$	26
	20	$(1.71 \pm 0.14) \times 10^{-6}$	21
	40	$(2.3 \pm 0.2) \times 10^{-6}$	31
	55	$(2.01 \pm 0.13) \times 10^{-6}$	36
	75	$(2.3 \pm 0.2) \times 10^{-6}$	32
NaC _{18:1} /NaCl	0	$(4.0 \pm 0.2) \times 10^{-7}$	30
	20	$(1.27 \pm 0.09) \times 10^{-6}$	26
	40	$(1.70 \pm 0.13) \times 10^{-6}$	37
	55	$(2.07 \pm 0.14) \times 10^{-6}$	35
	65	$(2.2 \pm 0.2) \times 10^{-6}$	28

Tab. 6.8 Averaged measured NO₂ initial uptake coefficient (γ_0) on NaCl and palmitate or oleate-coated NaCl as a function of RH% at $[\text{NO}_2]_0 = (8.7 \pm 0.3) \times 10^{16}$ molec cm⁻³.

The experimental points are much less dispersed compared to the low $[\text{NO}_2]_0$ measures and all the wall loss correction factors are inferior to 40%. This is an indicator of reliability for this set of experimental data.

The main observations that derive from the experimental values are the following:

- Compared to the low $[\text{NO}_2]$ experiments the absolute values for the uptake coefficient are here multiplied by a factor of 10, showing a dependence of $\gamma_{\text{NO}_2/\text{NaCl}}$ on the used gas trace concentration.
- The reactivity of the NaCl/NO₂ system increases with increasing humidity with a similar trend observed at low concentration. There is a factor of 4 between the uptake coefficient at 40-55 RH% and the one obtained in dry conditions. At RH%=70 the reaction seems to slightly slow down.
- When F.A. cover the reactive surface they lower the reactivity of about 30% with the larger difference between γ values in the 40-60 RH% range.
- For the palmitate-coated surfaces the uptake coefficient is constant above 40% RH.
- For oleate-coated surfaces the uptake coefficient seems to increase monotonically with the humidity, but the absolute values are comparable to the palmitate-coated ones.

A direct comparison of the obtained γ values with the literature ones is only possible with [Yoshitake H., 2000] where the uptake coefficient was measured following NO₃⁻ formation on the surface by DRIFTS in the same $[\text{NO}_2]_0$ range used in our experiments. On NaCl surfaces which were previously exposed to water vapour, they report a product formation rate of order 1 on p_{NO_2} . This further confirms our initial assumption, also experimentally verified, that the uptake follows a first order kinetic. In this work the author reports, at RH=0%, a value of $\gamma_0 = (1.5 \pm 0.2) \times 10^{-8}$ on moist salt, to be compared to our $\gamma_0 = (3.8 \pm 0.2) \times 10^{-7}$ obtained at RH=0%. Taking into account the experimental differences between the two works and the discrepancies of some orders of magnitude between γ values obtained with different experimental set-ups, the two data are in quite good agreement.

6.4 Uptake coefficient following N₂O₄ depletion

In the reactivity experiments where high NO₂ initial concentrations are used the IR signature of the dimer N₂O₄ is sufficiently clear to allow to follow its kinetics. From the equilibrium constant, $[N_2O_4] = (2.0 \pm 0.3) \times 10^{15}$ molec cm⁻³ are estimated to be present in the reactive system, so that about 4.5 ± 0.5 % of NO₂ is under the form of N₂O₄.

In this case we can, for the first time, gain access to the direct measure of the order uptake coefficient of N₂O₄ on NaCl and no objections to the data treatment procedure because of the hypothesised 1st order uptake and obtained data can be directly compared to the ones given by previous works.

Similarly to NO₂, N₂O₄ signal is followed on its most intense band, labeled as ν₁₁, centered at 1265 cm⁻¹, and integrated in the interval [1288-1229] cm⁻¹ with correction for a linear baseline [1288-1209] cm⁻¹. An example of the temporal evolution of the IR integrated area of N₂O₄ at RH=0% is given in fig. 6.9:

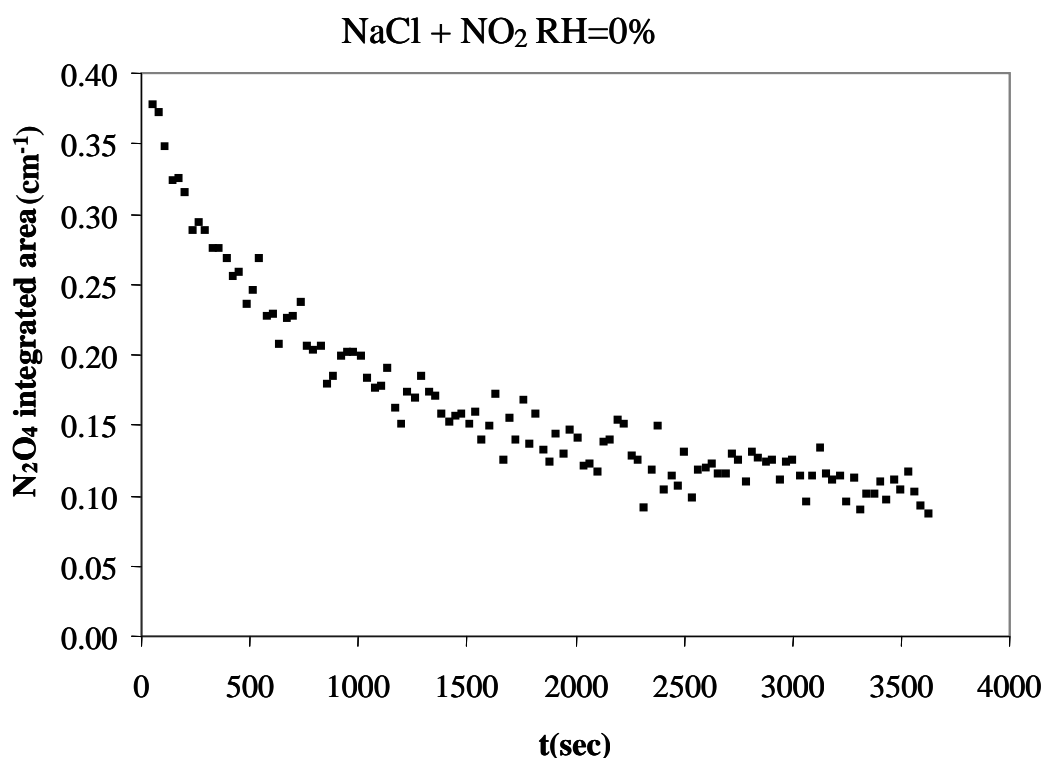


Fig. 6.9 A typical profile of $[N_2O_4]$ evolution measured as the integrated area of its ν₁₁ IR peak when the gaseous phase is put in contact with NaCl at RH=0%. $[N_2O_4]_0 = (2.0 \pm 0.3) \times 10^{15}$ molec cm⁻³.

The initial uptake rate is determined as in the case of NO₂ from a linear fit of $\ln \frac{[N_2O_4]}{[N_2O_4]_0}$ vs time from where we can determine, after correction for the wall absorption, the initial reactive uptake coefficient.

In fig. 6.10 we report the measured N₂O₄ uptake coefficient values for the high [NO₂] exposure of 8 NaCl tablets simply dipped in EtOH or coated with NaC₁₆ or NaC_{18:1} as a function of the relative humidity. The averaged results of the repeated measurements are resumed, with their associated experimental error, in tab. 6.9.

N₂O₄ uptake coefficient on NaCl

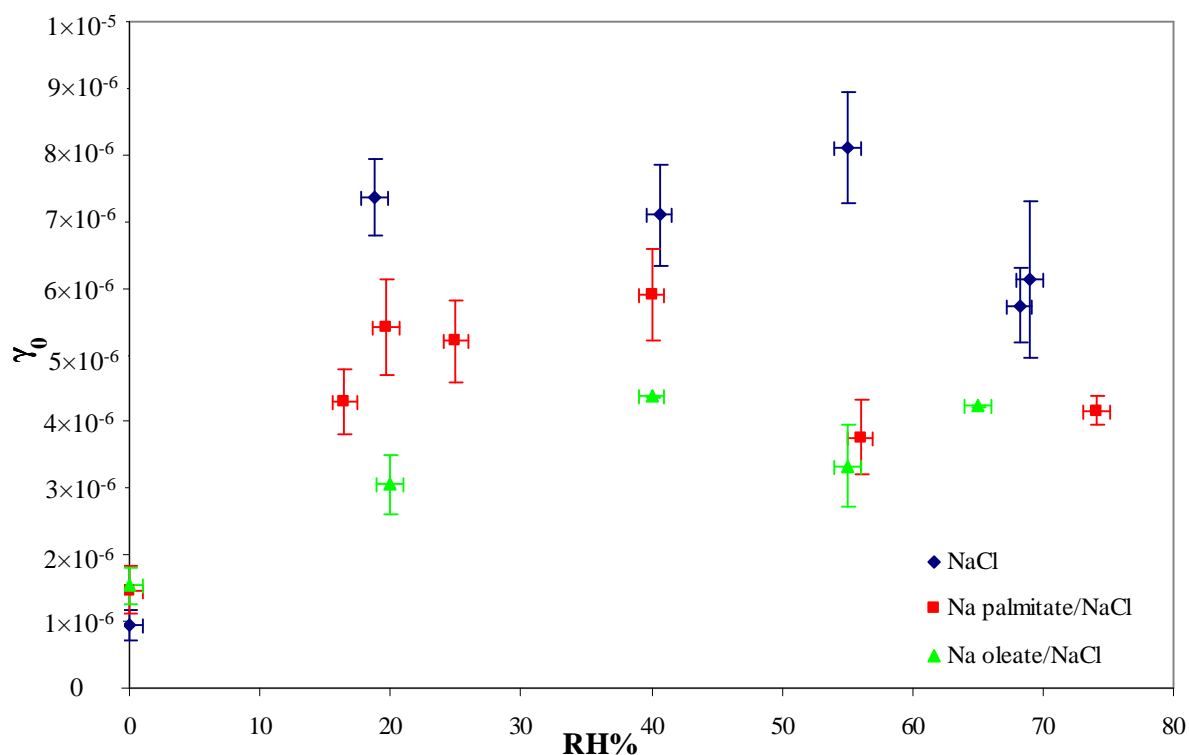


Fig. 6.10 Measured N₂O₄ initial uptake coefficient as a function of RH%. $[\text{N}_2\text{O}_4]_0 = (2.0 \pm 0.3) \times 10^{15}$ molec cm⁻³.

solid phase	RH%	γ_0	correction %
NaCl	0	$(9 \pm 2) \times 10^{-7}$	28
	20	$(7.4 \pm 0.6) \times 10^{-6}$	5
	40	$(7.1 \pm 0.8) \times 10^{-6}$	7
	55	$(8.1 \pm 0.8) \times 10^{-6}$	16
	70	$(5.94 \pm 0.19) \times 10^{-6}$	15
NaC ₁₆ /NaCl	0	$(1.5 \pm 0.4) \times 10^{-6}$	20
	20	$(5.0 \pm 0.6) \times 10^{-6}$	4
	40	$(5.9 \pm 0.7) \times 10^{-6}$	8
	55	$(3.8 \pm 0.6) \times 10^{-6}$	29
	74	$(4.2 \pm 0.2) \times 10^{-6}$	20
NaC _{18:1} /NaCl	0	$(1.5 \pm 0.3) \times 10^{-6}$	20
	20	$(3.1 \pm 0.4) \times 10^{-6}$	10
	40	$(4.38 \pm 0.02) \times 10^{-6}$	11
	55	$(3.3 \pm 0.6) \times 10^{-6}$	32
	70	$(4.23 \pm 0.08) \times 10^{-6}$	27

Tab. 6.9 Averaged measured N₂O₄ initial uptake coefficient as a function of RH% at $[\text{N}_2\text{O}_4]_0 = (2.0 \pm 0.3) \times 10^{15}$ molec cm⁻³.

Once again the corrections by the wall absorption are below the 40% suggested limit. A decreased S/N ratio caused by weaker IR absorptions of N₂O₄ reflects on increased relative uncertainties.

The effect of water vapour on the heterogeneous reactivity is reported by [Sverdrup G. M. et al., 1980], with high RH increasing of a factor of ten the N₂O₄ uptake coefficient on sea salt particles. We observed a similar, but less pronounced effect in our experiments, with the difference that the reactivity does not seem to monotonically increase with humidity content.

Also the relative intensities of γ_0 between the coated/uncoated NaCl are maintained as well, even if the differences become less evident because of an increased data dispersion: the F.A. presence induces a lowered heterogeneous reactivity of about 30%.

Comparing with previous work, we notice that the uptake coefficients we have measured are situated between the lower values of $(1.3 \pm 0.3) \times 10^{-6}$ measured on NaCl(100) in [Peters S. J. et al., 1996] and $\gamma = 10^{-7} \div 10^{-6}$ (RH \div 88%) reported for sea salt in [Sverdrup G. M. et al., 1980], and the higher $\gamma \sim 10^{-5}$ obtained on NaCl particles ([Yoshitake H., 2000], [Li H. et al., 2006]). These works mainly differ for the surface status and defect sites, reflecting into uptake coefficients sweeping over two or three orders of magnitude, as already suggested in [Peters S. J. et al., 1996].

6.4.1 Comparing NO₂ and N₂O₄ uptake coefficient

We can directly compare the absolute values of γ obtained by following NO₂ and N₂O₄. We consider that $MW_{N_2O_4} = 2 MW_{NO_2}$ and suppose that at every instant we are in the equilibrium conditions regarding the dimerisation/dissociation reaction of NO₂/N₂O₄ (eq. 2.1), so that their concentration are linked by a dimerisation constant:

$$(6.9) \quad [N_2O_4] = K_{dim} [NO_2]^2$$

We obtain the relationship between the two measured uptake coefficients as described in eq. 6.10 and 6.11:

$$(6.10) \quad \frac{\gamma_{N_2O_4}}{\gamma_{NO_2}} = \frac{k_{N_2O_4}}{k_{NO_2}} \frac{\langle c \rangle_{NO_2}}{\langle c \rangle_{N_2O_4}}$$

$$(6.11) \quad \gamma_{N_2O_4} = 2\sqrt{2}\gamma_{NO_2} \approx 2.8 \gamma_{NO_2}$$

We can plot the ratio between the N₂O₄ and NO₂ uptake coefficients measured following their depletion, as in fig. 6.11.

We can see that this ratio is actually between 2 and 3.5, with a slight tendency to decrease (~30%) for higher RH values. This cannot give more details about the mechanism or which of the two species are involved. The comparison between the uptake coefficients obtained by following these two species is a further proof of the quality of the measurements and consists of an internal cross validation.

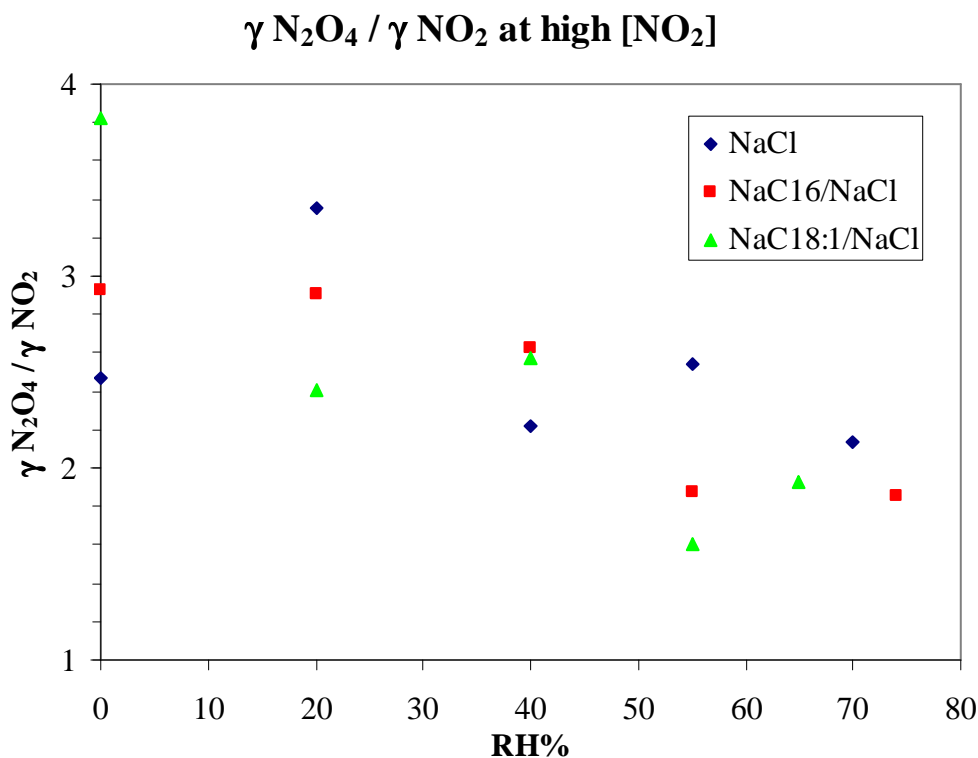


Fig. 6.11 N_2O_4 and NO_2 initial uptake coefficient ratio as a function of RH% at $[\text{NO}_2]_0 = (8.7 \pm 0.3) \times 10^{16}$ molec cm^{-3} .

6.5 NaCl reactivity following ClNO formation

The static exposition conditions used in our experiments allow us to follow the gas-phase kinetics of ClNO because of its accumulation inside the reactor (see fig. 6.13). $[\text{ClNO}]$ is determined by integrating the area of its most intense IR absorption, the ν_1 band centered at 1801 cm^{-1} , in the interval $1826\text{--}1776 \text{ cm}^{-1}$ with a correction for a linear baseline $1163\text{--}1944 \text{ cm}^{-1}$.

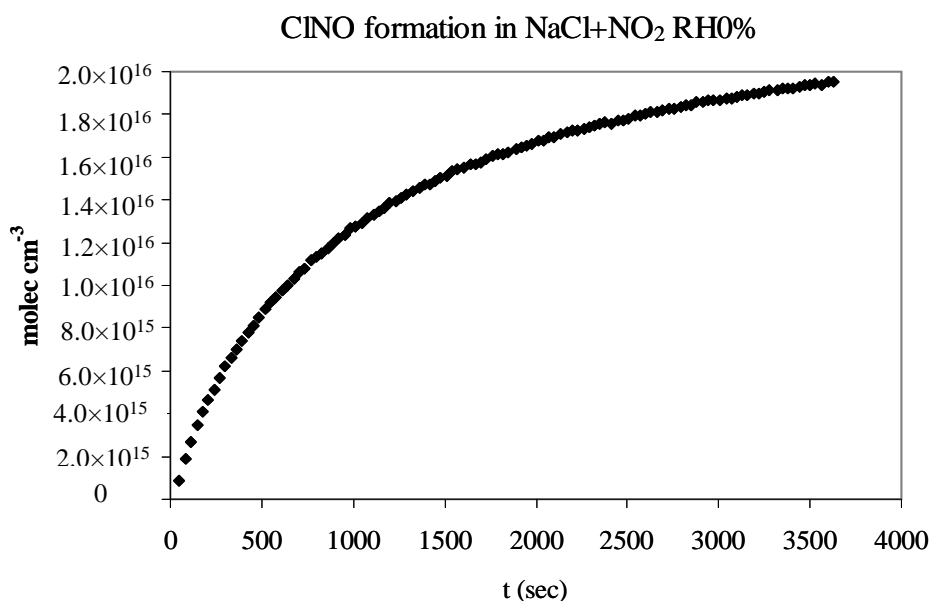


Fig. 6.13 Gaseous ClNO formation when NO_2 and NaCl are put in contact in a closed reactor at RH=0%. $[\text{NO}_2]_0 = (8.7 \pm 0.3) \times 10^{16}$ molec cm^{-3} .

As previously described in ch.2.4.1, this leads to the measurement of the reaction probability coefficient, directly derived from the product formation for the reactions 2.10 and 2.11. From eq. 2.29 we can obtain the following expression for this kinetic parameter, referring to NO_2 and N_2O_4 respectively:

$$(6.12) \quad \phi_{\text{NO}_2} = \frac{8V}{S\langle c \rangle [\text{NO}_2]} \frac{d[\text{ClNO}]}{dt}$$

$$(6.13) \quad \phi_{\text{N}_2\text{O}_4} = \frac{4V}{S\langle c \rangle [\text{N}_2\text{O}_4]} \frac{d[\text{ClNO}]}{dt}$$

The production rate of ClNO is calculated by a linear fitting over three values of [ClNO] as a function of t (a graphical representation is in fig. 6.14). An error deriving from the linear fitting (the slope standard deviation) is associated to every calculated rate.

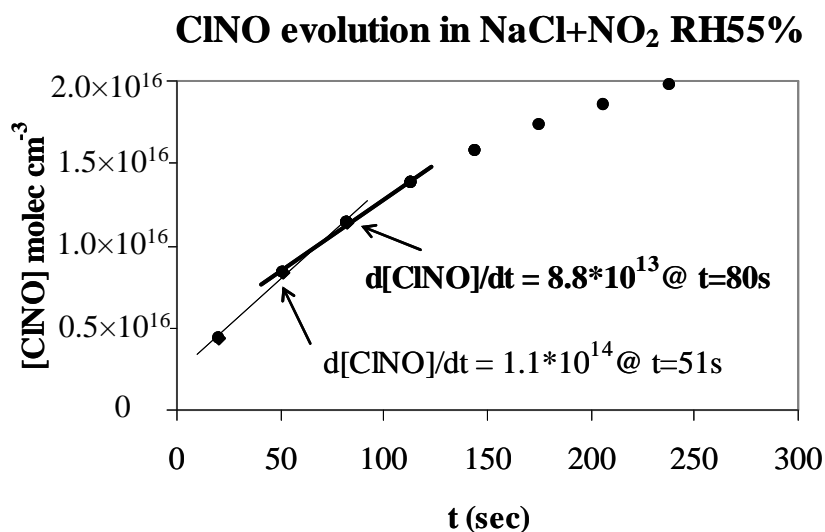


Fig. 6.14 ClNO rate production determination: a linear fitting over 3 consequent points of the [ClNO] vs time.

This formation rate is strongly time-dependent in cases of high RH. In fig.6.15 we report i.e. the production rates as a function of the starting point of this fitting for two experiments at RH=0% and RH=55% respectively.

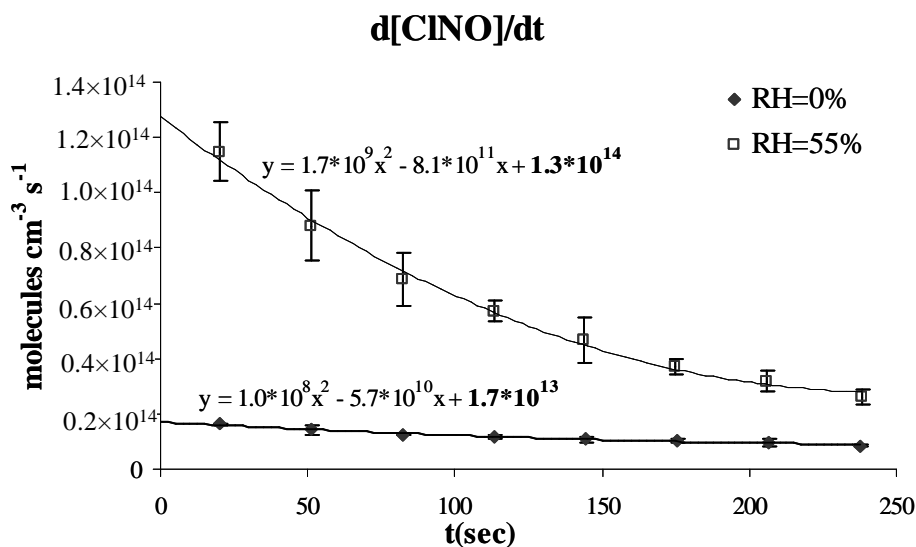


Fig. 6.15 ClNO formation velocity on the uncoated NaCl surface as a function of the position of the first fitting point at two different humidities. $[\text{NO}_2]_0 = (8.7 \pm 0.3) \times 10^{16} \text{ molec cm}^{-3}$.

In both cases CINO production rate in the gaseous phase is maximum at the beginning of the reaction and decreases as long as the reaction proceeds. The time-dependence is much more pronounced when RH=55%.

For this reason the initial reaction rate is estimated by fitting with a second-order polynomial the CINO formation.

The resulting reaction probability coefficients referred to the NO₂ species as the reactive one are reported in fig. 6.16 for the high [NO₂] experiments (the plotted lines are a eye-guide):

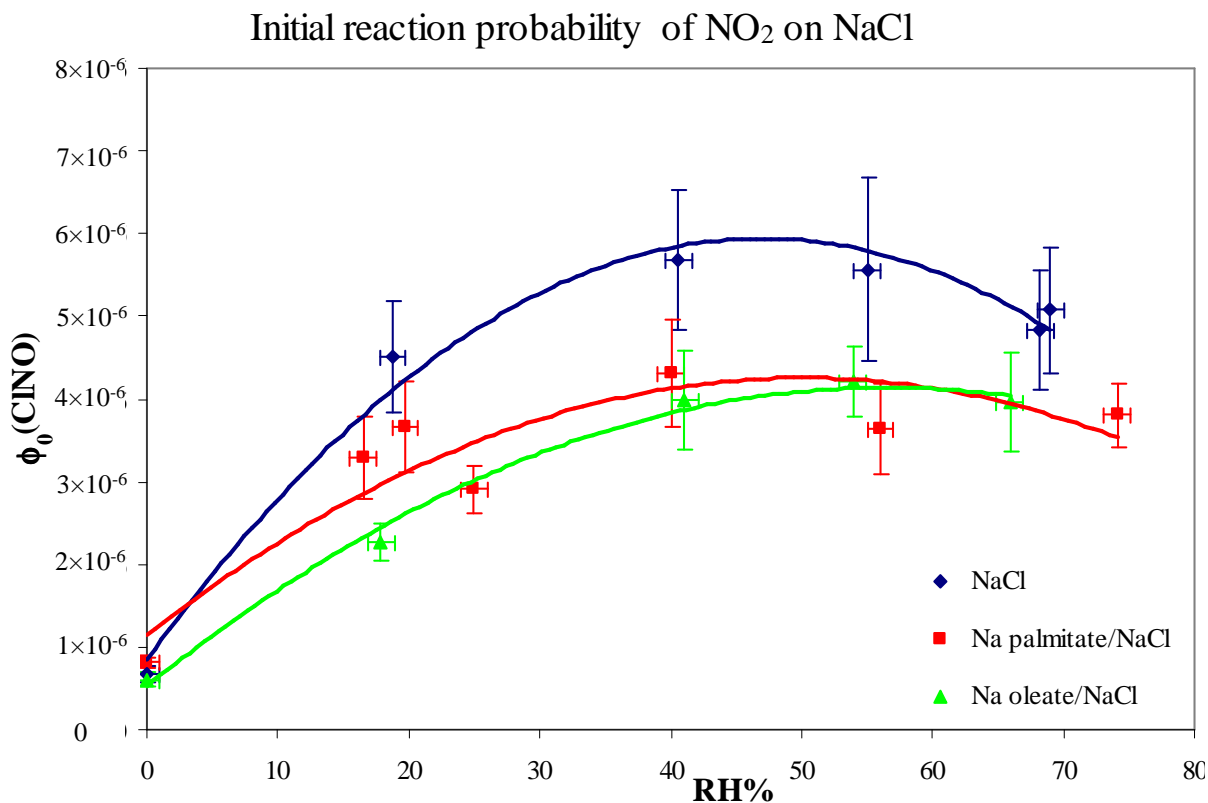


Fig. 6.16 Measured reaction probability of NO₂ as a function of RH% for [NO₂]₀=(8.7±0.3) × 10¹⁶ molec cm⁻³.

As a confirmation of the previously done observations, the reactivity trend as a function of RH is confirmed: it is increasing of a factor 5 comparing the dry exposition with the ones at 40-60% RH, with a slight decrease for higher humidity values.

The presence of the oleic and palmitic sodium salts coatings decrease of about 30% the reactivity around 40-60% RH, with the effect becoming less pronounced at higher and lower humidities.

In tables 6.10 and 6.11 the averaged values for NO₂ and N₂O₄ initial reaction probability measured following CINO formation at high and low [NO₂] are reported with their associated error (error propagation considering no uncertainties on S, V and T).

solid phase	RH%	$\phi_0 \text{NO}_2$	$\phi_0 \text{N}_2\text{O}_4$
NaCl	0	$(6.8 \pm 1.0) \times 10^{-7}$	$(2.0 \pm 0.3) \times 10^{-5}$
	20	$(4.5 \pm 0.7) \times 10^{-6}$	$(1.28 \pm 0.19) \times 10^{-4}$
	40	$(5.7 \pm 0.9) \times 10^{-6}$	$(1.7 \pm 0.2) \times 10^{-4}$
	55	$(5.6 \pm 1.1) \times 10^{-6}$	$(1.7 \pm 0.3) \times 10^{-4}$
	70	$(4.96 \pm 0.12) \times 10^{-6}$	$(1.78 \pm 0.03) \times 10^{-4}$
NaC ₁₆ /NaCl	0	$(8.1 \pm 0.7) \times 10^{-7}$	$(2.19 \pm 0.18) \times 10^{-5}$
	20	$(3.3 \pm 0.4) \times 10^{-6}$	$(9.04 \pm 0.013) \times 10^{-5}$
	40	$(4.3 \pm 0.6) \times 10^{-6}$	$(1.38 \pm 0.2) \times 10^{-4}$
	55	$(3.6 \pm 0.5) \times 10^{-6}$	$(1.19 \pm 0.18) \times 10^{-4}$
	74	$(3.8 \pm 0.4) \times 10^{-6}$	$(1.26 \pm 0.13) \times 10^{-4}$
NaC _{18:1} /NaCl	0	$(6.1 \pm 0.9) \times 10^{-7}$	$(1.6 \pm 0.2) \times 10^{-5}$
	20	$(2.2 \pm 0.2) \times 10^{-6}$	$(6.3 \pm 0.6) \times 10^{-5}$
	40	$(4.0 \pm 0.6) \times 10^{-6}$	$(1.2 \pm 0.18) \times 10^{-4}$
	55	$(4.2 \pm 0.6) \times 10^{-6}$	$(1.33 \pm 0.13) \times 10^{-4}$
	65	$(4.0 \pm 0.6) \times 10^{-6}$	$(1.30 \pm 0.19) \times 10^{-4}$

Tab. 6.10 Averaged measured initial reaction probability of NO₂ and N₂O₄ as a function of RH% for [NO₂]= $(8.7 \pm 0.3) \times 10^{16}$ molec cm⁻³ and [N₂O₄]₀= $(2.0 \pm 0.3) \cdot 1 \times 10^{15}$ molec cm⁻³.

solid phase	RH%	$\phi_0 \text{NO}_2$	$\phi_0 \text{N}_2\text{O}_4$
NaCl	0	$(3 \pm 2) \times 10^{-8}$	$(1.0 \pm 0.6) \times 10^{-5}$
	15	$(5 \pm 3) \times 10^{-8}$	$(1.6 \pm 0.7) \times 10^{-5}$
	35	$(1.1 \pm 0.5) \times 10^{-7}$	$(3.4 \pm 1.5) \times 10^{-5}$
	50	$(2.9 \pm 1.2) \times 10^{-8}$	$(9 \pm 4) \times 10^{-6}$
	85	$(1.7 \pm 0.7) \times 10^{-8}$	$(5 \pm 2) \times 10^{-6}$
NaC ₁₆ /NaCl	0	3.8×10^{-8}	1.1×10^{-5}
	15	4.4×10^{-8}	1.3×10^{-5}
	35	9.9×10^{-8}	3.0×10^{-5}
	65	$(8.6 \pm 0.3) \times 10^{-9}$	$(3.0 \pm 0.4) \times 10^{-6}$
	85	2.0×10^{-9}	6.2×10^{-7}
NaC _{18:1} /NaCl	0	8.4×10^{-9}	2.6×10^{-6}
	30	$(5.4 \pm 1.6) \times 10^{-8}$	$(1.6 \pm 0.5) \times 10^{-5}$
	50	7.5×10^{-8}	2.3×10^{-5}
	85	1.1×10^{-8}	3.5×10^{-6}

Tab. 6.11 Averaged measured initial reaction probability of NO₂ and N₂O₄ as a function of RH% for [NO₂]= $(8.4 \pm 0.3) \times 10^{15}$ molec cm⁻³ and [N₂O₄]₀= $(1.76 \pm 0.02) \cdot 1 \times 10^{13}$ molec cm⁻³.

The only reference value reported in the literature for $\phi(\text{NO}_2)$ measured following ClNO formation is given in [Finlayson-Pitts B. J., 1983] as a lower limit $\phi > 5 \times 10^{-8}$ for [NO₂] $\sim 10^{14}$ molec/cm³. In experiments at $\sim 10^{15}$ molec/cm³ the measured value at RH=0% is $(3 \pm 2) \times 10^{-8}$, therefore in good agreement with this reference value.

The found values of $\phi_0(\text{N}_2\text{O}_4)$ deriving by ClNO kinetics can be directly compared to $\phi(\text{N}_2\text{O}_4)$ from previous works measured by following NaNO₃ kinetics. A graphical representation can be found in fig. 6.17.

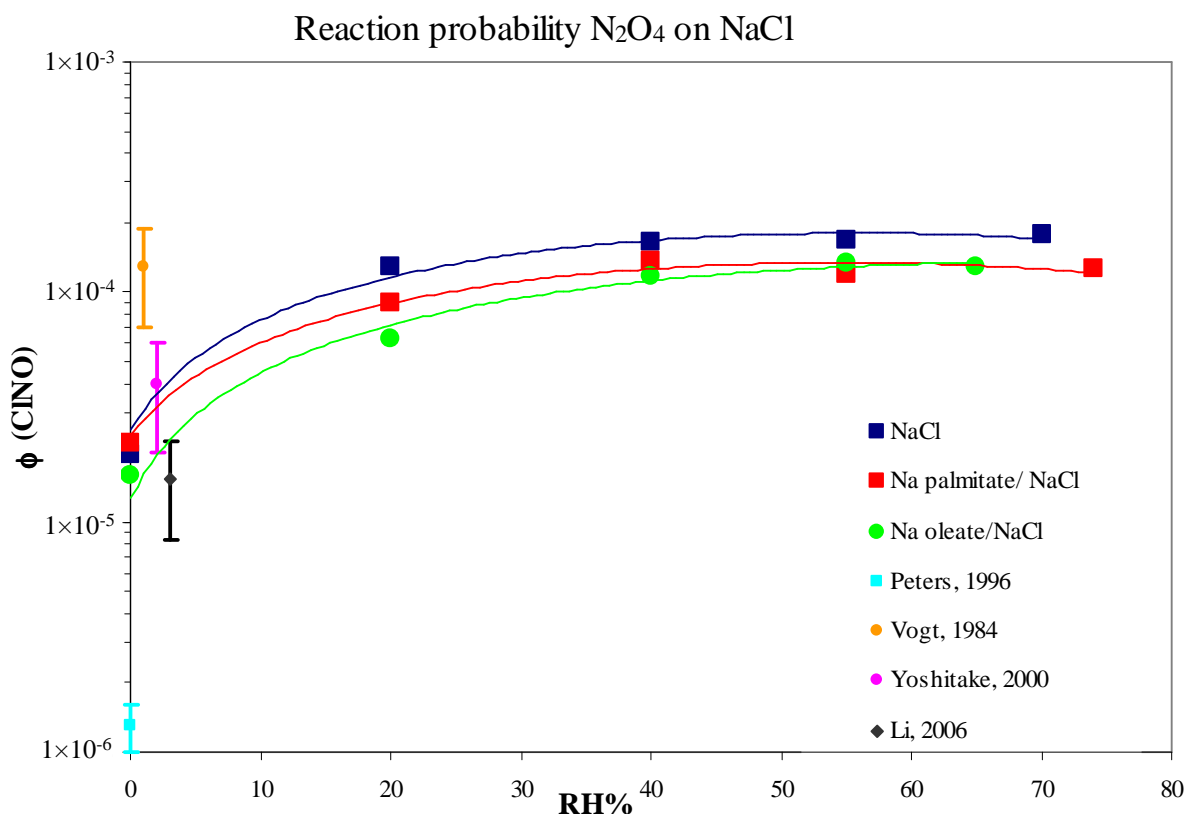


Fig. 6.17 A comparison between the reaction probability values ϕ obtained in this work and the literature reference values. The y-axis is in logarithmic scale and the reference works, obtained in RH=0% condition, are shifted along the x-axis for a more clear visualisation.

Again we are coherent with literature works, except for [*Peters S. J. et al., 1996*] in which freshly cleaved NaCl(100) surfaces were used after special cleaning procedures from impurities.

6.6 Comparing uptake and reactivity coefficients

The superposition of reaction probability and uptake coefficient trends for the coated and uncoated NaCl surfaces as a function of humidity is somehow astonishing if we consider that in the literature the increased NaCl/NO₂ reactivity in the presence of water vapor is attributed to the much faster reaction of HNO₃ on NaCl:



This reaction should produce HCl, which eventually remains stuck to the condensed phase. Since on the reactive salt surface [Cl⁻] is particularly high and the surface is thought to be strongly acidic because of the presence of the NO₂ hydrolysis products HNO₂ and HNO₃, there is no particular reason for HCl to remain ab/adsorbed on the surface. As a logic consequence the equilibrium should be shifted towards its gaseous form instead:



The presence of HCl in the gaseous phase is not detected maybe because of further rapid repartition on the reactor walls. Even if possible, this reaction schemes does not justify the large amounts of CINO detected in the gas phase if we do not introduce some extra elements.

We want to remind here some reactions, already introduced in ch.2.4, which involve the formation of ClNO(g) other than NO₂ reacting on NaCl:



These reactions have been studied in the homogeneous gaseous phase, but they could also take place heterogeneously on the NaCl surface, where the freshly produced HCl from the heterogeneous reaction 2.14 could be, in large proportions, transformed into ClNO(g) thanks to the heterogeneous hydrolysis NO₂ products.

A reformulation as an overall reaction for the production of nitrate on the NaCl surface could then justify such important amounts of ClNO formed even in the presence of water vapour:



The main consequence of such a reactive path is that ClNO, the typical product of the dry reaction (2.8), can be produced even in humid conditions and water has a catalytic role on the overall reaction.

The uptake coefficient of NO₂ and of the dimer N₂O₄ can be concomitantly compared also to their reaction probability coefficients measured following ClNO appearance. In fig.6.18 there is a direct comparison of the absolute values of γ and ϕ for the high [NO₂] experiments (coated and uncoated surfaces are reported with the same symbols).

If the quantity of taken up reactive gas is actually directly involved a heterogeneous reaction with production of ClNO, we should obtain a value around 1 for ϕ/γ in both cases.

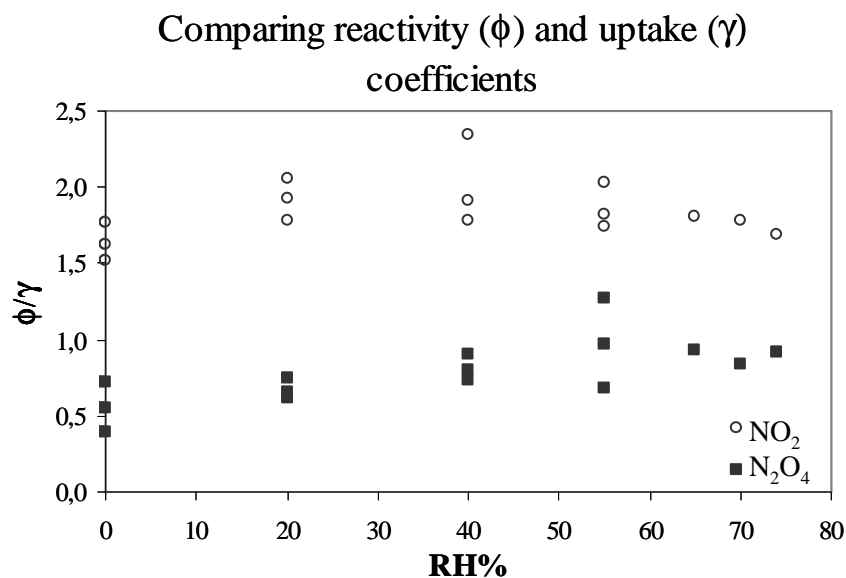


Fig. 6.18 Initial reaction probability to uptake coefficient ratio as a function of RH% for NO₂ and N₂O₄ species at [NO₂]₀=(8.7±0.3) × 10¹⁶ molec/cm³ and [N₂O₄]₀=(2.0±0.3) · 1 × 10¹⁵ molec cm⁻³. In empty symbols NO₂ is the reactive gas, in filled symbols N₂O₄ is considered the reactive species.

We observe in fig. 6.18 that the experimental ϕ/γ ratios are dispersed around 1.5 and 2, regardless the RH of the gas phase, when we consider NO₂ as the reactive species.

The same experimental ratios have values between 0.5 and 1 for N₂O₄, with a slightly tendency to increase at higher moist conditions.

Uncertainties on the IR absorption coefficient values σ used for determining the gaseous species concentrations (ClNO and NO₂) could explain the slight offset of ± 0.5 units in the ϕ_0/γ_0 vs RH experimental data.

Chapter 7 - Fitting the experimental kinetic profiles with a simple reactivity model

7. Fitting the experimental kinetic profiles with a simple reactivity model

The whole temporal profiles of NO_2 and ClNO concentration contain more information than the first minutes explored for deriving the initial uptake or reaction probability coefficients. If we consider the entire temporal evolution of the gas-phase species that can be followed by the FTIR spectrometer we could try to fit the experimental data (fig. 7.1) with their profiles derived from a simplified kinetic model.

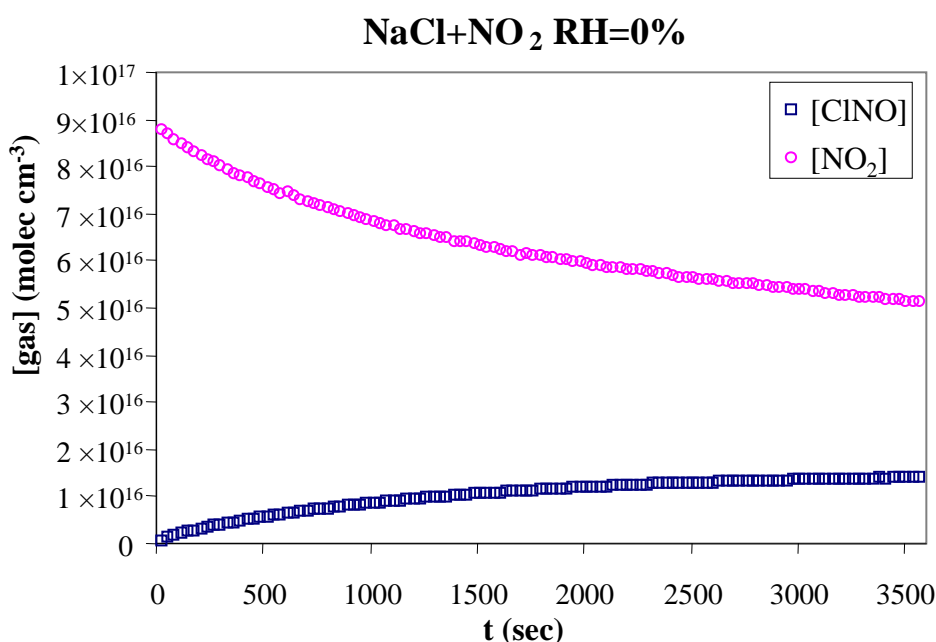


Fig. 7.1 An example of kinetic profiles of NO_2 and ClNO obtained from FTIR spectroscopy of the gas-phase when NaCl is exposed to NO_2 at $\text{RH}=0\%$.

If a good convergence between the experimental data and the modelled profiles is achieved, then we have access to some information about a hypothetical reaction mechanism. In particular we are interested in understanding the effect of humidity on the reactivity and in any possible change in the mechanism when the NaCl surface is coated with FA.

This simple reactivity model would take into account the main reactions and processes we consider to occur inside the closed reactor.

As in chapter 6 we will first describe the case of NaCl exposed to NO_2 in dry conditions, while in the second part the presence of water vapour is taken into account. In the third part the presence of the FA coating is analysed in terms of kinetic effect on the reactivity. We will conclude by quantifying the total reactivity of the NaCl/NO_2 through measurements of the total amount of formed NaNO_3 .

7.1 Kinetic model when RH=0%

When no water vapour is present in the reactor, we can assume that the main reactions occurring are the heterogeneous reactivity between NO₂ and NaCl (“dry reaction”) and the NO₂ loss on the reactor walls *****:



where eq. 7.1 and 7.2 express the reaction rates as a function of the reactant gas concentration (in molec cm⁻³) and of the total number of active surface sites {NaCl} (in sites).

7.1.1 Hypothesis

In the mathematical expression of the reaction rates (i.e. eq. 7.1 and 7.2) we use equations which are typical of a homogeneous processes, such as $v = k[A]^\alpha[B]^\beta$ for the general reaction $A + B \rightarrow \text{products}$. Moreover we also assume that there are:

- First order uptake: of NO₂ on the NaCl surface. A short discussion on the possible reaction order has already been reported at pg.140. Some tests run with the hypothesis of a second order NO₂ uptake did not give satisfactory results, particularly in presence of water vapour.
- Salt surface saturation: the dry reaction between NaCl and NO₂ forms NaNO₃ which progressively occupies the active sites of the (100) surface - the reaction rates contain then the number of the active sites expressed as {NaCl}. Taking into account the surface saturation is a realistic approach which has already been used in the literature for modelling heterogeneous reactions [Kirchner U. et al., 2000].
- Constant wall loss: the absorption of NO₂ on the reactor walls does not give saturation so that k_{wall} is constant all long the reaction.

7.1.2 Explicit Euler method and input data

The differential equations describing the evolution of the concentrations of the different chemical species (A) involved in the reaction is:

$$(7.3) \quad \frac{d[A]_t}{dt} = v_A(t)$$

The explicit Euler method is used for solving this differential equation. It is based on the approximation of a curve - in this case $[A]_t = f(t)$ - with a polygonal one. The time axis has to be divided in discrete intervals (Δt) and the function value at a given time t_n is calculated knowing its value and its derivative (v_A) at t_{n-1} . Therefore the kinetic profiles of the species A can be described as:

$$(7.4) \quad [A]_{t_n} = v_A(t_{n-1}) \cdot \Delta t + [A]_{t_{n-1}} ; \quad t_n = t_{n-1} + \Delta t$$

***** Observed from the gaseous NO₂ depletion even in absence of the reactive salt surface.

The kinetic mathematical model consists then in calculating an estimation of $[A]_t^{\text{mod}}$ and $v_A(t_n)$ for all the involved species, which in our case are NO_2 , ClNO and NaCl , through an iterative procedure which is repeated with an imposed increment Δt .

$$(7.5) \quad [\text{NO}_2]_{t_n}^{\text{mod}} = v_{\text{NO}_2}(t_{n-1}) \cdot \Delta t + [\text{NO}_2]_{t_{n-1}}^{\text{mod}} \quad v_{\text{NO}_2} = -\frac{d[\text{NO}_2]}{dt} = -2v_1 - v_2$$

$$(7.6) \quad [\text{ClNO}]_{t_n}^{\text{mod}} = v_{\text{ClNO}}(t_{n-1}) \cdot \Delta t + [\text{ClNO}]_{t_{n-1}}^{\text{mod}} \quad v_{\text{ClNO}} = \frac{d\text{ClNO}}{dt} = v_1$$

$$(7.7) \quad \{\text{NaCl}\}_{t_n}^{\text{mod}} = v_{\text{NaCl}}(t_{n-1}) \cdot \Delta t + \{\text{NaCl}\}_{t_{n-1}}^{\text{mod}} \quad v_{\text{NaCl}} = -\frac{d\{\text{NaCl}\}}{dt} = -v_1$$

We used $\Delta t = 20\text{s}$, an interval coherent with the experimental data interval, since a spectrum acquisition time is 19s . This Δt is, moreover, very small compared to the timescales characteristic of the studied reactions.

The initial concentration of NO_2 and ClNO are those experimentally measured:

$$(7.8) \quad [\text{NO}_2]_0^{\text{mod}} = [\text{NO}_2]_0^{\text{exp}}$$

$$(7.9) \quad [\text{ClNO}]_0^{\text{mod}} = [\text{ClNO}]_0^{\text{exp}}$$

whilst an initial estimation of $\{\text{NaCl}\}_0$, k_{slow} and k_{wall} has also to be given. These are the parameters have to be adjusted for achieving a good fitting between the experimental and modelled temporal profiles of NO_2 and ClNO .

7.1.3 Outputs and Results

The quality of the fitting can be evaluated by the parameter σ_{FIT} which has to be minimised:

$$(7.10) \quad \sigma_{\text{FIT}} = \sigma_{\text{NO}_2} + \sigma_{\text{ClNO}}$$

It derives from the standard deviation for both ClNO and NO_2 curves:

$$(7.11) \quad \sigma = \sqrt{\frac{\sum (Y^{\text{mod}} - Y^{\text{exp}})^2}{n}}$$

The quality of the fitting can also be appreciated by a graphical method as reported in fig. 7.2. A good agreement with the experimental data is obtained, meaning that from this simple kinetic model we can obtain a good estimation of the surface active sites and of the rate constants:

$$\begin{aligned} \{\text{NaCl}\}_0 &= 1.46 \times 10^{16} \text{ sites} \\ k_{\text{slow}} &= 1.05 \times 10^{-20} \text{ sites}^{-1} \text{ s}^{-1}; \\ k_{\text{wall}} &= 4.3 \times 10^{-5} \text{ s}^{-1}. \end{aligned}$$

From fig. 7.2 we can observe, by following $\{\text{NaCl}\}$ profile in yellow, a progressive surface saturation that can therefore explain the experimentally observed deviation from a first order kinetic for both NO_2 consumption and ClNO formation at longer reaction times. Indeed the experimental and modelled loss rate of NO_2 are described by the kinetic parameters as in eq. 7.12:

$$(eq. 7.12) \quad k_{\text{obs}} = (k_{\text{het}} + k_{\text{wall}})^{\text{exp}} \equiv (2k_{\text{slow}} \{\text{NaCl}\} + k_{\text{wall}})^{\text{mod}}$$

where we can see the real dependence of the observed loss rate on the number of active sites $\{NaCl\}$.

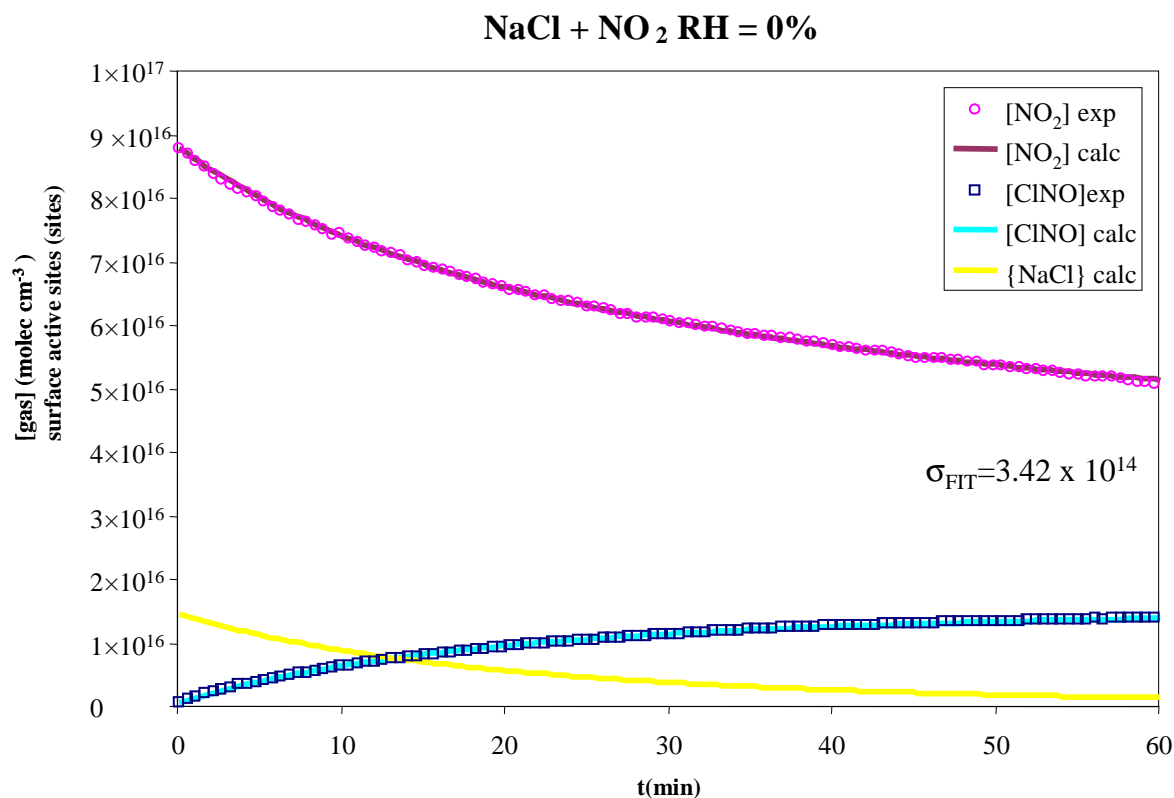


Fig. 7.2 Experimental and calculated profiles of $[NO_2]$, $[ClNO]$ (and $\{NaCl\}$) for the $NaCl/NO_2$ system at $RH=0\%$.

The optimised rate constants k_{slow} and k_{wall} can be used to evaluate the rates of the heterogeneous reaction (R1, eq. 7.1) and of the parasite wall loss process (R2, eq. 7.2). Their temporal evolutions are showed in fig. 7.3, from where can observe that within the first 30 minutes of the reaction the heterogeneous $NaCl/NO_2$ process predominates in the kinetics, whilst for longer contact times the reactant losses on the wall become more important.

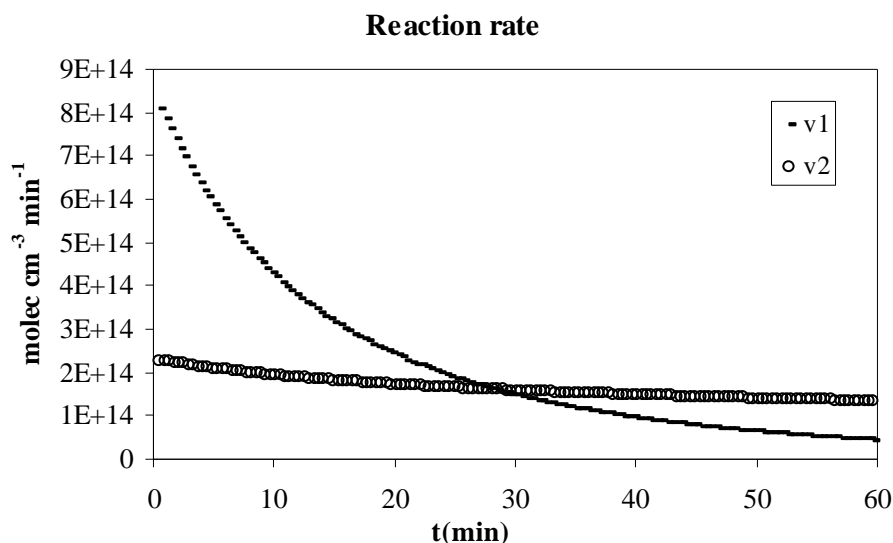


Fig. 7.3 Calculated reaction rates for the heterogeneous and wall loss reactions in the $NaCl/NO_2$ system at $RH=0\%$.

The same figure, when plotted for the lower [NO₂] experiments, clearly shows that the wall loss process is always more important than the heterogeneous NaCl/NO₂ reaction. This is a further confirmation of the difficulty in exploiting the data obtained in that conditions.

The initial heterogeneous reactivity of the NaCl/NO₂ system can also be estimated from the rate constant k_{slow} so that we can calculate the values of γ_0^{mod} and ϕ_0^{mod} (eq. 7.13, eq. 7.14):

$$\text{(eq. 7.13)} \quad \gamma_0^{\text{mod}} = \frac{4V}{S\langle c \rangle} k_{\text{het}}^{\text{mod}} \quad \text{with} \quad k_{\text{het}}^{\text{mod}} = 2k_{\text{slow}} \{ \text{NaCl} \}$$

$$\text{(eq. 7.14)} \quad \phi_0^{\text{mod}}_{\text{NO}_2} = \frac{8V}{S\langle c \rangle [\text{NO}_2]} v_{\text{ClNO}} \quad \text{with} \quad v_{\text{ClNO}} = k_{\text{slow}} [\text{NO}_2] \{ \text{NaCl} \}$$

The initial values of uptake and reactivity coming from the model can be directly compared to the experimental ones, obtained as described in ch.6. We observe that they are in quite good agreement within the experimental error, as reported in tab.7.1.

7.1.4 Fatty acids-coated surfaces

The same kinetic model can be applied also to the F.A. coated salt surfaces, from which we obtain a satisfying agreement between experimental and modelled kinetic parameter as well. These values for the case of RH=0% are reported in tab.7.1:

	NaCl	NaC ₁₆ /NaCl	NaC _{18:1} /NaCl
$k_{\text{het}}^{\text{mod}} \text{ (s}^{-1}\text{)}$	3.1×10^{-4}	3.5×10^{-4}	2.5×10^{-4}
$k_{\text{het}}^{\text{exp}} \text{ (s}^{-1}\text{)}$	$(2.34 \pm 0.11) \times 10^{-4}$	$(3.1 \pm 0.2) \times 10^{-4}$	$(2.44 \pm 0.12) \times 10^{-4}$
difference experimental/ model (%)	- 30 %	- 13 %	- 2 %

Tab. 7.1 Comparison between the modelled and experimental values of k_{het} of the coated/uncoated NaCl surfaces exposed to NO₂ at RH=0%.

We can observe that the modelled and experimental data are coherent (within a 30% interval) and that there is not a big difference between the behaviour of the coated or uncoated NaCl(100) surfaces when they are exposed to NO₂ at RH=0%.

A possible systematic underestimation of the experimental heterogeneous reactivity compared to the modelled one is easily explained by the correction used for taking into account the wall losses. This is indeed obtained from a direct measurement of NO₂ loss rate in the empty reactor, but it overestimates the real wall loss rate in presence of a reactive surface.

This is verified by the necessity of adjusting, in the model, the k_{wall} parameter when its initial estimation is $k_{\text{wall}}^{\text{exp}} (=1.05 \times 10^{-4} \text{ s}^{-1})$. The difference between modelled and experimentally measured k_{wall} (-60% for NaCl) satisfactory explains the discrepancy between the values of k_{het} .

7.2 Kinetic model when RH ≠ 0%

When some water vapour is present in the gaseous phase, using only R₁ and R₂ reactions for fitting the experimental NO₂ and ClNO profiles is not adequate any more. In fig. 7.4 you can see, i.e., the case of NaCl/NO₂ at RH=40%, where the need of a supplementary sink process for NO₂ is evident. At higher RH% ClNO depletion has also to be modelled.

The problem of taking into account the effect of gaseous or surface adsorbed water can be solved by introducing some supplementary reactions such as NO₂ and ClNO hydrolysis (R3 and R5) as well as the surface reconstruction process (R4). Their rate expressions are defined by the rate coefficient k_{hum} , k_{cat} and k_{dest} as in eq. 7.15-17:

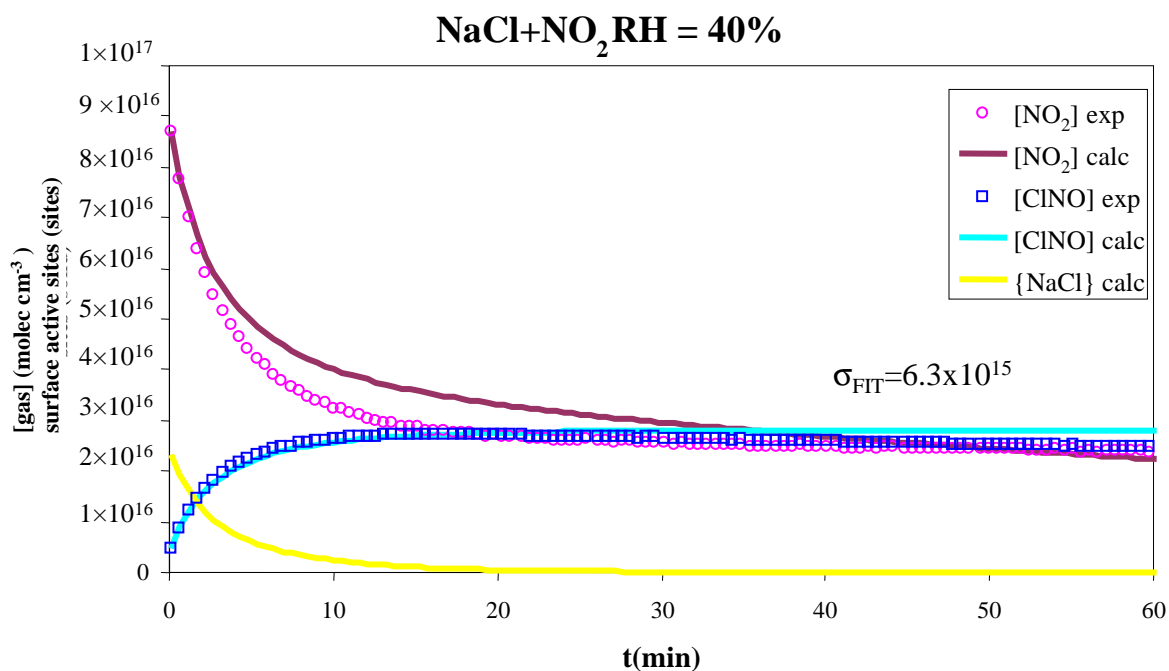
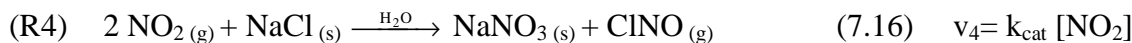
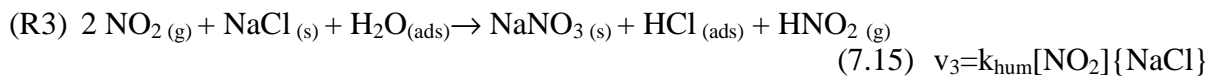


Fig. 7.4 Experimental and calculated profiles of [NO₂], [ClNO] and {NaCl} for the NaCl/NO₂ system at RH=40%.

7.2.1 Hypothesis

- NO₂ hydrolysis (R3): happens on the salt surface itself, producing HNO₂ and HNO₃ which immediately reacts with NaCl to give gaseous HCl, and solid NaNO₃. NaNO₃ physically occupies a portion of the surface and contributes to its progressive saturation (i.e. [Zangmeister C. D. et al., 2001]). No ClNO is produced in this reaction path. The reaction rate is of first order in both NO₂ and surface active sites.
- Surface reconstruction (R4): is usually linked to the presence of surface thin nitrate so that we can assume that a portion of the forming nitrate is not dependent on the concentration of active surface Cl⁻ sites. In the reaction occurring between NO₂ and NaCl the adsorbed water plays a catalytic role as already suggested in ch. 6.6. The surface reorganisation generates fresh NaCl and the overall reaction, through the adsorbed HCl and HNO₂ intermediates, forms nitrate on the (100) surface and releases ClNO into the gas phase. We assume a rate constant which depends only on [NO₂] (eq. 7.16). The different amounts of surface adsorbed water, considered as constant during

the whole reaction, are taken into account in the reaction constant k_{cat} , which therefore can vary for different relative humidity regimes.

- CINO loss (R5): is a first order, probably heterogeneous hydrolysis reaction, as it is suggested in previous works [Karlsson R. et al., 1996]. This process becomes particularly important at higher values of RH. The water concentration is assumed to be constant as long as the reaction occurs and is therefore incorporated inside the constant k_{dest} .

From the mechanism R1-R5 [NO₂], [CINO] and {NaCl} temporal profiles can be calculated in terms of the equation rates described below:

$$(7.18) \quad v_{\text{NO}_2} = -2v_1 - v_2 - 2v_3 - 2v_4$$

$$(7.19) \quad v_{\text{CINO}} = v_1 + v_4 - v_5$$

$$(7.20) \quad v_{\text{NaCl}} = -v_1 - v_3$$

7.2.2 Outputs

As in the case of the kinetic model validated for RH=0%, this model provides the following outputs:

- The estimation of the initial concentration of active surface sites {NaCl}₀ and their temporal evolution
- The estimation of the rate constants of the different reactions and processes involved: k_{slow} , k_{wall} , k_{hum} , k_{cat} , k_{dest} .

From the two previous outputs we can calculate the reaction rate profiles. This supplies an estimation of the contributions to the overall heterogeneous reactivity of the different processes involved. Indeed at every instant t we have access to each term of the following expression:

$$(7.21) \quad (k_{\text{het}})_t^{\text{mod}} = 2(k_{\text{slow}} \{\text{NaCl}\}_t + k_{\text{hum}} \{\text{NaCl}\}_t + k_{\text{rap}})^{\text{mod}}$$

In particular we can:

- determine the contributions of the different reactions to the initial uptake or reactivity coefficient values;
- compare the calculated and experimental values of the initial uptake and reactivity.

7.2.3 Results

We report here, as examples, two cases of NaCl/NO₂ reactivity at two different humidities. At RH=40% we show the effect of the additional reactions on the quality of the fitting and the supplementary information we can obtain with this more refined, but still very simple, model. The case of RH=70%, a highly moist environment typical of the marine boundary layer, is also presented.

RH=40%

We have already shown in fig. 7.4 the lack of fit between the modelled and experimental data if only reactions 7.1 and 7.2 are taken into account. This can be observed also in fig. 7.5, where $\sqrt{(Y^{\text{mod}} - Y^{\text{exp}})^2}$, taken as an indicator of the fitting error, is plotted for the simple and

for the “extended” kinetic models. In the first case (empty squares) there is a particular failure in the 3-30 minutes range, where NO_2 is underestimated. At longer reaction times the error increases again due to the presence of ClNO hydrolysis which is not taken into account in the model.

If we add the hydrolysis reactions (of both ClNO and NO_2) and the surface reconstruction process, we can observe a clear improvement in the quality of the model: the total fitting error diminishes by a factor 12 and its repartition all along the kinetic experiment is more homogeneous (fig. 7.5, filled squares).

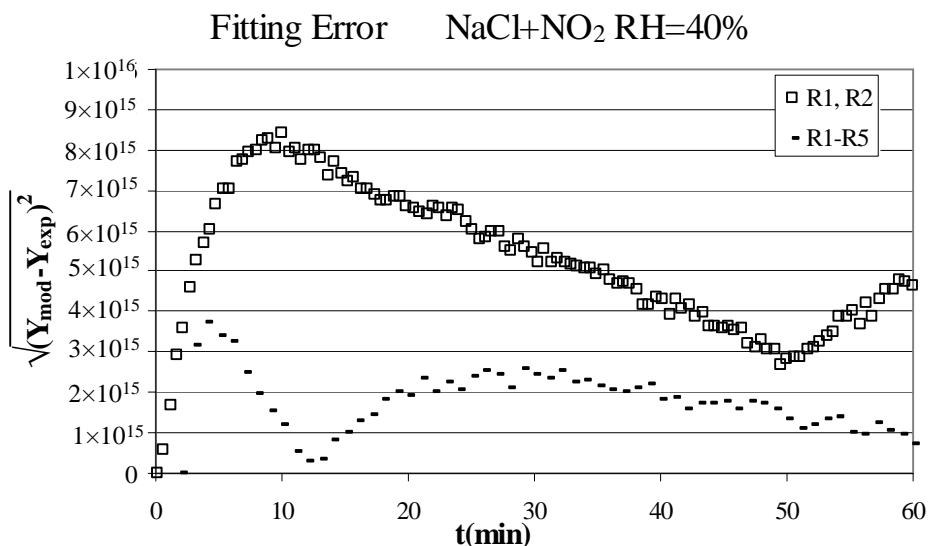


Fig. 7.5 Fitting errors of the two kinetic modes for the NaCl/NO_2 system when $\text{RH}=40\%$ (sum of both NO_2 and ClNO profiles): in empty squares the model is constituted of only R1 and R2 ; in filled squares the R1-R5 reactions are considered in the model.

The $\text{RH}=40\%$ calculated and experimental data are plotted together in fig. 7.6, where the good agreement between the two set of data can be also graphically appreciated. It can also be observed that after 20 minutes the NaCl surface becomes totally saturated.

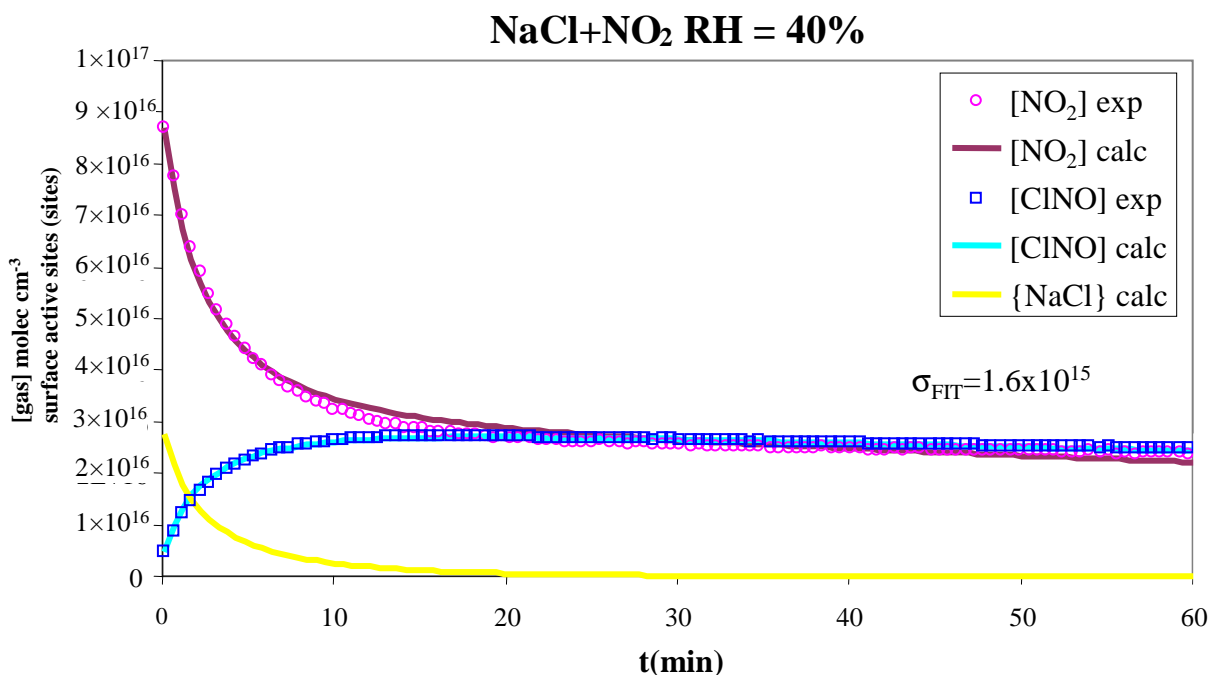


Fig. 7.6 Experimental and calculated temporal profiles of $[\text{NO}_2]$, $[\text{ClNO}]$ and $\{\text{NaCl}\}$ for the NaCl/NO_2 system at $\text{RH}=40\%$ when NO_2 and ClNO hydrolysis and surface reconstruction processes are taken into account.

The outputs of the model are the followings:

$$\{\text{NaCl}\}_0 = 2.83 \times 10^{16} \text{ sites}$$

reaction	k	m.u.
R1 - slow	6.67×10^{-20}	sites s ⁻¹
R2 - wall	7.50×10^{-5}	s ⁻¹
R3 - hum	1.00×10^{-20}	sites s ⁻¹
R4 - cat	1.67×10^{-5}	s ⁻¹
R5 - dest	6.67×10^{-5}	s ⁻¹

Tab.7.2 Outputs of the kinetic model for the NaCl/NO₂ system at RH=40%.

We can compare the obtained ClNO hydrolysis rate constant with the value reported in [Karlsson R. et al., 1996], where two possible heterogeneous reactions for ClNO disappearance inside their glass reactor are indicated, dry deposit and hydrolysis respectively:

$$(7.21) \quad v = k_{\text{dry}}[\text{ClNO}] \quad \text{with} \quad k_{\text{dry}} = (1.0 \pm 0.3) \times 10^{-5} \text{ s}^{-1}$$

$$(7.22) \quad v = k_{\text{hyd}}[\text{ClNO}][\text{H}_2\text{O}] \quad \text{with} \quad k_{\text{hydr}} < (7.4 \pm 2.4) \times 10^{-22} \text{ cm}^3 \text{ molec}^{-1} \text{ s}^{-1} \text{ at } 296\text{K}$$

If we calculate k_{dest} as in eq. 7.22 for our experimental conditions (RH=40% and T=297K; [H₂O]~ $3.1 \times 10^{17} \text{ molec cm}^{-3}$) we obtain the upper limit of $(23 \pm 7) \times 10^{-5} \text{ s}^{-1}$. The value we obtained by the modelling, without any assumption on the mechanism, is in good agreement with the reported values, with $k_{\text{dry}} = 1 \times 10^{-5} < k_{\text{dest}} = 6.7 \times 10^{-5} < 23 \times 10^{-5} \text{ s}^{-1}$.

Another important result that we can obtain from these constants are the different reaction rates. They are plotted in fig. 7.7, where their evolution can indicate the weight of the different processes all long the experiment.

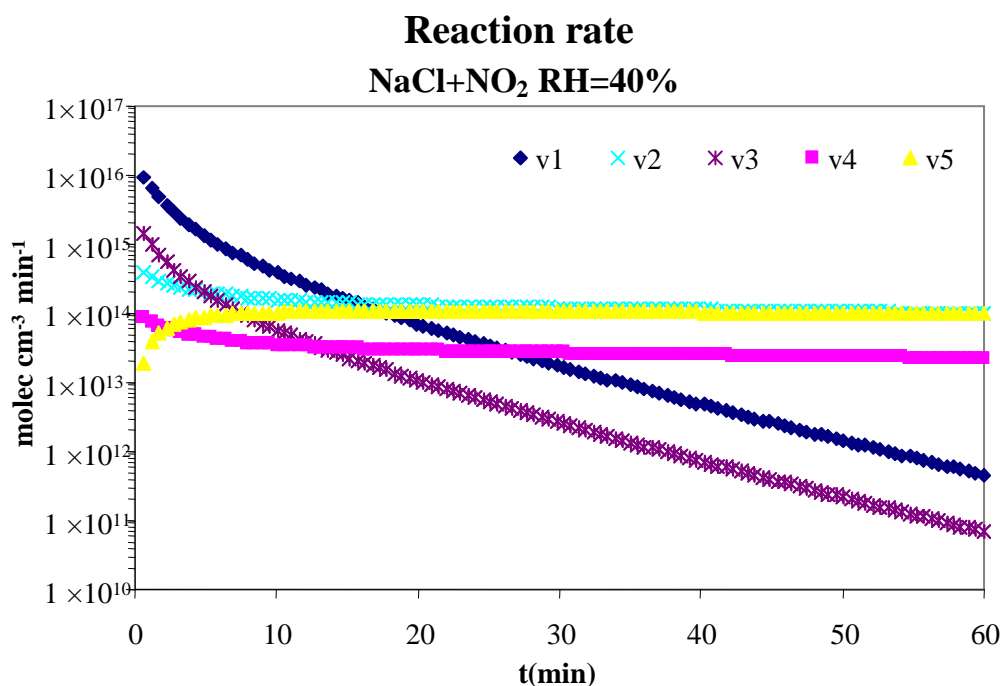


Fig. 7.7 Reaction rates for the NaCl/NO₂ system at RH=40% with the R1-R5 model.

In particular we can notice that:

- The “dry reaction” (R1) is the most important process in the first 15 minutes of the kinetics;
- The “humid reaction” (R3) is more important at the beginning, but, as the dry one, decreases as long as the surface become saturated in NaNO_3 . It contributes for less then 15% to the initial heterogeneous reactivity.
- The heterogeneous reaction accompanied by the surface reconstruction (the “catalytic reaction” R4) does not give a significant contribution to the initial reactivity, but becomes more important as long as the surface saturates. After 25 minutes it becomes the main reaction of NO_2 on the surface.
- ClNO hydrolysis (R5) equilibrates the ClNO production rate after approximately 20 minutes. Also in the ClNO kinetic profile (fig. 7.6, blue squares) we observed that a plateau is reached in this zone, before the losses become more important than the release from the surface.
- NO_2 wall losses are less important than any other heterogeneous reaction during the first 15 minutes. Its contribution to the overall NO_2 depletion process is negligible at the beginning, when γ is measured.
- In our closed system, almost all the reactivity is expressed in the first minutes of contact between the solid and gaseous phase because after 10 minutes the reactivity has already decreased at least of a factor 10.

By comparing the calculated and measured reaction rates of NO_2 (fig. 7.8) we can observe that the calculated values underestimate the initial global reactivity of about 14%. The main difference is observed in the v_2/v_{wall} component: a possible explanation could be that NO_2 wall loss is indeed not constant all long the process, but it is faster at the beginning and slows down after some saturation on the reactor wall occurs.

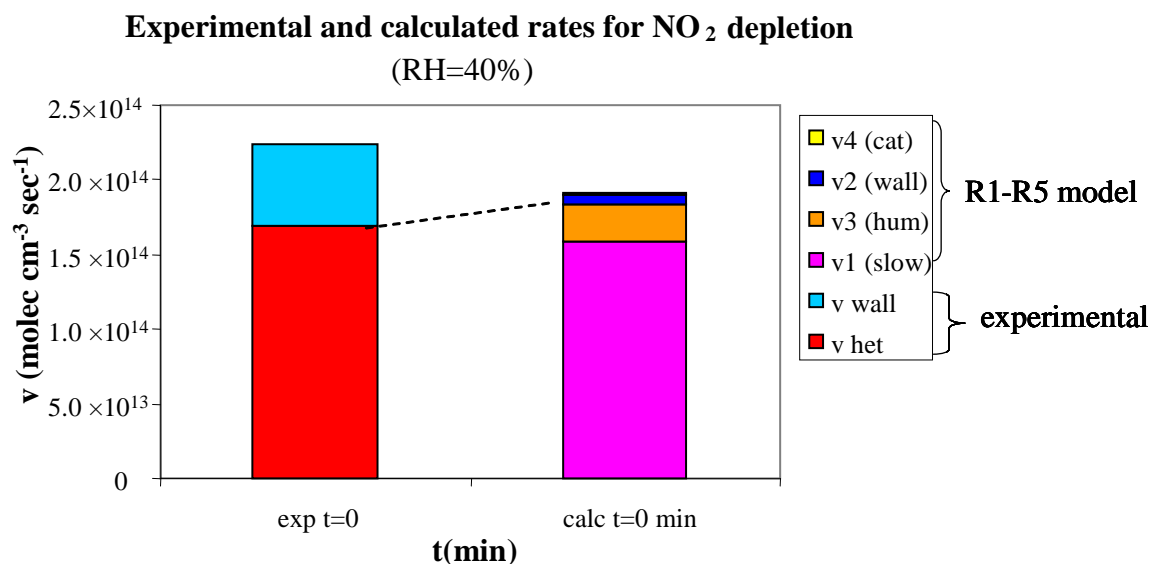


Fig. 7.8 Comparison between the total NO_2 initial depletion rates in the experimental and modelled data at RH=40%.

The main aim of the kinetic model is to assess the contribution from the different reactions to the observed reactivity. Since all the three NaCl/NO_2 reactions we considered in the model are assumed to be of first order in $[\text{NO}_2]$, their relative contributions, which are plotted in fig. 7.9, reflect what would be observed also in an open system where NO_2 can continuously be available (like in the atmosphere).

We can see that at the very beginning the overall reactivity is mainly due to the “dry” reaction and about 10% is due to NO₂ hydrolysis products. The surface reconstruction process is totally negligible compared to the other two processes. After 30 minutes more than 50% of the heterogeneous uptake of NO₂ on NaCl is due to the surface reconstruction process.

We can extrapolate these observations to a case in which [NO₂] is constant so that, inside the kinetic model assumptions, also v₄ would be constant all over the reaction. Since the absolute value of v₄ is very low compared to the initial v₁ and v₃, the total heterogeneous reactivity would decrease because the very rapid surface saturation is only partially compensated by its slow, water-induced, reorganisation.

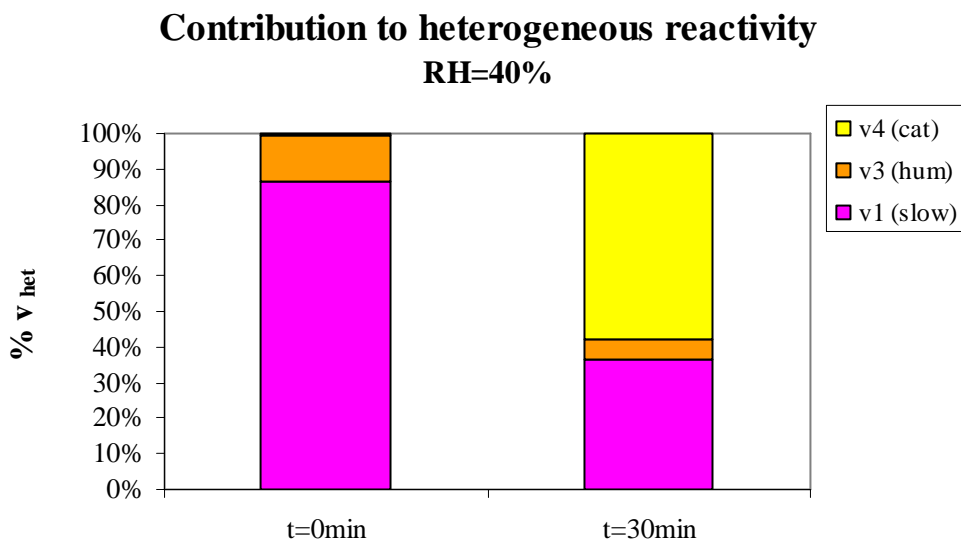


Fig. 7.9 Contribution of the different processes to the global heterogeneous reactivity at t=0 and t=30min (RH=40%).

RH=70%

We report here an exemple of analysis of the experimentally observed profiles of the gaseous NO₂ and ClNO concentrations also in the case of a much higher RH, near to the deliquescence point of bulk NaCl. The kinetic model fits well to the experimental points, as it can be observed in fig. 7.10.

From the fitting procedure we obtain the following outputs:

$$\{\text{NaCl}\}_0 = 2.46 \times 10^{16} \text{ sites}$$

reaction	k	m.u.
R1 - slow	5.83×10^{-20}	sites s ⁻¹
R2 - wall	1.42×10^{-4}	s ⁻¹
R3 - hum	1.00×10^{-20}	sites s ⁻¹
R4 - cat	1.67×10^{-5}	s ⁻¹
R5 - dest	1.22×10^{-4}	s ⁻¹

Tab. 7.3 Outputs of the kinetic model for the NaCl/NO₂ system when RH=70%.

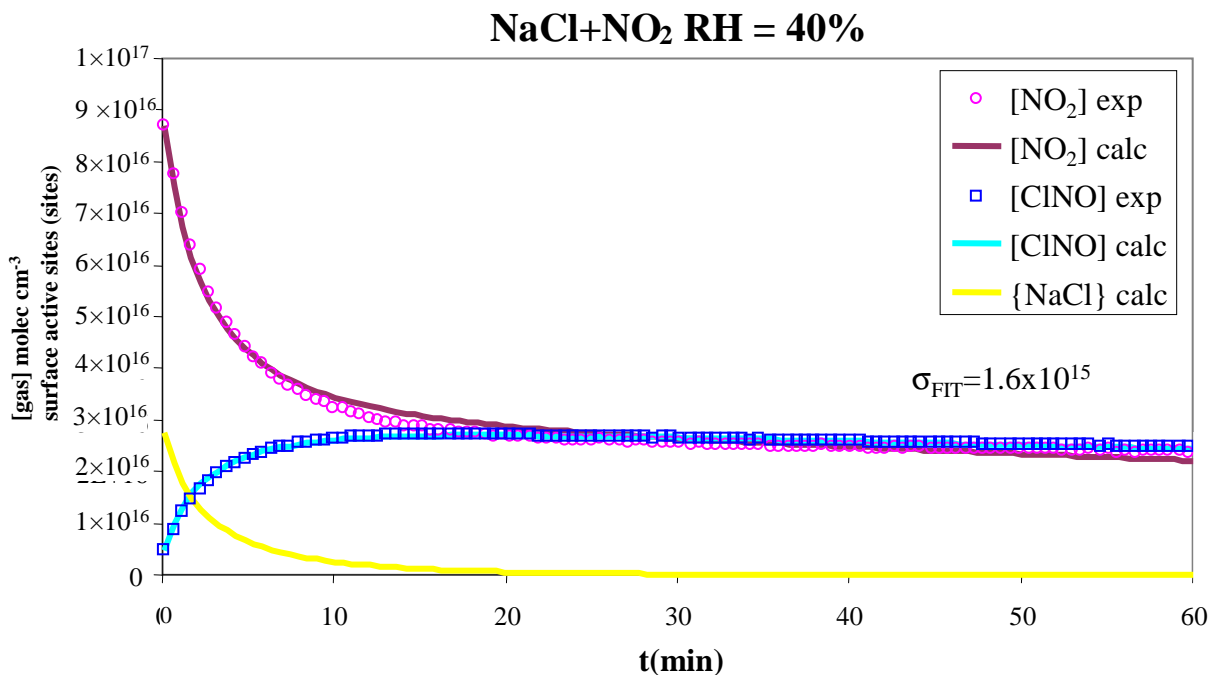


Fig. 7.10 Experimental and calculated profiles of [NO₂], [ClNO] and {NaCl} for the system NaCl/NO₂ at RH=70%.

As in the previously reported case of RH=40%, from these kinetic constants the different reaction rates can be calculated. In fig. 7.11 their temporal evolutions are plotted and we can observe that the profiles at RH=70% are very similar to the ones already observed for RH=40%.

The already mentioned underestimation of the initial wall losses explains the observed difference (-25%) between the global measured and modelled initial NO₂ depletion rates (fig. 7.12) and again about 15% of initial heterogeneous reactivity comes from NO₂ hydrolysis. Similar conclusions on how the different reactions contribute to the global reactivity can then be inferred also because the catalytic reaction has a comparable rate constant. No particular effect appears even if the reactive condensed phase is very close to the deliquescence.

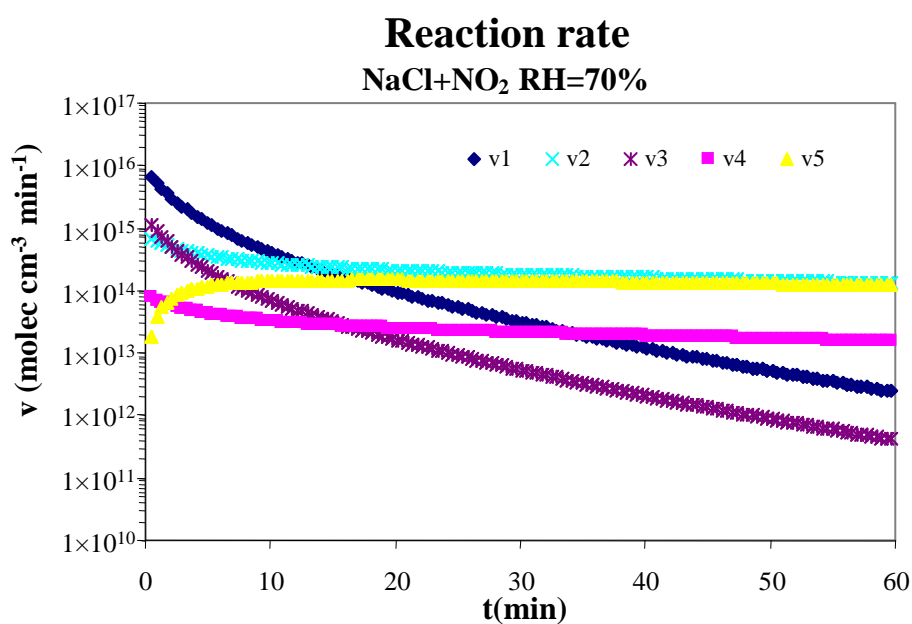


Fig. 7.11 Reaction rates for the NaCl/NO₂ system at RH=70% with the R1-R5 model.

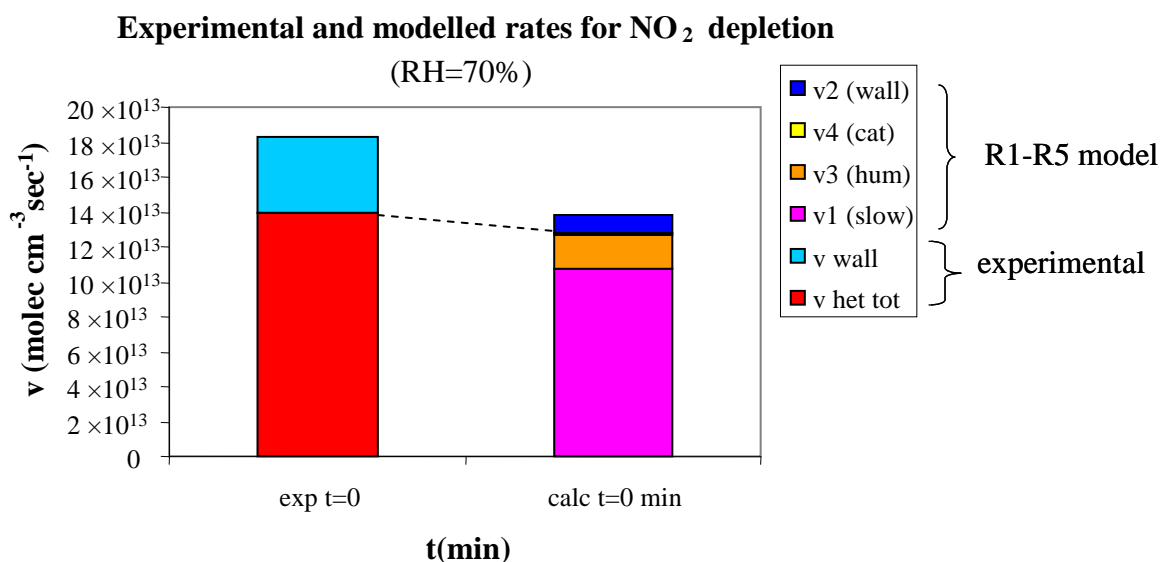


Fig. 7.12 Comparison between the total NO₂ initial depletion rates in the experimental and calculated data at RH=70%.

7.2.4 Kinetic model for FA coated NaCl when RH=0%

The same kinetic model used for the uncoated NaCl surfaces exposed to NO₂ in presence of water vapour is used for fitting NO₂ and ClNO profiles when a fatty acid coating was added on the salt surface. We obtain, as in the previous cases, a good agreement between the experimental and calculated concentration profiles and NO₂ depletion/ClNO formation rates, meaning that the chemical and kinetic mechanisms involved are probably the same. The obtained output values are commented through a direct comparison to the uncoated surfaces behaviour in the next part.

7.3 Evaluating the effect of humidity and FA coating on the heterogeneous reactivity

We introduced some supplementary reactions in a very simple kinetic model for describing the ClNO formation and NO₂ depletion profiles even in presence of water vapour. In this model we take into account three possible heterogeneous reactions of NO₂ on NaCl, two of them involving the release of gaseous ClNO (R1 and R4) and another evolving HCl instead (R3).

The surface reactive sites saturation is considered by introducing the dependence of the reaction rate on the parameter {NaCl}.

The surface reorganisation, which is observed by AFM and micro-Raman, is also taken into account in reaction R4, where, after NO₂ hydrolysis, the surface nitration rate does not depend on {NaCl}.

The quality of the fitting is evaluated by the parameter σ_{FIT} , by a graphical method and by comparing the experimentally measured γ (or k_{het}^{exp}) to the reaction rates calculated from the fitting rate constants, which show to be in good agreement within a 30% interval.

Through the rate constant estimations obtained from this model we can express the global kinetic parameter k_{het} like the linear combination of the three different reaction rates and assess their relative importance in the overall reactivity.

NO_2 hydrolysis reaction (R_3) is not the most important even when high quantity of water vapour are present. It usually counts up to 15% of the total NO_2 uptake on NaCl surface. This means that the measured γ_0^{exp} values increasing with humidity cannot then be totally expressed by an increase of NO_2 hydrolysis.

The model outputs, plotted in fig. 7.13, confirm what we already expected: NO_2 hydrolysis increases with increasing humidity. At the same time NO_2 hydrolysis seems to be less sensitive to the amount of water vapour on oleate-coated NaCl surfaces, so that this FA coating could somewhat diminish NO_2 hydrolysis.

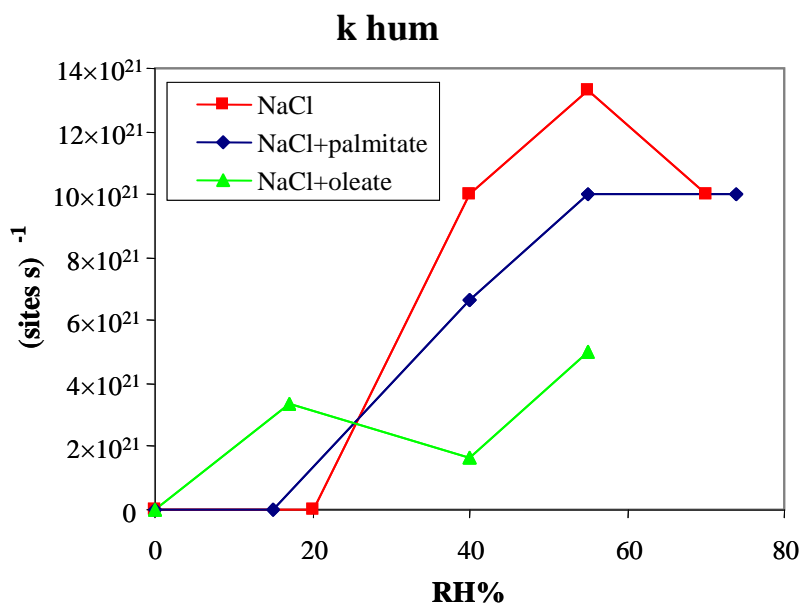


Fig. 7.13 Calculated k_{hum} values expressed as a function of RH%.

The surface reorganisation is also very slow compared to the other NaCl/ NO_2 reactions and, even if it does play any role in the initial uptake, it becomes relatively more important as long as the surface saturates.

The surface saturation easily explains the observed deviations of the experimental data from a theoretical pseudo-first order uptake and the consequent rapid decrease of the NaCl/ NO_2 reactivity at longer contact time.

We have already observed that the initial uptake is always dominated, even at higher RH, by v_1 , the “dry” reaction R_1 . This reaction is not explicitly involving any water in the kinetic expression or in the chemical balance, therefore the rate constant k_{slow} should not be influenced by RH. This is actually what we observe from fig. 7.14, where k_{slow} seems to have a constant value when $\text{RH} \neq 0$. For $\text{RH}=0\%$ we have an exception, with a reaction rate noticeably lower.

We cannot miss to observe that the absolute values of k_{slow} reflect the uptake and reactivity order experimentally measured for the three different surfaces, with $k_{\text{slow}}(\text{NaCl}) > k_{\text{slow}}(\text{NaC}_{16}/\text{NaCl}) > k_{\text{slow}}(\text{NaC}_{18:1}/\text{NaCl})$. The presence of an insoluble, even if incomplete and inhomogeneous, FA coating seems to slow down the heterogeneous reaction reported in eq. 7.1. The chemical mechanism could then be modified, but we do not have enough elements for investigating further. Similarly, in [Cosman L. M. et al., 2008] the authors report that N_2O_5 uptake to H_2SO_4 aerosols is affected by less than a monolayer of densely packed organic coating: γ diminishes of a factor 10 when the fractional coverage is 0.75.

The effect of the organic coating which we observed is much less pronounced but at the same time we do not have detailed information on the real coverage of the NaCl surface at higher RH, where more than a monolayer of water could spread the surfactants all over the surface.

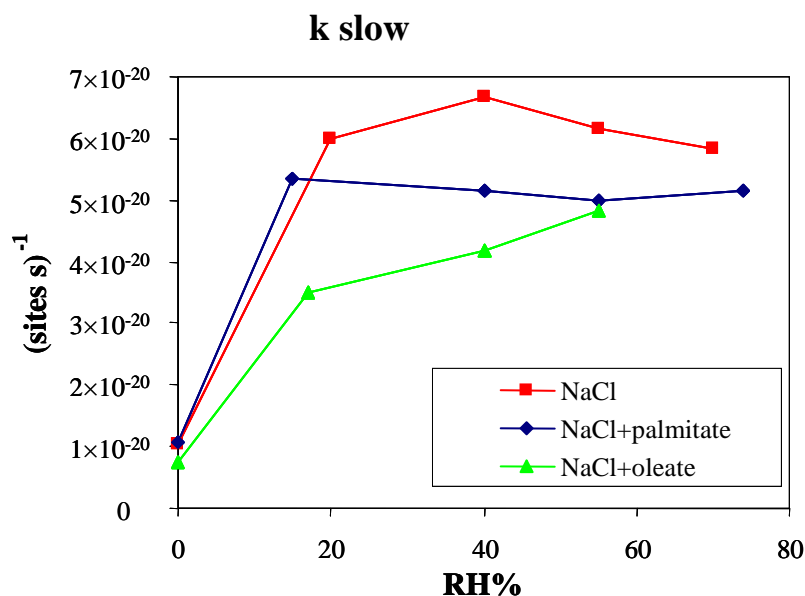


Fig. 7.14 Calculated k_{slow} values expressed as a function of RH%.

On the contrary in [Stemmler K. et al., 2008] the authors found that for the much more soluble HNO_3 species only a total coverage by a tightly packed and ordered monolayer of saturated FA can hinder its uptake to deliquescent NaCl aerosol particles. In their work an oleic acid monolayer had no noticeable effect on HNO_3 uptake. They justified their findings by the impossibility for the unsaturated cis-oleic acid to form a condensed state liquid monolayer. Our experimental results go in a different reaction, probably because we used the sodium salts instead of the acidic forms of FA, reflecting on the ability of forming auto-assembling structures in different conditions (see fig. 2.5).

From these examples and many others that can be found in the literature (i.e. [Park S.-C. et al., 2007], [McNeill V. F. et al., 2006], [Folkers M. et al., 2003], [Badger C. L. et al., 2006], [Clifford D. et al., 2007] and [Glass S. V. et al., 2006], for citing some of the most recent work), we can suggest that the effect of a monolayer or sub-monolayer of condensed phase surfactants can have different effect on the uptake of different gases depending on the mechanism itself of their uptake.

The other terms present in the expression of v_1 are $[\text{NO}_2]$ and $\{\text{NaCl}\}$.

The initial estimation of the number of reactive surface sites, $\{\text{NaCl}\}_0$, can find a confirmation from crystallographic data estimations [Kittel C., 1986]: considering 13.88 cm^2 of perfect NaCl(100) surface, 8.7×10^{15} is the total number of NaCl units. This calculated value is half of the optimised value of $\{\text{NaCl}\}_0$ parameter at RH=0% in our model, where we used no hypothesis on the real NaCl surface status. It is easy to imagine that a pressed NaCl powder surface contains much more defective sites than a theoretical monocrystal surface.

Another important observation on $\{\text{NaCl}\}_0$ is that it shows a strong dependence from humidity conditions. In fig. 7.15 we can clearly see a difference for both coated or uncoated surfaces, between the number of available reactive sites in relatively dry conditions and if $\text{RH} > 30\text{-}35\%$. This is indeed the value which indicates the formation of at least one monolayer of water on the NaCl (100) surface. The mobility of the surface ions is induced by the presence of surface water ($\text{RH} > 35\%$) and had the consequence of an increased availability of active sites. The FA seems to have a slight effect of coating only in the 40-60% RH range, without a particular difference between the saturated (NaC_{16}) and the unsaturated ($\text{NaC}_{18:1}$) chain. The presence of FA on the surface could partially inhibit the ion mobility, but this effects is not very pronounced.

The global effect of FA on the initial uptake and reactivity coefficients can hardly be assessed to a specific and preferential element, but it seems to be a mixed contribution of the different kinetics and reaction mechanism aspects instead.

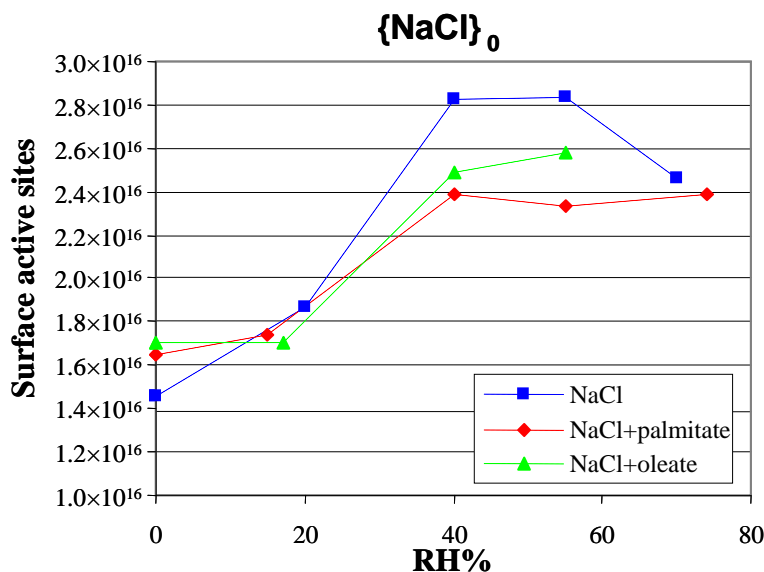


Fig. 7.15 Estimation of the initial number of surface active sites $\{NaCl\}_0$, as a function of RH and surface F.A. coating. The dashed lines are an eye-guide.

7.4 Quantification of the total reactivity of the NaCl/NO₂ system

The integrated reactivity of the NaCl/NO₂ system can be quantified by measuring the total amount of formed nitrate on the exposed pellets after 60 minutes of reaction.

The presence of a fatty acid coating slows down the initial reactivity but does not protect NaCl against NO₂ attack, as it can be seen by the equal amount, inside the experimental error, of NaNO₃ formed on both coated or uncoated NaCl pellets (fig. 7.16). Moreover, with the exception of pure NaCl at RH=70%, the Cl⁻ to NaNO₃⁻ conversion linearly increases with increasing relative humidity. For comparison, two values for pure NaCl pellets which were not pre-treated with the dip-coating technique are also reported in black, showing the effect of increased surface roughness on the total reactivity of the pellets (RH=5 and 40%).

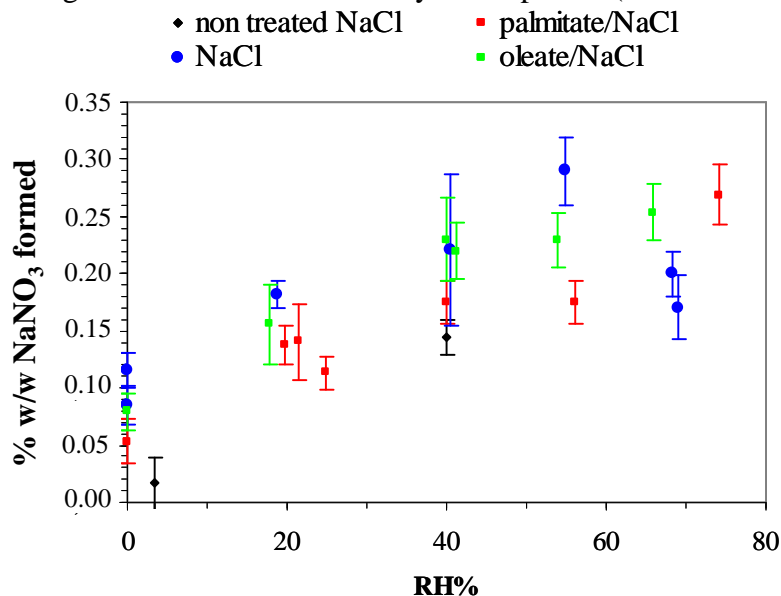


Fig. 7.16 Total formed NaNO₃ on NaCl pellets after 60 min of reaction with NO₂ $(8.7 \pm 0.3) \times 10^{16}$ molec cm⁻³.

7.5 Discussion and atmospheric implications

The uptake and reactivity coefficients as a function of RH have an increasing trend reaching a maximum around 40-55% RH and decreasing again for higher RH. A similar trend was already observed for HNO₃ uptake to NaCl, NaCl/MgCl₂, and sea-salt aerosols in [Liu Y. et al., 2007] and [Saul T. D. et al., 2006] as graphically represented in fig. 7.17a; for comparison we report the NO₂/NaCl uptake measurements we obtained in this work in b.

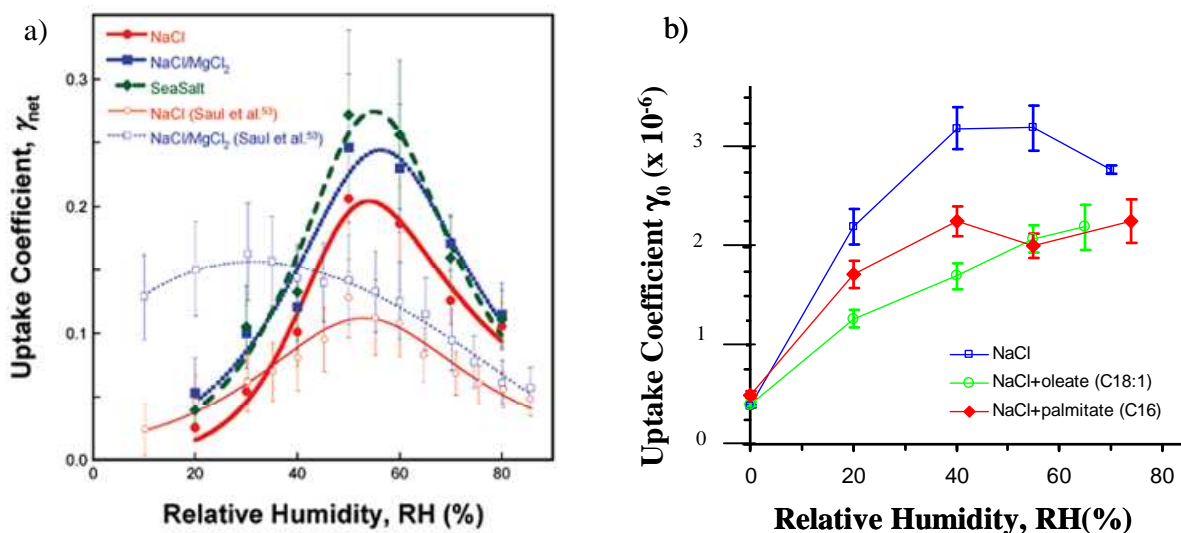


Fig. 7.17 a) Initial HNO₃ uptake coefficient as a function of relative humidity on NaCl, mixtures of NaCl/MgCl₂ (X Mg/Na = 0.114) and sea salt particles. Open symbols represent data taken from [Liu Y. et al., 2007] where the particle mean diameter is 0.9 μ m ; open symbols are data obtained for particle mean diameter of ~ 0.1 μ m taken from [Saul T. D. et al., 2006]. **b)** Initial NO₂ uptake coefficient as a function of humidity on NaCl pellets in this work.

These are the only previous work studying the effect of RH on the uptake coefficient of a gas to the marine aerosol (or its surrogates). They generated deliquescent aerosols and suggested that the enhanced reactivity at RH > 40% (EDR of NaCl) was due to HNO₃ uptake on salt solution which are progressively more concentrated going from 80 down to 40% RH. When RH < 40% the aerosol particles effloresced and therefore they measured HNO₃ uptake to dried NaCl particles on which uptake coefficient is ~1/3 of the maximum value. In our case we approach the deliquescence/efflorescence diagram of NaCl from the opposite site, starting from dry surfaces and adding humidity inside the reactor cell so that surface can equilibrate but cannot become fully deliquescent before RH ~ 75%. What we observe is mainly a progressive enhancement in reactivity by a water-induced activation of Cl⁻ reactive sites which are easily raised from the solid surface [Cabrera-Sanfeliix P. et al., 2007]. For RH \geq 75% NO₂/NaCl uptake diminishes, meaning that probably the reaction path changes or that there is a salting-out effect diminishing the gaseous reactive solubility as previously reported in [Aghnatiou C., 2008].

The main conclusion is that in atmospheric model simulations where γ values are used for estimating heterogeneous reactions, the RH parameter is very important because reactivity can change of almost an order of magnitude between dry and humid conditions, as observed for NO₂ and HNO₃ on NaCl surfaces or aerosol particles.

Another experimental observation is that the initial uptake coefficient is not a good parameter for describing a reactivity integrated over a “long” period of time: surface readily saturation is only partially compensated by a much slower surface reconstruction. This phenomenon is stressed at higher RH, as reported in fig. 6.15 and the timescale can depend from the type of surface taken into account. Further studies on the surface status of reacted aerosol particles

would be recommended, and the introduction of reaction probability per active site γ' as suggested by [Moise T. et al., 2000] would lead to a more realistic description.

The presence of an incomplete and inhomogeneous FA coating can slightly influence the initial kinetic of the NO₂ to NaCl uptake and reactivity, but does not have any important effect on the global reactivity of NaCl/NO₂ integrated over 1 h, as it was seen by the comparable amounts of formed NaNO₃ at the different humidities in presence or not of coating. Its presence cannot alter substantially neither the total reactivity towards NO₂ trace gas or its reaction mechanism: in the gaseous or on the solid phase no new or different products were detected in presence of organics. In a similar way marine aerosol particles are supposed not to be efficaciously screen by the 0.4-15% estimated FA coverage.

The main result we obtained from the kinetic studies is the equivalence of NO₂ or N₂O₄ uptake and ClNO release rates (taking into account the stoichiometry). This can have important atmospheric implications because NO₂ reactivity on NaCl was always thought to pass through NO₂ hydrolysis releasing, after the heterogeneous reaction, HCl and HNO₂. In our, as well as in previous studies on NaCl/NO₂ reactivity, we did not observe the formation of HCl in the gaseous phase. Moreover ClNO was largely the most abundant gaseous species we detected, together with the reactant NO₂, even at higher humidities.

We can give an estimation of the released number of ClNO molecules (N_{ClNO}) in a coastal polluted area like Dunkerque agglomeration - harbour, industrial and urban area on the North Sea in Nord-Pas de Calais region, France from the following expression:

$$(7.23) \quad N_{\text{ClNO}} = \phi \frac{\langle c \rangle [\text{NO}_2]}{8} S$$

where

- ϕ is the reactivity coefficient; for its upper limit value we consider ϕ_0 at RH=40% for the high [NO₂] measurements: $\phi < 5.68 \times 10^{-6}$;
- $\langle c \rangle$ the mean velocity of NO₂ in the gas phase; at T=298K its value is 37032 cm s⁻¹;
- [NO₂] the trace gas concentration; we consider the maximum average hour value for 2008 year measured in the Calais (France) station, [ADEME, 2008]: 250 μg m⁻³ equivalent to 3.27 × 10¹⁸ molec m⁻³.
- S the aerosol surface that can be estimated (eq. 7.24) from field measurement data of aerosol concentration (L in μg m⁻³) and from an estimation of the surface density for 1 μg m⁻³ of aerosol concentration (D_S in cm² cm⁻³):

$$(7.24) \quad S = L \times D_S$$

In a first approximation we can consider spherical aerosol particles of 1 μm geometrical diameter made of pure NaCl then a surface density D_S = 1.89 × 10⁻⁸ cm² cm⁻³ m³ μg⁻¹.

L is estimated from the average daily value for PM_{2.5} in Dunkerque [ADEME, 2008] considering that all particles are made of NaCl: L = 13 μg m⁻³.

Therefore the daily average of S is 2.5 × 10⁻⁷ cm² cm⁻³.

We obtain:

$$N_{\text{ClNO}} < 2 \times 10^{10} \text{ molec s}^{-1} \text{ m}^{-3}$$

meaning that in 10 minutes the upper limit of the quantity of ClNO released into the atmosphere in these conditions can be 1.2 × 10¹³ molec m⁻³.

Even considering the lower value for NO₂ uptake measured at much lower NO₂ concentrations ($\gamma > 5 \times 10^{-8}$ in [Finlayson-Pitts B. J., 1983]) we would obtain a release, in 10 minutes, of $> 1 \times 10^{11}$ molec m⁻³.

These values, even if calculated in a very simplified scenario, mainly indicate that NaCl/NO₂ reaction has to be taken into account because of its significant release a precursor of chloride radicals and that can therefore can have a strong impact on its concentration in the marine boundary layer, where the background values in Cl[·] are $\sim 1 \times 10^{11}$ molec m⁻³ [Spicer C. W. et al., 1998].

Chapter 8 – Conclusions and Future Work

8. Conclusions and Future Work

In this work we studied the reactivity of insoluble fatty acid-coated NaCl surfaces to gaseous NO₂ at different relative humidities via two complementary approaches:

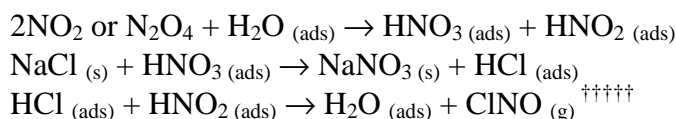
- The analysis of the solid phase before and after reaction with high spatial resolution and spectroscopic techniques: Atomic Force Microscopy gives fine details about the surface morphology, and Raman microspectrometry records spectra and images giving information about molecular identification and surface distribution of the products (ch. 4-5). By FTIR spectroscopy we could give semi-quantitative information on the total amount of nitrate formed (ch.7.3).
- FTIR analysis of the gaseous phase during heterogeneous reactions at the chosen RH (0-80%) and ambient temperature and pressure in a closed reactor, which has been suitably optimised. From NO₂, N₂O₄ and ClNO concentration profiles we measured the initial uptake and reactivity coefficients of NO₂/NaCl and N₂O₄/NaCl at different atmospheric conditions (ch. 6). Through a simple reactivity model which fits the experimental data well, we tried to assess the contributions of the different possible heterogeneous reactions to the overall observed reactivity (ch. 7).

8.1 Main results

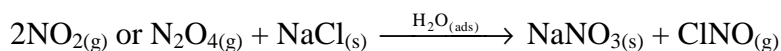
The main results we obtained and the possible atmospheric implications are the following:

- 1) The initial NO₂ uptake (γ_0) to the NaCl(100) surface increases with increasing relative humidity and reaches a maximum before decreasing again when the surface becomes deliquescent (RH>68%). We measured $\gamma_0 = (3.8 \pm 0.2) \times 10^{-7}$ at RH=0% and $(3.2 \pm 0.2) \times 10^{-6}$ at RH>35%, an increase of almost an order of magnitude. A similar trend was previously observed for HNO₃ on NaCl, NaCl/MgCl₂, and sea-salt; the relative humidity parameter has therefore to be taken into account when considering these heterogeneous reactions in atmospheric chemistry models.
 - 2) The presence of at least a monolayer of water on the surface (for RH>35%) leads to surface reconstruction as long as the reaction occurs. As a consequence, the surface saturation by the product is partially compensated by the appearance of freshly generated Cl⁻ active sites. In this way the total conversion of chloride into nitrate in marine aerosol particles is possible at longer contact time, as observed in field measurements.
- 1) When the topmost layer of the surface becomes deliquescent, NO₂ can diffuse more deeply inside the condensed phase with the consequence of formation of NaNO₃ some micrometers under the surface. This gas-liquid interaction lowers the heterogeneous reactivity due to the salt-out effect, with the consequence that NO₂ is relatively unreactive on deliquescent NaCl aerosol.
 - 2) The formation of nitrate crystals of regular rhombohedral shape is a sign of surface ageing, otherwise small crystals with different geometries and morphology or deliquescent nitrate are present on freshly reacted surfaces.

- 3) The presence of a sodium palmitate or oleate non homogeneous coating does not efficiently protect the NaCl(100) surface from NO₂ attack, with an increasing Cl⁻ to NO₃⁻ conversion with increasing RH, on uncoated as well as on coated surfaces. The initial reactivity is slowed down by both saturated (palmitic) and unsaturated (oleic) fatty acids of ~ 30% in the 40-55% RH range by decreasing the number of available water-activated Cl⁻ sites. Only tightly packed liquid crystals seem to act as an effective barrier for the heterogeneous reaction, as observed by the absence of nitrate where these type of deposits are present. In a similar way, marine aerosol particles are not thought to have a complete or homogeneous insoluble organic coating: their heterogeneous reactivity is therefore not hampered, but only slowly retarded in the presence of these coatings.
- 4) Such weak heterogeneous NO₂/NaCl reactivity should lead us to conclude that this reaction is “unimportant in the marine boundary layer at atmospheric NO₂ concentrations” [Rossi M. J., 2003]. On the contrary, this reaction, even if it is if not an important sink for NO₂ compared to other photolysis or oxidation paths, is a source of ClNO instead of HCl, which was expected to be released in presence of water vapour. We experimentally measured the equivalence between NO₂ depletion and ClNO production kinetics, so that NO₂/NaCl reactivity in moist condition can be described by the following reactions:



Giving the overall reaction:



The main atmospheric implication is that the ClNO species is an efficient precursor of atmospheric radicals during the daytime as it can be readily photolysed into Cl and NO, with a quantum yield near to unity. During the night time the most probable ClNO fate is the efficient heterogeneous hydrolysis to HCl and HNO₂ ([Scheer V. *et al.*, 1997], [Karlsson R. *et al.*, 1996]) contributing to the acidification of aqueous particles or droplets and the formation of reservoir molecules which can be transported even to the stratosphere.

All these processes can be summarised in the schematic representation of fig. 8.1.

^{†††††} A known production path of ClNO also in the stratosphere through reaction of gaseous HNO₂ to frozen HCl (Finlayson-Pitts B. J. and Pitts J. N., Jr. (2000). Chemistry of the upper and lower atmosphere. San Diego, Academic Press.).

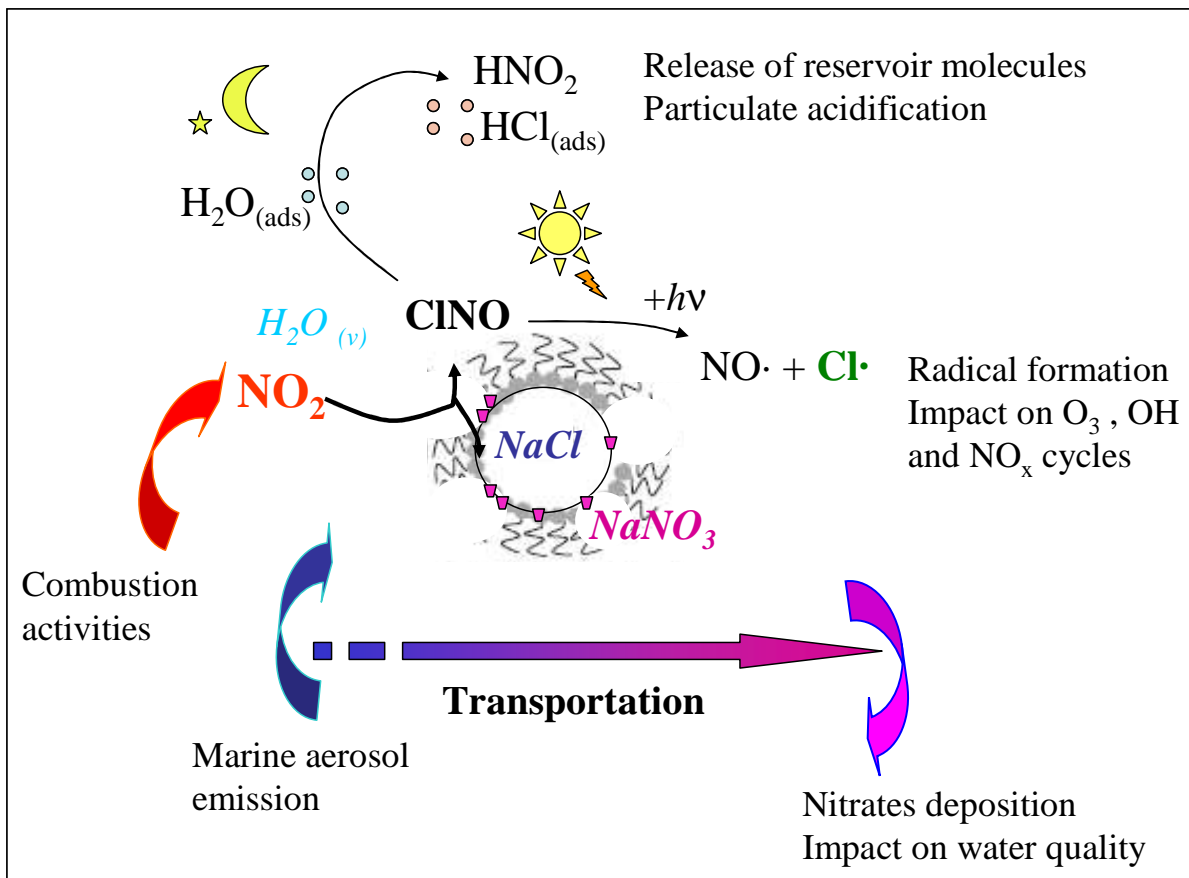


Fig. 8.1 Schematic representation of the heterogeneous NaCl/NO₂ reaction on a marine aerosol in a polluted coastal region: the NaCl fraction progressively transforms to nitrate and releases CINO gaseous species. CINO heterogeneous hydrolysis during the nighttime can produce HNO₂ and HCl, whilst during daytime photolysis generates the active Cl and NO species, which are further involved in several complex atmospheric chemistry cycles, i.e. ozone, OH and NO_x cycles. The inhomogeneous surfactant coating slows down the initial reactivity but does not protect the airborne particle against NO₂ or other gaseous attack. Moisture has the double role of catalysing the heterogeneous reaction and of promoting surface reorganisation leading to a total conversion of NaCl to NaNO₃.

8.2 Future Work

The importance of NO₂ or NO_y gases on atmospheric chemistry, particularly in the marine boundary layer is nowadays well established. The interaction between the mainly anthropogenic pollutant gas NO₂ and sea-salt aerosol leads to the formation of chlorine and bromine atom precursors that are photolysed to generate radicals. Previous laboratory studies on model solid salt showed that small amounts of minor components such as adsorbed water, MgCl₂ and an organic coating can induce or remove the surface passivation of NaCl. Particularly the role of organic films at the air-marine particle interface has started to be studied only very recently [Donaldson D. J. et al., 2006]. The major part of previous studies concerning heterogeneous reactions between NO_y and sea salts has been performed using bulk model surfaces. The development of a new experiment in which relative humidity, aerosol sizes, aerosol internal mixtures and gases could be controlled would be more representative of the conditions of the marine troposphere. Laboratory experiments on atmospheric heterogeneous chemistry are moving towards the generation of organic coatings directly on NaCl aerosols. Particles can be generated by atomisation of a liquid jet of a saturated salt solution; after drying, the organic coating can be formed on microscopic suspended particles by condensation of organic vapours, as briefly presented in ch. 2.2.4. The concentration and size of the individual particles can be measured by using a scanning mobility particle analyser (SMPS). The aerosol reactivity can be quantified in an aerosol flow tube with relatively

reactive species such as O_3 , OH or other radicals. The reactivity of FA coated NaCl aerosol with NO_2 could also be studied in an atmospheric simulation chamber where the measurements of slower heterogeneous reactions can be made. In both cases reactivity studies can be coupled to single particle analysis after sampling of the particulate phase. Morphological and molecular aspects already investigated by AFM and Raman microspectrometry can be coupled to electron microscopy and energy dispersive X-ray imaging as well as ToF-SIMS imaging. The latter technique is particularly sensitive to the outer layer ($\sim 3\text{nm}$) of particles with an accurate lateral resolution ($\sim 100\text{nm}$).

Some other opportunities come from particle-on-substrate stagnation flow reactor under realistic atmospheric conditions. The reaction can be followed by monitoring deposited individual particles under *in-situ* conditions by the surface techniques previously cited.

Reactivity studies could also be performed in the presence of UV-Visible radiation, to reproduce daytime reactions between the NO_2 species and NaCl. Both reactant and product (NO_2 and $NaNO_3$) have interesting photolytic properties, the former producing NO, the latter $NaNO_2$, NO_2 and $O(^3P)$. Moreover a recent study showed an enhanced photolysis of $NaNO_3$ on mixed NaCl/ $NaNO_3$ films [Wingen L. M. *et al.*, 2008] and another reported the nitrite-induced oxidation of organic coatings on model airborne particles [Karagulian F. *et al.*, 2009].

The possibility of adding other minor mineral species to NaCl for a more realistic description of the chemical composition of marine aerosols can be taken into account in a second step.

Of course more realistic trace gas concentration has to be achieved, by coupling the reactors to more sensitive detection techniques, i.e. gas analysers or mass spectrometers.

Finally, exposing surfaces or aerosols to pollutants mixtures (i.e. NO_2 and HNO_3) so that different reactions can compete for the surface active sites, can bring us closer to describing the reality of the atmosphere.

Bibliographic references

Bibliographic references

- Abbatt J. P. D. and Waschewsky G. C. G. (1998). "Heterogeneous Interactions of HOBr, HNO₃, O₃, and NO₂ with Deliquescent NaCl Aerosols at Room Temperature." *Journal of Physical Chemistry A* 102(21).
- ADEME. (2008). "www.atmonet.org."
- Aghnatos C. (2008). Etude d'interactions entre le dioxyde d'azote et des particules minérales d'intérêt atmosphérique. *Laser and Optics- Chemical-Physics - Atmosphère*. Villeneuve d'Ascq, Université de Sciences et Technologies de Lille. PhD pg 189.
- Akhter M. S. (1997). "Effect of acetamide on the critical micelle concentration of aqueous solutions of some surfactants." *Colloids and Surfaces, A: Physicochemical and Engineering Aspects* 121(2-3).
- Allouche A. (1998). "Water Dissociation on Defective Sites on the NaCl(100) Surface. A Quantum ab Initio Study." *Journal of Physical Chemistry B* 102(50).
- Anuradha P. and Bhagavan Raju I. V. K. (1985). "Study of Oriented Overgrowth of Sodium Nitrate Crystals." *Crystal Res. Technology* 20(6) pg. 795.
- Apostolescu N., Schroder T. and Kureti S. (2004). "Study on the mechanism of the reaction of NO₂ with aluminium oxide." *Applied Catalysis, B: Environmental* 51(1).
- Badger C. L., Griffiths P. T., George I., et al. (2006). "Reactive Uptake of N₂O₅ by Aerosol Particles Containing Mixtures of Humic Acid and Ammonium Sulfate." *Journal of Physical Chemistry A* 110(21).
- Bailey A. I. and Price A. G. (1970). "Interfacial energies of monomolecular films of fatty acids deposited on mica in aqueous and nonaqueous media; strength of hydrophobic interactions." *Journal of Chemical Physics* 53(9).
- Barger W. R. and Garrett W. D. (1976). "Surface Active Organic Material in Air Over the Mediterranean and Over the Eastern Equatorial Pacific." *J. Geophys. Res.* 81.
- Barney W. S. and Finlayson-Pitts B. J. (2000). "Enhancement of N₂O₄ on Porous Glass at Room Temperature: A Key Intermediate in the Heterogeneous Hydrolysis of NO₂?" *The Journal of Physical Chemistry A* 104(2).
- Batonneau Y., Bremard C., Laureyns J., et al. (2000). "Microscopic and imaging Raman scattering study of PbS and its photo-oxidation products." *Journal of Raman Spectroscopy* 31(12).
- Batonneau Y., Bremard C., Laureyns J., et al. (2003). "Polarization Effects of Confocal Raman Microspectrometry of Crystal Powders Using Interactive Self-Modeling Analysis." *The Journal of Physical Chemistry B* 107(7).

- Brémard C., Dhamelin court P., Laureyns J., et al. (1985). "The effect of High-Numerical-Aperture Objectives on Polarization Measurements in Micro-Raman Spectroscopy." *Applied Spectroscopy* 39(6) pg. 1036.
- Brewer P. G., Malby G., Pasteris J. D., et al. (2004). "Development of a laser Raman spectrometer for deep-ocean science." *Deep Sea Research Part I: Oceanographic Research Papers* 51(5).
- Buajarern J., Mitchem L. and Reid J. P. (2007a). "Characterizing Multiphase Organic/Inorganic/Aqueous Aerosol Droplets." *Journal of Physical Chemistry A* 111(37).
- Buajarern J., Mitchem L. and Reid J. P. (2007b). "Characterizing the Formation of Organic Layers on the Surface of Inorganic/Aqueous Aerosols by Raman Spectroscopy." *Journal of Physical Chemistry A* 111(46).
- Butler J. R., Mitchem L., Hanford K. L., et al. (2008). "In situ comparative measurements of the properties of aerosol droplets of different chemical composition." *Faraday Discussions* 137.
- Cabrera-Sanfeli x P., Portal D. S., Verdaguer A., et al. (2007). "Spontaneous Emergence of Cl⁻ Anions from NaCl(100) at Low Relative Humidity." *Journal of Physical Chemistry C* 111(22).
- Carloz F., Fenter F. F., Tabor K. D., et al. (1997). "paper I: Design and construction of a Knudsen cell reactor for the study of heterogeneous reactions over the temperature range 130-750K: performances and limitations." *Reviews of Scientific Instruments* 68.
- Chakraborty P. and Zachariah M. R. (2008). "Sticking Coefficient and Processing of Water Vapor on Organic-Coated Nanoaerosols." *Journal of Physical Chemistry A* 112(5).
- Cheung J. L., Li Y. Q., Boniface J., et al. (2000). "Heterogeneous Interactions of NO₂ with Aqueous Surfaces." *The Journal of Physical Chemistry A* 104(12).
- Cistola D. P., Hamilton J. A., Jackson D., et al. (1988). "Ionization and phase behavior of fatty acids in water: application of the Gibbs phase rule." *Biochemistry FIELD Full Journal Title:Biochemistry* 27(6).
- Clegg S. L. and Brimblecombe P. (1967). "The dissociation constant and Henry's law constant of HCl in aqueous solution." *Atmospheric Environment* 20(12) pg. 2484.
- Clifford D., Bartels-Rausch T. and Donaldson D. J. (2007). "Suppression of aqueous surface hydrolysis by monolayers of short chain organic amphiphiles." *Physical Chemistry Chemical Physics* 9(11).
- Cosman L. M. and Bertram A. K. (2008). "Reactive Uptake of N₂O₅ on Aqueous H₂SO₄ Solutions Coated with 1-Component and 2-Component Monolayers." *Journal of Physical Chemistry A* 112(20).
- Dai D., Peters S. and Ewing G. (1995). "Water Adsorption and Dissociation on NaCl Surfaces." *The Journal of Physical Chemistry* 99(25).

- Dai Q., Hu J. and Salmeron M. (1997). "Adsorption of Water on NaCl (100) Surfaces: Role of Atomic Steps." *Journal of Physical Chemistry B* 101(11).
- Daumer B., Niessner R. and Klockow D. (1992). "Laboratory studies of the influence of thin organic films on the neutralization reaction of H₂SO₄ aerosol with ammonia." *Journal of Aerosol Science* 23(4).
- Decious J. C. and Hexter R. M. (1977). *Molecular vibration in crystals*. New York.
- DeMore W., Sander S., Golden D., et al. (1997). "Chemical Kinetics and Photochemical Data for Use in Stratospheric Modeling: Evaluation Number 12, JPL Publication 97-4." Jet Propulsion Laboratory, California Institute of Technology, Pasadena, CA.
- Donaldson D. J. and Vaida V. (2006). "The Influence of Organic Films at the Air-Aqueous Boundary on Atmospheric Processes." *Chemical Reviews* 106(4).
- Dubowski Y., Vieceli J., Tobias D. J., et al. (2004). "Interaction of Gas-Phase Ozone at 296 K with Unsaturated Self-Assembled Monolayers: A New Look at an Old System." *Journal of Physical Chemistry A* 108(47).
- Feierabend K., Havey D. and Vaida V. (2004). "Gas phase spectroscopy of HNO₃ in the region 2000–8500cm⁻¹." *Spectrochimica Acta Part A: Molecular and Biomolecular Spectroscopy* 60(12) pg. 2775.
- Finlayson-Pitts B. J. (1983). "Reaction of nitrogen dioxide with sodium chloride and atmospheric implications of nitrosyl chloride formation." *Nature (London, United Kingdom)* 306(5944).
- Finlayson-Pitts B. J. and Pitts J. N., Jr. (2000). *Chemistry of the upper and lower atmosphere*. San Diego, Academic Press.
- Finlayson-Pitts B. J. (2003). "The Tropospheric Chemistry of Sea Salt: A Molecular-Level View of the Chemistry of NaCl and NaBr." *Chemical Reviews* 103(12).
- Finlayson-Pitts B. J., Wingen L. M., Sumner A. L., et al. (2003). "The heterogeneous hydrolysis of NO₂ in laboratory systems and in outdoor and indoor atmospheres: An integrated mechanism." *Phys. Chem. Chem. Phys.* 5.
- Folkers M., Mentel T. F. and Wahner A. (2003). "Influence of an organic coating on the reactivity of aqueous aerosols probed by the heterogeneous hydrolysis of N₂O₅." *Geophys. Res. Lett.* 30.
- Forster P., Ramaswamy V., Artaxo P., et al. (2007). *IPCC Fourth Assessment Report*
- Foster M. C. and Erwing G. E. (2000) "Adsorption of water on the NaCl(001) surface. An infrared study at ambient temperatures." *J. Chem. Physics* 112 DOI: 10.1063/1.481256
- Gagosian R. B., Peltzer E. T. and Zafiriou O. C. (1981). "Atmospheric transport of continentally derived lipids to the tropical North Pacific." *Nature* 291(5813).
- Gagosian R. B., Zafiriou O. C., Peltzer E. T., et al. (1982). "Lipids in aerosols from the tropical north Pacific: temporal variability." *Journal of Geophysical Research, [Atmospheres]* 87C pg. 11133.

- Gao Y., Chen S. B. and Yu L. E. (2007). "Efflorescence relative humidity of airborne sodium chloride particles: A theoretical investigation." *Atmospheric Environment* 41(9).
- Garland E. R., Rosen E. P., Clarke L. I., et al. (2008). "Structure of submonolayer oleic acid coverages on inorganic aerosol particles: evidence of island formation." *Physical Chemistry Chemical Physics* 10(21).
- Garland R. M., Wise M. E., Beaver M. R., et al. (2005). "Impact of palmitic acid coating on the water uptake and loss of ammonium sulfate particles." *Atmos. Chem. Phys.* 5 pg. 1951.
- George C., Strekowski R. S., Kleffmann J., et al. (2005). "Photoenhanced uptake of gaseous NO₂ on solid organic compounds: A photochemical source of HONO?" *Faraday Discussions* 130(Atmospheric Chemistry).
- Gilman J. B., Tervahattu H. and Vaida V. (2006). "Interfacial properties of mixed films of long-chain organics at the air-water interface." *Atmospheric Environment* 40(34).
- Glass S. V., Park S.-C. and Nathanson G. M. (2006). "Evaporation of Water and Uptake of HCl and HBr through Hexanol Films at the Surface of Supercooled Sulfuric Acid." *Journal of Physical Chemistry A* 110(24).
- Gogou A., Stratigakis N., Kanakidou M., et al. (1996). "Organic aerosols in Eastern Mediterranean: components source reconciliation by using molecular markers and atmospheric back trajectories." *Organic Geochemistry* 25(1-2).
- Gong S. L., Barrie L. A. and Lazare M. (2002). "Canadian Aerosol Module (CAM): A size-segregated simulation of atmospheric aerosol processes for climate and air quality models 2. Global sea-salt aerosol and its budgets." *J. Geophys. Res.* 107.
- Goodman A. L., Underwood G. M. and Grassian V. H. (1999). "Heterogeneous Reaction of NO₂: Characterization of Gas-Phase and Adsorbed Products from the Reaction, 2NO₂(g) + H₂O(a) → HONO(g) + HNO₃(a) on Hydrated Silica Particles." *Journal of Physical Chemistry A* 103(36).
- Grassian V. H. (2002). "Chemical Reactions of Nitrogen Oxides on the Surface of Oxide, Carbonate, Soot, and Mineral Dust Particles: Implications for the Chemical Balance of the Troposphere." *Journal of Physical Chemistry A* 106(6).
- Guimbaud C., Arens F., Gutzwiller L., et al. (2002). "Uptake of HNO₃ to deliquescent sea-salt particles: a study using the short-lived radioactive isotope tracer ¹³N." *Atmospheric Chemistry and Physics* [online computer file] 2.
- Hallou A., Schriver-Mazzuoli L., Schriver A., et al. (1998). "Matrix photochemistry of nitrosyl chloride.: Interconversion of ClNO and ClON species by irradiation and tunneling effect." *Chemical Physics* 237(3).
- Hearn J. D., Lovett A. J. and Smith G. D. (2005). "Ozonolysis of oleic acid particles: evidence for a surface reaction and secondary reactions involving Criegee intermediates." *Physical Chemistry Chemical Physics* 7(3).

- Heilderberg I. Mondial Tropospheric NO₂ vertical column density 01/2003 - 06/2004, ESA, ESA pg The image shows the global mean tropospheric nitrogen dioxide (NO₂) vertical column density (VCD) between January 2003 and June 2004.
- Hoffman R. C., Gebel M. E., Fox B. S., et al. (2003a). "Knudsen cell studies of the uptake and reaction of HNO₃ and N₂O₅ on sub-layers of NaCl." Combined Preprints CD-ROM - AMS Annual Meeting, 83rd, Long Beach, CA, United States, Feb. 9-13, 2003.
- Hoffman R. C., Gebel M. E., Fox B. S., et al. (2003b). "Knudsen cell studies of the reactions of N₂O₅ and ClONO₂ with NaCl: development and application of a model for estimating available surface areas and corrected uptake coefficients." *Physical Chemistry Chemical Physics* 5(9).
- Hoffman R. C., Kaleuati M. A. and Finlayson-Pitts B. J. (2003). "Knudsen cell studies of the reaction of gaseous HNO₃ with NaCl using less than a single layer of particles at 298 K: A modified mechanism." *Journal of Physical Chemistry A* 107(39).
- Hopkins R. J., Mitchem L., Wardw A. D., et al. (2004). "Control and characterisation of a single aerosol droplet in a single-beam gradient-force optical trap." *Phys . Chem. Chem. Phys .* 6 pg. 4924.
- Iimura K.-i., Yamauchi Y., Tsuchiya Y., et al. (2001). "Two-Dimensional Dendritic Growth of Condensed Phase Domains in Spread Monolayers of cis-Unsaturated Fatty Acids." *Langmuir* 17(15).
- Jen S., Clark N. A., Pershan P. S., et al. (1977). "Polarized Raman scattering studies of orientational order in uniaxial liquid crystalline phases." *The Journal of Chemical Physics* 66(10).
- Johnson E. R., Sciegienka J., Carlos-Cuellar S., et al. (2005). "Heterogeneous Uptake of Gaseous Nitric Acid on Dolomite (CaMg(CO₃)₂) and Calcite (CaCO₃) Particles: A Knudsen Cell Study Using Multiple, Single, and Fractional Particle Layers." *Journal of Physical Chemistry A* 109(31).
- Jores K. (2004). Lipid nanodispersions as drug carrier systems - a physicochemical characterization pg No pp given.
- Kajiyama T., Oishi Y., Hirose F., et al. (1994). "Direct Observation of Molecular Arrangements in Fatty Acid Monolayers with an Atomic Force Microscope." *Langmuir* 10(4).
- Kajiyama T. and Aizawa M. (1996). New developments in construction and functions of organic thin films. Amsterdam, Elsevier.
- Kajiyama T., Oishi Y. and Kuri T. (1996). "Direct observation of defect-diminished fatty acid monolayers and their optical applications." *Thin Solid Films* 273(1-2).
- Kamboures M. A., van der Veer W., Gerber R. B., et al. (2008). "Raman spectra of complexes of HNO₃ and NO₃⁻ with NO₂ at surfaces and with N₂O₄ in solution." *Phys . Chem. Chem. Phys .* 10 pg. 4748.

- Karagulian F., Dilbeck C. W. and Finlayson-Pitts B. J. (2009). "Nitrite-Induced Oxidation of Organic Coatings on Models for Airborne Particles" *The Journal of Physical Chemistry A* 113(26).
- Karlsson R. and Ljungström E. (1996). "Laboratory Study of ClNO: Hydrolysis." *Environmental Science & Technology* 30(6).
- Katrib Y., Martin S. T., Hung H.-M., et al. (2004). "Products and Mechanisms of Ozone Reactions with Oleic Acid for Aerosol Particles Having Core-Shell Morphologies." *The Journal of Physical Chemistry A* 108(32).
- Kirchner U., Scheer V. and Vogt R. (2000). "FTIR Spectroscopic Investigation of the Mechanism and Kinetics of the Heterogeneous Reactions of NO₂ and HNO₃ with Soot." *Journal of Physical Chemistry A* 104(39).
- Kittel C. (1986). *Introduction to Solid Phase Physics*. New York, Wiley.
- Knopf D. A., Anthony L. M. and Bertram A. K. (2005). "Reactive Uptake of O₃ by Multicomponent and Multiphase Mixtures Containing Oleic Acid." *Journal of Physical Chemistry A* 109(25).
- Kobayashi M., Kaneko F., Sato K., et al. (1986). "Vibrational spectroscopic study on polymorphism and order-disorder phase transition in oleic acid." *Journal of Physical Chemistry* 90(23).
- Kobayashi T., Ikezawa T. and Watanabe H. (1979). "Behavior of sea salt particles in the ambient air. Interaction between sea salt particles and nitrogen dioxide." *Taiki Osen Gakkaishi* 14(10).
- Langer S., Pemberton R. S. and Finlayson-Pitts B. J. (1997). "Diffuse Reflectance Infrared Studies of the Reaction of Synthetic Sea Salt Mixtures with NO₂: A Key Role for Hydrates in the Kinetics and Mechanism." *Journal of Physical Chemistry A* 101(7).
- Lapshin R. V. (1995). "Analytical model for the approximation of hysteresis loop and its application to the scanning tunneling microscope." *Review of Scientific Instruments* 66(9).
- Li H., Zhu T., Ding J., et al. (2006). "Heterogeneous reaction of NO₂ on the surface of NaCl particles." *Science in China, Series B: Chemistry* 49(4).
- Li P., Al-Abadleh H. A. and Grassian V. H. (2002). "Measuring Heterogeneous Uptake Coefficients of Gases on Solid Particle Surfaces with a Knudsen Cell Reactor: Complications Due to Surface Saturation and Gas Diffusion into Underlying Layers." *Journal of Physical Chemistry A* 106(7).
- Li X.-H., Wang F., Lu P.-D., et al. (2006). "Confocal Raman Observation of the Efflorescence/Deliquescence Processes of Individual NaNO₃ Particles on Quartz." *Journal of Physical Chemistry B* 110(49).
- Liu D.-Y., Prather K. A. and Hering S. V. (2000). "Variations in the size and chemical composition of nitrate-containing particles in Riverside, CA." *Aerosol Science and Technology* 33(1-2).

- Liu Y., Cain J. P., Wang H., et al. (2007). "Kinetic Study of Heterogeneous Reaction of Deliquesced NaCl Particles with Gaseous HNO₃ Using Particle-on-Substrate Stagnation Flow Reactor Approach." *Journal of Physical Chemistry A* 111(40).
- Luxenhofer O., Schneider M., Dambach M., et al. (1996). "Semivolatile long chain C₆-C₁₇ alkyl nitrates as trace compounds in air." *Chemosphere* 33(3).
- Marsh D. (1990). *Handbook of lipid bilayers*, CRC.
- McNeill V. F., Patterson J., Wolfe G. M., et al. (2006). "The effect of varying levels of surfactant on the reactive uptake of N₂O₅ to aqueous aerosol." *Atmospheric Chemistry and Physics* 6(6).
- McNeill V. F., Wolfe G. M. and Thornton J. A. (2007). "The Oxidation of Oleate in Submicron Aqueous Salt Aerosols: Evidence of a Surface Process." *Journal of Physical Chemistry A* 111(6).
- Ming Y. and Russell L. M. (2001). "Predicted hygroscopic growth of sea salt aerosol." *Journal of Geophysical Research*, [Atmospheres] 106(D22).
- Mmereki B. T., Donaldson D. J., Gilman J. B., et al. (2004). "Kinetics and products of the reaction of gas-phase ozone with anthracene adsorbed at the air-aqueous interface." *Atmospheric Environment* 38(36) pg. 6091.
- Mochida M., Kitamori Y., Kawamura K., et al. (2002). "Fatty acids in the marine atmosphere: factors governing their concentrations and evaluation of organic films on sea-salt particles." *Journal of Geophysical Research*, [Atmospheres] 107(D17).
- Mogili P. K., Kleiber P. D., Young M. A., et al. (2006). "N₂O₅ hydrolysis on the components of mineral dust and sea salt aerosol: Comparison study in an environmental aerosol reaction chamber." *Atmospheric Environment* 40(38).
- Moise T. and Rudich Y. (2000). "Reactive uptake of ozone by proxies for organic aerosols: Surface versus bulk processes." *Journal of Geophysical Research*, [Atmospheres] 105(D11).
- Mularczyk E. and Drzymala J. (1996). "Removal of Decomposition Products from Sodium Oleate." *Industrial & Engineering Chemistry Research* 35(3).
- Mylonas D. T., Allen D. T., Ehrman S. H., et al. (1991). "The sources and size distribution of organonitrates in Los Angeles aerosol." *Atmospheric Environment, Part A: General Topics* 25A(12).
- Najera J. J. (2007). "Phase transition behaviour of sodium oleate aerosol particles." *Atmospheric Environment* 41(5).
- NIST NIST Webbook.
- O'Brien J. M., Shepson P. B., Wu Q., et al. (1997). "Production and distribution of organic nitrates, and their relationship to carbonyl compounds in an urban environment." *Atmospheric Environment* 31(14).

- Osterroht C. (1993). "Extraction of dissolved fatty acids from sea water." *Fresenius' Journal of Analytical Chemistry* 345(12).
- Park S.-C., Burden D. K. and Nathanson G. M. (2007). "The Inhibition of N_2O_5 Hydrolysis in Sulfuric Acid by 1-Butanol and 1-Hexanol Surfactant Coatings." *Journal of Physical Chemistry A* 111(15).
- Perrin A. (1998). "Recent progress in the analysis of HNO_3 spectra." *Spectrochimica Acta Part A: Molecular and Biomolecular Spectroscopy* 54(3).
- Perrin A., Flaud J. M., Goldman A., et al. (1998). " NO_2 and SO_2 line parameters: 1996 hitran update and new results." *J. Quant. Spectrosc. Radiat. Transfer* 60(5) pg. 839.
- Peters S. J. and Ewing G. E. (1996). "Reaction of $NO_2(g)$ with $NaCl(100)$." *Journal of Physical Chemistry* 100(33).
- Peters S. J. and Erwing G. E. (1997). *Langmuir* 13 pg. 6345.
- Preszler Prince A., Grassian V. H., Kleiber P., et al. (2007). "Heterogeneous conversion of calcite aerosol by nitric acid." *Physical Chemistry Chemical Physics* 9(5).
- Prince A. P., Kleiber P., Grassian V. H., et al. (2007). "Heterogeneous interactions of calcite aerosol with sulfur dioxide and sulfur dioxide-nitric acid mixtures." *Physical Chemistry Chemical Physics* 9(26).
- Randles C. A., Russell L. M. and Ramaswamy V. (2004). "Hygroscopic and optical properties of organic sea salt aerosol and consequences for climate forcing." *Geophysical Research Letters* 31(16).
- Reid J. P. and Sayer R. M. (2003). "Heterogeneous atmospheric aerosol chemistry: laboratory studies of chemistry on water droplets." *Chemical Society Reviews* 32(2).
- Rimetz-Planchon J. (2007). *Les aérosols de pollution en zone urbaine et industrielle sous influence marine. Physico-chimie des particules. Structure et Dynamique des Systèmes réactifs.* Lille, Université des Sciences et Technologie de Lille. Docteur pg 263.
- Rossi M. J. (2003). "Heterogeneous Reactions on Salts." *Chem. Rev.* 2003 103 pg. 4823.
- Rousseau D. L., Miller R. E. and Leroi G. E. (1968). "Raman spectrum of crystalline sodium nitrate." *Journal of Chemical Physics* 48(8).
- Rudich Y. (2003). "Laboratory Perspectives on the Chemical Transformations of Organic Matter in Atmospheric Particles." *Chem. Rev.* 103(12).
- Russell L. M., Maria S. F. and Myneni S. C. B. (2002). "Mapping organic coatings on atmospheric particles." *Geophys. Res. Lett.* 29.
- Saul T. D., Tolocka M. P. and Johnston M. V. (2006). "Reactive Uptake of Nitric Acid onto Sodium Chloride Aerosols Across a Wide Range of Relative Humidities." *The Journal of Physical Chemistry A* 110(24).

- Sayer R. M. and Horn A. B. (2003). "Simultaneous spectroscopic detection of adsorbed and gas-phase species during atmospherically relevant heterogeneous reactions." *Physical Chemistry Chemical Physics* 5(23).
- Scheer V., Frenzel A., Behnke W., et al. (1997). "Uptake of Nitrosyl Chloride (NOCl) by Aqueous Solutions." *The Journal of Physical Chemistry A* 101(49).
- Schwartz S. E. and White W. H. (1981). *Solubility equilibria of the nitrogen oxides and oxyacids in dilute aqueous solution*. NY, Gordon and Breach Science Publishers.
- Scolaro S., Sobanska S., Barbillat J., et al. (2009). "Confocal Raman imaging and atomic force microscopy of the surface reaction of NO₂ and NaCl(100) under humidity." *Journal of Raman Spectroscopy* 40(2).
- Seidl W. (2000). "Model for a surface film of fatty acids on rain water and aerosol particles." *Atmospheric Environment* 49(17-34) 4917-4932 34 pg. 4917.
- Sicre M. A., Marty J. C. and Saliot A. (1990). "N-alkanes, fatty acid esters, and fatty acid salts in size fractionated aerosols collected over the Mediterranean Sea." *Journal of Geophysical Research* ; Vol/Issue: 95:D4.
- Sourisseau C. (2004). "Polarization Measurements in Macro- and Micro-Raman Spectroscopies: Molecular Orientations in Thin Films and Azo-Dye Containing Polymer Systems." *Chemical reviews* 104(9).
- Spicer C. W., Chapman E. G., Finlayson-Pitts B. J., et al. (1998). "Unexpectedly high concentrations of molecular chlorine in coastal air." *Nature* 394(6691).
- Stemmler K., Vlasenko A., Guimbaud C., et al. (2008). "The effect of fatty acid surfactants on the uptake of nitric acid to deliquesced NaCl aerosol." *Atmospheric Chemistry and Physics* 8(16).
- Stephanou E. G. (1992). "Biogenic and anthropogenic organic-compounds in eolian particulates in the east Mediterranean region. 1. Occurrence and origin." *Atmospheric Environment* 26(15) pg. 2821.
- Sverdrup G. M. and Kuhlman M. R. (1980). *Heterogeneous nitrogen oxide-particle reactions*.
- Tabazadeh A. (2005). "Organic aggregate formation in aerosols and its impact on the physicochemical properties of atmospheric particles." *Atmospheric Environment* 39 pg. 5472.
- Tang I. N. and Munkelwitz H. R. (1994). "Aerosol Phase Transformation and Growth in the Atmosphere." *Journal of Applied Meteorology* 33(7).
- Tang I. N., Fung K. H., Imre D. G., et al. (1995). "Phase transformation and metastability of hygroscopic microparticles." *Aerosol Science and Technology* 23(3).
- Tervahattu H., Juhanaja J. and Kupiainen K. (2002). "Identification of an organic coating on marine aerosol particles by TOF-SIMS." *J. Geophys. Res.* 107.
- Tervahattu H., Juhanaja J., Vaida V., et al. (2005). "Fatty acids on continental sulfate aerosol particles." *J. Geophys. Res.* 110.

- Thornberry T. and Abbatt J. P. D. (2004). "Heterogeneous reaction of ozone with liquid unsaturated fatty acids: detailed kinetics and gas-phase product studies." *Physical Chemistry Chemical Physics* 6(1).
- Thornton J. A. and Abbatt J. P. D. (2005). "N₂O₅ Reaction on Submicron Sea Salt Aerosol: Kinetics, Products, and the Effect of Surface Active Organics." *Journal of Physical Chemistry A* 109(44).
- Turrell G. (1972). "Infrared and Raman spectra of crystals." *Journal of Molecular Structure* 16(3) pg. 504.
- Ullerstam M., Johnson M. S., Vogt R., et al. (2003). "DRIFTS and Knudsen cell study of the heterogeneous reactivity of SO₂ and NO₂ on mineral dust." *Atmos. Chem. Phys.* 3(6).
- Underwood G. M., Miller T. M. and Grassian V. H. (1999). "Transmission FT-IR and Knudsen Cell Study of the Heterogeneous Reactivity of Gaseous Nitrogen Dioxide on Mineral Oxide Particles." *Journal of Physical Chemistry A* 103(31).
- Underwood G. M., Li P., Usher C. R., et al. (2000). "Determining accurate kinetic parameters of potentially important heterogeneous atmospheric reactions on solid particle surfaces with a Knudsen cell reactor." *Journal of Physical Chemistry A* 104(4).
- Underwood G. M., Song C. H., Phadnis M., et al. (2001). "Heterogeneous reactions of NO₂ and HNO₃ on oxides and mineral dust: a combined laboratory and modeling study." *Journal of Geophysical Research, [Atmospheres]* 106(D16).
- Usher C. R., Michel A. E. and Grassian V. H. (2003). "Reactions on Mineral Dust." *Chem. Rev.* 2003, 103, 4883-4939 103 pg. 4883.
- Verdaguer A., Segura J. J., Fraxedas J., et al. (2008). "Correlation between Charge State of Insulating NaCl Surfaces and Ionic Mobility Induced by Water Adsorption: A Combined Ambient Pressure X-ray Photoelectron Spectroscopy and Scanning Force Microscopy Study." *The Journal of Physical Chemistry C* 112(43).
- Vesna O., Gäggeler H. W., Kalberer M., et al. (2005). Quantitative analysis of the products of the heterogeneous reaction between oleic acid aerosol and ozone. *Ann. Rep. Univ. Bern & PSI* 2005.
- Vieceli J., Ma O. L. and Tobias D. J. (2004). "Uptake and Collision Dynamics of Gas Phase Ozone at Unsaturated Organic Interfaces." *Journal of Physical Chemistry A* 108(27).
- Vogt J. and Weiss H. (2001). "The structure of NaCl(100) and KCl(100) single crystal surfaces: a tensor low energy diffraction analysis." *Surface Science* 491(1-2) pg. 155.
- Vogt R. and Finlayson-Pitts B. J. (1994). "A Diffuse Reflectance Infrared Fourier Transform Spectroscopic Study of the Surface Reaction of NaCl with Gaseous NO₂ and HNO₃." *Journal of Physical Chemistry* 98(14).
- Voss L. F., Hadad C. M. and Allen H. C. (2006). "Competition between Atmospherically Relevant Fatty Acid Monolayers at the Air/Water Interface." *J. Phys. Chem. B* 110 pg. 19487.

- Wadia Y., Tobias D. J., Stafford R., et al. (2000). "Real-Time Monitoring of the Kinetics and Gas-Phase Products of the Reaction of Ozone with an Unsaturated Phospholipid at the Air-Water Interface." *Langmuir* 16(24).
- Wan J. K. S., Pitts J. N., Jr., Beichert P., et al. (1996). "The formation of free radical intermediates in the reactions of gaseous NO₂ with solid NaCl and NaBr - atmospheric and toxicological implications." *Atmospheric Environment* 30(18).
- Weis D. D. and Ewing G. E. (1999). "The reaction of nitrogen dioxide with sea salt aerosol." *Journal of Physical Chemistry A* 103(25).
- Wingen L. M., Moskun A. C., Johnson S. N., et al. (2008). "Enhanced surface photochemistry in chloride-nitrate ion mixtures." *Phys. Chem. Chem. Phys.* 10.
- Winkler T., Goschnick J. and Ache H. J. (1991). "Reactions of nitrogen oxides with NaCl as model of sea salt aerosol " *Journal of Aerosol Science* 22(S1) pg. S605.
- Wong P. T. T. and Mantsch H. H. (1983). "Temperature-induced phase transition and structural changes in micellar solutions of sodium oleate observed by Raman scattering." *Journal of Physical Chemistry* 87(13).
- Xiao H.-S., Dong J.-L., Wang L.-Y., et al. (2008). "Spatially Resolved Micro-Raman Observation on the Phase Separation of Effloresced Sea Salt Droplets." *Environmental Science & Technology* 42(23).
- Xiong J. Q., Zhong M., Fang C., et al. (1998). "Influence of Organic Films on the Hygroscopicity of Ultrafine Sulfuric Acid Aerosol." *Environmental Science and Technology* 32(22).
- Yoshitake H. (2000). "Effects of surface water on NO₂-NaCl reaction studied by diffuse reflectance infrared spectroscopy (DRIRS)." *Atmospheric Environment* 34(16).
- Zangmeister C. D. and Pemberton J. E. (1998). "In Situ Monitoring of the NaCl+HNO₃ Surface Reaction: The Observation of Mobile Surface Strings." *Journal of Physical Chemistry B* 102(45).
- Zangmeister C. D. and Pemberton J. E. (2001). "Raman spectroscopy of the reaction of sodium chloride with nitric acid: sodium nitrate growth and effect of water exposure." *Journal of Physical Chemistry A* 105(15).

Appendix A

Appendix A

Quantification of NO₂ in the gas phase:

NO₂ concentration in the gas mixture can be calculated by volumetric dilution from the expression:

$$(A.1) \quad [\text{NO}_2]_{\text{g}} = 7.25 \cdot 10^{21} \frac{Q_{\text{NO}_2}}{Q_{\text{TOT}}} \frac{P}{T}$$

Where

- [NO₂]_g is the concentration in molecules·cm⁻³,
- Q_{NO₂} is the volumetric flow of NO₂ at the standard temperature and pressure conditions in mL·min⁻¹,
- Q_{TOT} is the sum of the three volumetric flows at (T,P)_{STD} in mL·min⁻¹,
- P is the total pressure in bar
- T is the temperature in K

The values of NO₂ retained in this work come from optical spectroscopy measurements, because in presence of water vapour, real NO₂ concentration can diminish from the original volumetric dilution calculated concentration due to the instauration of complex equilibria with other acidic species.

We determined [NO₂]_g by FT-IR after a calibration by adding known quantity of dry NO₂ inside the spectrometer, so that:

$$(A.2) \quad [\text{NO}_2]_{\text{g}} = 2.06 \times 10^{17} \text{ molec cm}^{-3} \cdot I$$

Where I is the absorption intensity at 1627cm⁻¹ when the spectra are acquired with a 4cm⁻¹ spectral resolution and the eventual interference of water are substracted.

The use of absorption coefficients reported in previous works (i.e. [Perrin A. *et al.*, 1998]) was not possible because of the different acquisition conditions, especially the spectral resolution which is a critical parameter in gas-phase spectra. Moreover, in the same work great uncertainties are reported, especially for the more intense transition band centred at 1618 cm⁻¹.

Quantification of ClNO in the gas phase:

Optical measurement of the absorption intensities in the IR region can lead to the quantification of ClNO through the Beer-Lambert law:

$$(A.3) \quad [\text{ClNO}]_{\text{g}} = A / \epsilon b$$

Where A is the absorbance value (intensity or integrated area), b the optical path and ϵ the associated extinction coefficient.

[Karlsson R. *et al.*, 1996] gives a value ϵ at 1799 cm⁻¹ of $(9.34 \pm 0.22) \cdot 10^{-19}$ when the ClNO gaseous spectrum is acquired in the following experimental conditions:

- 1cm⁻¹ of spectral resolution,
- T=(296±1)K
- P=(101000±1000)Pa.

In our experiments the spectral resolution is 4 cm^{-1} , so that need to register two CINO spectra of the same gaseous sample at 1 and 4 cm^{-1} resolution for a direct comparison of their intensities. In fig. A3 you can see a zoom in the 1800 cm^{-1} ν_1 transition of the two IR spectra acquired at $T=298\pm 1\text{ K}$, $P=102480\pm 100\text{ Pa}$ where the effect of spectral resolution on the recorded intensities is highlighted:

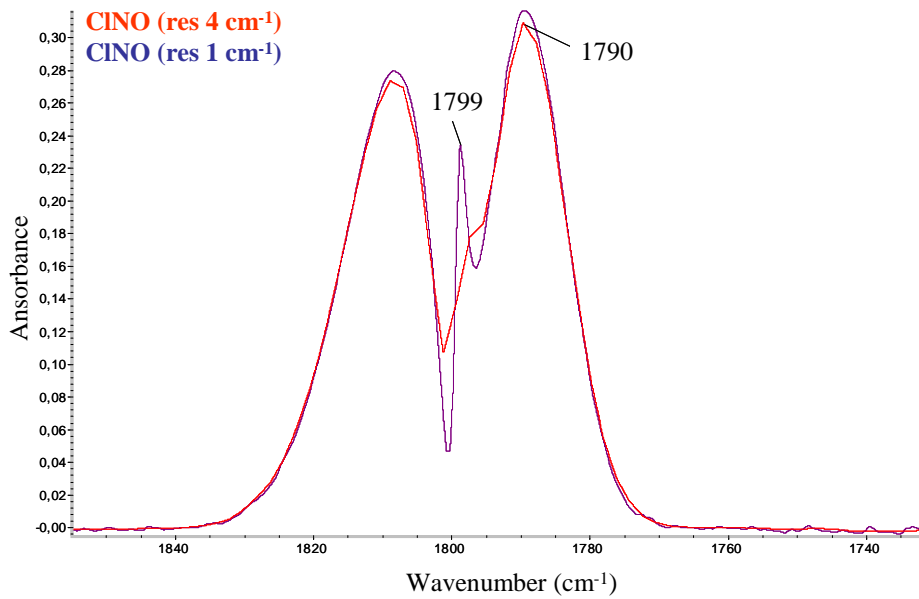


Fig.A.2 FTIR spectra of a gaseous sample of CINO with a spectral resolution of a 4 cm^{-1} (in red) and 1 cm^{-1} (in blue).

A direct comparison of the intensities of the two spectra at two different wavelengths ($\tilde{\nu}_1=1799\text{ cm}^{-1}$; $\tilde{\nu}_2=1790\text{ cm}^{-1}$) leads, from expression A.3 to:

$$(A.4) \quad [\text{CINO}] = \frac{A_1}{b \cdot \epsilon_1} = \frac{A_2}{b \cdot \epsilon_2}$$

Where:

- ϵ_1 is the reference value given from the reference work;
- A_2 is the absorption intensity in the 4 cm^{-1} spectrum at 1790 cm^{-1} ;
- A_1 is the absorption intensity in the 1 cm^{-1} spectrum at 1799 cm^{-1} .

We can then calculate the extinction coefficient ϵ_2 at 1790 cm^{-1} when the spectrum is acquired with a 4 cm^{-1} spectral:

$$(A.5) \quad \epsilon_2 = \frac{A_2}{A_1} \cdot \epsilon_1$$

With an estimated error $<5\%$ we can measure CINO gas concentration in our experimental conditions ($b=10\text{ cm}$) from the following expression:

$$(A.6) \quad [\text{CINO}] = \frac{I@1790\text{ cm}^{-1}}{10 * 1.21 \cdot 10^{-18}} \text{ molec cm}^{-3}$$

Effet de l'humidité et de molécules tensio-actives sur la capture du dioxyde d'azote (NO₂) par le chlorure de sodium (NaCl). Etude cinétique et analyse de surface.

Résumé

Des études cinétiques et des analyses de surface ont été effectuées sur la réaction multiphasique entre le gaz NO₂ et des cristaux de NaCl en présence de molécules tensio-actives sous air humide. Ces études de laboratoire contribuent à la validation de processus de chimie atmosphérique suggérés par des campagnes de mesure sur des aérosols d'origine marine. Les vents provoquant des vagues à la surface des océans propulsent de nombreuses gouttelettes d'eau de mer dans la troposphère où elles se déshydratent partiellement et forment l'aérosol marin, constitué de particules de taille micrométrique comportant du NaCl et de nombreux composés mineurs dont des acides gras (stéarique, oléique). Les concentrations en particules peuvent dépasser 20 µg/m³ dans l'air des zones côtières. Des quantités énormes d'oxydes d'azote (NO, NO₂) sont émises actuellement par les transports et le chauffage et leur concentrations peuvent dépasser 100 µg/m³ dans les zones fortement anthropisées. Le passage de masses d'air d'origine marine dans des zones fortement urbanisées a des impacts négatifs sur la qualité des eaux continentales par des pluies chargées en nitrates et sur la qualité de l'air par des dégagements de gaz chlorés. La cinétique de la réaction montre que la capture de NO₂ par NaCl est favorisée à des fortes humidités. Par contre un revêtement d'acides gras réduit peu la production de NaNO₃ et l'émission de NOCl. Les études de surfaces par microimagerie Raman polarisée et microscopie à force atomique mettent en évidence des processus de précipitation et de migration de surface dans la production de nanocristaux de NaNO₃ et le faible rôle protecteur des molécules tensio-actives.

Effects of humidity and fatty acid surfactants on the uptake of NO₂ to NaCl. Combined study of kinetics and surface analysis.

Abstract

In this laboratory work we studied an important atmospheric process typical of polluted coastal regions: the heterogeneous reaction of a gaseous pollutant of mainly anthropogenic origin, NO₂, on NaCl(100), taken as a surrogate for marine aerosol. Evidence of the presence of a native organic coating on field-collected marine aerosol particles inspired us to investigate the effect of insoluble fatty acids on the heterogeneous removal reaction of NO_x in the marine boundary layer.

The originality of this work consists in coupling reactivity studies with high spatial resolution surface analysis. The surface is followed, before and after reaction, via Raman micro-spectrometry and AFM techniques. Significant modifications in the morphology and orientation of the formed NaNO₃ crystals on the surface are found as a function of humidity during the reaction.

A thin organic coating on the salt surface is prepared and characterized. The reactivity of the coated/uncoated salt is measured in a static reactor where the gaseous phase composition can be monitored by FTIR spectrometry in different humidities (RH=0-80%). From NO₂ and ClNO kinetics we can independently estimate both the uptake (γ) and the reaction probability (ϕ) coefficients. The presence of a palmitic or oleic acid coating slightly hinders the reactivity, especially in some humidities.

By coupling all experimental information to a simple reactivity model which fits the experimental data well, we can conclude that the NO₂/NaCl reaction directly releases a precursor of active chlorine atoms (ClNO) into the atmosphere, even at high humidities.

Sciences de la Matière, du Rayonnement et de l'Environnement – Université Lille1

Laboratories: Laboratoire de Spectrochimie Infrarouge et Raman, LASIR, UMR 8516, bât. C5 and Physicochimie des Processus de Combustion et de l'Atmosphère, PC2A, UMR 8522 bât. C11 - 59655 Villeneuve d'Ascq Cedex (France)